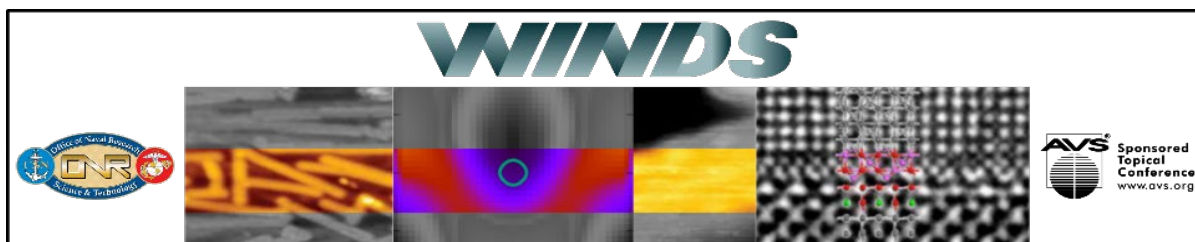


**2019 Workshop on  
Innovative Nanoscale Devices and Systems**

# WINDS

## Book of Abstracts

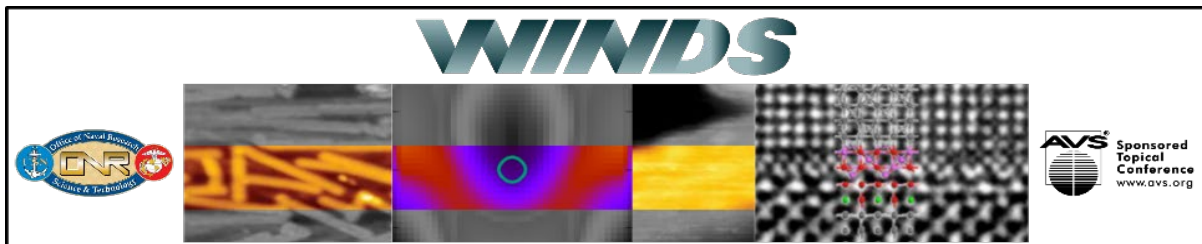


December 1 - 6, 2019, Fairmont Orchid Hotel, Kohala Coast, Hawaii, USA

# 2019 Workshop on Innovative Nanoscale Devices and Systems

# WINDS

## Book of Abstracts



December 1 – 6, 2019, Fairmont Orchid Hotel, Kohala Coast, Hawaii, USA

### Edited By

David Janes

Henning Riechert

Tomoki Machida

John F. Conley

Josef Weinbub

Stephen Goodnick

The 2019 Workshop on Innovative Nanoscale Devices and Systems (WINDS) was held December 1 – 6, 2019, at the Fairmont Orchid Hotel, Kohala Coast, Hawaii, USA.

WINDS is a week-long, international, and interactive workshop designed to explore the fundamental properties of nanoscale devices and applications thereof. In particular, WINDS provides a forum for material, device, and characterization as well as experimental and modeling researchers to interact.

The program consists of invited talks, regular talks, and poster presentations. All contributions have been peer-reviewed by the program committee.

This workshop is composed of morning and evening sessions, with afternoons free for ad hoc meetings to encourage extended interaction and discussion among participants. It is the successor of the original WINDS and the International Symposium on Advanced Nanodevices and Nanotechnology (ISANN), which were held on alternate years. WINDS itself began as an outgrowth of the successful Advanced Heterostructures Workshop, which has a long history dating from the 1980s.

WINDS 2019 is an AVS Sponsored Topical Conference, with financial support from the US Office of Naval Research. The conference committee greatly appreciates their support.



ISBN 978-0-578-61722-0

© 2019 Institute for Microelectronics, TU Wien

Gußhausstraße 27-29, 1040 Wien, Austria

**Conference Chairs**

General Chair: David Janes, Purdue University, USA  
Europe Co-Chair: Henning Riechert, Paul Drude Institute, Germany  
Japan Co-Chair: Tomoki Machida, University of Tokyo, Japan  
US Co-Chair: John F. Conley, Oregon State University, USA  
Communications Chair: Josef Weinbub, TU Wien, Austria  
Local Arrangements: Stephen Goodnick, Arizona State University, USA

**Program Committee**

Alexander Balandin, University of California at Riverside, USA  
Jaroslav Fabian, University of Regensburg, Germany  
David K. Ferry, Arizona State University, USA  
Matthew Gilbert, Stanford University, USA  
Koji Ishibashi, RIKEN, Japan  
Berend T. Jonker, Naval Research Laboratory, USA  
Akinobu Kanda, University of Tsukuba, Japan  
Victor Klimov, Los Alamos National Laboratory, USA  
Valeria Lauter, Oak Ridge National Laboratory, USA  
Saulius Marcinkevičius, KTH Royal Institute of Technology, Sweden  
Kazuhiko Matsumoto, Osaka University, Japan  
Wolfgang Porod, University of Notre Dame, USA  
Viktor Sverdlov, TU Wien, Austria



**WINDS 2019 Program**

**Sunday, December 1**

**15:00-18:00 Registration, Plaza 3 Foyer**

**18:00-20:00 Gala Reception, Croquet Lawn**

**Monday, December 2 – Plaza Ballroom**

9:00-9:15 **Welcome and Conference Overview**, Stephen Goodnick

**Session 1. Topological and Quantum Systems - I**

Session Chair: Jaroslav Fabian

- 9:15-9:45 S. Parkin, *Max Planck Institute, Germany*  
 “Chiral and Spatial Spin Textures” (invited)..... 1
- 9:45-10:15 B. Bradlyn, *University of Illinois at Urbana-Champaign, USA*, “Chiral Currents in a Correlated Compound: Weyl-Charge Density Waves” (invited)..... 2
- 10:15-10:30 J. Vayrynen, R. Lutchyn, *Microsoft Quantum, Station Q, USA*, and A. Feiguin, *Northeastern University, USA*, “Microscopic Description of Coulomb Blockaded Topological Superconducting Island Coupled to Many Leads” ..... 3
- 10:30-11:00 **Coffee Break**
- 11:00-11:15 D. Vanmaekelbergh, I. Swart, C. M. Smith, *University of Utrecht, Netherlands*, and C. Delerue, *Université Polytechnique Hauts-de-France, France*, “2-D Electronic Systems with s- and p Orbital Dirac Physics Created in a Scanning Tunnelling Microscope” ..... 5
- 11:15-11:30 M.-Y. Im, *Lawrence Berkeley National Laboratory, USA*, H.-S. Lee, and K.-S. Lee, *Ulsan National Institute of Science and Technology, Republic of Korea*, “Dynamic Behavior of Topological Spin Singularity Studied by Soft X-ray Microscopy” ..... 7
- 11:30-12:00 D.R. Candido, J.C. Egues, *Universidade de São Paulo, Brazil*, and M.E. Flatté, *University of Iowa, USA*, “Topological and Nontopological Edge States in Ordinary Quantum Matter” (invited)..... 9
- 12:00-12:15 I. Zutic, T. Zhou, J. Han, *University at Buffalo, USA*, M.C. Dartailh, W. Mayer, A. Kent, J. Shabani, *New York University, USA*, N. Mohanta, and A. Matos-Abiague, *Wayne State University, USA*, “Scalable Majorana States and Phase Measurement of Topological Superconductivity” ..... 11
- 12:15-12:30 L. Zhao, E. Arnault, A. Bondarev, A. Seredinski, T. Larson, A. Draelos, H. Li, T. Taniguchi, K. Watanabe, F. Amet, H. Baranger, and G. Finkelstein, *Duke University, USA*, *Appalachian State University, USA* and *Advanced Materials Laboratory, Japan*, “Detection of Chiral Andreev Edge States at the Quantum Hall – Superconductor Interface” ..... 13
- 12:30-12:45 M. Gilbert, *University of Illinois at Urbana-Champaign, USA*, “Coulomb Interactions in Magnetic Topological Heterostructures” ..... 15

12:45-13:00	<u>K. Semba</u> , <i>National Institute of Information and Communications Technology, Japan</i> , and <u>S. Ashhab</u> , <i>Hamad Bin Khalifa University, Qatar</i> , “Conical-Intersection and Berry Phase in Deep-Strongly Coupled Superconducting-Qubit-Resonator System” ..... 16
-------------	---

**13:00- 19:00 Ad Hoc Session**

**Session 2: Emerging Device and Processing Technologies**

Session Chairs: Saulius Marcinkevičius and Kathleen McCreary

19:00-19:15	<u>T.A. Zirkle</u> , <u>M.J. Filmer</u> , <u>A.O. Orlov</u> , <u>A.M. Mintairov</u> , and <u>G.L. Snider</u> , <i>University of Notre Dame, USA and Ioffe Institute, Russia</i> , “Application of RF Single Electron Devices for Scanning Probe Microscopy” ..... 18
19:15-19:30	<u>R. Wolkow</u> , <i>University Alberta, National Research Council, and Quantum Silicon Inc., Canada</i> , “Far Faster Fabrication of Binary Atomic Silicon Logic Circuitry” ..... 20
19:30-19:45	<u>X. Gao</u> , <u>D. Mamaluy</u> , <u>E. Anderson</u> , <u>D. Campbell</u> , <u>A. Grine</u> , <u>A. Katzenmeyer</u> , <u>T.-M. Lu</u> , <u>S. Schmucker</u> , <u>L. Tracy</u> , <u>D. Ward</u> , and <u>S. Misra</u> , <i>Sandia National Laboratories, USA</i> , “Modeling Assisted Atomic Precision Advanced Manufacturing (APAM) Towards Room Temperature Operation” ..... 22
19:45-20:00	<u>K.E.K. Holden</u> , <u>Y. Qi</u> , <u>M.A. Jenkins</u> , and <u>J.F. Conley</u> , <i>Oregon State University, USA</i> , “Atomic Layer Deposition Engineering of Metal/Insulator/Metal (MIM) Diodes using Localized Impurity Defects” ..... 24
20:00-20:15	<u>R.J. Waskiewicz</u> , <u>B. Manning</u> , and <u>P.M. Lenahan</u> , <i>Pennsylvania State University, USA</i> , “Electrically Detected Electron Nuclear Double Resonance in Fully Processed Transistors” ..... 26

**Session 3: Quantum Information Systems**

Session Chairs: Kathleen McCreary and Saulius Marcinkevičius

20:15-20:30	<u>A. Khitun</u> , <i>University of California at Riverside, USA</i> , “Quantum Computing without Quantum Computers: Database Search and Data Processing Using Classical Wave Superposition” ..... 28
20:30-20:45	<u>A. Mintairov</u> , <i>University of Notre Dame, USA and Ioffe Institute, Russia</i> , “Probing of Composite Fermions in Natural InP/GaInP <sub>2</sub> Quantum Hall Puddles using Near-field Scanning Optical Microscopy” ..... 30

**Tuesday, December 3– Plaza Ballroom**

**Session 4: Special Topical Session**

Session Chair: Stephen Goodnick

**9:00-9:30** C. Baatar, *Office of Naval Research, USA*, “Synthetic Electronics” (invited) .....32

**Session 5: Bioelectronics: Interfaces and Sensors**

Session Chair: Wolfgang Porod

9:30-10:00 M. Taniguchi, *Osaka University, Japan*, “Quantitative Analysis of DNA via Single-molecule Quantum Sequencing” (invited) .....33

10:00-10:30 A. Smolyanitsky and A. Fang, *National Institute of Standards and Technology, USA*, “Ion Transport Across Crown-like Sub-Nanoscale Pores in 2D Materials” (invited).....35

**10:30-11:00 Coffee Break**

11:00-11:30 H.T. Soh, *Stanford University, USA*, “Real-time Biosensors for Continuous Measurements of Biomolecules in Live Subjects” (invited).....36

11:30-11:45 S.T. Le, *National Institute of Standards and Technology, USA and Theiss Research, USA*, C.A. Richter, N.B. Guros, A. Balijepalli, *National Institute of Standards and Technology, USA*, N.D. Amin, and H.C. Pant, *National Institute of Neurological Disorders and Stroke, National Institutes of Health, USA*, “High Performance Dual-Gate 2-Dimensional MoS<sub>2</sub> pH and Biosensors” .....38

11:45-12:00 K. Matsumoto, *Osaka University, Japan*, “Towards the Practical Use of Graphene Bio-Sensor for Virus Detection” .....40

12:00-12:30 V.D. Bhatt, S. Joshi, B.D. Abera, G. Cantarella, and P. Lugli, *Free University of Bozen-Bolzano, Italy and Technical University of Munich, Germany*, “Printed Biosensors: Applications and Perspectives” (invited) .....41

12:30-12:45 S.V. Sridharan, J.F. Rivera, J. Nolan, S. Miloro, Z. (C.) Xing, M.A. Alam, J.L. Rickus, E. Tran, and D.B. Janes, *Purdue University, USA*, “Real-Time Measurements of Glucose Uptake in 2D Cell Cultures Using On-Chip Microelectrode Arrays” .....43

**12:45- 19:00 Ad Hoc Session**

**Session 6: Spintronics: Materials and Spin-Based Phenomena**

Session Chair: Valeria Lauter

19:00-19:30 D.K. Singh, *University of Missouri, USA*, “New Artificial Magnetic Honeycomb Lattice for Emergent Physics and Spintronics Application” (invited) .....45

19:30-19:45 J. Fabian, *University of Regensburg, Germany*, “Spin Physics in Ferromagnet/ Superconductor Tunnel Junctions” .....47

19:45-20:00 H. Aquino, D. Connelly, A. Papp, M. Becherer, G. Csaba, J. Chisum, A. Orlov, G.H. Bernstein, and W. Porod, *University of Notre Dame, USA, Pázmány University, Hungary and Technical University of Munich, Germany*, “Towards Spin-Wave-Based Devices: Experiments and Simulations” .....49

20:00-20:15	<u>N. Arabchigavkani</u> , R. Somphonsane, H. Ramamoorthy, G. He, J. Nathawat, S. Yin, B. Barut, J. Fransson, and J.P. Bird, <i>University at Buffalo, USA, King Mongkut’s Institute of Technology, Thailand and Uppsala University, Sweden</i> , “Suppression of Weak Localization in Bilayer Graphene due to Proximity Induced Spin Orbit Coupling” .....51
20:15-20:30	<u>Y. Takamura</u> , J.P. Cascales, R. Gonçalves, G. Stephen, D. Heiman, A. Altinkok, C.I.L. de Araujo, B. Satpati, V. Lauter, and J.S. Moodera, <i>Massachusetts Institute of Technology, Cambridge, USA, Tokyo Institute of Technology, Japan, Universidade Federal de Viçosa, Brazil, Northeastern University, USA, Giresun University, Turkey, Saha Institute of Nuclear Physics, India, and Oak Ridge National Laboratory, USA</i> , “Enhancement of the Interfacial Exchange Field in Superconducting Spin Valves of GdN/NbN/GdN Trilayers” .....53
20:30-20:45	<u>R. Lacerda de Orio</u> , S. Selberherr, J. Ender, S. Fiorentini, V. Sverdlov, <i>TU Wien, Austria</i> , and W. Goes, <i>Silvaco Europe Ltd., UK, United Kingdom</i> , “Robustness of the Two-Pulse Switching Scheme for SOT-MRAM” .....54

**Wednesday, December 4– Plaza Ballroom**

**Session 7: Wide Bandgap and Oxide Materials and Devices**

Session Chair: Viktor Sverdlov

9:00-9:30	<u>R. Kaplar</u> , A. Armstrong, A. Baca, B. Klein, E. Douglas, S. Reza, A. Allerman, M. Crawford, J. Dickerson, A. Binder, J. Flicker, J. Neely, and O. Slobodyan, <i>Sandia National Laboratories, USA</i> , “Ultra-Wide-Bandgap Aluminum Gallium Nitride for High-Performance Power-Switching and Radio-Frequency Devices” (invited).....56
9:30-9:45	<u>S. Marcinkevičius</u> , R. Yapparov, <i>KTH Royal Institute of Technology, Sweden</i> , L.Y. Kuritzky, S. Nakamura, and J.S. Speck, <i>University of California at Santa Barbara, USA</i> , “Carrier Transport Across Multiple InGaN Quantum Wells: Evidence of Ballistic Hole Transport” .....58
9:45-10:15	<u>K. Char</u> , <i>Seoul National University, Republic of Korea</i> , “Oxide Electronics Based on Wide Bandgap Perovskite BaSnO <sub>3</sub> ” (invited).....60
10:15-10:30	A.K. Hamze, K.D. Fredrickson, W. Li, and <u>A.A. Demkov</u> , <i>The University of Texas, USA</i> , “Pockels Effect in Si-integrated Perovskite Oxides” .....62

**10:30-11:00 Coffee Break**

11:00-11:30	<u>M. Higashiwaki</u> , M.H. Wong, Y. Kumagai, <i>National Institute of Information and Communications Technology, Japan</i> , K. Goto, and H. Murakami, <i>Tokyo University of Agriculture and Technology, Japan</i> , “Vertical Ga <sub>2</sub> O <sub>3</sub> MOSFETs Fabricated by Ion Implantation Process” (invited).....64
-------------	---

**Session 8: Topological and Quantum Systems -- II**

Session Chair: Matthew Gilbert

11:30-12:00	<u>C. Felser</u> , K. Manna, E. Lui, and Y. Sun, <i>Max Planck Institute Chemical Physics of Solids, Germany</i> , “Magnetic Weyl Semimetals!” (invited) .....66
-------------	--

12:00-12:15	T. Wu, Z. Wan, A. Kazakov, Y. Wang, G. Simion, J. Liang, K.W. West, K. Baldwin, L.N. Pfeiffer, Y. Lyanda-Geller, and <u>L.P. Rokhinson</u> , <i>Purdue University, USA</i> , “Formation of Helical States in the Fractional Quantum Hall Regime” ..... 67	67
12:15-12:30	Y. Tokura, <i>University of Tsukuba, Japan</i> , “Quantum Adiabatic Pumping with Modulating Electron Phase” ..... 69	69
12:30-12:45	<u>D. Mamaluy</u> , J.P. Mendez, and X. Gao, <i>Sandia National Laboratories, USA</i> , “Quantum Transport in APAM Wires” ..... 71	71
12:45-13:00	Y.-H. Lee, S. Xiao, <u>J.P. Bird</u> , J.E. Han, <i>University at Buffalo, USA</i> , K.W. Kim, <i>Institute for Basic Science, Republic of Korea</i> , and, J.L. Reno, <i>Sandia National Laboratories, USA</i> , “Giant Zero Bias Anomaly due to Coherent Scattering from Frozen Phonon Disorder in Quantum Point Contacts” ..... 73	73
<b>13:00-18:30</b>	<b>Ad Hoc Session</b>	
<b>18:30-20:30</b>	<b>Luau Reception and Dinner -- <i>Plantation Estates</i></b>	

**Thursday, December 5– *Plaza Ballroom***

**Session 9: Two-Dimensional Materials and van der Waals Heterostructures**

Session Chairs: Akira Oiwa and John F. Conley

9:00-9:30	C. McClellan, S. Vaziri, I. Datye, C. Bailey, A. Gabourie, M. Chen, V. Chen, K. Schauble, R. Grady, and <u>E. Pop</u> , <i>Stanford University, USA</i> , “Electrical, Thermal, and (Some) Unusual Applications of 2D Materials and Heterostructures” (invited)..... 75	75
9:30-10:00	R.M. Wallace, <i>University of Texas at Dallas, USA</i> , “2D Materials for Nanoelectronics: Prospects and Materials Integration Challenges” (invited) ..... 76	76
10:00-10:15	M. Ersfeld, L. Rathmann, F. Volmer, M. Heithoff, C. Stampfer, and <u>B. Beschoten</u> , <i>RWTH Aachen University, Germany</i> , “Gate-Dependent Valley Lifetimes in Monolayer WSe <sub>2</sub> ” ..... 78	78
10:55-10:30	<u>V. Ryzhii</u> , T. Otsuji, <i>Tohoku University, Japan</i> , M. Ryzhii, <i>University of Aizu, Japan</i> , V. Mitin, <i>University at Buffalo, USA</i> , and M.S. Shur, <i>Rensselaer Polytechnic Institute, USA</i> , “Infrared Interband Photodetectors Based on Graphene/Black-AsP Heterostructures” ..... 80	80
<b>10:30-11:00</b>	<b>Coffee Break</b>	
11:00-11:30	M.R. Rosenberger, H.-J. Chuang, M. Phillips, S.V. Sivaram, K.M. McCreary, C.S. Hellberg, and <u>B.T. Jonker</u> , <i>Naval Research Laboratory, USA</i> , and C.K. Dass and J.R. Hendrickson, <i>Air Force Research Laboratory, USA</i> , “Moire Superpotentials and Quantum Calligraphy of Single Photon Emitters in van der Waals Heterostructures” (invited) ..... 82	82

11:30-12:00	<u>T. Machida</u> , <i>University of Tokyo and CREST, Japan</i> , and R. Moriya, M. Onodera, K. Kinoshita, Y. Wakafuji, S. Park, S. Masubuchi, <i>University of Tokyo, Japan</i> , K. Watanabe, and T. Taniguchi, <i>National Institute for Materials Science, Japan</i> , “Cyclotron Resonance Absorption of Mid-infrared Light in van der Waals Heterostructures of Graphene and 2D materials” (invited).....	84
12:45-12:15	S. Sivaram, A. Hanbicki, M. Rosenberger, G. Jernigan, H.-J. Chuang, <u>K. McCreary</u> , and B.T. Jonker, <i>Naval Research Laboratory and Laboratory for Physical Sciences, USA</i> , “Spatially Selective Enhancement of Photoluminescence in MoS <sub>2</sub> by Exciton-Mediated Adsorption and Defect Passivation”.....	85
12:15-12:30	<u>C. Marquez</u> , N. Salazar, F. Gity, C. Navarro, G. Mirabelli, R. Duffy, J.C. Galdon, P. Hurley, and F. Gamiz, <i>University of Granada, Spain and University College Cork, Ireland</i> , “On the Reliability of Back-gated MoS <sub>2</sub> Field-effect Transistors”.....	87
12:30-12:45	<u>S.V. Rotkin</u> , X. Li, N. Briggs, B. Bersch, A. de la Fuente Duran, and J. Robinson, <i>The Pennsylvania State University, USA</i> , “sSNOM Multimodal Imaging of 2D Polar Metals”.....	89

**12:45-19:00 Ad Hoc Session**

**19:00-21:00 Session 10: Poster Session -- Ballroom Courtyard**

P1	<u>H. Yanagisawa</u> , C. Liu, Q. Chen, Y. Wang, N. Miyazaki, Y. Ootani, N. Ozawa, and M. Kubo, <i>Tohoku University, Japan</i> , “Molecular Dynamics Analysis of Effect of Dissolved Hydrogen on Deformation Behavior in Ni-based Superalloys”.....	91
P2	<u>S. Kimura</u> , W. Yang, N. Miyazaki, Y. Ootani, N. Ozawa, and M. Kubo, <i>Tohoku University, Japan</i> , “Large-Scale Molecular Dynamics Simulations on Chemical Mechanical Polishing Process of AlN Substrate with Nanobubbles”.....	93
P3	T.H. Park, T.H. Lee, M.S. Chae, and <u>T.G. Kim</u> , <i>Korea University, Republic of Korea</i> , “AlGaN-based UV Light-Emitting Diodes using Nickel-doped Aluminum Zinc Oxide Electrodes”.....	95
P4	<u>W. Lee</u> , C. Lee, J. Kim, J. Lee, D. Eom, J. Park, D. Kim, T. Park, and H. Kim, <i>Sungkyunkwan University and Hanyang University, Republic of Korea</i> , “Electrical Properties of HfO <sub>2</sub> Formed on the p-type Si <sub>1-x</sub> Ge <sub>x</sub> Pretreated with H <sub>2</sub> S Annealing”.....	97
P5	<u>K. Nagai</u> , Y. Wang, N. Miyazaki, Y. Ootani, N. Ozawa, and M. Kubo, <i>Tohoku University, Japan</i> , “Molecular Dynamics Simulation on Interfacial Reaction between LiC <sub>6</sub> / Li <sub>3</sub> PS <sub>4</sub> in All-Solid-State Li Ion Battery Anode”.....	98
P6	<u>S. Yamashita</u> , Y. Wang, N. Miyazaki, Y. Ootani, N. Ozawa, and M. Kubo, <i>Tohoku University, Japan</i> , “Effect of Water in Grain Boundaries on Shear Failure Strength of Silica: Reactive Molecular Dynamics Simulation”.....	100
P7	<u>K. Yamamoto</u> , T. Ono, N. Miyakawa, Y. Kanai, T. Koyama, M. Tanioku, S. Ushiba, A. Shinagawa, K. Inoue, Y. Watanabe, S. Nakakita, T. Kawahara, Y. Suzuki, M. Kimura, D. Chiba, and K. Matsumoto, <i>Osaka University, Murata Mfg., Kyoto Prefecture University of Medicine, Kagawa University and Chubu University, Japan</i> “New Modification Method of Sugar Chain on Graphene FET for Selective Detection of Virus”.....	102

P8	<u>N. Kim</u> , H.J. Kim, Y. Kim, K.S. Min, and S.K. Kim, <i>Kongju National University, Seoul National University, and LumiMac, Inc., Republic of Korea</i> , “Direct and Precise Length Measurement of Single, Stretched DNA Fragments by Dynamic Molecular Combing and STED Nanoscopy” ..... 105
P9	S. Fiorentini, R. Lacerda de Orio, S. Selberherr, J. Ender, W. Goes, and <u>V. Sverdlov</u> , <i>TU Wien, Austria and Silvaco Europe Ltd., UK</i> , “Comprehensive Modeling of Switching in Perpendicular STT-MRAM” ..... 107
P10	D. Shin, H. Cho, S. Park, D.-H. Ko, and <u>H.-J. Oh</u> , <i>Yonsei University, Republic of Korea</i> , “Properties of Gallium Oxide Grown by In-situ Plasma Oxidation and Its Effect on High-k MOS Capacitor on GaAs” ..... 109
P11	M. Ballicchia, M. Nedjalkov, <u>S. Selberherr</u> , and J. Weinbub, <i>TU Wien, Austria</i> , “Potentials for Single Electron State Processing” ..... 111
P12	V.A. Petrov, <i>Russian Academy of Sciences, Russia</i> , “On the Theory of the Energetic Spectrum of Vicinal Superlattices: The Role of Crystal Potential” ..... 113
P13	<u>W. Ahn</u> , H. Lee, Y. Cho, H. Kim, M. Leem, H. Lee, K.-E. Byun, H.-J. Shin, and H. Kim, <i>Sungkyunkwan University and Samsung Advanced Institute of Technology, Republic of Korea</i> , “Substrate-dependent Morphological Change of MoS <sub>2</sub> During Atomic Layer Deposition”... 114
P14	<u>H. Kim</u> , T. Park, M. Leem, H. Lee, W. Ahn, E. Lee, and H. Kim, <i>Sungkyunkwan University, Samsung Electronics, and Samsung Advanced Institute of Technology, Republic of Korea</i> , “Synthesis of MoS <sub>2</sub> via Sulfurization of a MoO <sub>2</sub> -Evaporated Film” ..... 115
P15	I.H. Jung, <i>Kookmin University, Republic of Korea</i> , “Enhancement of Power Conversion Efficiency of Quantum-Dot and Perovskite Solar Cells by Controlling Electron Transporting Layer” ..... 116
P16	Y.W. Noh and <u>J.W. Jung</u> , <i>Kyung Hee University, Republic of Korea</i> , “Tailored Electronic Properties of Zr-doped SnO <sub>2</sub> Nanoparticles for Efficient Planar Perovskite Solar Cells with Marginal Hysteresis” ..... 118
P17	<u>J. Kim</u> , C.K. Lee, and Y.J. Kim, <i>Kyonggi University and Spectris Korea Ltd., Republic of Korea</i> , “The Modification of the Band Gap, Energy Transfer Between Dopants, and Crystal Structure Refinement of Ce <sup>3+</sup> and Cr <sup>3+</sup> Co-doped Lu <sub>3</sub> (Al,Ga) <sub>5</sub> O <sub>12</sub> Persistent Luminescence Phosphors” ..... 120

**Friday, December 6– Plaza Ballroom**

**Session 11: Quantum Photonics**

Session Chair: Tomoki Machida

9:00-9:30	V.I. Klimov, <i>Los Alamos National Laboratory, USA</i> , “Nanocrystal Quantum Dot Lasing: From Novel Concepts to Novel Devices” (invited) ..... 122
9:30-9:45	<u>M. Kawasaki</u> , M. Nakamura, H. Hatada, S. Inagaki, M. Sotome, T. Morimoto, T. Kaneko, N. Ogawa, N. Nagaosa, and Y. Tokura, <i>RIKEN Center for Emergent Matter Science (CMES), Japan, and University of Tokyo, Japan</i> , “Quantum Mechanical Shift Current in Polar Semiconductors” ..... 124

9:45-10:00	G.G. Maia, <u>A. Oiwa</u> , <i>Osaka University, Japan</i> , and K. Sawano, <i>Tokyo City University, Japan</i> , “Magneto-Transports in a Light Irradiated Ge/SiGe Two-Dimensional Hole System” .....	126
10:00-10:15	R. Yahiaou, Z.A. Chase, C. Kyaw, and <u>T.A. Searles</u> , <i>Howard University, USA</i> , “Tunable Strong Coupling in Terahertz Metasurfaces” .....	127
10:15-10:30	G.T. Adamashvili, <i>Technical University of Georgia, Georgia</i> , “Optical Nonlinear Waves in a Graphene Waveguide” .....	129
10:30-11:00	<b>Coffee Break</b>	
11:00-11:15	D.R. Gulevich, Y.V. Zhumagulov, <i>ITMO University, Russia</i> , A.V. Vagov, <i>University at Bayreuth, Germany</i> , and <u>V. Perebeinos</u> , <i>University at Buffalo, USA</i> , “Bethe Salpeter Calculations of Trions in MoS <sub>2</sub> ” .....	130
11:15-11:30	<u>V. Semenenko</u> and V. Perebeinos, <i>University at Buffalo, USA</i> , “Plasmon Reflection in Graphene Junctions: Transfer Matrix Approach” .....	132
<b>Session 12: Energy Conversion and Harvesting</b>		
Session Chair: Victor Klimov		
11:30-11:45	A.R. Shaik and <u>D. Vasileska</u> , <i>Arizona State University, USA</i> , “PVRD-FASP: A Tool for Modeling Reliability and Durability of CdTe Solar Cells” .....	134
11:45-12:00	<u>T. Sugaya</u> , R. Oshima, Y. Shoji, K. Makita, <i>National Institute of Advanced Industrial Science and Technology (AIST), Japan</i> , and A. Ubukata, <i>Taiyo Nippon Sanso Corporation</i> , “High-speed Growth of III-V Materials by HVPE for Low-cost Smart Stacked Multijunction Solar Cells” .....	136
12:00-12:15	Y. Zou, R. V. Meidanshahi, C. Honsberg, and <u>S. Goodnick</u> , <i>Arizona State University, USA</i> , “Lattice-Matched Dilute-N GaNPAs on Silicon for Tandem Solar Cells” .....	138
12:15-12:30	<u>V.R. Whiteside</u> , H. Esmailpour, and I.R. Sellers, <i>University of Oklahoma, USA</i> , and G.E. Eperon, M.C. Beard, <i>National Renewable Energy Laboratory, USA</i> , “Hot Carrier Dynamics in Bulk and 2D Perovskites” .....	140
12:30-12:45	<u>D.K. Ferry</u> , <i>Arizona State University, USA</i> , H. Esmailpour, K.R. Dorman, T.B. Mishima, M.B. Santos, V R. Whiteside, and I.R. Sellers, <i>University of Oklahoma, USA</i> , “Valley Photovoltaics: Evidence for a True Hot Carrier Solar Cell” .....	142
12:45-13:00	<b>Concluding Remarks</b> , Stephen Goodnick	

## **Chiral and Spatial Spin Textures**

S. Parkin

*Max Planck Institute, Germany*

*stuart.parkin@mpi-halle.mpg.de*

An abstract is not printed due to the author's request.

## **Chiral Currents in a Correlated Compound: Weyl-Charge Density Waves**

B. Bradlyn

*Department of Physics, University of Illinois at Urbana-Champaign, USA*

*bbradlyn@illinois.edu*

The recent discover of Weyl semimetals has shown that topological effects can play a significant role in the behavior of gapless systems. However, correlation effects in known Weyl semimetals do not seem to play a significant role. Here we will show that the charge density wave compound  $(\text{TaSe}_2)_4\text{I}$  is a Weyl semimetal with strong correlations due to electron-phonon coupling. It undergoes a metal-to-insulator transition near room temperature, forming a novel correlated topological state. I will show how the topological charge of the Weyl nodes leaves its mark on the behavior of the collective phase mode of the charge density wave, which we verified in nonlinear transport experiments.

## Microscopic Description of Coulomb Blockaded Topological Superconducting Island Coupled to Many Leads

J. Vayrynen<sup>1</sup>, A. Feiguin<sup>2</sup>, and R. Lutchyn<sup>1</sup>

<sup>1</sup>*Microsoft Quantum, Station Q, University of California, Santa Barbara, California 93106-6105, USA*

<sup>2</sup>*Department of Physics, Northeastern University, Boston, Massachusetts 02115, USA*

*jukka.vayrynen@microsoft.com*

We introduce a microscopic Hamiltonian of a Coulomb blockaded multi-Majorana island in the limit of zero level spacing. Our bosonized model allows us to study both limits of  $E_c/\Delta_P \ll 1$  as well as  $E_c/\Delta_P \gg 1$  where  $\Delta_P$  is the proximity-induced gap of the topological superconductor and  $E_c$  is the island charging energy. At low temperatures,  $T \ll T_K$ , both limits exhibit the universal topological Kondo effect with the conductance depending on temperature as a power law with a non-Fermi-liquid exponent. At intermediate temperatures, the two scenarios differ. Furthermore, our model can be used to access the regime of strong tunneling, where the island-lead junctions are almost fully transparent in normal state. In this regime the non-Fermi-liquid behavior extends to the highest temperature,  $T_K \rightarrow \min(E_c, \Delta_P)$ . By using analytical calculations in perturbation theory as well as numerical DMRG studies, we find the average charge as a function of the gate-induced charge in various limits of  $E_c/\Delta_P$  and the junction conductances.

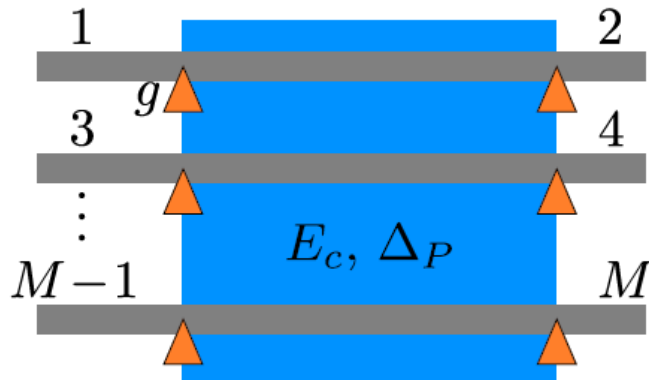


Fig.1: Schematic diagram of the device build out of  $M/2$  nanowires connected to a central floating superconducting island (charging energy  $E_c$ , proximity-induced superconducting gap  $\Delta_P$ ). The nanowires serve as  $M$  leads with normal state conductances.

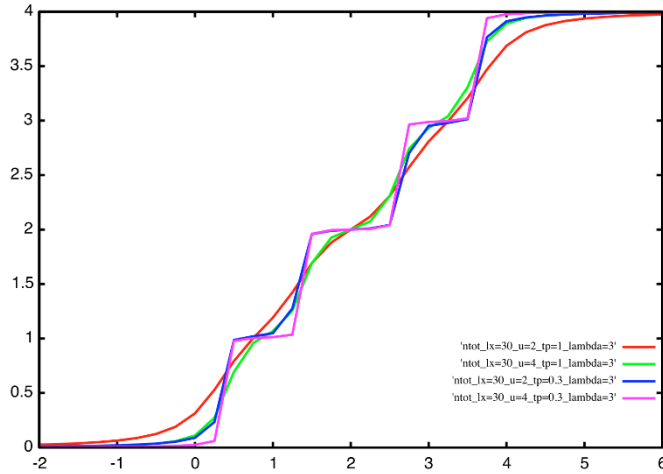


Fig.2: The average charge on the island as a function of dimensionless gate voltage calculated in a DMRG simulation. The charging energy takes values  $E_c = 2\Delta_P, 4\Delta_P$  while tunnel-couplings to normal metal leads take values  $t = 0.3\Delta_P, \Delta_P$ . Coulomb blockade with quantized charge is seen for large charging energies and weak couplings to the leads.

## 2-D Electronic Systems with s- and p Orbital Dirac Physics Created in a Scanning Tunnelling Microscope

D. Vanmaekelbergh<sup>1</sup>, I. Swart<sup>1</sup>, C.M. Smith<sup>2</sup>, and C. Delerue<sup>3</sup>

<sup>1</sup>*Debye Institute for Nanomaterials Science, University of Utrecht, The Netherlands*

<sup>2</sup>*Institute for Theoretical Physics, University of Utrecht, The Netherlands*

<sup>3</sup>*Université de Lille, CNRS, Centrale Lille, Yncréa-ISEN,*

*Université Polytechnique Hauts-de-France, France*

*d.vanmaekelbergh@uu.nl*

The field of (topological) quantum materials knows a rapid development and has attracted enormous interest in the last decade [1-3]. The electronic band structure of quantum materials is decided by the crystal structure and nature of the atoms on one hand, and by the overall dimensions and nanoscale geometry on the other hand. Inspired by the emergence of graphene, there is a class of rather conventional semiconductors that can obtain a Dirac band structure in the valence- and conduction bands due to the honeycomb geometry on the nanoscale. The physics and application of honeycomb semiconductors may go far beyond graphene itself due to two reasons: (i) Orbital degree of freedom: The geometric lattice sites host *s*- and *p* orbitals that can result in separated *s*- and in-plane *p* orbital Dirac bands; the in-plane *p* orbitals also provide non-trivial flat bands [4-5]. (ii) strong intrinsic spin-orbit coupling, resulting in gap formation at the Dirac points, especially in the *p* orbital system; this gap host quantum spin-Hall edge states. The realization of honeycomb semiconductors is technologically demanding, but bottom-up [6] and top-down routes [7] have provided the first honeycomb semiconductors with indications of Dirac physics. In my lecture, I will present the first results obtained in a collaboration with the Université de Lille. Meanwhile, we and others realized that many of the theoretical predictions on geometric (topological) quantum materials can be simulated by using artificial lattices [8]. We have developed an experimental platform based on the Cu(111) surface state, and CO molecules as repulsive electron scatters to define artificial atoms, molecules, and lattices in 2 dimensions. We then created artificial lattices with a square, Lieb [9-10], honeycomb [11], Kekule [12], Kagome and dimerized kagome [13] geometry in order to study Dirac physics, flat bands and topological protected edge and corner states. Moreover, we have studied electronic states hosted in fractal structures [14]. In my lecture, I will present the results we have obtained with the honeycomb lattice. We have designed honeycomb lattices with separated *s*- and *p* orbital Dirac physics, such that the long-sought *p* orbital band structure could fully emerge. We measured the LDOS and wavefunctions of an *s* orbital Dirac cone, followed by the in-plane *p* orbital system that consists of a flat band, a Dirac cone and a second flat band.

The flat bands reflect orbital interferences of orthogonal  $p_x, p_y$  orbitals in the incommensurate honeycomb lattice. This is the first time that  $p$  orbital physics fully emerges in an electronic realm. I will contrast this remarkable behaviour with the results obtained in a square and a Lieb lattice, where the orthogonal  $p_x, p_y$  orbital set fits with the lattice symmetry. The next efforts will be to involve strong spin-orbit coupling and superconductivity in these highly interesting systems. Since the physics depends on the geometry, the physics can be directly imprinted in real materials: semiconductor systems that host a 2-D electron gas.

- [1] B. Keimer and J. E. Moore, *Nat. Phys.* **13**, 1045 (2017).
  - [2] B. Bradlyn *et al.*, *Nature* **547**, 298 (2017).
  - [3] B. Bradlyn *et al.*, *Science* **353** (2016).
  - [4] E. Kalesaki *et al.*, *Phys. Rev. X* **4**, 011010 (2014). \*
  - [5] W. Beugeling *et al.*, *Nat. Commun.* **6**, 6316 (2015). \*
  - [6] M.P. Boneschanscher *et al.*, *Science* **344**, 1377 (2014). \*
  - [7] L.C. Post *et al.*, *Nanotechnology* **30**, 155301 (2019). \*
  - [8] K.K. Gomes *et al.*, *Nature* **483**, 306 (2012).
  - [9] M.R. Slot *et al.*, *Nat. Phys.* **13**, 672 (2017). \*
  - [10] M.R. Slot *et al.*, *Phys. Rev. X* **9**, 011009 (2019). \*
  - [11] T. Gardenier *et al.*,  $p$  Orbital Flat Band and Dirac Cone in the Electronic Honeycomb Lattice. (submitted). \*
  - [12] S.E. Freeney *et al.*, Edge-Dependent Topology in Kekule Lattices. (submitted). \*
  - [13] S.N. Kempkes *et al.*, *Nature Mater.* **18**, 1292 (2019). \*
  - [14] S. N. Kempkes *et al.*, *Nat. Phys.* **15**, 127 (2019). \*
- (The references with \* are from joint collaborations by the authors)

## **Dynamic Behavior of Topological Spin Singularity Studied by Soft X-ray Microscopy**

M.-Y. Im<sup>1</sup>, H.-S. Lee<sup>2</sup>, and K.-S. Lee<sup>2</sup>

<sup>1</sup>*Center for X-ray Optics, Lawrence Berkeley National Laboratory, Berkeley CA 94720, USA*

<sup>2</sup>*School of Materials Science and Engineering,*

*Ulsan National Institute of Science and Technology, Ulsan, 44919, Republic of Korea*

*mim@lbl.gov*

A Bloch point (BP) is a three-dimensional (3D) topological spin singularity in a ferromagnet at which the local magnetization vanishes and it is defined by the skyrmion charge  $q=\pm 1$  [1, 2]. While the two-dimensional (2D) magnetic topological spin structures such as vortices and skyrmions have long been the central theme of research in magnetism, their 3D counterpart, the BP, has been mostly a subject of theoretical investigation due to the difficulty in achieving stable BPs within magnetic nanostructures. With the difficulty the intrinsic nature of a BP and its dynamic behavior associated with its atomically discontinuous spin texture has not yet been experimentally explored even there has been theoretically proposed to bear critical roles in dynamic phenomena of 1D and 2D spin structures such as domain wall motion, vortex core switching, and skyrmion dynamics [3, 4]. In our work [5], we have successfully established stable BPs embedded within nontrivially distorted magnetic vortex cores in asymmetric Ni<sub>80</sub>Fe<sub>20</sub> nanostructures (see Fig. 1). Time-resolved nanoscale magnetic X-ray imaging utilizing a full-field magnetic transmission soft X-ray microscope (XM-1, BL6.1.2 at ALS, USA) combined with micromagnetic simulation shows detailed dynamic character of BPs, revealing rigid and limited lateral movements under magnetic field pulses as well as its crucial role in vortex-core dynamics (see Fig. 2). Direct visualizations of magnetic structures disclose the unique dynamical feature of a BP as an atomic scale discrete spin texture and allude its influence on the neighbouring spin structures such as magnetic vortices.

[1] E. Feldtkeller, Z. Angew. Phys. **19**, 530 (1965).

[2] W. Döring, J. Appl. Phys. **39**, 1006 (1968).

[3] P. Wohlhüter, et al. Nat. Commun. **6**, 7836 (2015).

[4] M. Noske et al. Phys. Rev. B **91**, 014414 (2015).

[5] M.-Y. Im et al. Nat. Commun. **10**, 593 (2019).

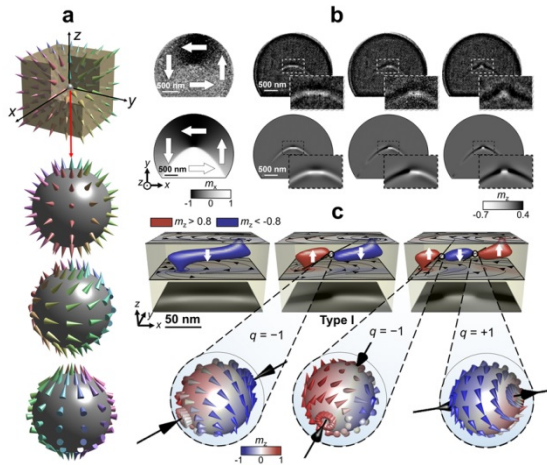


Fig. 1: a, Schematic diagram of three possible configurations of a BP with skyrmion charge  $q = +1$ , namely, hedgehog, circulating, and spiralling configurations. b, In-plane (IP) and out-of-plane (OOP) magnetic components observed by X-ray microscopy, and the corresponding magnetic structures determined by micromagnetic simulations. c, Images of the distorted vortex core structures with no BP (left), a single BP (middle), and double BPs (right), and the configurations of the BPs embedded in the vortex cores. The OOP magnetic components with  $m_z > +0.8$  (red) and  $m_z < -0.8$  (blue) were extracted and the BP configurations were obtained by interpolation from the simulated vortex core structures. The single BP is characterized by  $q = -1$ , while the double BPs are defined by  $q = -1$  and  $+1$ , respectively.

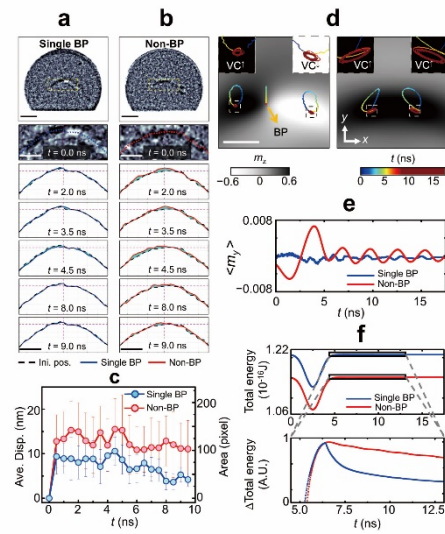


Fig. 2: a-b, Representative images of the vortex core structures with (a) and without (b) a BP (the first row) along with positions of core structures measured at  $t = 0, 2, 3.5, 4.5, 8, 9$  ns during their dynamic processes triggered by the injection of a field pulse with an amplitude of 50 Oe and the width of 3 ns in the  $+x$ -direction. c, Quantitatively analysed differences between initial ( $t = 0$ , black line) and perturbed positions ( $t > 0$ ) of the single BP core (blue line) and non-BP core structure (red line). d, Trajectory curves of the simulated dynamic motions of the BP and vortex cores with up ( $VC^\uparrow$ ) and down ( $VC^\downarrow$ ) polarizations in the single BP and non-BP cores (scale bar : 50 nm). e-f, The variations of normalized y-components of magnetizations,  $\langle m_y \rangle = \langle M_y / M_s \rangle$  (e) and total energy (f) during the dynamic relaxation processes of the single BP and non-BP cores. Raw data of Fig. 4c are provided as the Source Data files.

## Topological and Nontopological Edge States in Ordinary Quantum Matter

D.R. Candido<sup>1,2</sup>, M.E. Flatté<sup>2</sup>, and J.C. Egues<sup>1</sup>

<sup>1</sup>*Instituto de Física de São Carlos, Universidade de São Paulo,  
13560-970 São Carlos, SP, Brazil*

<sup>2</sup>*Department of Physics and Astronomy and Optical Science and Technology Center,  
University of Iowa, Iowa City, Iowa 52242, USA  
egues@ifsc.usp.br*

Common wisdom has it that edge states appear only in topological systems, e.g., topological insulators and topological superconductors. In this work I will discuss edge states in topological and *nontopological* InAsBi quantum dots described by a confined Bernevig-Hughes-Zhang (BHZ) model – the paradigmatic two-band 2D insulator displaying a topological quantum phase transition. Surprisingly we find that these BHZ dots exhibit protected helical edges states in *both* the topological and non-topological regimes, Fig. 1, featuring spin-angular momentum locking [1]. This clearly contrasts the bulk-edge correspondence. Our calculated transport properties, e.g., two-terminal conductance, are essentially identical in both regimes. Hence our findings blur the boundaries between topological and non-topological phenomena in small systems. I should also touch upon Chern insulators and nodal semimetals, which display trivial edge states not arising from band topology [2] and skyrmionic textures in ordinary noninteracting GaAs wells [3]. In this case the approximate chiral symmetry of the Chern insulator, exact only in the nodal semimetal, is the relevant ingredient behind the appearance of these trivial edge states. This work has been supported by FAPESP (grant No. 2016/08468-0) and CNPq.

[1] D. R. Candido *et al.*, Phys. Rev. Lett. **121**, 256804 (2018).

[2] D. R. Candido *et al.*, Phys. Rev. B **98**, 161111(R) (2018), (Editors' Suggestion).

[3] J. Fu. *et al.*, Phys. Rev. Lett. **17**, 226401 (2016).

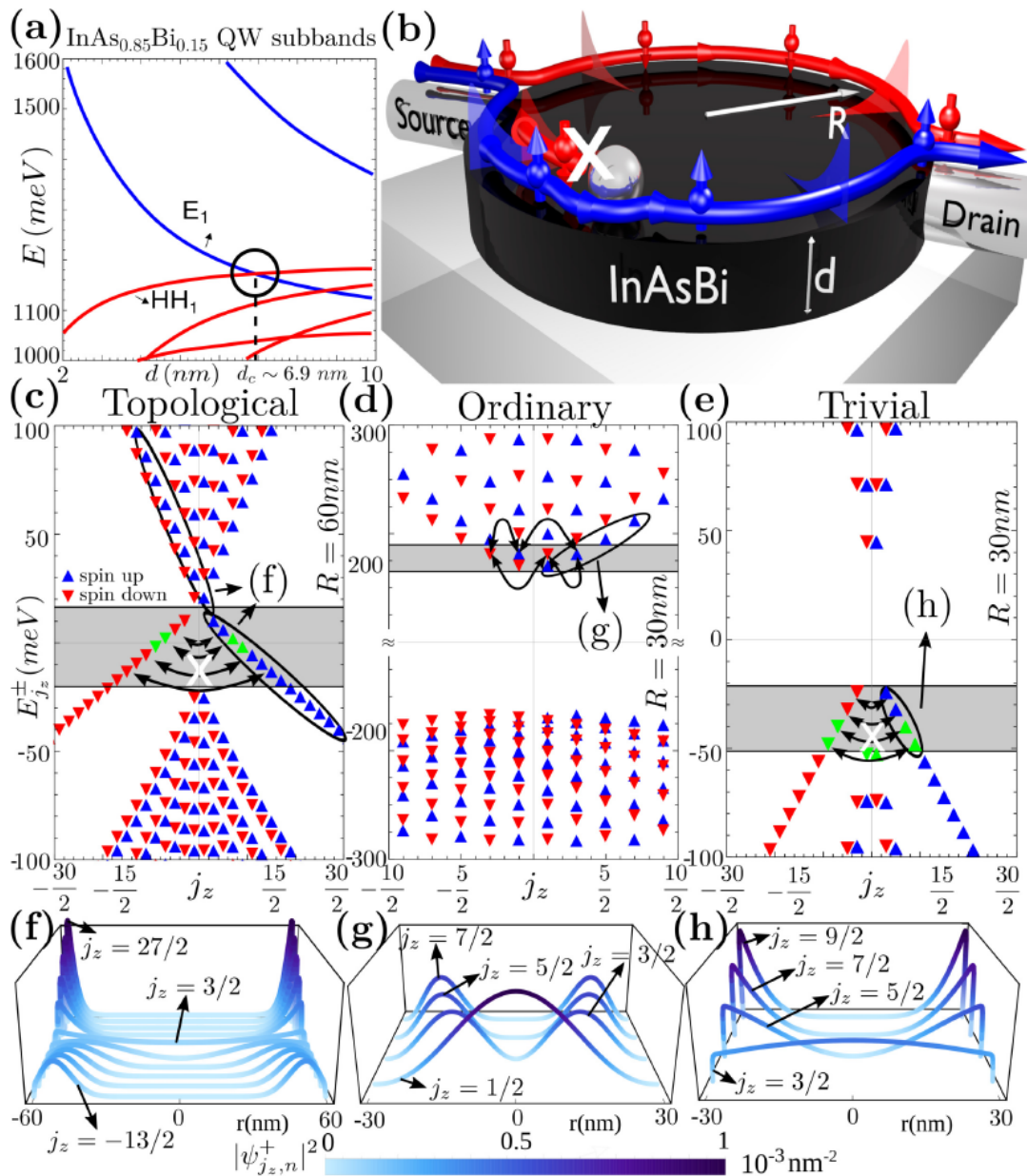


Fig. 1: (a) InAs<sub>0.85</sub>Bi<sub>0.15</sub> quantum well subbands versus the well thickness  $d$ . (b) Schematic of a cylindrical quantum dot with helical edge states. Energy levels versus the total angular momentum  $j_z$  for (c) a topological InAs<sub>0.85</sub>Bi<sub>0.15</sub> BHZ dot with  $R=60$  nm, (d) an ordinary (non-BHZ) InAs dot with  $R=30$  nm, and (e) a trivial InAs<sub>0.85</sub>Bi<sub>0.15</sub> BHZ dot with  $R=30$  nm. The curved arrows denote the forbidden and allowed transitions. (f)–(h) Probability densities for the edge states in (c) and (d) and bulk states (g) (see ellipses).

## Scalable Majorana States and Phase Measurement of Topological Superconductivity

I. Zutic<sup>1</sup>, T. Zhou<sup>1</sup>, J. Han<sup>1</sup>, M.C. Dartiailh<sup>2</sup>, W. Mayer<sup>2</sup>, A. Kent<sup>2</sup>,  
J. Shabani<sup>2</sup>, N. Mohanta<sup>3</sup>, and A. Matos-Abiague<sup>3</sup>

<sup>1</sup>*Department of Physics, University at Buffalo, SUNY, Buffalo NY 14260, USA*

<sup>2</sup>*Department of Physics, New York University, NY 10003, USA*

<sup>3</sup>*Department of Physics and Astronomy, Wayne State University, Detroit, MI 48201, USA*  
*zigor@buffalo.edu*

Topological transition transforms common superconductivity into an exotic phase of matter, which holds promise for fault-tolerant quantum computing [1]. A hallmark of this topological transition is the emergence of Majorana bound states (MBS), quasiparticles that nonlocally store a single electron. Their non-Abelian exchange statistics allows for the implementation of quantum gates through braiding operations [1]. While most of the MBS proposals were focused on 1D systems [2], their geometry has inherent difficulties for technological implementation and realizing braiding. MBS detection typically relies on the measurement of zero-bias conductance peak [2,3] that could also arise in topologically-trivial systems. To overcome these challenges, we propose 2D platforms, which could support scalable MBS and their braiding. First we discuss how spin valves, common in spintronics, can be used through their fringing fields [4,5] to proximitize two-dimensional electron gas to implement MBS and their braiding [6,7]. Next we show our measurements of topological superconductivity in epitaxial Al/InAs Josephson junctions [8]. The closing and reopening of the superconducting gap with increasing magnetic field is simultaneously accompanied by the measurement of  $\pi$ -jump in the superconducting phase [8]. Remarkably, this topological transition can be controlled by gate voltage. We propose X-shaped topological junctions [9] in which the observed topological transition can be used to realize scalable MBS and their braiding.

- [1] D. Aasen *et al.*, Phys. Rev. X **6**, 031016 (2016).
- [2] H. Zhang *et al.*, Nature **556**, 74 (2018).
- [3] K. Sengupta *et al.*, Phys. Rev. B **63**, 144531 (2001).
- [4] T. Zhou *et al.*, Phys. Rev. B **99**, 134505 (2019).
- [5] N. Mohanta *et al.*, Phys. Rev. Appl. **12**, 034048 (2019).
- [6] G. Fatin *et al.*, Phys. Rev. Lett. **117**, 077002 (2016).
- [7] A. Matos-Abiague *et al.*, Solid State Commun. **262**, 1 (2017).
- [8] W. Mayer *et al.*, arXiv:1906.01179, Nat. Matter, under review.
- [9] T. Zhou *et al.*, arXiv:1909:05386, Phys. Rev. Lett., under review.

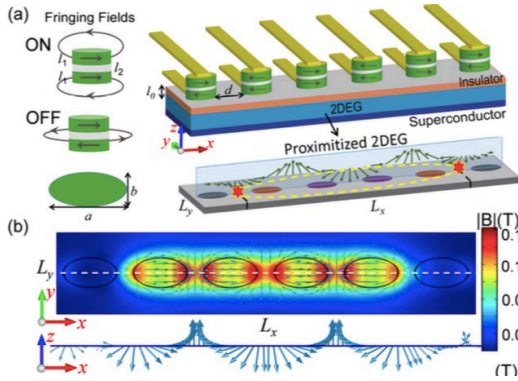


Fig.1: (a) 2DEG proximitized by a superconductor and array of tunable spin valves hosts Majorana states (red stars). (b) Micromagnetic modeling of fringing fields from spin valves that support Majorana states.

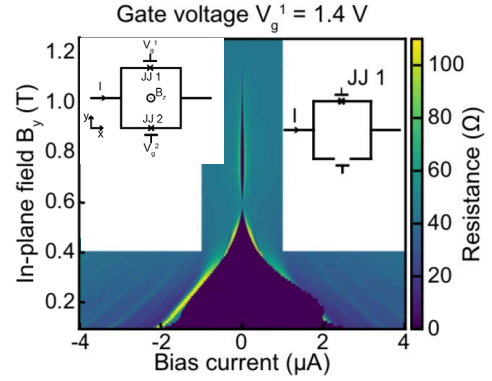


Fig.2: Closing the trivial and reopening a topological superconducting gap with increasing in-plane B-field using SQUID with 2 individually gateable Josephson junctions (JJs).

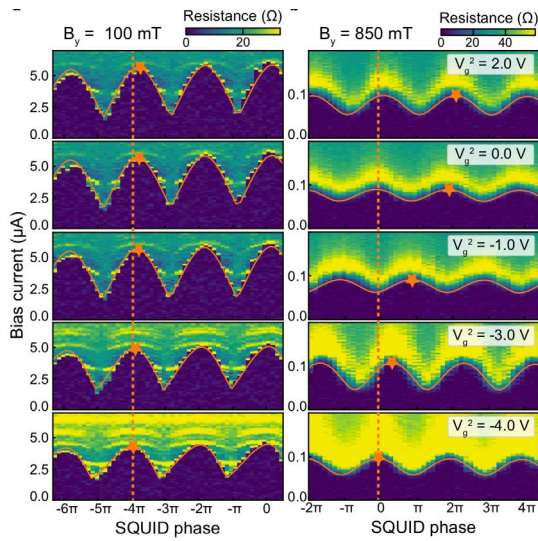


Fig.3: Phase signature of topological transition from SQUID interferometry at  $B_y=850$  mT and the trivial reference results at 100 mT.

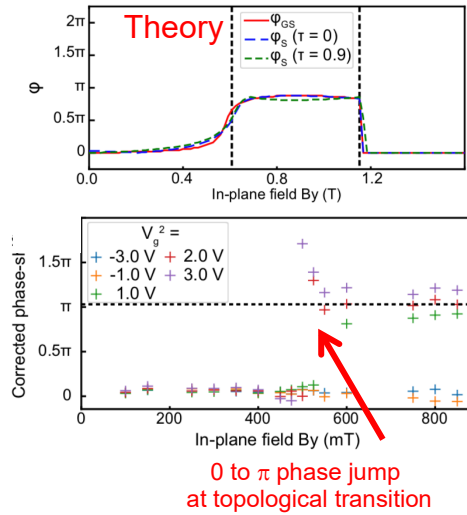


Fig.4: Top: Calculated ground-state phase (red) and SQUID phase-shift (blue, green). Bottom: Phase evolution with in-plane B-field reveals topological transition for two higher  $V_g$ .

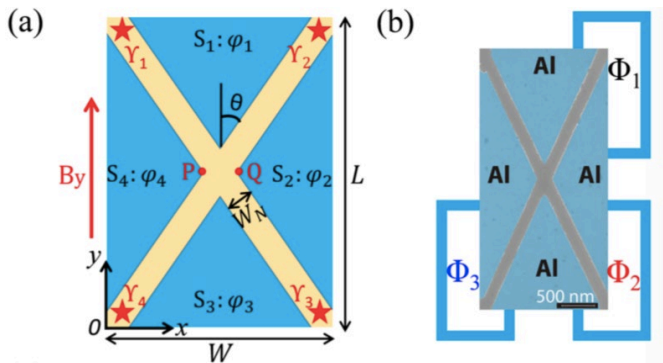


Fig.5: (a) X junction (XJ) formed by epitaxial superconducting (S) regions (blue) covering a 2DEG (yellow). (b) XJ SEM image with schematic external fluxes  $\Phi_1$  (between  $S_1, S_2$ ),  $\Phi_2$  ( $S_2, S_3$ ), and  $\Phi_3$  ( $S_3, S_4$ ).

## Detection of Chiral Andreev Edge States at the Quantum Hall – Superconductor Interface

L. Zhao<sup>1</sup>, E. Arnault<sup>1</sup>, A. Bondarev<sup>1</sup>, A. Seredinski<sup>1</sup>, T. Larson<sup>1</sup>, A. Draelos<sup>1</sup>, H. Li<sup>2</sup>,  
T. Taniguchi<sup>3</sup>, K. Watanabe<sup>3</sup>, F. Amet<sup>2</sup>, H. Baranger<sup>1</sup>, and G. Finkelstein<sup>1</sup>

<sup>1</sup>*Department of Physics, Duke University, Durham, NC 27708, U.S.A.*

<sup>2</sup>*Department of Physics, Appalachian State University, Boone, NC 28607, U.S.A.*

<sup>3</sup>*Advanced Materials Laboratory, NIMS, Tsukuba 305-0044, Japan*

*gleb@duke.edu*

The search for topological excitations such as Majorana fermions has spurred interest in the boundaries between distinct quantum states. In a series of recent works, we have explored the interface between two prototypical phases of electronic matter with conceptually different ground states: the integer quantum Hall (QH) and the s-wave superconductor (SC) [1-4].

Our new measurements demonstrate a clear evidence of the chiral Andreev edge states (CAES): hybridized electron and hole states similar to chiral Majorana fermions, which propagate along the QH-SC interface in one direction. Semiclassically, CAES result from skipping orbit trajectories, in which an electron turns into a hole and back to an electron upon successive Andreev reflections from a SC interface. Quantum-mechanically, inducing superconducting proximity into the QH edge states yields fermionic modes in which an electron and a hole are hybridized and propagate chirally along the QH-SC interface.

Experimentally, we have detected the CAES by measuring the propagation of electrical signal in a QH sample past a grounded superconducting contact (Fig. 1A) [5]. Naively, one might expect that any electrical signal spreading along the superconducting interface would be shunted by the superconductor. However, we have demonstrated that this is not the case. The main mechanism allowing us to detect the CAES is their interference, which can turn an incoming electron into an outgoing electron or a hole, depending on the phase accumulated by the CAES along the QH-SC interface (Fig. 1D). Our results demonstrate that these elusive excitations can propagate and interfere over a significant length, opening future possibilities for their coherent manipulation.

[1] I. Borzenets *et al.*, Physical Review Letters **117**, 237002 (2016).

[2] F. Amet *et al.*, Science **352**, p. 966-969 (2016).

[3] A. Draelos *et al.*, Journal of Low Temperature Physics **191**, p. 288 (2018).

[4] A. Seredinski *et al.*, Science Advances **5**, eaaw8693 (2019).

[5] L. Zhao *et al.*, preprint at <https://arxiv.org/abs/1907.01722>. (2019).

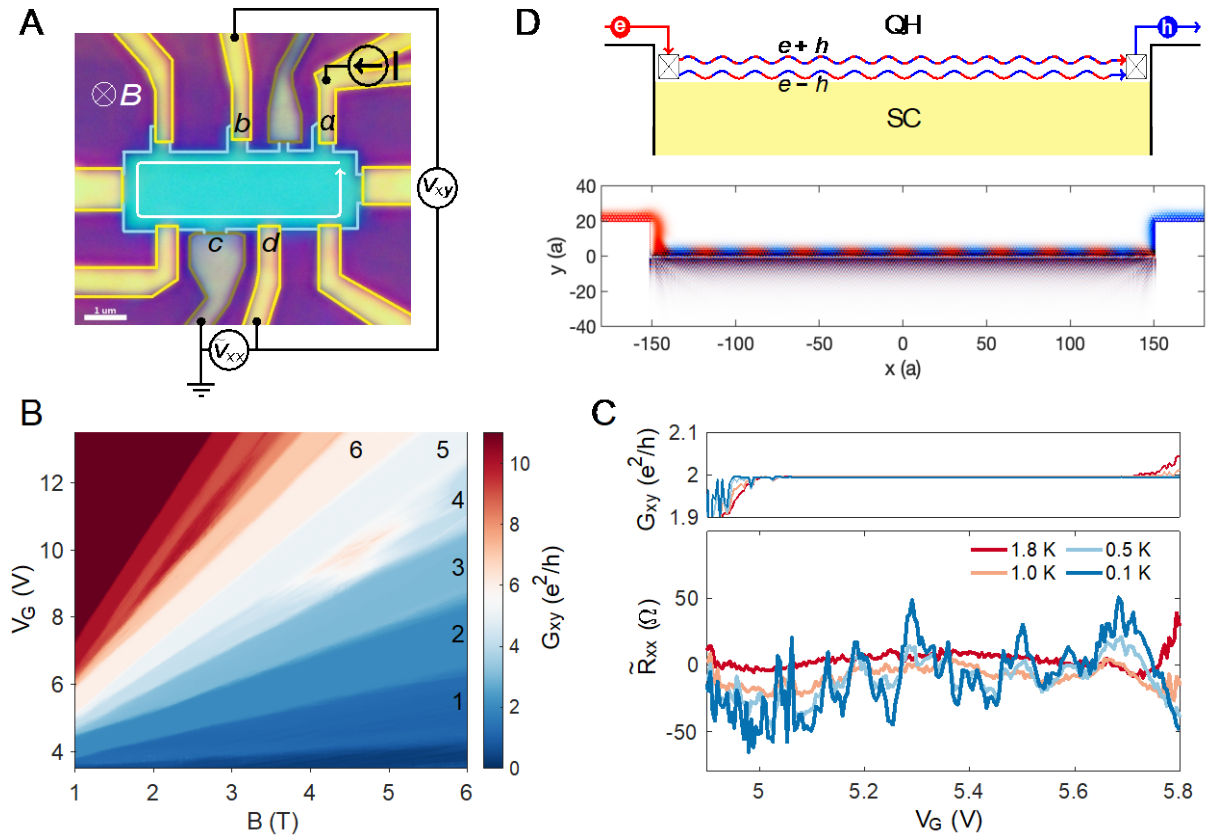


Fig. 1: Andreev reflection in the QH regime. (A) Optical image of the sample. Graphene mesa is blue. Superconducting contacts (gray) are placed between normal contacts (gold). The magnetic field is applied into the plane, resulting in counterclockwise direction of motion of both electrons and holes when the graphene is n-doped. We use a four-terminal scheme to measure the Hall voltage  $V_{xy}$  simultaneously with the longitudinal voltage downstream from the superconductor,  $V_{xx}$ . (B) Fan diagram of the zero-bias Hall conductance  $G_{xy}$ . The filling factors are labeled on the plateaus. The broken symmetry integer filling factors appear already around  $B = 1$  T, suggesting the high quality of the graphene region. (C) Temperature dependence of  $R_{xx}$ , zero-bias longitudinal resistance measured downstream of the SC contact, and the Hall conductance,  $G_{xy}$ . (The filling factor is  $\nu = 2$  and  $B = 3$  T). While  $G_{xy}$  is well-quantized on the  $\nu = 2$  plateau, the  $R_{xx}$  demonstrates reproducible fluctuations of both positive and negative sign. These fluctuations disappear as the temperature is raised to 1.8 K, resulting in a conventional behavior of vanishing quantum Hall resistance on the plateau. We conclude that the fluctuations at lower temperatures should be due to the superconductivity in contact c. Detailed analysis in Ref. [1] attributes these fluctuations to the interference of the Chiral Andreev Edge States, as schematically shown in panel D. (D) Top: an electron injected at the left end of a SC-QH interface turns into a pair of CAES. The CAES propagate along the interface with different wave vectors, resulting in the beatings of the electron and hole amplitudes. Depending on the gate voltage and magnetic field, the resulting state at the right end of the interface may be either an electron or a hole. The bottom panel shows the electron (red) and hole (blue) wave function densities in the lowest Landau level obtained from a realistic tight-binding calculation using the KWANT package.

**Coulomb Interactions in  
Magnetic Topological Heterostructures**

M. Gilbert

*University of Illinois at Urbana-Champaign, USA*

*matthewg@illinois.edu*

An abstract is not printed due to the author's request.

## Conical-Intersection and Berry Phase in Deep-Strongly Coupled Superconducting-Qubit-Resonator System

K. Semba<sup>1</sup> and S. Ashhab<sup>2</sup>

<sup>1</sup>*National Institute of Information and Communications Technology,  
4-2-1, Nukuikitamachi, Koganei, Tokyo 184-8795, Japan*

<sup>2</sup>*Qatar Environment and Energy Research Institute, Hamad Bin Khalifa University,  
Qatar Foundation, PO Box 5825, Doha, Qatar.  
[semba@nict.go.jp](mailto:semba@nict.go.jp), [sashhab@hbku.edu.qa](mailto:sashhab@hbku.edu.qa)*

In recent years, conical intersections, or Dirac cones, have been observed in various low-dimensional electronic systems such as graphene and various topological materials [1]. Observing and using geometric phases, which could be observed by going around a phase singularity, a conical intersection, is an interesting topic that has attracted much attention [2]. There is also an interesting proposal that a potentially fault-tolerant qubit may be formed using Bogoliubov quasiparticle states such as Majorana fermions [3].

$$H = -\frac{\hbar}{2}(\Delta\sigma_x + \varepsilon\sigma_z) + \hbar\omega(a^\dagger a + \frac{1}{2}) + \hbar g\sigma_z(a + a^\dagger) \quad (1)$$

Superconducting flux-qubit oscillator circuits can be well described by the generalized quantum Rabi-model shown in Eq. (1), even in the deep strong coupling regime [4]. The first, second and third terms represent, respectively, the energy of the qubit, the energy of the harmonic oscillator, and the interaction energy. Numerical analysis reveals that conical intersections occur not only in the symmetric quantum Rabi-model, which has clear parity symmetry (in the case  $\varepsilon=0$ ), but also in the asymmetric generalized quantum Rabi-model (in the case  $\varepsilon \neq 0$ ) where a finite magnetic field is applied as the energy bias to the qubit [2]. The occurrence of conical intersections in the asymmetric Rabi-model provides indirect evidence that there should be a hidden symmetry in the model. Here, we propose an experimental scheme to observe conical-intersections in the energy landscape and the Berry phase in ultra-strongly and deep-strongly coupled qubit resonator systems. This will also provide a clue to understand the hidden symmetry in this system.

[1] D. Xiao *et al.*, Rev. Mod. Phys. **82**, 1959-2007 (2010).

[2] M.T. Batchelor *et al.*, J. Phys. A: Math. Theor. **49**, 01LT01 (2016).

[3] M. Sato and S. Fujimoto, J. Phys. Soc. Jap. **85**, 072001 (2016).

[4] F. Yoshihara *et al.*, Nature Phys. **13**, 44 (2017).

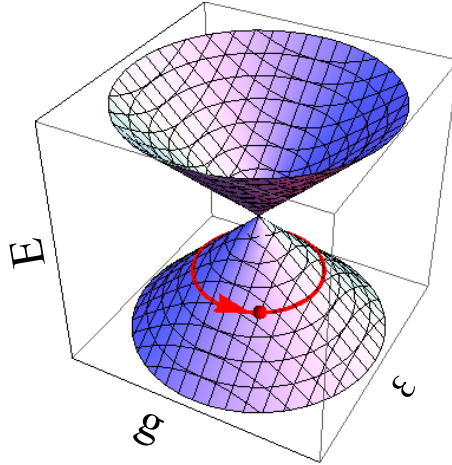


Fig.1: Conical intersection and a trajectory around the Dirac point in the quantum Rabi-model

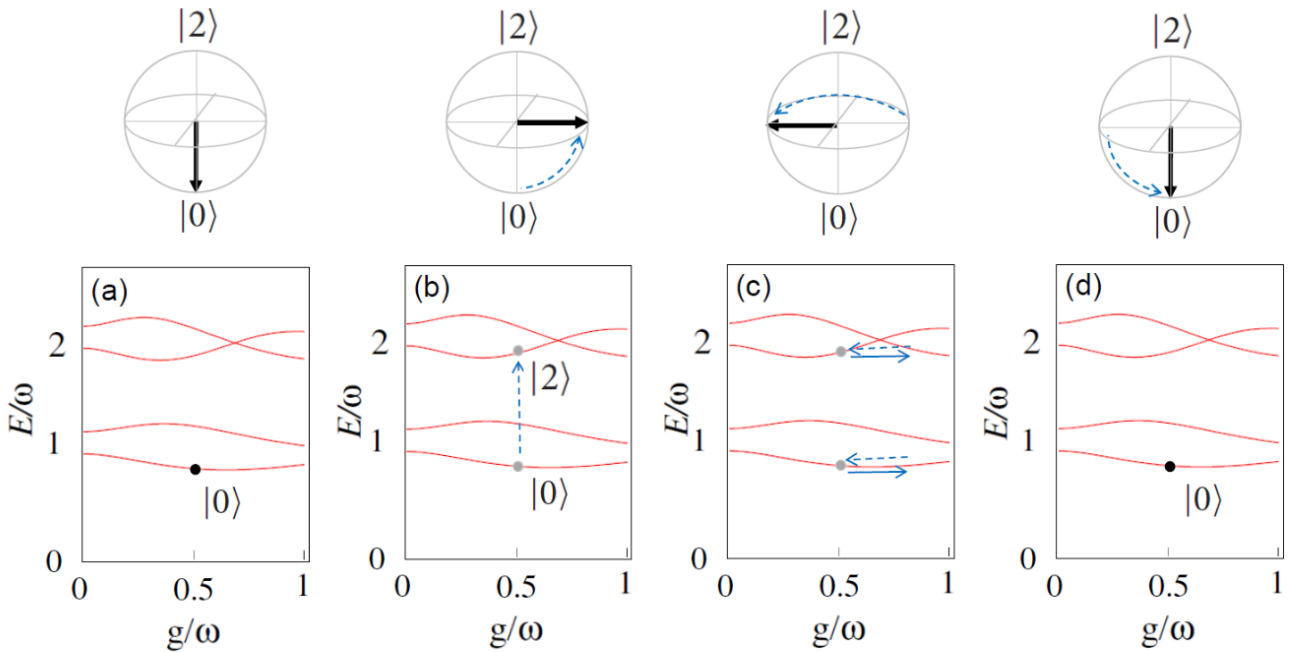


Fig.2: Proposed scheme to measure Berry phase in the deep-strong coupling system

(a) Prepare the ground state  $|0\rangle$  as the initial state. (b) Create superposition of  $|0\rangle$  and  $|2\rangle$  using  $E_{02}$  resonant  $\pi/2$  pulse. (c) Change parameters  $\varepsilon$  and  $g$  adiabatically so that the state  $|2\rangle$  goes around the Dirac point. During this process, the state  $|2\rangle$  acquires geometrical phase  $\pi$  relative to the state  $|0\rangle$ . (d) Using the same  $\pi/2$  pulse to get the final state. If the geometrical phase difference is  $\pi$ , the final state is the ground state  $|0\rangle$ . If there are no geometrical phase difference, the final state is state  $|2\rangle$ . Bloch spheres corresponding to (a), (b), (c), (d) are shown. Consideration is made after the contribution from the dynamical phase is removed.

## Application of RF Single Electron Devices for Scanning Probe Microscopy

T.A. Zirkle<sup>1</sup>, M.J. Filmer<sup>1</sup>, A.O. Orlov<sup>1</sup>,  
A.M. Mintairov<sup>1,2</sup>, and G.L. Snider<sup>1</sup>

<sup>1</sup>*Dept of Electrical Engineering, University of Notre Dame, Notre Dame, USA*

<sup>2</sup>*Ioffe Institute, St. Petersburg, Russia*  
*mfilmer@nd.edu*

A high-resolution surface-charge/work-function scanning probe requires a highly sensitive electrometer [1]. Single-electron devices, being the most sensitive electrometers available, are therefore a strong candidate for use in this application. Previous work into fabricating scanning probes with single-electron electrometers [2] have failed to address some of the key figures of merit that are crucial for an optimal device: charging energy, sensitivity, and resolution. We present our work toward developing a scanning probe employing arrays of single electron (SE) devices: boxes (SEBs) and AC-coupled transistors (SETs). Devices are fabricated using Dolan bridge technology [3] using Al and are capacitively coupled to the scanning tip. To measure the response, devices are coupled to a matching resonant network probed by radio-frequency reflectometry [4]. There are two key development with these electrometers over conventional SET detectors. First, neither SEBs nor AC-coupled SETs have a direct current path through the device. This enables a high tolerance against damage due to electrostatic discharge; and individual devices with damaged (shorted) junctions do not perturb the performance of the array. Second, we demonstrate that by carefully choosing the operating bias point, the voltage sensitivity of the array of N parallel SE devices can be increased by a factor significantly greater than  $\sqrt{N}$ . In general, SETs have much stronger coupling to the RF line than SEB, and therefore exhibit better performance compared to SEB arrays. However, AC-SETs have additional design challenges over SEBs: each SET in the array needs a capacitor in series with the drain, which significantly increases the area required for an individual device (Fig. 1). Scanning tips are fabricated on low stress silicon nitride membranes (Fig. 2), removed from the support by a plasma etch, and attached to a quartz tuning fork (Fig. 3). Fig. 4 shows an array of 100 SEBs wired in parallel and positioned close to the tip to minimize parasitic capacitance. They share a common sensing gate connected to a scanning probe, and a control gate, to properly bias the devices for maximum sensitivity (Fig. 5). Varying both gates of an SEB array results in a 2D map (Fig. 6) where a high sensitivity region with the largest value of  $d\Gamma/dV_g$  can be selected.

[1] W. Melitz *et al.*, Surf. Sci. Rep. **66**, 1 (2011).

[2] M.J. Yoo *et al.*, Science **276**, 579 (1997). H.T.A. Brenning *et al.*, Nano Lett. **6**, 937 (2006).

[3] G.J. Dolan, Appl Phys. Lett. **31**, 337 (1977).

[4] A. Aassime *et al.*, Appl. Phys. Lett. **79**, 4031 (2001).

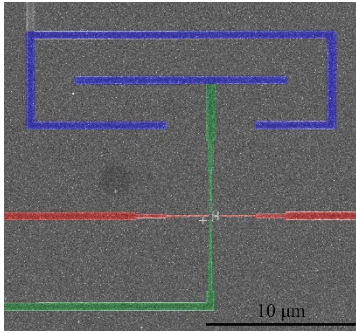


Fig.1: SEM micrograph in false color of an AC coupled SET. The drain coupling capacitor is shown in blue, the source and drain leads in green, and the gates in red.

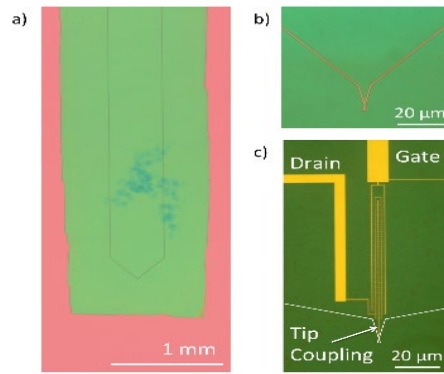


Fig.2: a)  $\text{SiN}_x$  membrane (green) supported by silicon (pink). b)  $\text{SiN}_x$  tip c) Sensing tip with 100 SEBA detector on  $\text{SiN}_x$ .

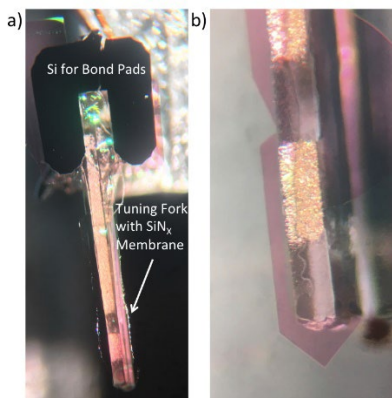


Fig.3: a) A tip mounted on a tuning fork. b) Closer view showing that the tip cleanly breaks free of the support membrane.

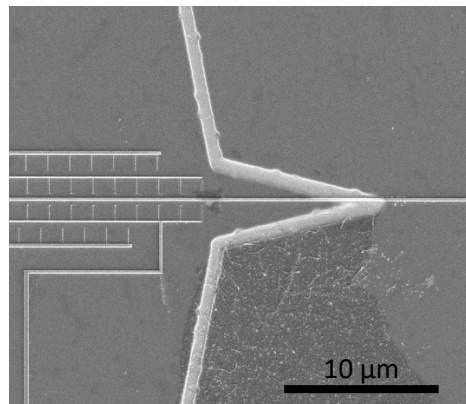


Fig.4: SEM micrograph of a single electron box array positioned near a scanning probe tip.

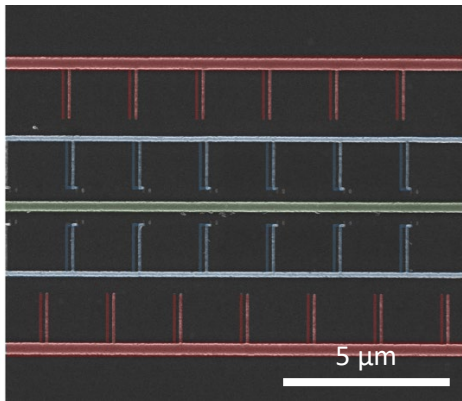


Fig.5: SEM micrograph in false color of a single electron box array. SEBs are shown in blue, the control gates are red, and the sensing gate is green.

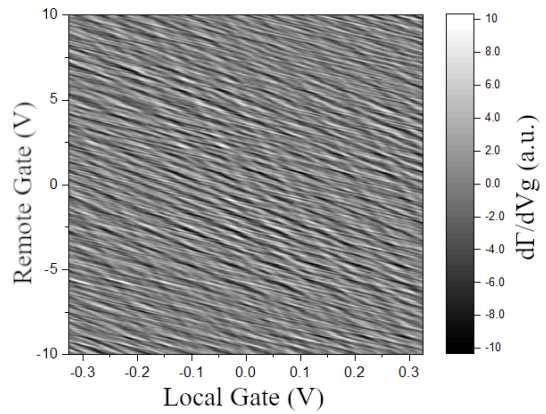


Fig.6: 2D map of the derivative of the reflection of an SEBA.

## **Far Faster Fabrication of Binary Atomic Silicon Logic Circuitry**

R. Wolkow

*Professor, iCORE Chair, Dept. Physics,*

*University Alberta, Edmonton, Alberta, T6G 2J1, Canada*

*Principal Research Officer, Nano Research Centre, National Research Council*

*CTO, Quantum Silicon Inc., Edmonton, Alberta, T6G 2M9, Canada*

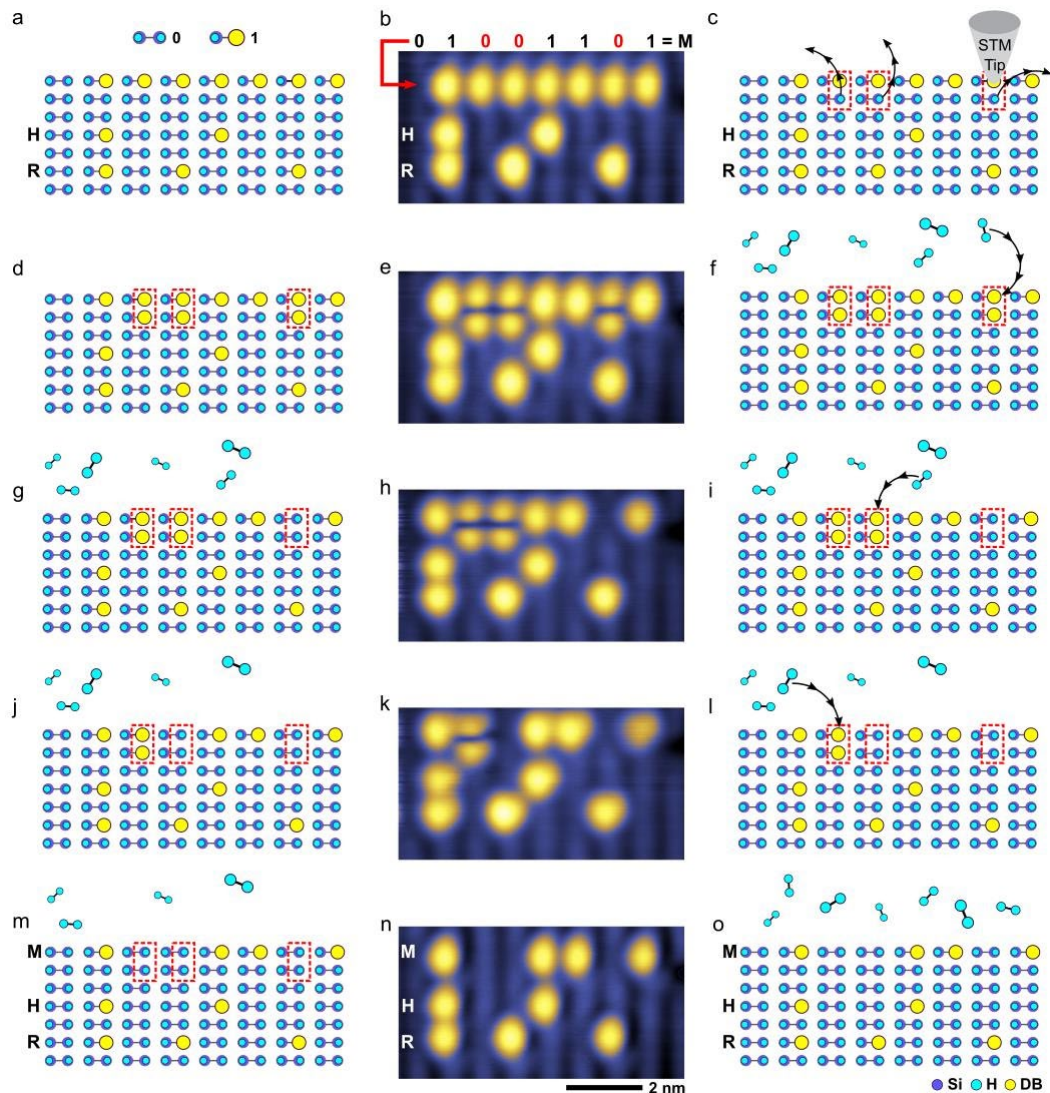
*rwolkow@ualberta.ca*

The long persistent barriers to atom-defined fabrication of silicon have been overcome. In the last year or two, Artificial Intelligence-enabled printing and editing of atomically-perfect ensembles has become routine, enabling the initiation of atomic circuitry composed of individual silicon surface dangling bonds that has the potential to address the shortcomings of CMOS – high power density and limited speed – and to enable new device concepts.

In this circuitry, an ideal bit is composed of paired atoms that form a double well potential that is occupied by one electron. Such a bit can be biased to yield a preferred occupation of one side or the other of the double well, thereby spatially mapping binary 0 and 1 states. “Binary wires” and logic gates that enable ultra-low power, ultra-fast “Binary Atomic Silicon Logic” have been demonstrated (Nature Electronics 1, 636 (2018)). Also, ensembles of such coupled multi-electron atomic structures enable a new atomic-scale embodiment of the Ising model Hamiltonian that provides unique simulation opportunities (PRL 121, 166801 (2018)).

Unlike most other atom-defined patterns, ours are robust above cryogenic temperatures, indeed are perfectly stable to 200 C, and moreover are of electrical utility; our structures exist in the bulk band gap and are not “shorted-out” by the substrate. This new atomic silicon circuitry also mates with CMOS, enabling hybrid CMOS/Atom circuits, thereby retaining the enormous investment in conventional fabrication technologies and providing potential market entry.

The focus of this talk is a new, extremely fast and “easy” variant on our patterning method. Paradoxically, when removing a dangling bond, we now add a second adjacent dangling bond, and the resulting pair is instantly, automatically removed by spontaneous reaction with gaseous H<sub>2</sub>, resulting in a perfectly H-terminated surface (arXiv:1907.03218 [cond-mat.mtrl-sci]). This obviates the relatively slow process of “picking and placing” a single H atom.



**Rewriting a 24-bit memory array ( $V = -1.65$  V,  $I = 50$  pA,  $T = 4.5$  K,  $4 \times 7.5$  nm<sup>2</sup>).**

**a)** A schematic of a 24-bit memory array created from dangling bonds (DBs). The first line of the array is blank (01111111), the next two lines are the ASCII binary forms of the letters H (01001000) and R (01010010). **b)** An STM image of the 24-bit array of DBs. The first line will be rewritten to M (01001101). **c)** The automated STM tip will create reactive inter-dimer sites. **d)** A schematic of the surface after the three hydrogen atoms shown in **c)** have been removed. **e)** An STM image of the 24-bit DB array after three surface hydrogen atoms have been removed. **f)** Hydrogen gas is introduced. **g-i)** Schematics and associated STM images of each molecular hydrogen repassivation event. The first line of the array shown in **a)** has been rewritten to the letter M, now that hydrogen molecules have dissociatively reacted with the inter-dimer sites shown in **d)**. **n)** An STM image of the 24-bit memory array after the inter-dimer sites have reacted with hydrogen molecules, rewriting the stored information. **o)** The remaining hydrogen gas in the chamber does not react with remaining DBs.

## **Modeling Assisted Atomic Precision Advanced Manufacturing (APAM) Towards Room Temperature Operation**

X. Gao, D. Mamaluy, E. Anderson, D. Campbell, A. Grine, A. Katzenmeyer, T.-M. Lu,  
S. Schmucker, L. Tracy, D. Ward, and S. Misra

*Sandia National Laboratories, 1515 Eubank SE, Albuquerque, NM 87123, USA*

*xngao@sandia.gov*

Atomic Precision Advanced Manufacturing (APAM) [1] is a process of area-selective chemical incorporation of dopants (Fig. 1) at an atomic scale using the scanning tunneling microscope (STM) technique. Expanding what APAM can do unlocks the door to revolutionary opportunities in digital electronics from the very physical limit of atoms. Nevertheless, current APAM devices can only work at cryogenic temperatures [2]. To make any impact to microelectronics, APAM devices must be able to work at room temperature (RT). To address this challenge, an interdisciplinary experimental and modeling team at Sandia National Laboratories work closely together to enable APAM devices towards RT operation.

One big problem with current APAM devices (Fig. 2, top) is that a few current leakage paths become important at RT. Using contact isolation (Fig. 2, bottom) can reduce some leakage paths, but we may still have leakage near APAM channel. TCAD device modeling is needed to understand the trade-off between current leakage and device geometry to engineer APAM devices for RT. We employ semiclassical TCAD tool [3] because of its numerical efficiency and ability to simulate arbitrary 2D/3D structures. More importantly, our calculated electron mobility (Fig. 3, black symbols) is consistent with measured data at 4.2 K [1] for APAM donor density close to silicon atomic density. This result not only explains that low electron mobility in APAM channel is caused by ionized impurity scattering, but also suggests we can model APAM devices using semiclassical approach. Our 2D TCAD simulation results show that hole current leakage in the cap layer is a trade-off between p-doping density and layer thickness. Given  $10^{18} \text{ cm}^{-3}$  p-doping in the cap (Fig. 4), the layer thickness must be  $\leq 30 \text{ nm}$  to result in negligible hole current leakage in the cap at RT. This is because the charge depletion width is about 30 nm (Fig. 5). Using the same cap doping and layer thickness, our 3D TCAD simulation (Fig. 6) also indicates negligible hole leakage. The simulation results are supported by RT optical measurements which detect a well-defined, isolated sheet of electrons. We will be able to experimentally study RT electrical transport in an APAM device in the near future and compare to TCAD modeling.

Sandia National Laboratories is a multimission laboratory managed and operated by National Technology and Engineering Solutions of Sandia, LLC., a wholly owned subsidiary of Honeywell International, Inc., for the U.S. Department of Energy's National Nuclear Security Administration under contract DE-NA-0003525

[1] K. Goh *et al.*, Phys. Rev. B **73**, 035401 (2006). [2] K. Goh *et al.*, Appl. Phys. Lett. **93**, 142105 (2008). [3] <https://charon.sandia.gov>.

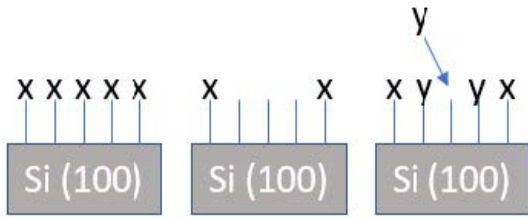


Fig.1: The abstracted APAM process. Molecule X is attached to the surface of silicon (left) and serves as a resist. It can be selectively removed, exposing reactive silicon dangling bonds (middle). Certain molecular precursors y will selectively bond to reactive sites. For conventional APAM, x is hydrogen, patterning is done with an STM, y is phosphine, and the entire patterned structure is capped with a thin film of silicon to preserve the planar device.

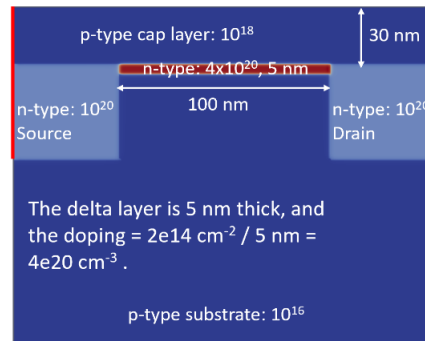


Fig.4: Simulated 2D structure representing cross section of an APAM wire, where the delta-doped layer is approximated by a 5-nm doped region. Current leakage is simulated using the current difference between contacting and not contacting the cap layer.

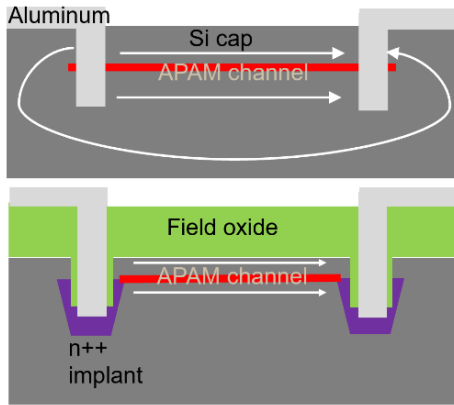


Fig.2: Schematic of APAM wire devices with leakage paths denoted by white lines. Leakage paths through cap layer and substrate become important at RT (top). Contact isolation can remove some leakage paths but still have leakage near APAM channel (bottom).

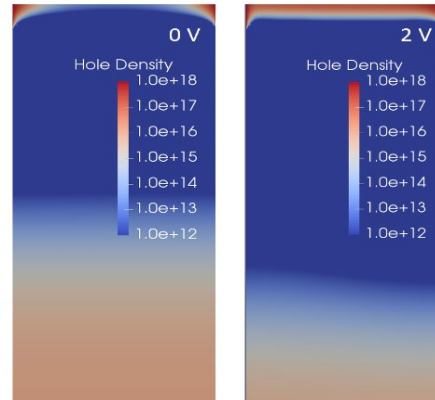


Fig.5: Simulated hole density at 0 V (left) and 2 V (right) for the structure in Fig. 4. The cap layer has no holes at 0V due to charge depletion; the cap layer top contains holes at 2V, but hole density is much smaller than the  $\delta$ -layer electron density, hence little leakage.

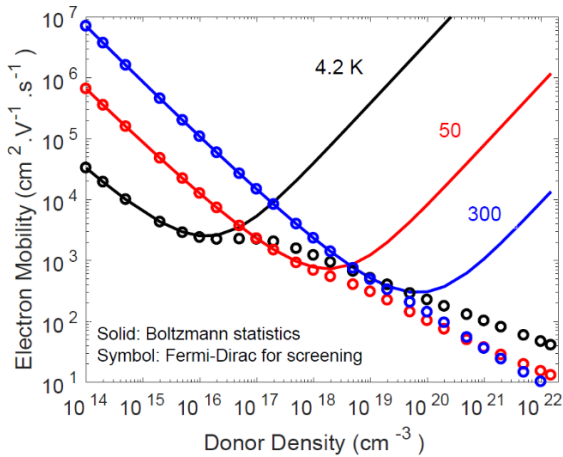


Fig.3: Doping dependent electron mobility at different temperatures modeled using Fermi Golden Rule and ionized impurity scattering. Clearly, Boltzmann statistics is invalid for high doping density, while the mobility with Fermi-Dirac is very small for dopant density close to silicon atomic density.

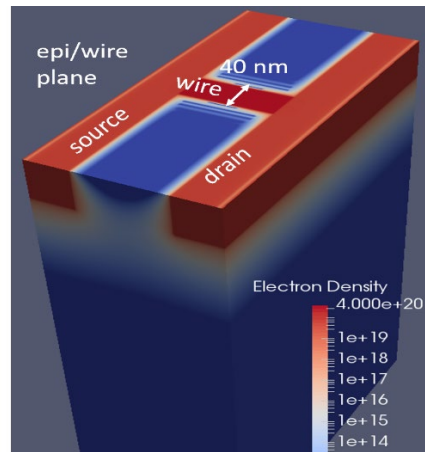


Fig.6: Simulated electron density at 0 V for a 3D APAM wire (extension of Fig. 4) with the top p-cap layer not shown. Inclusion of the wire width (40 nm) in 3D simulation still shows negligible hole current leakage through the top cap layer due to charge depletion.

## Atomic Layer Deposition Engineering of Metal/Insulator/Metal (MIM) Diodes using Localized Impurity Defects

K.E.K. Holden, Y. Qi, M.A. Jenkins, and J. F. Conley, Jr.

*School of Electrical Engineering and Computer Science,*

*Oregon State University, Corvallis, OR, 97331, USA*

*jconley@eecs.oregonstate.edu*

Thin film MIM tunnel diodes are promising for high-speed rectifying applications such as rectenna based energy harvesting and THz detection. Conventionally, current density vs. electric field ( $J$ - $\mathcal{E}$ ) asymmetry,  $f_{\text{asym}} = J/J^+$ , in MIM diodes has been achieved using the metal electrode work function difference,  $\Delta\Phi_M$ . More recently, improved  $f_{\text{asym}}$  and responsivity ( $d^2I/dV)/(2dI/dV)$ ) at low voltage have been achieved in MIM diodes with nanolaminate bi-layer insulator tunnel barriers. For MIM diodes in which conduction in both insulators is dominated by quantum mechanical tunneling, enhancement may occur via "step tunneling" in which electrons tunnel directly through the wider bandgap ( $E_G$ ) insulator into the conduction band of the narrower  $E_G$  insulator [1]. If the narrow  $E_G$  insulator contains *intrinsic* defects that contribute to bulk conduction, low  $\mathcal{E}$  asymmetry may be further improved via "defect enhanced direct tunneling," DEDT, in which electrons may transport easily across the narrow  $E_G$  insulator via defect enhanced (DE) Frenkel-Poole emission before direct tunneling (DT) through the larger  $E_G$  insulator [2,3]. For both ST and DEDT, the asymmetry arises because electrons under the opposite polarity must tunnel through both dielectrics. In this work, we investigate the impact of localized *extrinsic* defects by using atomic layer deposition (ALD) to intentionally introduce Ni at precise thickness intervals in an  $\text{Al}_2\text{O}_3$  tunnel barrier.

ALD of  $\text{Al}_2\text{O}_3$  on TiN bottom electrodes was performed at 200 °C using tri-methyl aluminum and  $\text{H}_2\text{O}$ . Five samples were prepared in which a baseline 100 ALD cycle  $\text{Al}_2\text{O}_3$  sequence (10 nm thick) was interrupted by two ALD cycles of  $\text{Ni}(\text{tBu}^2\text{DAD})_2$  and  $\text{O}_3$  [4], after either 25, 50, 75, or every 25 cycles of  $\text{Al}_2\text{O}_3$ . Al top electrodes were then sputtered through a shadow mask to form MIM devices (inset Fig. 1).

DC  $J$ - $\mathcal{E}$  sweeps (Fig. 1) of the 100 ALD cycle  $\text{Al}_2\text{O}_3$ -only baseline device show Fowler-Nordheim tunneling (FNT) at high  $\mathcal{E}$ , with  $f_{\text{asym}} (= J/J^+) > 1$  (Fig. 2), due to a  $\Delta\Phi_M$  of roughly 0.2 eV. In all cases, the addition of the Ni ALD cycles leads to an increase in  $J$  at low  $\mathcal{E}$  compared to the baseline device, suggesting the creation of a defect related conduction path. At high  $\mathcal{E}$ , however,  $J$  of all the Ni containing devices is lower than the baseline device, suggesting suppression of FNT. The 25/2/75 and 75/2/25 ( $\text{Al}_2\text{O}_3/\text{NiO}/\text{Al}_2\text{O}_3$ ) devices show  $f_{\text{asym}}$  polarity opposite that of the baseline device, while the 50/2/50 and 25/(2/25)x3 devices are roughly symmetric (Fig. 1).

The greater reduction in  $J$  at large negative  $\mathcal{E}$ ,  $f_{\text{asym}}$  reversal, and reduced  $J$ - $\mathcal{E}$  slope for the 25/2/75 and 75/2/25 devices suggest that FNT is suppressed more for emission from the smaller  $\Phi_M$  electrode (Al) than for the larger  $\Phi_M$  (TiN). FNT suppression appears greatest for the 75/2/25 device in which Ni is closest to the Al, pointing to an increase in effective barrier height ( $\phi_{\text{Bn}}$ ), likely due to negative charge in the  $\text{Al}_2\text{O}_3$ . Capacitance ( $C$ ) vs.  $\mathcal{E}$  sweeps (Fig. 3) reveal a positive voltage shift in  $C_{\text{min}}$  for all Ni devices, consistent with negative charge.

The asymmetry reversal in Ni "doped" devices suggests the possibility of using ALD for precision defect engineering of MIM tunnel devices. This technique may find application for carrier selective contacts as well.

- [1] N. Alimardani *et al.*, Appl. Phys. Lett. **102** 143501 (2013).
- [2] N. Alimardani *et al.*, J. Appl. Phys. **116**, 024508 (2014).
- [3] N. Alimardani *et al.*, Appl. Phys. Lett. **105**, 082902 (2014).
- [4] K. Holden *et al.*, ACS Appl. Mater. Interfaces **11**, 30437-30445 (2019).

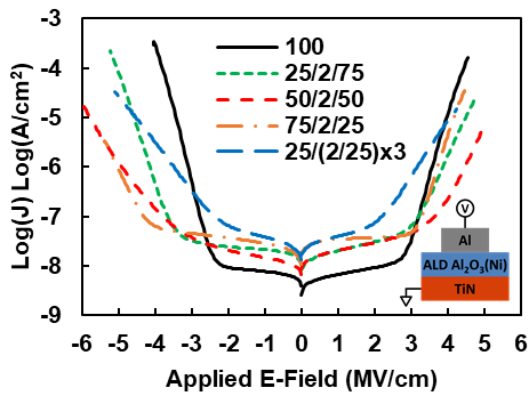


Fig. 1:  $J$ - $\mathcal{E}$  sweeps for  $\text{TiN}/\text{Al}_2\text{O}_3/\text{Al}$  devices with (dashed lines) and without (black solid line) intentionally placed Ni impurity defects.

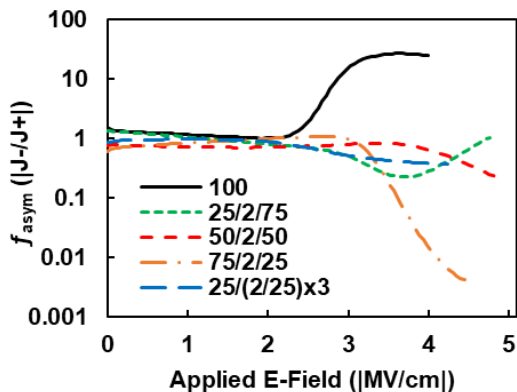


Fig. 2:  $f_{\text{asym}}$ - $\mathcal{E}$  curves for  $\text{TiN}/\text{Al}_2\text{O}_3/\text{Al}$  devices with (dashed lines) and without (black solid line) intentionally placed Ni defects.

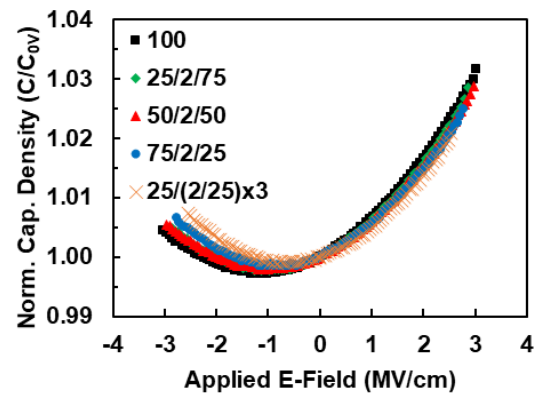


Fig. 3: Normalized capacitance density ( $C/C_{0V}$ ) vs.  $\mathcal{E}$  for  $\text{TiN}/\text{Al}_2\text{O}_3/\text{Al}$  MIM devices with and without intentionally placed Ni defects (as indicated).

## **Electrically Detected Electron Nuclear Double Resonance in Fully Processed Transistors**

R.J. Waskiewicz, B. Manning, and P.M. Lenahan

*Department of Engineering Science and Mechanics, Pennsylvania State University,  
University Park, PA 16802, USA  
pmlesm@enr.psu.edu*

Electron paramagnetic resonance (EPR) techniques are unrivalled in their analytical power in determining the physical and chemical nature of point defects in semiconductors and insulators. Among all EPR techniques, electron nuclear double resonance (ENDOR) is the most powerful. [1] ENDOR involves the simultaneous observation of EPR and nuclear magnetic resonance (NMR) at paramagnetic defects. The NMR response alters the EPR amplitude, allowing an indirect measurement of NMR which allows for identification of the nuclei under observation as well as providing often detailed information about the physical distributions of multiple nuclei. A limitation of all EPR techniques in the study of nanoscale devices has been sensitivity. Conventional EPR sensitivity is roughly ten billion total defects within the sample under study. The sensitivity of ENDOR is several orders of magnitude lower than that of classical EPR, making classical ENDOR essentially impossible in micro or nanoscale devices. However, various electrically detected magnetic resonance (EDMR) techniques provide an enormous increase in sensitivity over that of classical EPR, at least an improvement of a factor of ten million, making measurements of EPR in nanoscale devices possible. In this study we show how EDMR detection of ENDOR can provide an enormous improvement in sensitivity, allowing electrically detected ENDOR (EDENDOR) measurements to be made with high sensitivity at room temperature in a fully processed transistor. Although our work does not constitute the first observation of EDENDOR in any system, [2] to the best of our knowledge it does represent the first observation in a fully processed transistor. We observe EDENDOR of nearby nitrogen donors interacting with deep level (recombination centers) in the base collector junction of a 4H SiC bipolar junction transistor. The measurements were made with X-band EDMR detection while sweeping over RF frequencies from 10 KHz to 15 MHz. We believe that the defects under observation are likely of particular interest for spin based quantum computation. We have tentatively identified the recombination centers as silicon vacancies.

[1] L. Kevan and D. Kispert, *Electron Spin Double Resonance Spectroscopy*, (John Wiley and Sons, New York, 1976).

[2] F. Hohne *et al.*, Phys. Rev. Lett. **106**, 187601 (2011).

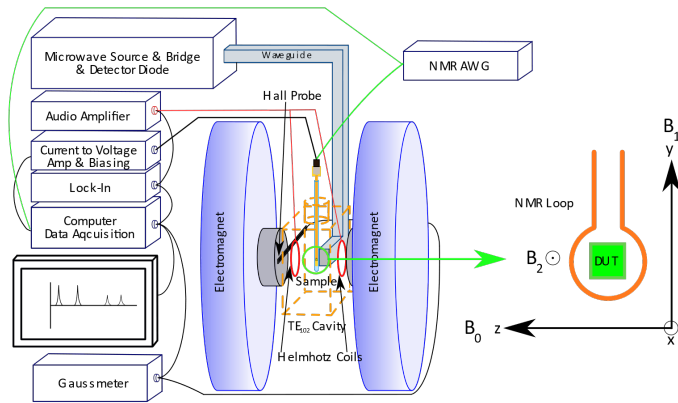


Fig.1: A schematic of the EDENDOR spectrometer. For EDMR, the NMR RF loop and NMR arbitrary waveform generator (AWG) are bypassed and device current is monitored as magnetic field is swept. For EDENDOR, the magnetic field is held constant while the NMR AWG supplies a RF sweep and device current is monitored.

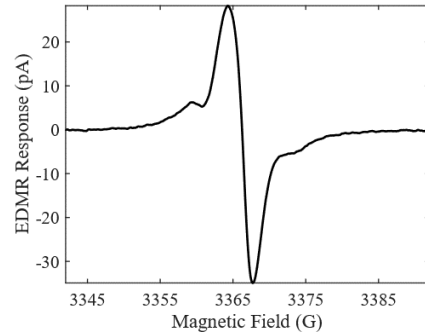


Fig.2: Measured EDMR response as a function of applied magnetic field. The central feature has zero-crossing  $g=2.003$  and linewidth of 3.4 G. A very similar EDMR spectrum has been linked to a  $V_{Si}$  defect in 4H-SiC MOSFETs.

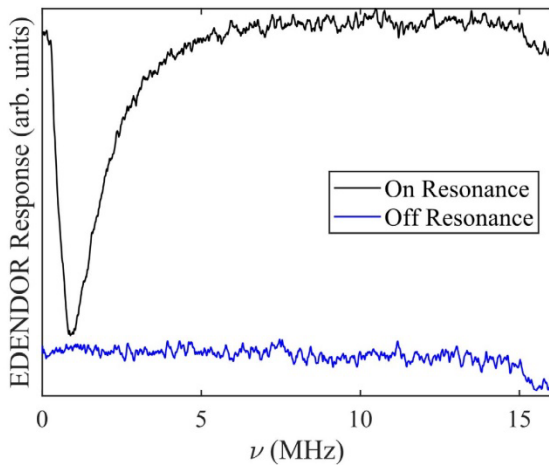


Fig.3: The EDENDOR response (above, black) measured for constant magnetic field of 3366.5 Gauss. The large response peaks at 1.04 MHz. The nuclear frequency for nitrogen at this field is 1.036 MHz. The off-resonance-field EDENDOR response is shown below in blue for comparison.

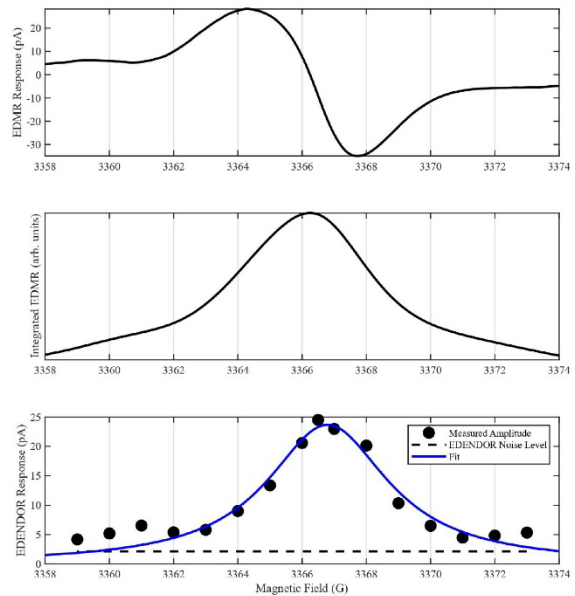


Fig.4: EDMR response (top), integrated EDMR response (middle), and corresponding EDENDOR response (bottom) as a function of magnetic field. In the EDENDOR measurement, the noise level is indicated in a black dashed line and a standard Lorentzian fit to the data is indicated in a blue solid line.

## **Quantum Computing without Quantum Computers: Database Search and Data Processing Using Classical Wave Superposition**

A. Khitun

*Department of Electrical and Computer Engineering, University of California -Riverside,  
Riverside, 92521 California, USA*

*akhitun@engr.ucr.edu*

Quantum computing is an emerging field of science which will lead us to new and powerful logic devices with capabilities far beyond the limits of current transistor-based technology [1]. There are certain types of problems which quantum computers can solve fundamentally faster than the tradition digital computers. For example, Peter Shor developed a quantum algorithm which solves the factoring and discrete logarithm problems in time  $O(n^3)$ , compared with the exponential time required for the best known classical algorithm [2]. Quantum computers can search an “unsorted database” (that is, for  $f(x): \{0, N\} \rightarrow \{0,1\}$ , find  $x_0$  such that  $f(x_0) = 1$ ) in time  $O(\sqrt{N})$ , compared with the  $O(N)$  time that would be required classically [3]. Superposition of states and entanglement are the key two ingredients which make quantum computing so powerful. Superposition of states allows us to speedup database search by checking a number of bits in parallel, while quantum entanglement is critically important for quantum cryptography [4]. There are quantum algorithms which require both superposition and entanglement (e.g., Shor’s algorithm). But neither the Grover algorithm nor the very first quantum algorithm due to Deutsch and Jozsa [5] needs entanglement [6]. *Is it possible to utilize classical wave superposition to speedup database search?* This interesting question was analyzed by S. Lloyd [7]. It was concluded that classical devices that rely on *wave interference may provide the same speedup over classical digital devices as quantum devices* [7]. There were several experimental works using optical beam superposition for emulating Grover’s algorithm. It was concluded that the use of classical wave superposition comes with the cost of the exponential increase of the resources [9]. Since then, it is widely believed that the use of classical wave superposition for quantum algorithms is inevitably leading to an exponential resources overhead (e.g., number of devices, precision, and/or power consumption). In this work, we describe a classical Oracle machine which utilizes classical wave superposition. We argue that the classical wave-based approach provides the same speedup in database search as quantum computers. We also present experimental data on database search through a magnetic database using spin wave superposition.

- [1] National Academies of Sciences, Engineering, and Medicine, Quantum Computing: Progress and Prospects. (The National Academies Press, 2018).
- [2] P.W. Shor, Proc. IEEE FOCS (1994).
- [3] L.K. Grover, Am. J. Phys. **69**, 769 (2001).
- [4] I. Chuang, in Quantum Entanglement and Information Processing Vol. 79 Les Houches Summer School Session (eds D. Esteve, J. M. Raimond, & J. Dalibard) (2004).
- [5] D. Deutsch *et al.*, Proc. Roy. Soc. London Ser. A – Math. Phys. Eng. Sci. **439**, 553 (1992).
- [6] P. Knight, Science **287**, 441 (2000).
- [7] S. Lloyd, Phys. Rev. A **61**, 010301 (2000).
- [8] A. Patel, Int. J. Quant. Inf. **4**, 815 (2006).
- [9] N. J. Cerf *et al.*, Phys. Rev. A **57**, R1477 (1998).

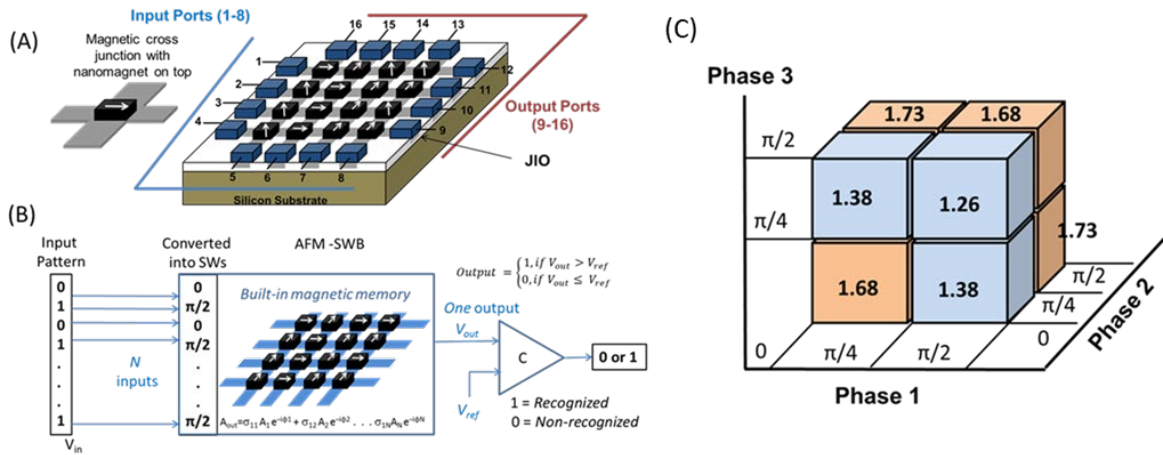


Fig.1: (A) Schematic of a magnonic database. It is shown a 4x4 magnonic matrix consisting of magnetic waveguides connected via cross-junctions. The magnets on the top of the junction are memory elements. Logic 0 and 1 are encoded into the magnetic polarization of the magnets. Spin waves are used for magnetic read-out. (B) Data processing: input signals are converted into spin wave phases. The output is recognized by the amplitude of the inductive voltage produced by the spin wave interference. (C) Illustration of the search algorithm based on classical wave superposition resulting in the same speedup as for quantum computers.

## Probing of Composite Fermions in Natural InP/GaInP<sub>2</sub> Quantum Hall Puddles Using Near-Field Scanning Optical Microscopy

A. Mintairov

*Ioffe Institute, St. Petersburg, Russia*

*Dept of Electrical Engineering, University of Notre Dame, Notre Dame, USA*

*amintairov@gmail.com*

Proposal for topological quantum computations (TQC) suggests the use of composite fermions (CFs) vortices in a p-wave superconductor, which obey non-Abelian quantum statistics and have known as non-Abelian anyons [1]. A physical realization of TQC implies the use of solid-state platforms providing a set of localized non-Abelian anyons, combined with a “tweezer” to perform their braiding and fusion. A TQC system most intensively investigated up to date is a two-dimensional electron gas semiconductor structure in a high perpendicular external magnetic field, in which non-Abelian anyons can be formed in the 5/2 fractional quantum Hall (QH) state [2]. Excising experimental approach of TQC includes Ahronov-Bohm phase interferometry of edge currents structures having hundreds of mobile CFs. In these structures, however, an intrinsic disorder smears out a localization of individual CFs on a length scale of up to half a micron preventing their precise braiding and fusion [3]. Here we demonstrate deterministic localization and self-confinement of CFs on the order of magnitude smaller length scale in the natural QH puddles represented by self-organized InP/GaInP<sub>2</sub> quantum dots having strong build-in magnetic field [4, 5]. We have used high-spatial-resolution cryo-magnetic near-field scanning photoluminescence [6] to demonstrate a molecular arrangement of CFs, possibility of their fusion/braiding (Fig.1) and formation of single CFs (Fig.2) at zero external magnetic field. Our results open routes for the creation of the “magnetic-field-free” topological quantum gates.

**Acknowledgment.** The author acknowledges a support from the Russian Science Foundation grant No 19-19-00246.

[1] A.Y. Kitaev, *Ann. Phys.* **303**, 2 (2003).

[2] C. Nayak *et al.*, *Rev. Mod. Phys.* **80**, 1083 (2008).

[3] H. Fu *et al.*, *PNAS* **113**, 12386 (2016).

[4] A.M. Mintairov *et al.*, *Phys. Rev B* **97**, 195443 (2018).

[5] A.M. Mintairov *et al.*, *Appl. Phys. Lett.* **115**, 202104 (2019).

[6] A.M. Mintairov, *Semiconductors* **54**, 138 (2020).

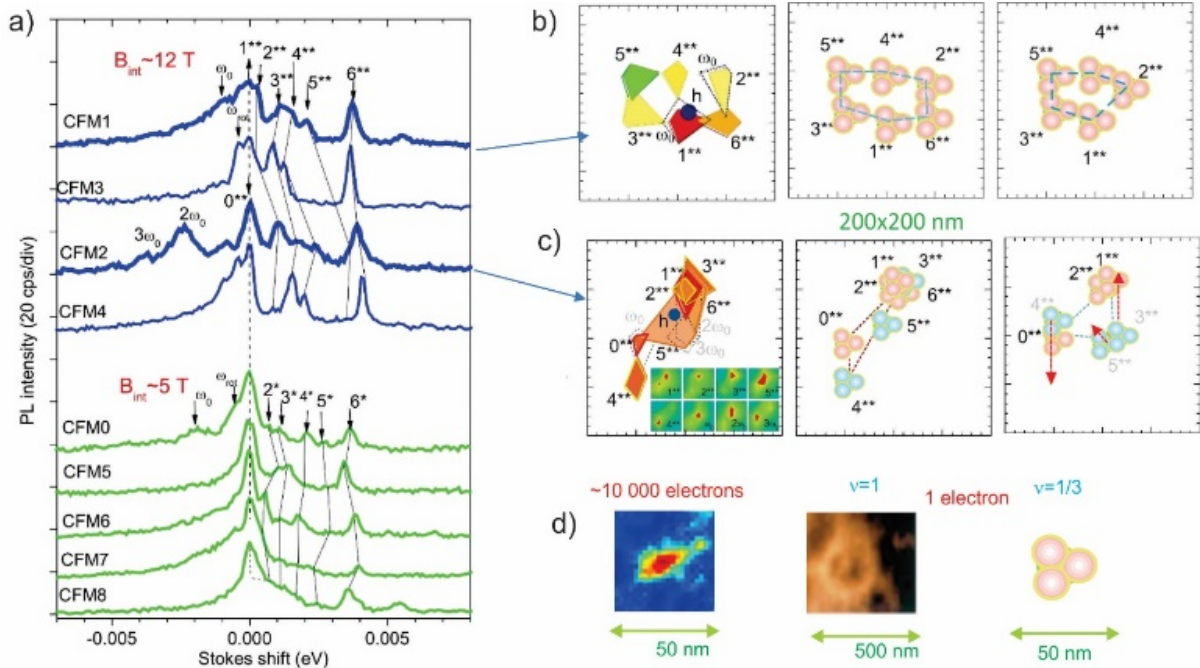


Fig.1: (a) The emission (PL) spectra of nine InP/GaInP<sub>2</sub> CF molecules having build-in magnetic field 5 T (lower, green) and 10 T (upper, blue). (b) and (c) 200x200 nm<sup>2</sup> integral NSOM image of PL peaks (left) and corresponding CF molecule configurations in phot-excited (center) and initial (right) states of CFM1 and CFM2, respectively. For CF2 individual NSOM images are shown in the insert of integral image. The CFM2 configurations reveal pairing of 1<sup>\*\*</sup>-2<sup>\*\*</sup>, 0<sup>\*\*</sup>-4<sup>\*\*</sup> and 3<sup>\*\*</sup>-5<sup>\*\*</sup> CF and possible braiding of 0<sup>\*\*</sup> and 4<sup>\*\*</sup> CFs (see red arrows showing CF displacement). (d) comparison of vortex structure measured in Bi<sub>2</sub>Te<sub>3</sub>/FeTe<sub>0.55</sub>Se<sub>0.45</sub> (left – from M. Chen et al, Sci. Adv. 4, 1, (2018)) and in QH structure for  $\nu=1$  single electron state (center - N. B. Zhitenev et al, Nature 104, 473, (2000)), and expected in CFMs for  $\nu=1/3$  single electron state (right).

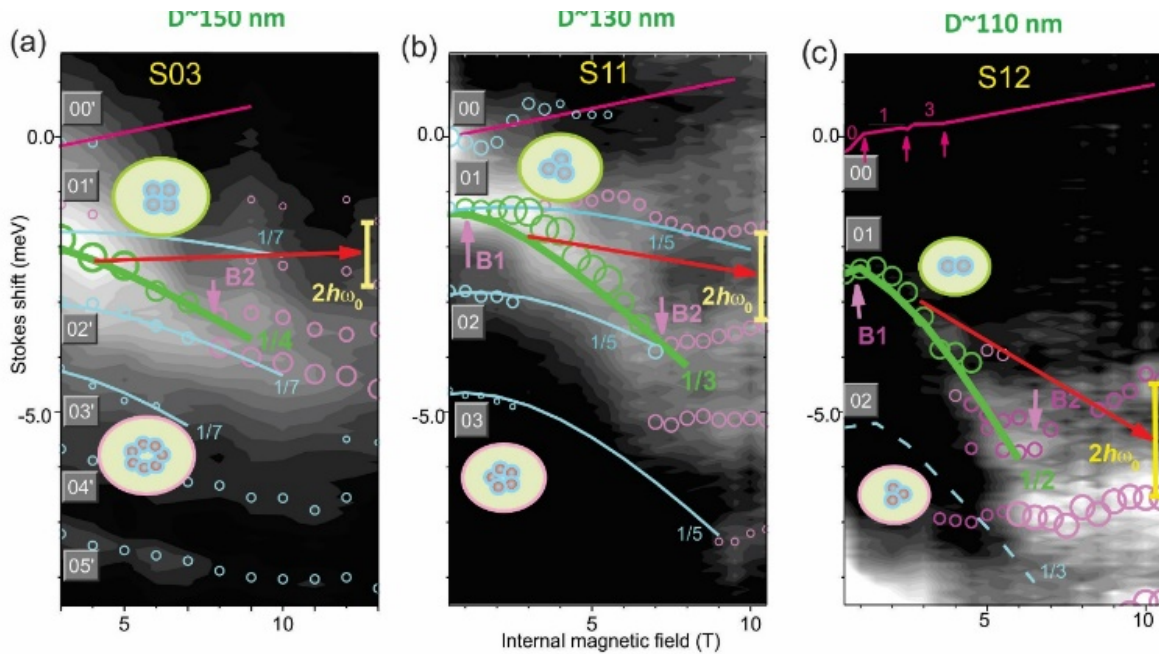


Fig.2: Contour plots of the emission spectra of single electron InP/GaInP<sub>2</sub> QDs having size  $D \sim 150, 130$  and  $110$  nm (a, b and c, respectively) versus internal magnetic field. Circles outline position and intensity of PL peaks, lines calculations of B-dispersion for different fractional charges  $1/2, 1/3, 1/4, 1/5$  and  $1/7$ . Red arrow outlines a connection between dispersion of the main PL peak (green) and quantum confinement, showing increase of fractional charge versus  $D$ , i.e. vortex self-confinement effect. Inserts show possible arrangement of vortices for ground (red outline) and excited state (green outline) of single CF.

## **Synthetic Electronics**

C. Baatar

*Office of Naval Research, USA*

*chagaan.baatar@navy.mil*

Building electronic circuitry with atomic precision is beyond the capability of current, and in the foreseeable future, top-down lithographic techniques. In recent years, the US Office of Naval Research (ONR) has championed several research initiatives that sought to address this key challenge. One of the most exciting development and initial success that resulted from these initiatives is a bottom-up chemical synthesis technique that has proven highly effective at assembling two-dimensional (2D) graphene nanostructures with spatial precision control down to single atom and single bond level. In this presentation, I will briefly review the current status of this exciting new research field, highlighting some of the main achievements thus far, as well as challenges that remain. I will share some personal perspectives and speculate on possible future directions. In particular, I believe that this new synthetic approach to post-lithography electronics is well-suited for building devices and circuitry that operate on the principle of coherent control and manipulation of individual quantum systems and their mutual interactions. The motivation behind the discussion is to socialize the basic ideas and capabilities with, and get feedback from, the relevant research communities, in order to further refine and improve future research agenda.

## Quantitative Analysis of DNA via Single-Molecule Quantum Sequencing

M. Taniguchi

*The Institute of Scientific and Industrial Research, Osaka University,*

*8-1 Mihogaoka, Ibaraki, Osaka 567-0047, Japan*

*taniguti@sanken.osaka-u.ac.jp*

Single-molecule quantum sequencing using a tunneling current to read out the electronic states of a molecule enables the determination of a base sequence from the single-molecule conductance of the base molecule [1]. This approach offers a low-cost, high-speed, and portable sequencing method for realizing personalized medicine based on genomic information.

Single-molecule quantum sequencing can be applied to directly determine the base sequences of RNA and amino acid sequences of peptides, which is not possible with existing DNA-sequencing methods [2–4]. Furthermore, chemically modified base and amino acid molecules that turn on and off gene functions as well as disease markers for illnesses such as cancer can be directly determined.

To accurately diagnose diseases using DNA and RNA, a quantitative analytical procedure is required that can simultaneously determine the base sequences of DNA and RNA and the mixing ratio in the sample. However, existing DNA-sequencing methods cannot be applied to perform quantitative analyses in principle. In the case of single-molecule quantum sequencing, the number of signals in the base sequence is the same as the number of molecules, thus enabling quantitative analysis. When a sample containing two types of RNA for cancer markers mixed at a 3:1 ratio was analyzed by this method, a mixing ratio of 2.6:1 was obtained in addition to two base sequences [5].

The quantitative analysis method sheds new light on the field of drug discovery. There is an anticancer drug, which is used worldwide and is considered to decrease the number of cancer cells via an exchange with the thymine in DNA. However, this drug has not been directly observed in the DNA. Single-molecule quantum sequencing has now succeeded in directly observing the insertion of anticancer drugs into DNA [6].

[1] M. Di Ventra and M. Taniguchi, *Nat. Nanotech.* **11**, 117 (2016).

[2] M. Taniguchi *et al.*, *Nat. Nanotech.* **5**, 286 (2010).

[3] M. Taniguchi *et al.*, *Sci. Rep.* **2**, 00501 (2012).

[4] M. Taniguchi *et al.*, *Nat. Nanotech.* **9**, 835 (2014).

[5] M. Taniguchi *et al.*, *Sci. Rep.* **8**, 8517 (2018).

[6] M. Taniguchi *et al.*, *Sci. Rep.* **9**, 3886 (2019).

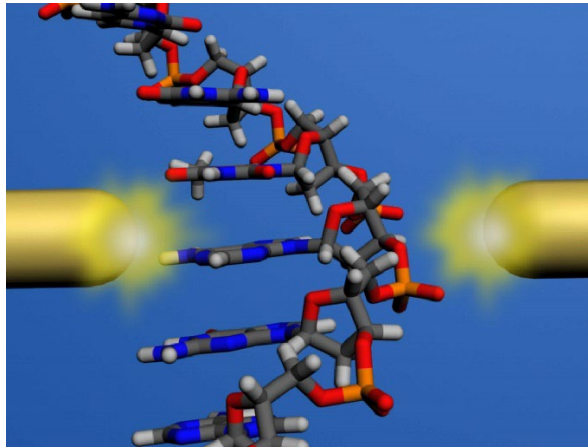


*Fig.1: Operating principle of single-molecule quantum sequencing. When single-stranded DNA passes through nanogap electrode, the device can measure tunneling currents that conducted via single base molecules passing between nanogap electrodes.*

## Ion Transport Across Crown-Like Sub-Nanoscale Pores in 2D Materials

A. Smolyanitsky and A. Fang  
*Applied Chemicals and Materials Division  
National Institute of Standards and Technology  
Boulder, CO, USA  
alex.smolyanitsky@nist.gov*

The ability to control aqueous ion flow across nanoporous membranes is a key component in applications ranging from water desalination to drug delivery. It is also a critical function of protein ion channels, which play a central role in controlling salinity in living cells for many biological processes. It is not surprising that historically the inspiration for achieving selective, controllable ion flow in human-made nanopores came from biophysics. In contrast, for the new class of nanopores presented here, we draw initial inspiration from the chemistry of crown ether molecules.

Crown ethers, a class of cyclical polyethers, are known to form highly selective complexes with a variety of solvated metal cation guests by hosting them in symmetric electrostatic cavities formed by radially oriented O-C<sub>2</sub><sup>+</sup> dipoles. For example, aqueous K<sup>+</sup> ions form stable room-temperature complexes with 18-crown-6 molecules, while Na<sup>+</sup> ions do not. Such a strong binding selectivity is driven by the delicate balance between the bulk solvation of the ions and the solvent-mediated binding of ions to the crowns. Recent experiments have shown that atomically symmetric sub-nanoscale pores can be fabricated in graphene [1], hexagonal boron nitride [2], and molybdenum disulfide (MoS<sub>2</sub>) [3]. When immersed in water-dissolved salts, such pores effectively mimic the locally symmetric electrostatic environments featured by aqueous crown ethers and promise a rich set of novel pore properties.

We use extensive all-atom molecular dynamics simulations and transition state theory to demonstrate a broad range of host-guest recognition effects in crown-like sub-nanoscale pores embedded in monolayer two-dimensional (2D) membranes. In particular, we demonstrate selective trapping of K<sup>+</sup> ions in graphene-embedded crown pores [4], the first examples of highly mechanosensitive graphene- [5] and MoS<sub>2</sub>-based [6] solid-state ion channels, and concentration-dependent, strain-tunable salt mixture sieving by graphene-embedded crown pores [5]. We discuss the fundamental mechanisms driving the observed phenomena and propose a novel class of nanoporous 2D materials, whose permeation properties can be determined by the pore structure, without requiring additional chemical functionalization. Finally, we discuss the prospects of porous membranes possessing ion permeation, selectivity, and sieving properties controlled by dynamically applied tensile membrane stress.

- [1] J. Guo *et al.*, Nat. Comm. **5**, 5389 (2014).
- [2] S.M. Gilbert *et al.*, Nat. Sci. Rep. **7**, 15096 (2017).
- [3] J.P. Thiruraman *et al.*, Nano Lett. **18**, 1651 (2018).
- [4] A. Smolyanitsky *et al.*, ACS Nano **12**, 6677 (2018).
- [5] A. Fang *et al.*, Nat. Mater. **18**, 76 (2019).
- [6] A. Fang *et al.*, J. Phys. Chem. C **123**, 3588 (2019).

## **Real-Time Biosensors for Continuous Measurements of Biomolecules in Live Subjects**

H.T. Soh

*Department of Electrical Engineering & Department of Radiology*

*Stanford University, Stanford CA, 94305 USA*

*tsoh@stanford.edu*

A biosensor capable of continuously measuring specific molecules *in vivo* would provide a valuable window into patients' health status and their response to therapeutics. Unfortunately, continuous, real-time molecular measurement is currently limited to a handful of analytes (*i.e.* glucose and oxygen) and these sensors cannot be generalized to measure other analytes. In this talk, we will present a biosensor technology that can be generalized to measure a wide range of biomolecules in living subjects (Fig. 1) [1]. To achieve this, we develop synthetic antibodies (aptamers) that change its structure upon binding to its target analyte and produce an electrochemical current or emit light. Our real-time biosensor requires no exogenous reagents and can be readily reconfigured to measure different target analytes by exchanging the aptamer probes in a modular manner (Fig. 2). Using our real-time biosensor, we demonstrate the first closed loop feedback control of drug concentration in live animals and discuss potential applications of this technology (Fig. 3) [2]. Finally, we will discuss methods for generating the aptamer probes which are at the heart of this biosensor technology [3, 4].

[1] B.S. Ferguson *et al.*, *Sci. Transl. Med.* **5**, 213ra165 (2013).

[2] P.L. Mage *et al.*, *Nature Biomed. Eng.* **1**, 0070 (2017).

[3] C. Gordon *et al.*, *bioRxiv* (2019)

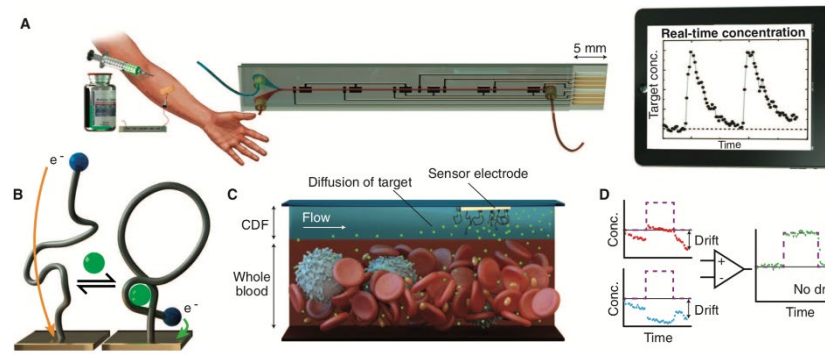


*Fig. 1: Real-time biosensor achieves real-time quantitative measurement of specific molecules in the blood of living animals. (A) The device is connected to the patient's bloodstream to measure drug pharmacokinetics. (B) The aptamer probe is tethered to the gold electrode. Binding of target (green) induces a reversible conformational change in the probe, increasing the rate of electron transfer between an electrochemical redox reporter (blue) and a microfabricated electrode, yielding a measurable current change as a function of time. (C) The continuous-flow diffusion filter (CDF), formed by vertically stacked laminar flow of buffer (blue) and blood (red), as shown in the microfluidic device in (A), permits access to the target molecules while selectively excluding blood-borne interferences. (D) Signal-on (red) and signal-off (blue) both exhibit significant drift in response to a pulse of target (purple). Kinetic differential measurement (KDM; green) improves accuracy of real-time current measurements by minimizing drift and enhancing SNR.*

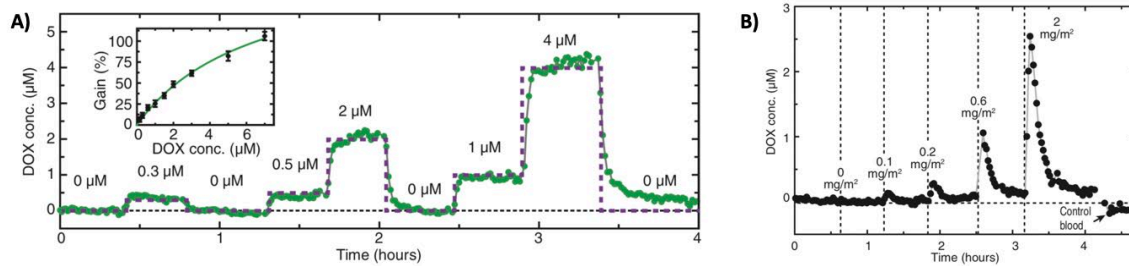


*Fig. 2: Continuous measurements using the real-time biosensor. A) Real-time measurement of DOX in vitro in human whole blood (green) relative to actual concentrations (purple) over the course of 4 hours. B) In vivo measurement of changing DOX concentrations in a live rat over several hours.*

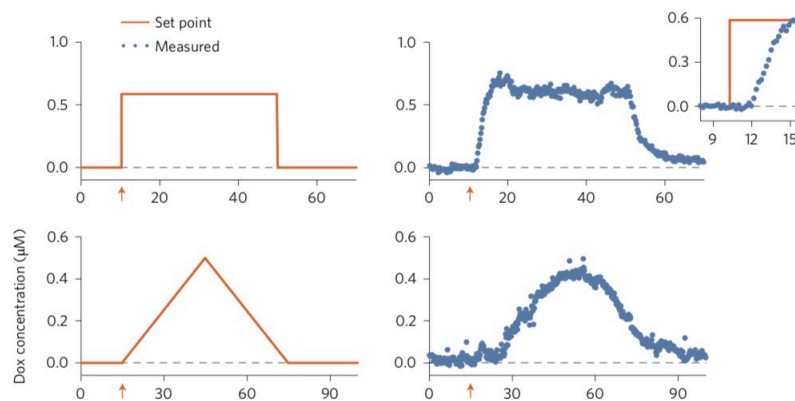


*Fig. 3: Closed-loop feedback control of Dox in vivo. Our system accurately maintained in vivo drug concentrations (blue dots) at the desired set point (orange line) with a response time of 5–10 min in live, conscious New Zealand White rabbits. A variety of concentration profiles can be realized continuously as a function of time. Orange arrows indicate start time of controlled infusion, and each row of panels represents a single experiment in one animal. Inset shows detail of initial rise in upper-right panel.*

## High Performance Dual-Gate 2-Dimensional MoS<sub>2</sub> pH and Biosensors

S.T. Le<sup>1,2</sup>, C.A. Richter<sup>1</sup>, N.B. Guros<sup>3</sup>, N.D. Amin<sup>4</sup>,  
H.C. Pant<sup>4</sup>, and A. Balijepalli<sup>3</sup>

<sup>1</sup>*Nanoscale Device Characterization Division,  
National Institute of Standards and Technology,  
Gaithersburg, MD 20899, USA*

<sup>2</sup>*Theiss Research, La Jolla, CA 92037, USA*

<sup>3</sup>*Microsystems and Nanotechnology Division,  
National Institute of Standards and Technology, Gaithersburg, MD 20899, USA*

<sup>4</sup>*National Institute of Neurological Disorders and Stroke,  
National Institutes of Health, Bethesda, MD 20892, USA*  
*son.le@NIST.gov*

We previously developed sensors based on ionic liquid gated field-effect transistors (FETs) operating at the quantum capacitance limit that allow ultrasensitive pH measurements for biophysics applications [1]. To improve the durability and accessibility of the devices for the broader biological research community, we have developed a solid-state version of these high-performance devices and applied them to measure the activity of enzymes relevant to Alzheimer's disease. The FETs are fabricated with a single-monolayer of the 2D transition metal dichalcogenide MoS<sub>2</sub> and are top-gated with a high-κ dielectric gate oxide. The asymmetric capacitive coupling between the high-κ top-gate and the back-gate dielectric (SiO<sub>2</sub> substrate oxide) enables amplification of a voltage applied to the top gate by up to 8 times. We leveraged the high performance of the devices to enable pH measurements with sensitivities that exceed the Nernst value of 59 mV/pH at room temperature. The improved sensitivity allows the detection of pH changes as small as 0.004, which in turn facilitates the measurements of activity and kinetics of enzyme catalyzed phosphorylation of substrate proteins at physiological concentration. Accurate and rapid measurements of enzyme activity are critical to the development of therapeutics that target neurological disorders. The super-Nerstian pH measurements enabled by the dual-gate 2D transistors allow the rapid and quantitative estimation of the kinetics of enzymes that are implicated in Alzheimer's disease. For example, we have demonstrated the ability of dual-gated FETs to detect small changes in the solution pH during phosphorylation of the substrate protein, histone H1. We compared these FET measurements against enzyme activity measurements obtained from a radioactively labeled γ-<sup>32</sup>P-ATP assay (which involves handling radioactive materials and is slow to perform). The FET-based measurements are in excellent quantitative agreement with this existing technique (Fig. 4), while enabling results in minutes to allow rapid therapeutic screening.

[1] S. T. Le *et al.*, *Nanoscale* **11**, 15622 (2019).

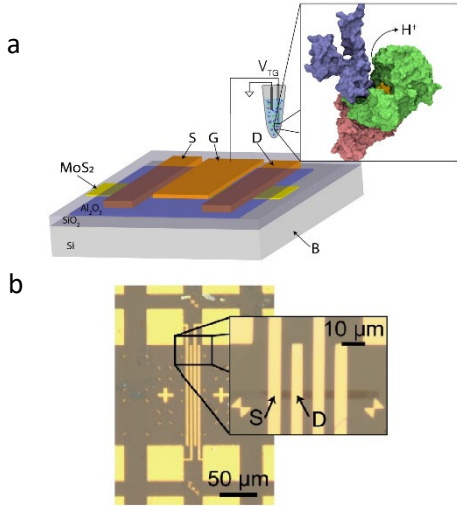


Fig. 1: High-k dual-gate 2D FETs for biosensing. (a) Device schematic of a dual-gate FET for biosensing. A channel formed between the source (S) and drain (D) terminals is controlled electrostatically by a voltage applied to the silicon substrate (B) or the high-k top-gate (G). A voltage applied to the top-gate ( $V_{TG}$ ) can be switched between a voltage source for characterization or a biosensing element. (b) An array of dual-gate 2D FETs fabricated using a 2D MoS<sub>2</sub> film on a 70 nm SiO<sub>2</sub> substrate before top-gate oxide and top-gate metal deposition.

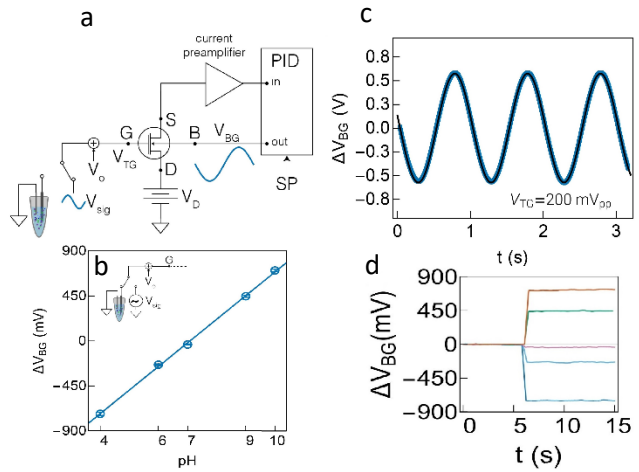


Fig. 3: (a) The FETs were used in a constant current mode by using a proportional-integral-derivative (PID) controller to leverage the signal amplification ( $\alpha$ ) afforded by dual-gate devices.  $I_D$  was held constant in response to small changes to  $V_{TG}$ . Measurements of pH were performed by connecting the top-gate (G) to a sensing element. (b) A standard sine wave signal was used to calibrate the measurement system that shows the amplification of the top-gate voltage with dual-gate setup. (c)  $\Delta V_{BG}$  as a function of the solution pH. (d) Time-series measurements of the back-gate voltage ( $V_{BG}$ ) response to buffered pH solutions.

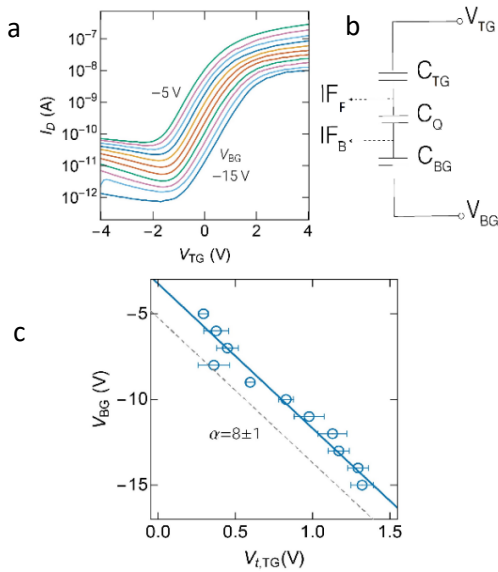


Fig. 2: Transfer characteristics show the drain current ( $I_D$ ) as a function of  $V_{TG}$  and varying back-gate voltage ( $V_{BG}$ ). (b) The dual-gate 2D FET was modeled with three capacitors in series. The quantum capacitance ( $C_Q$ ) of the 2D channel controls the capacitive coupling between the back ( $IF_B$ ) and front ( $IF_F$ ) gate interfaces. For this device, since both the top and back gate capacitance are much smaller than the quantum capacitance of the 2D channel, we ignore the contribution of  $C_Q$  in estimating the device gain,  $\alpha$  [1] (c) A plot of  $V_{BG}$  as a function of  $V_{t,TG}$  for a device with back-gate oxide thickness of 70 nm is shown. The solid line is a linear fit of the data allows the extraction of  $\alpha$ .

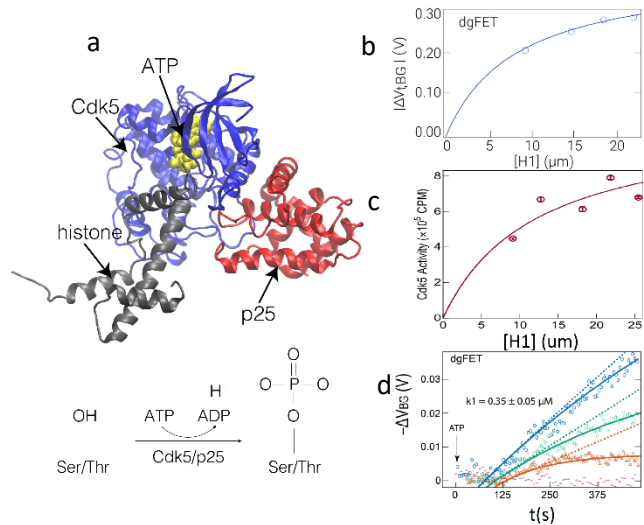


Fig. 4: High-k top-gate 2D FETs for label-free enzyme activity and kinetics measurements. (a) The proline directed kinase Cdk5 catalyzes the phosphorylation of substrate proteins (e.g., histone H1) in the presence of an activator (e.g., p25) and adenosine triphosphate (ATP). The hydrolysis of ATP results in a change in solution pH. (b) Dual-gate 2D FETs (gain,  $\alpha=8$ ) were used to measure the change in solution pH as a function of the histone H1 concentration ( $[H1]$ ). (c) The FET measurements are in agreement with an assay that used radioactively labeled  $\gamma$ -<sup>32</sup>P-ATP as a reporter of Cdk5 activity. (d) Time-series measurements of enzyme catalyzed phosphorylation as a function of  $[H1]$  allow the direct estimation of the reaction dynamics.

## Towards the Practical Use of Graphene Bio-Sensor for Virus Detection

K. Matsumoto

*Institute of Scientific & Industrial Research, Osaka University, Osaka, Japan*

*k-matsumoto@sanken.osaka-u.ac.jp*

Using the feature of graphene, such that the two dimensional electron gas is on the surface of graphene, the carrier mobility is extremely high, it is hard to be oxidised, etc., we have succeeded in fabricating the graphene biosensor modified by sugar chain, which could selectively detect the influenza virus whether the virus infect to the human or not. The limited number of detectable virus is as small as 3. For the future real application, we should also get the information of the subtype of virus which tell us the level of the pathogenicity. In order to know the subtype of virus, we try to modify the surface of graphene by antibody of influenza virus. There are 144 kinds of subtype of influenza virus. In principle, we should use 144 antibody to know the subtype of virus. We have already succeeded in the integration of 82 graphene FET on one chip and can measure all at once. Using this integrated graphene FET chip, we try to selectively modify the surface by sugar chain and also antibodies of virus for the subtype detection(a). For this selective modification, we introduce the bio-inkjet printer, which can selectively deposit the various antibody(b). We as a first step, modify the surface of graphene by BSA and St Avidin and now checking the difference of the shift of the Dirac point. For the further future application, the automation of the measurement is necessary. For this purpose, we introduce the micro TAS system and automated pumping systems(c). These projects are undergoing. This work is financially supported by JST CREST, Japan.

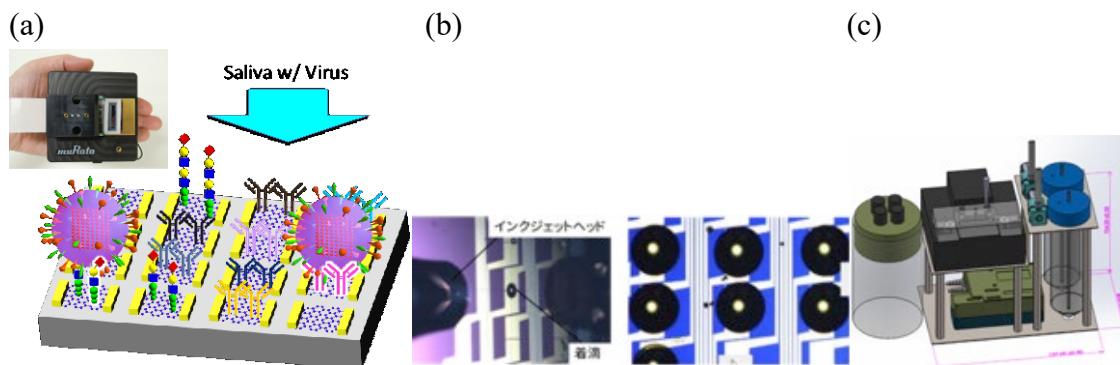


*Fig.1: Sugar chain & antibody modified graphene FET for the detection of virus. Integrated 82 graphene FETs on one chip for the virus detection and its measurement system. (b) Inkjet printing system for the selective modification of graphene FET by antibodies and sugar chains. (c) Micro TAS system and automated pumping systems.*

## Printed Biosensors: Applications and Perspectives

V.D. Bhatt<sup>2</sup>, S. Joshi<sup>2</sup>, B.D. Abera<sup>1</sup>, S. Bajramshahe<sup>1</sup>, G. Cantarella<sup>1</sup>, L. Petti<sup>1</sup>, and P. Lugli<sup>1</sup>

<sup>1</sup>*Faculty of Science and Technology, Free University of Bozen-Bolzano, Italy*

<sup>2</sup>*Institute for Nanoelectronics, Technical University of Munich, Germany*

*paolo.lugli@unibz.it*

Semiconductor devices have been proven in recent years excellent candidates for a variety of applications due to their reliability, reduced size and the computational strength of CMOS circuitry. Since cost is often a critical factor, a large research effort has been dedicated to the development of printed devices which could guarantee low costs and environmental friendliness. The low cost is guaranteed by the use of production techniques based on printing methods. In this context nanomaterials such carbon nanotubes or metallic nanostructures are promising materials for electronic devices. They can be dispersed in a solvent to form an ink which in turn can be easily printed. Such sensors can also find application in agriculture, allowing a direct monitoring of the characteristics of fields and plants. A further advantage of solution-based printable materials comes from their biocompatibility, which is a necessary requirement in several biological and medical applications. A necessary condition for biomedical use is the stability of the active material when it interacts directly with an electrolyte. Thus, new types of components and transistors have been realized, such as the solution-gated field-effect-transistors, where the gating effect is achieved via an electrode immersed in the solution. Such transistors can potentially work as biosensors. Two semiconductors, carbon nanotube and indium gallium zinc oxide are used which can be deposited by low cost solution processable techniques like spray deposition. Several different sensing systems like enzyme-based, non enzymatic and immunosensing have been demonstrated. The use of ion-selective membranes in transistors for sensing ions like H<sup>+</sup> and NH<sub>4</sub><sup>+</sup> has been investigated. Logic circuits like inverters have been demonstrated in sensing of molecules like H<sup>+</sup> ions. In addition, flexible dispense-printed electrochemical biosensors for Aflatoxin M1 (AFM1) and Histamine detection were fabricated on PET substrates, which are able to detect a minimum AFM1 concentration of 0.010 µg/L and 0.05 ng/ml for AFM1 and Histamine, respectively.

A. Abdelhalim *et al.*, Carbon **61**, 72–79 (2013).

A.L. Münzer *et al.*, J. Mater. Chem. B **1**, 3797 (2013).

V.D. Bhatt *et al.*, IEEE T. Electron Dev. **64**, 1375 (2017).

S. Joshi *et al.*, P, IEEE Sensors J. **17**, 4315 (2017).

S. Joshi *et al.*, Biosensors **8**, 9 (2018).

S. Joshi *et al.*, Sci. Rep. **8**, 11386 (2018).

B.D. Abera *et al.*, Sensors **19**, 3912 (2019).

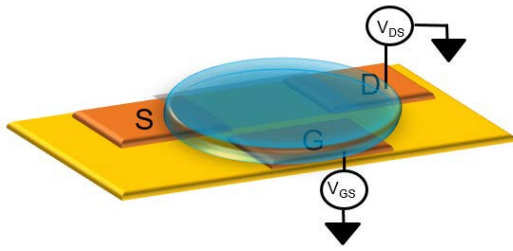


Fig.1: Schematic of a planar electrolyte gated field effect transistor.

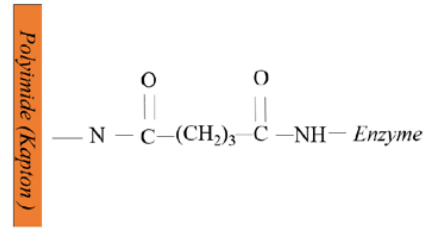


Fig.2: Enzyme immobilization scheme for glucose oxidase and lactate oxidase.

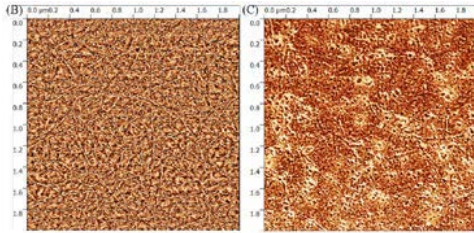


Fig.3: AFM image of the polyimide substrate (B) before and (C) after immobilization of enzyme (GOx).

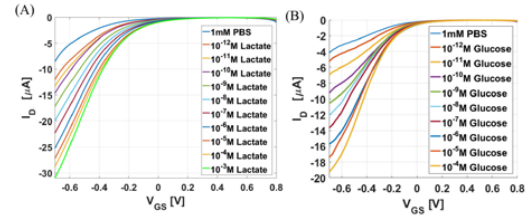


Fig.4: Response of glucose (A) and lactate (B) sensors to varying concentrations of glucose and lactate, respectively.

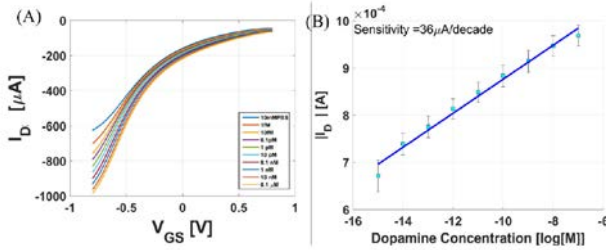


Fig.5: (A) Transfer curve for a dopamine sensor measured with different dopamine concentrations. (B) Maximum current versus concentration curve to extract sensitivity of the sensor.

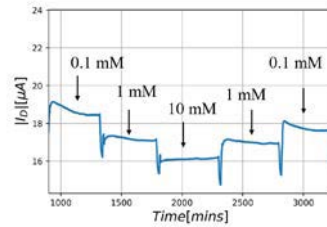


Fig.6: Real time measurement for NH<sub>4</sub><sup>+</sup> selective CNT-ISFET. The gate to source voltage V<sub>GS</sub> and drain to source voltage V<sub>DS</sub> are fixed to -0.8 V.

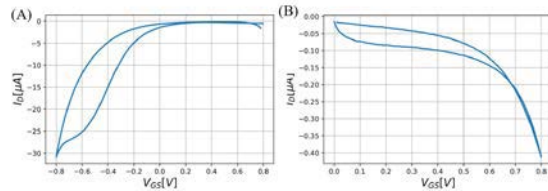


Fig.7: Transfer curve for (A) p-type CNTFET and (B) n-type CNTFET, used to fabricate a CMOS inverter.

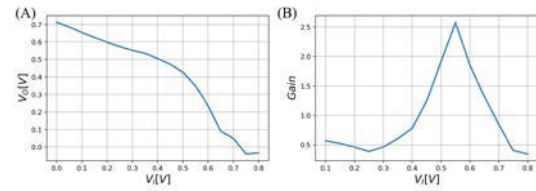


Fig.8: (A) Voltage transfer characteristics and (B) Gain versus input voltage for a CMOS inverter.

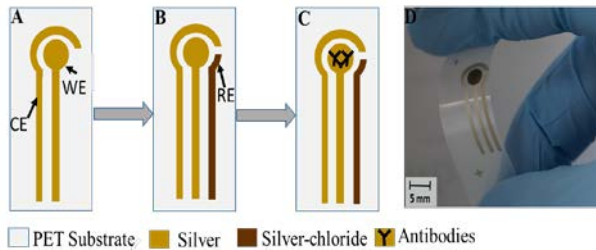


Fig.9: Schematic of a flexible printed Aflatoxin M<sub>1</sub> (AFM<sub>1</sub>) sensor: A) printing of working (WE) and counter electrode (CE), B) printing of reference electrode (RE), C) immobilization of antibodies, D) optical picture of the final device on PET substrate.

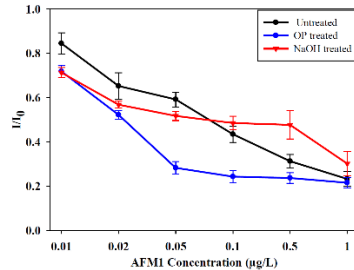


Fig.10: Chronoamperometric measurement of AFM<sub>1</sub> in buffer solution for the developed flexible biosensors including normalized error bars for three different surface functionalizations.

## **Real-Time Measurements of Glucose Uptake in 2D Cell Cultures Using On-Chip Microelectrode Arrays**

S.V. Sridharan<sup>1,5</sup>, J.F. Rivera<sup>1,5</sup>, J. Nolan<sup>2</sup>, S. Miloro<sup>2</sup>, Z. (C.) Xing<sup>4</sup>, M.A. Alam<sup>1,5</sup>,  
J.L. Rickus<sup>2,3,5</sup>, E. Tran<sup>4</sup>, and D.B. Janes<sup>1,5</sup>

<sup>1</sup>*School of Electrical and Computer Engineering, Purdue University, W.Lafayette, IN, USA*

<sup>2</sup>*School of Agricultural and Biological Engineering, Purdue University, W.Lafayette, IN, USA*

<sup>3</sup>*Weldon School of Biomedical Engineering, Purdue University, W.Lafayette, IN, USA*

<sup>4</sup>*Department of Biochemistry, Purdue University, W.Lafayette, IN, USA*

<sup>5</sup>*Birck Nanotechnology Center, Purdue University, W.Lafayette, IN, USA*

*janes@purdue.edu*

Glucose metabolism is of interest in understanding differences between various cell types, e.g. normal versus cancer cells, and responses to changes in local micro-environment. Various approaches involving assays, labels and/or analogs are used for volumetric measurements, generally providing initial uptake rate, end-point detection or coarse time steps. An optical-based technique (Seahorse flux analyzer) provides high temporal resolution of energy components of metabolism (O<sub>2</sub> and lactate), but does not measure total glucose uptake. The current study employs microelectrode arrays (MEAs) to simultaneously measure glucose concentrations at multiple positions near a 2D cell culture. Extrapolation to the cell surface allows determination of the surface concentration (C<sub>s</sub>) and uptake rate (UR), as well as the reaction rate coefficient, for the cells, with high temporal resolution (< 1 sec). Extending prior studies on H<sub>2</sub>O<sub>2</sub> uptake [1], amperometric MEAs are enzyme-functionalized to provide selectivity for glucose and *in-situ* transient calibration approaches are employed. The ability to quantify time-dependent glucose UR and C<sub>s</sub> is demonstrated using comparisons between normal, cancer and genetically-modified cells, including glial cells from the central nervous system and lung epithelial cells. The approach allows observation of concentration-dependent UR, as well as up/down-regulation during prolonged exposure. Time- and concentration-dependent measurements allow fitting to various mechanistic models for cell behavior.

[1] J.F. Rivera *et al.*, *Analyst* **143**, 4954 (2018).

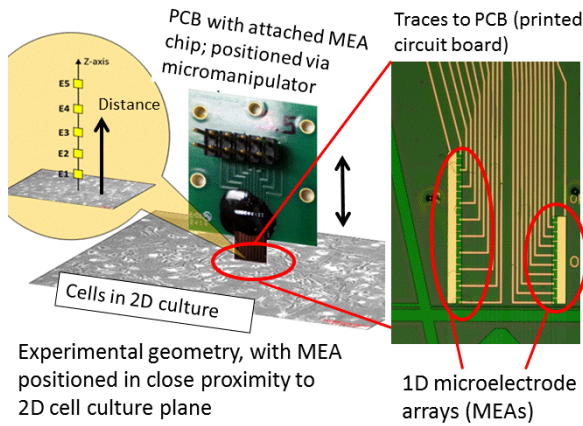


Fig.1: Experimental set-up, showing microelectrode array (MEA) positioned above 2D cell culture. MEA is fabricated on a silicon chip and mounted on a printed circuit board (PCB), which allows positioning above cell plane.

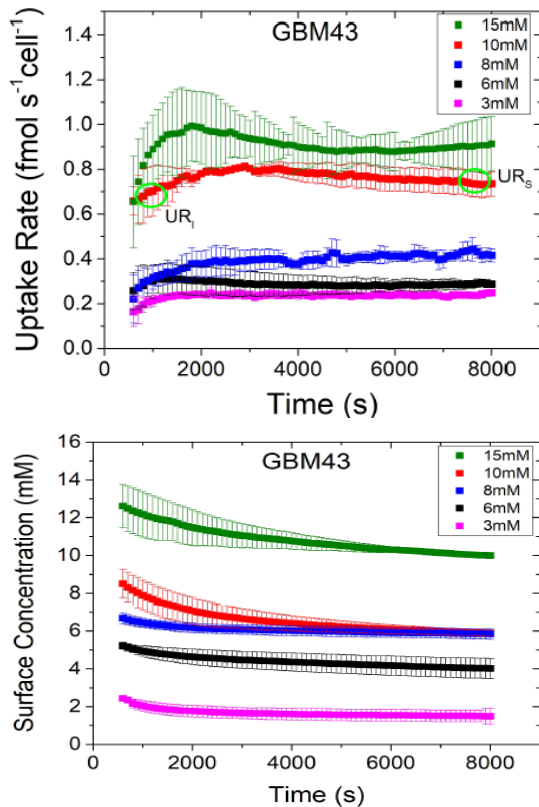


Fig.2: MEA-based approach yields total glucose uptake rate (top) and surface concentration (bottom) versus time, illustrated for 2D culture of glioblastoma (GBM43) at indicated initial glucose concentrations. Glioblastoma are cancerous glial cells. The uptake rate is observed to change from initial ( $UR_i$ ) to final ( $UR_f$ ) values.

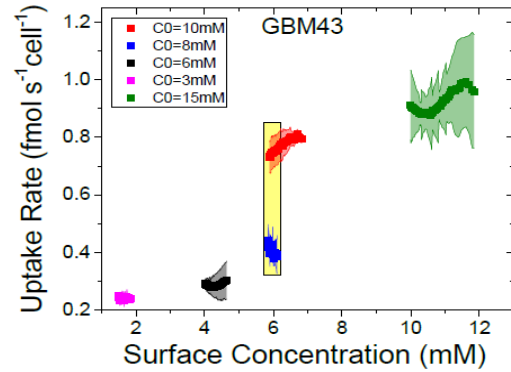


Fig.3: Uptake rate versus surface concentration for glioblastoma (GBM43) cells. For each initial concentration ( $C_0$ ), curve represent time trajectory. For same instantaneous concentration, uptake rate depends on concentration history (yellow box).

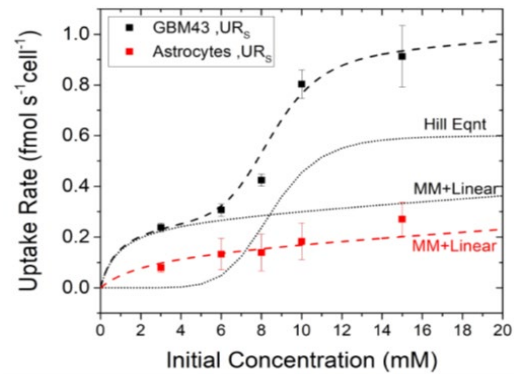


Fig.4: Concentration-dependent glucose uptake rate for normal (Astrocyte) and cancerous (glioblastoma, GBM43) glial cells. Curves represent respective fits to Hill Equation or Michaelis-Menten relationships.

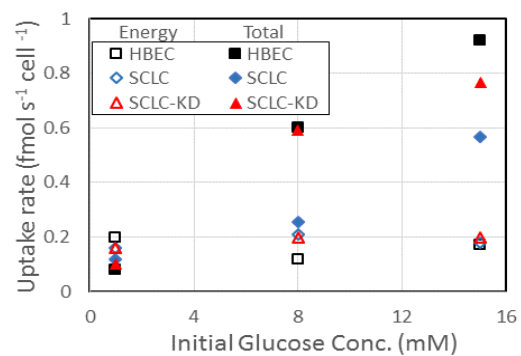


Fig.5: Measured glucose uptake rates versus initial concentration at  $\sim 1500$  s for energy metabolism (Seahorse) and total uptake (MEA) for indicated epithelial lung cell types. Total glucose uptake increases by 5-10x with increasing concentration, while energy metabolism remains  $\sim$  constant. HBEC is wild type, SCLC is small-cell lung cancer and SCLC-KD is SCLC with DDX5 gene knocked down. Error bars from triplicate experiments are omitted for clarity.

## **New Artificial Magnetic Honeycomb Lattice for Emergent Physics and Spintronics Application**

D.K. Singh

*Department of Physics and Astronomy, University of Missouri, Columbia, MO, USA*  
*singhdk@missouri.edu*

Nanostructured two-dimensional magnetic material with frustrated geometry, such as an artificial magnetic honeycomb lattice, provides facile platform to explore emergent phenomena of fundamental and practical importance. Originally envisaged to explore the physics of effective magnetic monopoles and magnetic field-induced avalanche of Dirac string, artificial magnetic honeycomb lattice has emerged as a key playground to discover new and exotic magnetic phases in disorder free environment, such as magnetic charge ordered state and the spin solid state. We have created thermally tunable artificial permalloy honeycomb lattice of ultra-small connected elements, with a typical length of  $\sim 12$  nm, in this pursuit. Using neutron scattering and complementary measurements on the newly created honeycomb lattice, the development of long range spin solid order, see Fig. 1, and the associated phase transition is investigated in this artificial geometry.[1] Additionally, two new properties of the Wigner crystal type state of magnetic charges and the magnetic diode-type asymmetric conduction are discovered, see Fig. 2-3.[2-3] Concurrent measurements of the polarized neutron reflectivity and electrical conductivity further reveal the effect of current induced near surface tuning of magnetization in honeycomb lattice, thereby making it a topological effect with fractional change in the magnetic charge density.[4] Experimental researches are supplemented with model calculations that elucidate the role of magnetic charges on the vertices of honeycomb lattice behind the anomalous effects. The thermally tunable honeycomb lattice provides a new vista to explore emergent novel physical phenomena with strong implication to the design of next generation spintronics devices. Research at MU is supported by the U.S. Department of Energy, Office of Basic Energy Sciences under Grant No. DE-SC0014461.

[1] A. Glavic *et al.*, *Adv. Sci.* **5**, 1700856 (2018).

[2] Y. Chen *et al.*, *Adv. Mat.* **31**, 1808298 (2019).

[3] B. Summers *et al.*, *Adv. Electron. Mat.* **4**, 1700500 (2018).

[4] G. Yumnam *et al.*, "Mechanism Behind Asymmetric Electrical Conduction in Permalloy Honeycomb Lattice", in preparation (2019).

Fig.1: Newly created artificial magnetic honeycomb lattice of ultra-small connected elements (Fig. a) provides a facile platform to explore multitude of novel magnetic phases, including the realization of the spin solid order (Fig. b). Using neutron reflectometry, GISANS measurements and temperature dependent micromagnetic simulations, the development of spin solid order was demonstrated in the newly designed permalloy ( $\text{Ni}_{0.8}\text{Fe}_{0.2}$ ) honeycomb lattice of ultra-small connected elements. Fig. c shows the model calculation of spin solid order, which is consistent with low temperature polarized neutron reflectometry data.

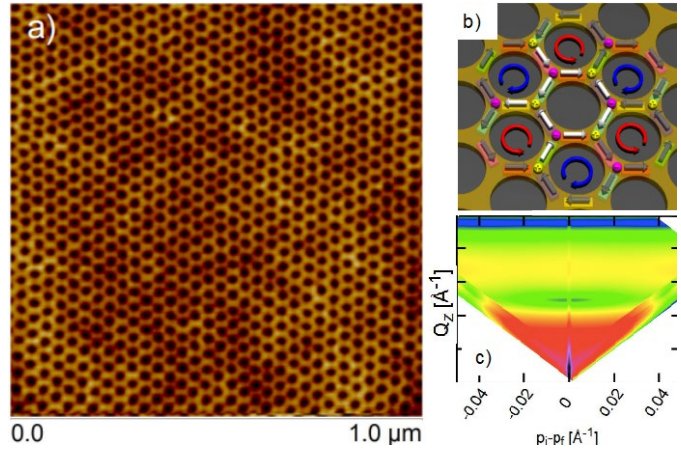


Fig.2: Magnetic charge movement can profoundly impact the electrical properties of a magnetic material; essentially manifesting the spintronic model of electrical conduction. Artificial magnetic honeycomb provides a facile platform to realize it. This figure shows that the rearrangement of magnetic charges to a Wigner crystal type novel state gives rise to the colossal change in electrical conductivity in neodymium (Nd) honeycomb lattice. Measurements were performed at  $T = 30\text{ K}$ .

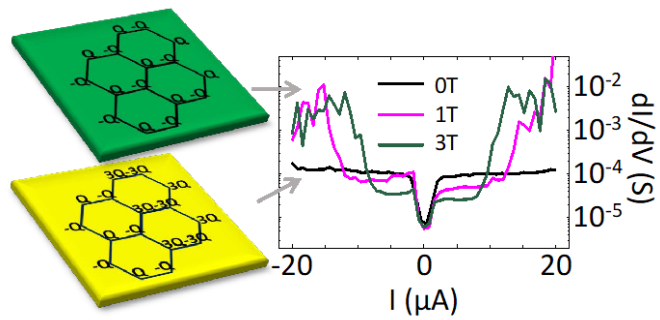
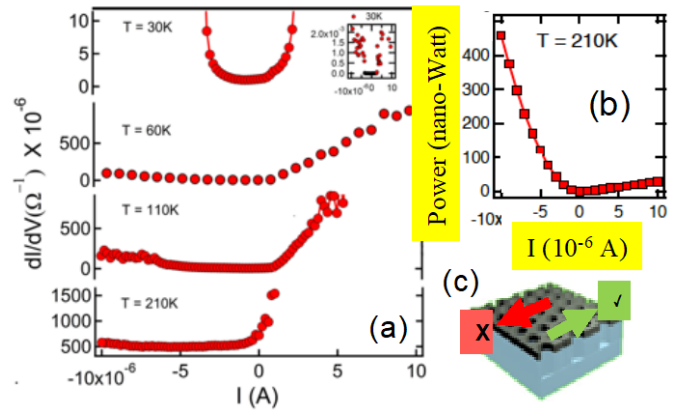


Fig.3: In a first discovery of its kind, the observation of magnetic diode rectification in thermally tunable artificial permalloy ( $\text{Ni}_{0.8}\text{Fe}_{0.2}$ ) honeycomb lattice of ultra-small elements was reported. Figure a and b show the development of diode-type rectification, as temperature increases, and the nano-Watt power dissipation in rectification regime, respectively. The unidirectional current biasing is schematically described in Figure c.



## Spin Physics in Ferromagnet/Superconductor Tunnel Junctions

J. Fabian

*Department of Physics, University of Regensburg, 93040 Regensburg, Germany*

*jaroslav.fabian@ur.de*

The interplay between exchange, spin-orbit, and superconducting coupling is a source of fascinating physics. I will discuss in particular the physics related to transport in vertical tunnel junctions, comprising ferromagnetic layers and superconductors, while the interfaces imprint spin-orbit fields in the electronic states. One example is the strongly anisotropic Josephson effect in SFS junctions, with regard to the magnetization orientation of the ferromagnetic layer [1]. The Josephson current is related to the emergence of Yu-Shiba-Rusinov states, which form at magnetic impurities in superconductors, but also appear as a result of ferromagnetic tunnel barriers in superconducting junctions. We showed that these robust states correlate with the  $0-\pi$  transitions, demonstrated by the reversal of Josephson current [2]. Experimentally, it was demonstrated in Regensburg [3] that Josephson currents can even coexist with the TMR effect, in FSIFS junctions. We have recently predicted that transverse superconducting current can flow in the presence of spin-orbit coupling in FIS junctions [4], as a result of conventional and Andreev (tunneling Cooper pair) skew scattering. The effect is potentially giant when compared with the normal counterpart, due to constructive addition of various transport channels.

[1] A. Costa *et al.*, Phys. Rev. B **95**, 024514 (2017).

[2] A. Costa *et al.*, Phys. Rev. B **98**, 134511 (2018).

[3] O. Vávra *et al.*, AIP Adv. **7**, 025008 (2017).

[4] A. Costa *et al.*, arXiv preprint arXiv:1905.12525

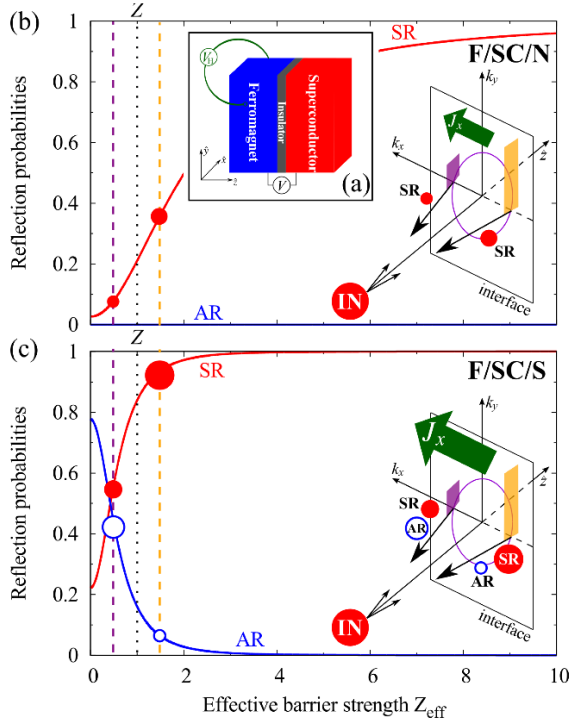


Fig.1: (a) Sketch of the considered F/SC/S junction, using  $C_{2v}$  principal crystallographic orientations,  $x[110]$ ,  $y[1\bar{1}0]$ , and  $z[001]$ . (b) Calculated (zero-bias)normal state reflection probabilities for incident spin up electrons (IN) at the SC interface, invoking Andreev (AR) and specular (SR) reflection, as a function of the barrier parameter  $Z$  [dimensionless BTK-like barrier parameter for the effective scattering potential]. Owing to skew reflection, electrons with  $k_x < 0$  feel an effectively lowered (dashed violet line) and those with  $k_x > 0$  a raised (dashed orange line) barrier; the carrier imbalance (carrier densities are proportional to the size of the red and blue circles) generated via skew SR generates then the transverse Hall current  $J_x$  (voltage drop  $V_H$ ). The skew reflection mechanism is schematically illustrated in the inset. (c) Same as in (b), but for the superconducting scenario in which additionally skew AR plays a key role. From [4].

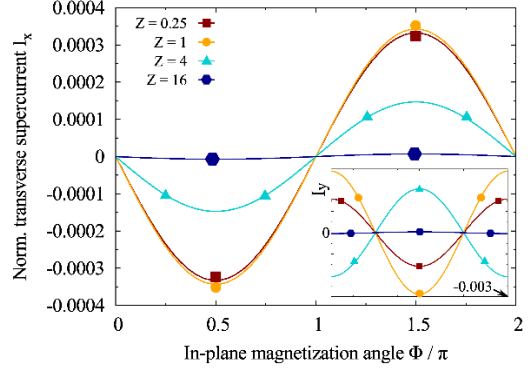


Fig.2: Calculated dependence of the zero-bias transverse supercurrent response,  $I_x$  ( $I_y$  in the inset), normalized according to  $[I_{x(y)}e]/(GS\pi|\Delta S|)$ , on the in-plane magnetization angle  $\Phi$ . From [4].

## Towards Spin-Wave-Based Devices: Experiments and Simulations

H. Aquino<sup>1</sup>, D. Connelly<sup>1</sup>, A. Papp<sup>2,3</sup>, M. Becherer<sup>3</sup>, G. Csaba<sup>2</sup>,  
J. Chisum<sup>1</sup>, A. Orlov<sup>1</sup>, G.H. Bernstein<sup>1</sup>, and W. Porod<sup>1</sup>

<sup>1</sup>*Department of Electrical Engineering, University of Notre Dame, Notre Dame, IN, USA*

<sup>2</sup>*Faculty for Information Technology and Bionics, Pázmány University, Budapest, Hungary*

<sup>3</sup>*Chair of Nanoelectronics, Technical University of Munich, Munich, Germany*

*porod@nd.edu*

There currently is significant interest in spin waves for applications in wave-based computing and information processing [1]. Here, we present an experimental study of launching and detecting spin waves, and matching the experimental data with simulation results from a combined electromagnetic / micromagnetic simulation tool.

In order to realize spin-wave devices, it is necessary to use magnetic films that have low Gilbert damping parameters ( $\alpha$ ) such as yttrium iron garnet (YIG,  $Y_3Fe_5O_{12}$ ). Ferromagnetic resonance (FMR) spectrometry is widely used to characterize the magnetic properties of magnetic films, and FMR measurements of our YIG film showed an  $\alpha$  of 0.0039. In order to launch spin waves in these YIG films, co-planar waveguides (CPW) were fabricated on top of our films. Time-resolved magneto-optic Kerr effect (TR-MOKE) measurements were taken to image the spin waves generated by the 750 MHz microwave signal on the CPWs, as shown in Fig. 1. The results of a TR-MOKE line scan (Fig. 2) clearly show the spin wave. Analysis of this data, shown in Fig. 3, yields a damping parameter  $\alpha$  of 0.0037, which is in very good agreement with the FMR data.

We also developed a simulation framework for spin-wave-based devices, schematically shown in Fig. 4, where an electromagnetic model is coupled to a full micromagnetic model of the magnetic material. The joint electromagnetic and micromagnetic problem is split into an electromagnetic domain and a micromagnetic domain. The problem is initially solved in HFSS to find incident fields upon the magnetic film. A micromagnetic simulator (OOMMF) then is used to solve for the magnetic material's response (scattered fields), and the result is integrated with the electromagnetic solution to obtain the complete solution. We applied this tool to the study of spin waves launched by CPWs on YIG, for the same geometry and parameters used in experiment. Figure 5 presents a comparison between the experimental TR-MOKE data and the results of our simulation tool for spin waves and their decay, and there is very good agreement. [1] A. Papp *et al.*, Phys. Lett. A **381**, 1471 (2017).

**Acknowledgment.** This work was supported, in part, by the National Science Foundation (NSF) under SpecEES Award ECCS-1731824, and by the Defense Advanced Research Projects Agency (DARPA) under Agreement No. HR00112090007.

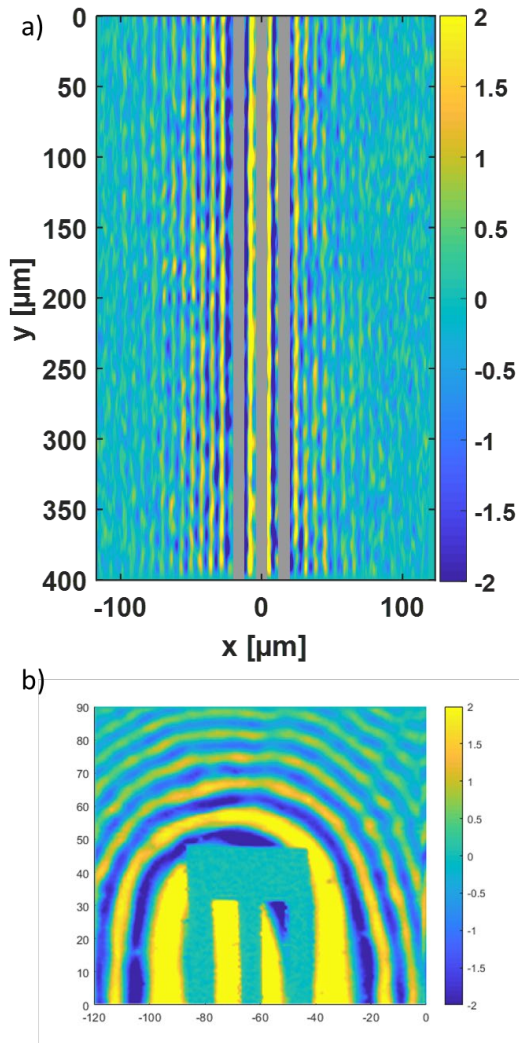


Fig.1: Results of a 2D TR-MOKE scan of 750 MHz spin waves.

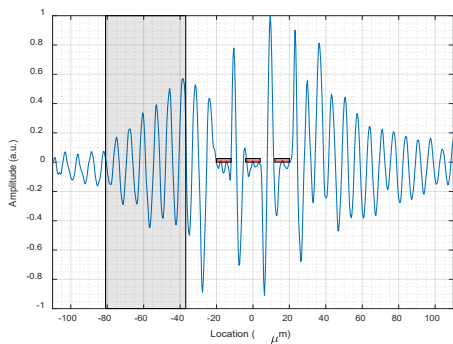


Fig.2: Results of a TR-MOKE line scan 200  $\mu\text{m}$  from the base of a CPW. The red rectangles show where the metal lines are. The gray rectangle shows the region that was used for the data analysis shown in Fig. 3.

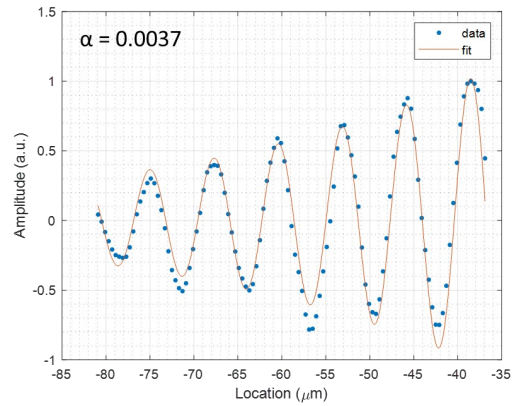


Fig.3: A section of the data shown in Fig. 2 to which a decaying sinusoid was fit to determine the decay length, which was found to be 35.4  $\mu\text{m}$ , which corresponds to a damping constant  $\alpha$  of 0.0037.

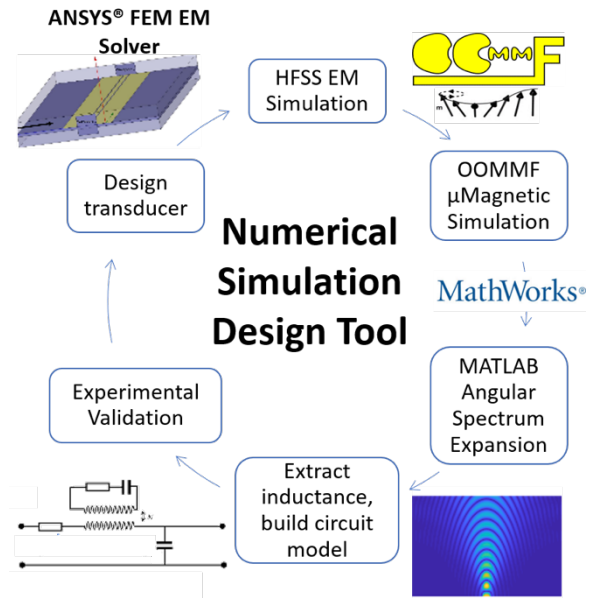


Fig.4: Schematic flow chart of the numerical simulation design tool.

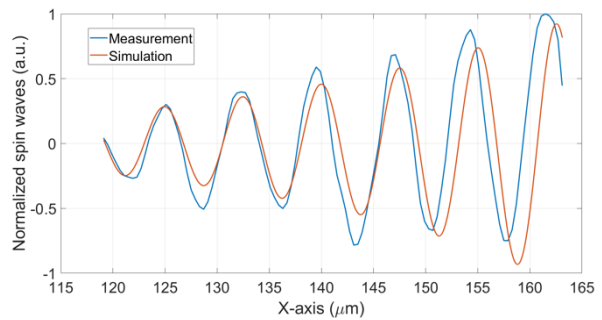


Fig.5: Comparison of experimental TR-MOKE data and results from the numerical simulation tool.

## Suppression of Weak Localization in Bilayer Graphene Due to Proximity Induced Spin Orbit Coupling

N. Arabchigavkani<sup>1</sup>, R. Somphonsane<sup>3</sup>, H. Ramamoorthy<sup>3</sup>, G. He<sup>2</sup>, J. Nathawat<sup>2</sup>,  
S. Yin<sup>2</sup>, B. Barut<sup>1</sup>, J. Fransson<sup>4</sup>, and J.P. Bird<sup>2</sup>

<sup>1</sup>*Department of Physics, University at Buffalo, Buffalo, New York, USA*

<sup>2</sup>*Department of Electrical Engineering, University at Buffalo, Buffalo, New York, USA*

<sup>3</sup>*Department of Physics, King Mongkut's Institute of Technology Ladkrabang,  
Bangkok, Thailand*

<sup>4</sup>*Department of Physics and Astronomy, Uppsala University, Uppsala, Sweden*  
*nargessa@buffalo.edu*

The transport properties of bilayer graphene (BLG) are known to be affected by weak localization (WL) at low temperatures [1]. This correction to the conductivity of disordered conductors is a result of the interference of time-reverse pairs of electron waves, which counterpropagate around closed loops in the absence of spin-orbit coupling [2]. In clean BLG, trigonal warping of the electron dispersion near the center of each valley leads to a suppression of WL; however, in experimentally available samples, the intervalley scattering from long-range disorder due to charged impurities in the substrate restores this phenomenon [1-3]. In this study, we use differential conductance mapping to explore the transport properties in BLG at low temperatures, under conditions for which they are influenced by the proximal of the graphene to a ferromagnet (Co, see Fig. 1). The low-temperature differential conductance is measured around the Dirac point, with the floating Co “gate” both included in, and absent from, the current path. In the latter case (i.e. with the Co gate excluded from the current path), the differential conductance shows (Fig. 2) the characteristic dip that is known to provide a signature of WL [5]. With the Co gate in the current path, however, the differential conductance shows a zero-bias anomaly (Fig. 3), implying the suppression of the WL at certain energies (that are insufficient to cause dephasing of the carriers [4]). This behavior is attributed to induced spin-orbit coupling of chiral charge carriers in the proximity of the Co gate.

[1] R.V. Gorbachev *et al.*, Phys. Rev. Lett. **98**, 176805 (2007).

[2] B.L. Altshuler *et al.*, Phys. Rev. B **22**, 5142 (1980).

[3] K.S. Novoselov *et al.*, Nature Phys. **2**, 177 (2006).

[4] R. Somphonsane *et al.*, arXiv preprint arXiv:1802.09922 (2018).

[5] R. Somphonsane *et al.*, Sci. Rep. **7**, 10317 (2017).

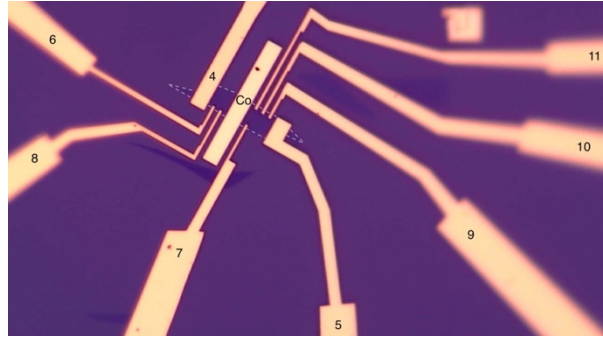


Fig.1: Bilayer graphene device. The of the Co bar is  $3\ \mu\text{m}$  wide and  $24\ \mu\text{m}$  long. the voltage probes are  $500\ \text{nm}$  wide and  $1\ \mu\text{m}$  apart from each other. The BLG sample is outlined with white dashed line. The device is fabricated on n-type Si substrate with  $300\ \text{nm}$  of  $\text{SiO}_2$  using standard electron beam lithography (EBL), Au/Cr contacts are deposited with  $50\text{nm}/5\text{nm}$  thickness and Co bar is fabricated in second EBL step to deposit Au/Co/Cr with  $45\text{nm}/20\text{nm}/3\text{nm}$  thickness.

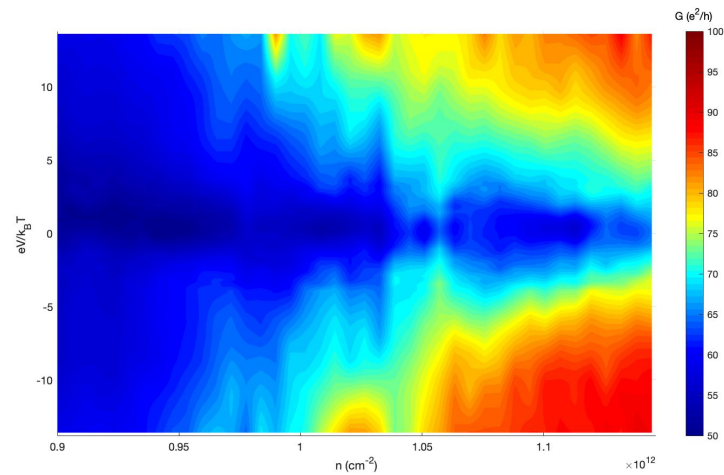


Fig.2: Differential conductance excluding the Co gate from the current path: the bias signal is applied to contact number 11, keeping number 5 grounded and probing the voltage drop across 9 and 10 in the device structure shown in Fig. 1. The WL dip is symmetric around  $eV/k_B T \sim 0$ .

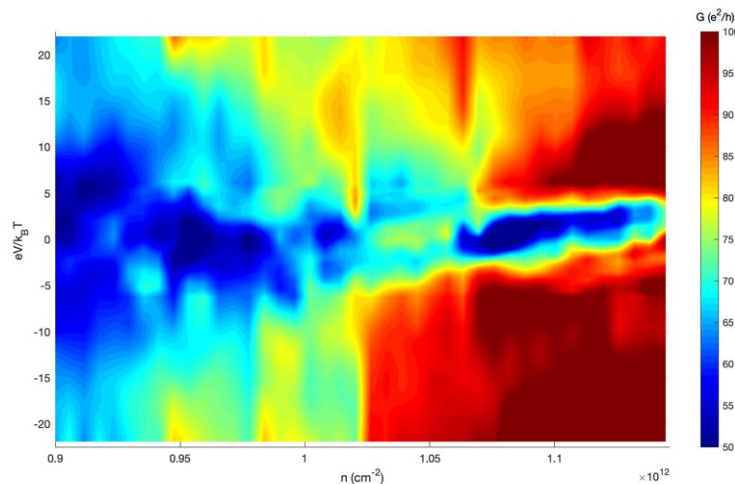


Fig.3: Differential conductance including the Co gate in the current path: the bias signal is applied to contact number 9, keeping number 8 grounded and probing the voltage drop across 10 and 11 in the device structure shown in Fig. 1. The suppression of WL is seen as a zero bias anomaly that leads to features that are present around  $eV/k_B T \sim 0$ .

## **Enhancement of the Interfacial Exchange Field in Superconducting Spin Vales of GdN/NbN/GdN Trilayers**

Y. Takamura<sup>1,2</sup>, J.P. Cascales<sup>1</sup>, R. Gonçalves<sup>1,3</sup>, G. Stephen<sup>4</sup>, D. Heiman<sup>4</sup>, A. Altinkok<sup>1,5</sup>,  
C.I. L. de Araujo<sup>3</sup>, B. Satpati<sup>6</sup>, V. Lauter<sup>7</sup>, and J.S. Moodera<sup>1,8</sup>

<sup>1</sup>*Francis Bitter Magnet Laboratory, Plasma Science and Fusion Center, Massachusetts  
Institute of Technology, Cambridge, MA, USA*

<sup>2</sup>*School of Engineering, Tokyo Institute of Technology, Tokyo, Japan*

<sup>3</sup>*Laboratory of Spintronics and Nanomagnetism (LabSpiN), Departamento de Física,  
Universidade Federal de Viçosa, Viçosa, Brazil*

<sup>4</sup>*Physics Department, Northeastern University, Boston, MA*

<sup>5</sup>*Department of Electrical and Electronics, Giresun University, Turkey*

<sup>6</sup>*Surface Physics & Material Science Division, Saha Institute of Nuclear Physics,  
Kolkata, India*

<sup>7</sup>*NSSD, Oak Ridge National Laboratory, Oak Ridge, TN, USA*

<sup>8</sup>*Physics Department, MIT, Cambridge, MA, USA*

*takamura@ee.e.titech.ac.jp*

This abstract is not printed due to the authors' request.

## Robustness of the Two-Pulse Switching Scheme for SOT-MRAM

R. Lacerda de Orio<sup>1</sup>, S. Selberherr<sup>2</sup>, J. Ender<sup>1</sup>, S. Fiorentini<sup>1</sup>, W. Goes<sup>3</sup>, and V. Sverdlov<sup>1</sup>

<sup>1</sup>Christian Doppler Laboratory for Nonvolatile Magnetoresistive Memory and Logic at the

<sup>2</sup>Institute for Microelectronics, TU Wien, Gußhausstraße 27-29/E360, 1040 Vienna, Austria

<sup>3</sup>Silvaco Europe Ltd., Cambridge, United Kingdom

orio@iue.tuwien.ac.at

The downscaling of semiconductor devices has sustained a continuous increase in density and performance of memories. However, this has also been followed by an increasing power consumption. Besides charge, the spin is also an inherent property of the electron, which yields energy-efficient and nonvolatile alternatives to charge-based memories [1]. Spin-orbit torque magnetoresistive random access memory (SOT-MRAM) combines non-volatility, high endurance and high speed, and is thus particularly suited for applications in caches [2].

In this work, we demonstrate the robustness of a magnetic field-free two-pulse switching scheme previously proposed [3] to switch a perpendicularly magnetized free layer (FL) by SOT. The structure consists of a perpendicularly magnetized square FL ( $25 \times 25 \times 2 \text{ nm}^3$ ) grown on top of a heavy metal wire (NM1) with another heavy metal wire (NM2) partially on top of the FL (Fig. 1). Two orthogonal current pulses of duration  $T_1 / T_2$  are applied through the wires NM1/NM2 (Fig. 2).  $\tau$  is the delay/overlap between the pulses, which models the non-idealities of signal propagation leading to pulse synchronization failures. Considering perfectly synchronized pulses ( $\tau=0$ ), the switching is deterministic for a broad range of the second pulse duration (Fig. 3). A fast ( $\sim 0.6 \text{ ns}$ ) switching time is obtained in the range of 30% - 50% of overlap between the NM2 wire and the FL (Fig.4). The impact of pulse delay/overlap on the magnetization is shown in Fig.5. A delay leads to an increase, while a short overlap can even reduce the switching time, as summarized in Fig. 6. Although a delay leads to a longer switching time, for a delay corresponding to as large as 50% of the pulses' durations (50ps /100ps), the switching time increases by only 10%, while for an overlap it improves by 10%. This shows that the scheme is extremely robust with respect to pulse timing variations, a very important feature for practical implementation.

[1] O. Golonzka *et al.*, Proc. IEDM, 36.2.1 (2018).

[2] S. Lee *et al.*, Proc. IEEE **104**, 1831 (2016).

[3] V. Sverdlov *et al.*, Solid-State Electron. **155**, 49 (2019).

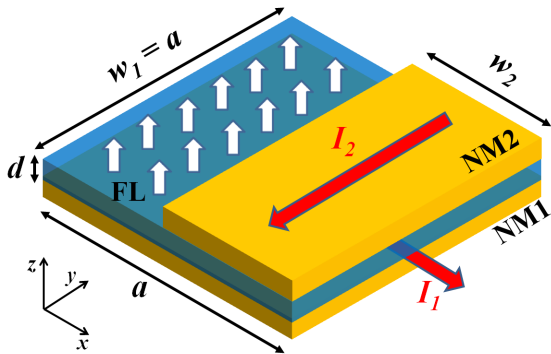


Fig.1: Two-pulse switching scheme applied to a perpendicularly magnetized square free layer with partial top heavy metal overlap.

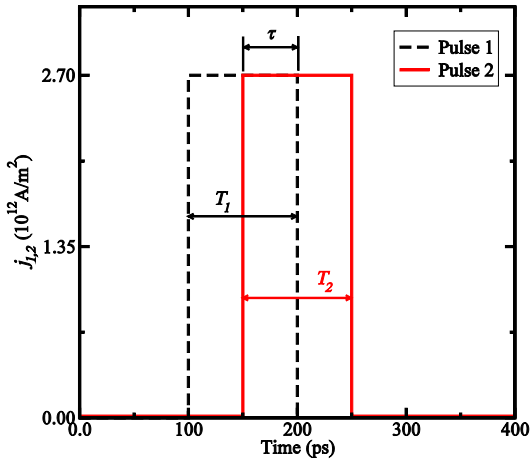


Fig.2: Current pulses applied to the bottom and the top heavy metal.  $T_1/T_2$  is the width of the first/second pulse and  $\tau$  is the delay/overlap between the pulses. A negative  $\tau$  represents an overlap, while a positive value represents a delay between the pulses.

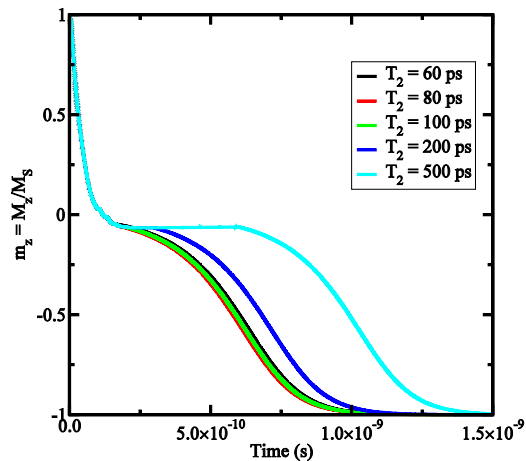


Fig.3: Average magnetization ( $z$ -component) of 20 switching realizations for  $w_2 = 10$  nm. Reliable switching is observed for all  $T_2$ .  $T_1 = 100$  ps and  $\tau = 0$ .

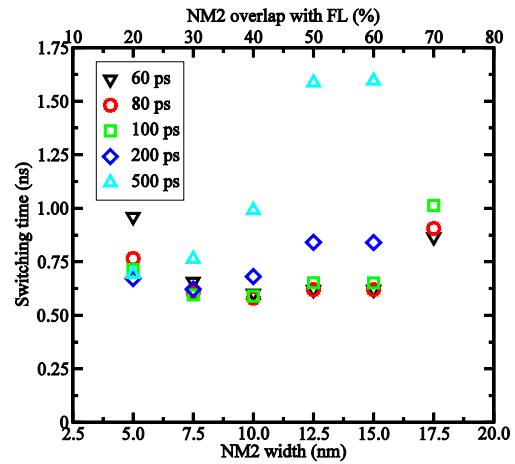


Fig.4: Switching times as function of the NM2 wire width ( $w_2$ ), for several second pulse durations ( $T_2$ ).  $T_1 = 100$  ps and  $\tau = 0$ .

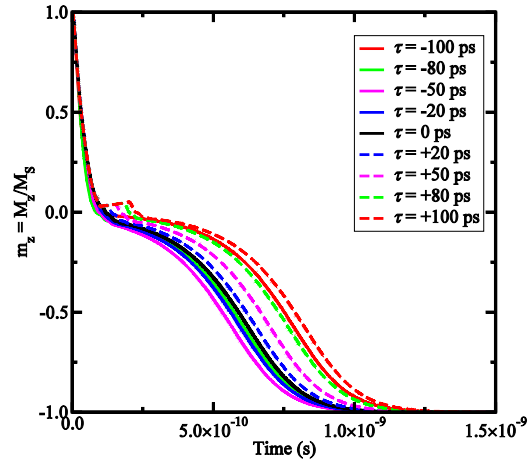


Fig.5 Magnetization as a function of time for several values of overlap/delay between the first and the second current pulse. A short overlap reduces the switching time. The switching is still reliable for a wide range of delay.  $T_1 = T_2 = 100$  ps.

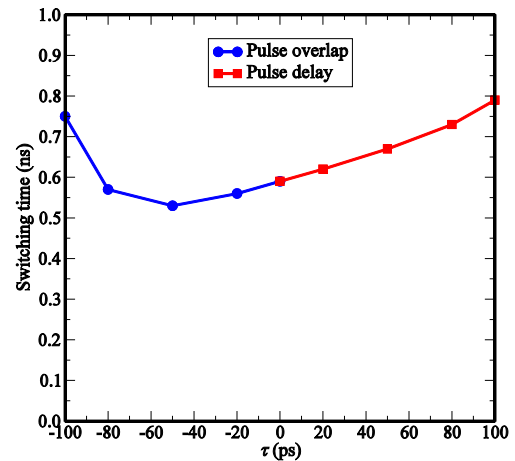


Fig.6: Switching time as function of the delay/overlap between the first and the second pulse.  $\tau < 0$  represents an overlap and  $\tau > 0$  indicates a delay between the pulses.  $T_1 = T_2 = 100$  ps.

## **Ultra-Wide-Bandgap Aluminum Gallium Nitride for High-Performance Power-Switching and Radio-Frequency Devices**

R. Kaplar, A. Armstrong, A. Baca, B. Klein, E. Douglas, S. Reza, A. Allerman,  
M. Crawford, J. Dickerson, A. Binder, J. Flicker, J. Neely, and O. Slobodyan  
*Sandia National Laboratories, Albuquerque, NM, USA*  
*rjkapla@sandia.gov*

As wide-bandgap (WBG) semiconductors such as Silicon Carbide (SiC) and Gallium Nitride (GaN) become increasingly mature, researchers are looking to a new class of materials, the Ultra-WBG (UWBG) semiconductors, as the next frontier in semiconductor physics. These materials promise increased performance for power-switching and radio-frequency (RF) devices and systems, but also face commensurate challenges in synthesis and fabrication [1]. While several such materials are currently being researched in the community, our group has focused on Aluminum Gallium Nitride (AlGa<sub>N</sub>). AlGa<sub>N</sub> has several potential advantages over other UWBG materials, including its similarity to the mature AlGa<sub>N</sub>/GaN system, plus the availability of varying alloy composition and heterostructures which enables novel approaches to challenges common to all UWBG semiconductors (such as effective and controllable doping) and flexibility in device design and fabrication. This talk will discuss the materials physics responsible for the interest in these semiconductors, including the expected scaling of the critical electric field for avalanche breakdown with bandgap, and the transport properties of charge carriers in these materials. The relevant figures-of-merit (FOMs) derived from these properties, such as the unipolar FOM for both vertical (Figure 1) and lateral (Figure 2) device configurations, as well as the Johnson FOM for RF devices (Figure 3), will be presented. Examples of fabricated devices will also be shown, including vertical power-switching devices (Figure 4 [2]), lateral power power-switching devices (Figure 5 [3]), and RF devices (Figure 6 [4]). The talk will include a discussion of application areas in which AlGa<sub>N</sub> may have a significant performance advantage over competing materials, such as high-temperature electronics. Challenges associated with the fabrication of Al-rich AlGa<sub>N</sub> devices will likewise be presented, for example the difficulty in forming low-resistance Ohmic contacts. The talk will conclude with a summary of the challenges facing the UWBG research community and potential pathways forward. SNL is managed and operated by NTESS under DOE NNSA contract DE-NA0003525.

[1] J.Y. Tsao *et al.*, *Adv. Elec. Mat.* **4**, 1600501 (2018).

[2] A.A. Allerman *et al.*, *Elec. Lett.* **52**, 1319 (2016).

[3] A.G. Baca *et al.*, *ECS J. Solid-State Sci. Tech.* **6**, Q161 (2017).

[4] A.G. Baca *et al.*, *IEEE Elec. Dev. Lett.* **40**, 17 (2019).

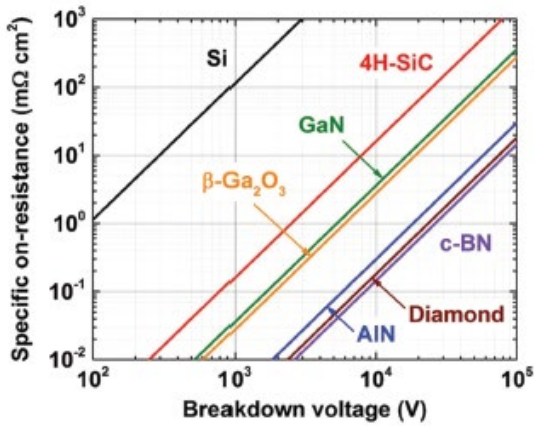


Fig.1: Specific on-resistance plotted vs. breakdown voltage calculated from the unipolar figure-of-merit for vertical power switching devices.

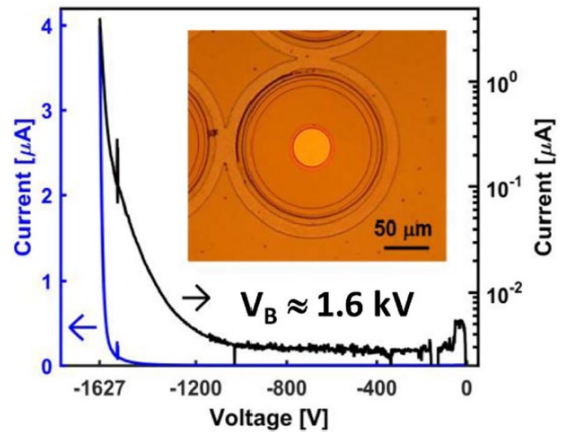


Fig.4: Main figure: Reverse IV characteristic of quasi-vertical  $Al_{0.7}Ga_{0.3}N$  pin diode on linear (left) and logarithmic (right) scales. Inset: Photograph of diode.

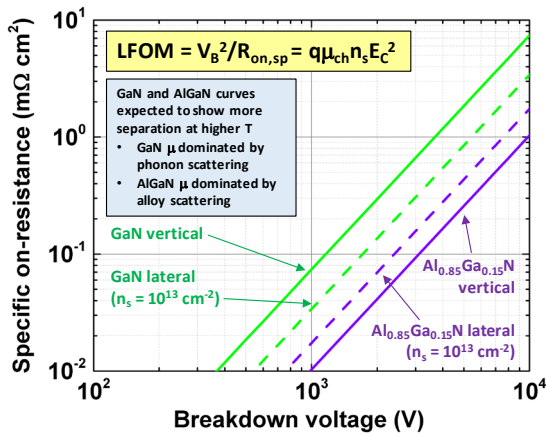


Fig.2: Lateral figure-of-merit compared to unipolar figure of merit for power switching devices based on GaN and  $Al_{0.85}Ga_{0.15}N$ .

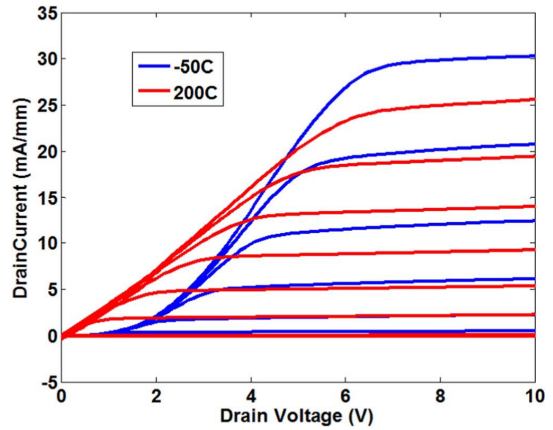


Fig.5:  $I_D-V_{DS}$  curves for  $Al_{0.85}Ga_{0.15}N/Al_{0.7}Ga_{0.30}N$  power switching HEMT measured at -50 and 200°C. Gate voltage ranges from -3 to +2 V in steps of 1 V.

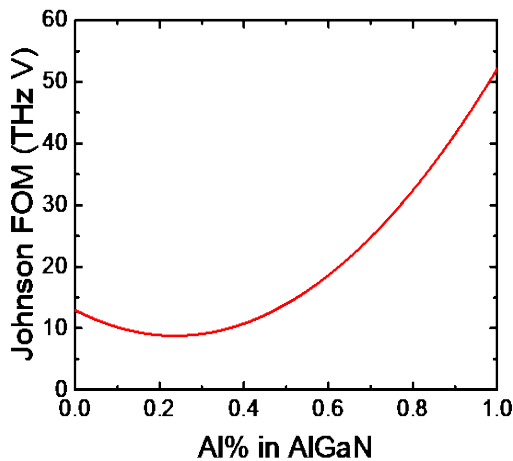


Fig.3: Johnson figure-of-merit for radio-frequency devices plotted as a function of Al composition in AlGaIn.

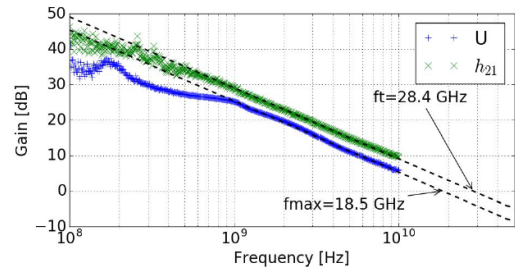


Fig.6: Small-signal RF data for  $Al_{0.85}Ga_{0.70}N/Al_{0.70}Ga_{0.30}N$  HEMT with 80 nm gate length at  $V_{GS} = 2.75$  V and  $V_{DS} = 20$  V.

## Carrier Transport Across Multiple InGaN Quantum Wells: Evidence of Ballistic Hole Transport

S. Marcinkevičius<sup>1</sup>, R. Yapparov<sup>1</sup>, L.Y. Kuritzky<sup>2</sup>, S. Nakamura<sup>2</sup>, and J.S. Speck<sup>2</sup>

<sup>1</sup>*Department of Applied Physics, KTH Royal Institute of Technology,  
Electrum 229, 16440 Kista, Sweden*

<sup>2</sup>*Materials Department, University of California, Santa Barbara, California 93106, USA  
sm@kth.se*

A uniform carrier distribution between quantum wells (QWs) of GaN-based multiple QW light emitting diodes (LEDs) is essential for an efficient high power LED operation. However, simulations and steady-state optical measurements suggest that in InGaN/GaN QW LEDs the interwell hole transport is not efficient and that light emission takes place only from the QW closest to the *p*-side of the device [1,2]. In this work, we study the interwell hole transport by directly monitoring it via time-resolved photoluminescence (PL) in multiple QW structures containing an optical marker (a deeper QW). Such measurements allow assessing transport times and reveal prevailing transport mechanisms under different experimental conditions.

Time-resolved PL experiments were performed on *n*-type structures containing 3–8 identical 3 nm thick In<sub>0.12</sub>Ga<sub>0.88</sub>N transport QWs with GaN barriers of different width (5.5 to 12.5 nm) and a 3 nm In<sub>0.18</sub>Ga<sub>0.82</sub>N marker QW. Carrier excitation primarily took place in the 100 nm thick GaN cap layer. The interwell transport times were estimated from PL rise times at the marker QW wavelength.

The measurements show that at high temperatures the interwell transport takes place via capture and thermionic emission. For InGaN/GaN QW structures the transport times are long, ~1 ns per well. At intermediate temperatures (80–220 K) the interwell transport ceases because the thermionic emission becomes slower than recombination. Surprisingly, at low temperatures (4–80 K) a strong increase of the hole transfer to the marker QW is observed. In addition, this transport is very fast, < 3 ps. The temperature dependence of this effect suggests that it is a manifestation of the ballistic hole transport over the transport QWs. Comparison of this effect in structures with different well and barrier parameters allows estimating the hole mean free path as ~10 nm. Measurements with low excess carrier energies suggests that hole transport via light hole and split-off valence bands contributes to this high value.

[1] Y.-K. Kuo *et al.*, Appl. Phys. Lett. **100**, 031112 (2012).

[2] A. David *et al.*, Appl. Phys. Lett. **92**, 053502 (2008).

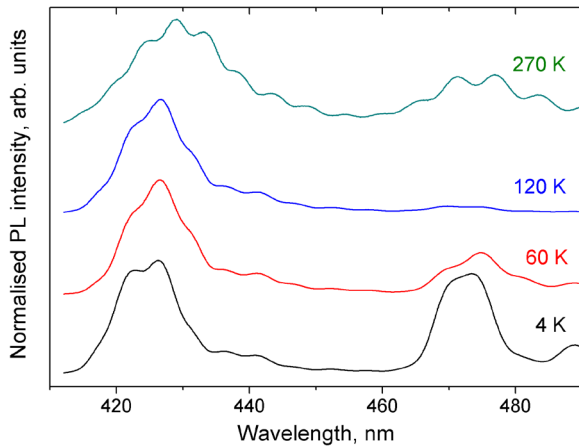


Fig.1: PL spectra of 5 transport QW and 5.5 nm barrier structure at different temperatures. The short and long wavelength peaks correspond to transport and marker QWs, respectively. At high temperature, the marker QW PL reflects thermionic hole transfer into this QW. At intermediate temperatures (120 K) PL is only due to carriers excited directly in the marker QW. At low temperatures, increase of the marker QW PL reflects ballistic hole transfer over the transport QWs. Oscillatory pattern of the spectra is due to Fabry-Perot interference.

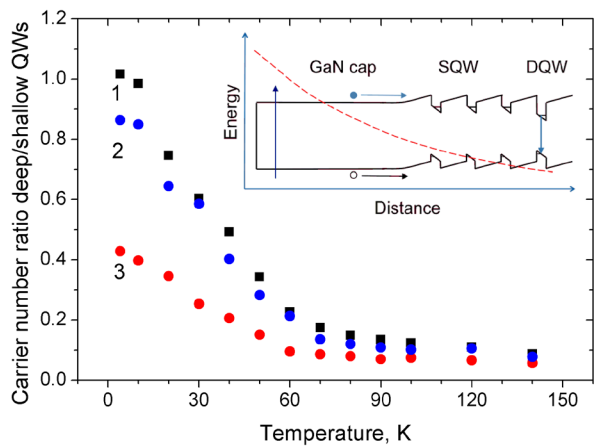


Fig.2: Ratio of carrier numbers in the marker and transport QWs for 5 QW structures with 5.5 nm (1), 8.5 nm (2) and 12.5 nm (3) barriers. With decreased temperature, the number of carriers in the marker QW experiences a strong increase. Its linear dependence on the inverse temperature is consistent with transport limited by acoustic phonon scattering. The inset shows schematics of the experiment with the red dashed line illustrating carrier excitation profile. The layer thicknesses are not in scale. SQW and DQW stand for transport and marker QWs, respectively.

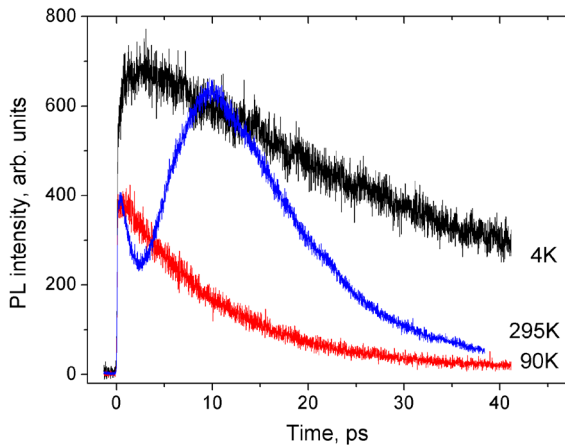


Fig.3: PL transients of the 5 transport QW 5.5 nm barrier structure at different temperatures, The fast PL rise at 295 K and 90 K reflects direct carrier excitation in the marker QW. The slow rise at 295 K – the thermionic transport. The increased transient amplitude at 4 K is due to the fast hole transfer into the marker QW.

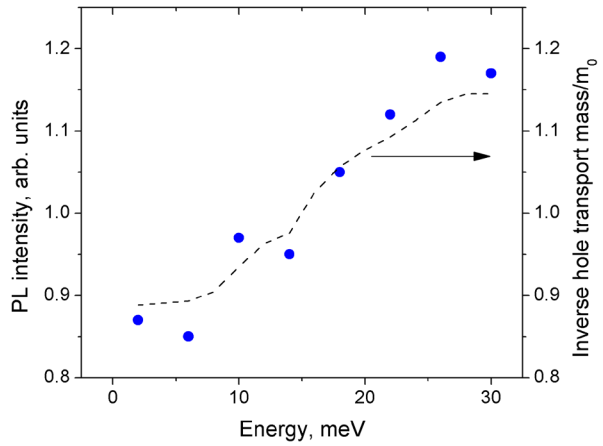


Fig.4: Deep QW PL intensity at 4 K measured at different hole excess energies. The dashed curve shows an estimation of the inverse effective hole transport mass in GaN. Decrease of the transport mass with increased energy over the valence band maximum is because of population of the light hole and split-off bands.

## Oxide Electronics Based on Wide Bandgap Perovskite BaSnO<sub>3</sub>

K. Char

*Institute of Applied Physics, Dept. of Physics and Astronomy*

*Seoul National University, Seoul 08826, Korea*

*kchar@phya.snu.ac.kr*

A wide-bandgap perovskite oxide semiconductor BaSnO<sub>3</sub> was recently found to possess high mobility and excellent stability. Its single crystal mobility value of about 300 cm<sup>2</sup>/V·sec in the doping range of 10<sup>19</sup>~10<sup>20</sup>/cm<sup>3</sup>, when n-type La dopants in place of Ba are used, is the highest among all the semiconductors. Furthermore, the oxygen diffusion constant in BaSnO<sub>3</sub> was measured to be several orders of magnitude lower than 3d transition metal perovskite oxides, demonstrating superb stability of the material.

Taking advantage of such properties, excellent field effect transistors were recently demonstrated using amorphous gate oxides (AlO<sub>x</sub> and HfO<sub>x</sub>) as well as high-k epitaxial gate oxides such as LaInO<sub>3</sub> and BaHfO<sub>3</sub>, which led to development of an all-perovskite transparent high mobility field effect transistor. In addition, p-type doping by K in place of Ba is feasible and the pn-junctions made with K-doped BaSnO<sub>3</sub> and La-doped BaSnO<sub>3</sub> were demonstrated to exhibit near-ideal IV characteristics. Moreover, 2DEG behavior is found at the polar interface of BaSnO<sub>3</sub> and LaInO<sub>3</sub>. Our recent simulation based on 1-dimensional Poisson-Schrödinger equation suggests that the 2DEG state at the BaSnO<sub>3</sub>/LaInO<sub>3</sub> interface has a confinement length of about 2 nm driven by the “interface polarization” created in LaInO<sub>3</sub> due to the coherent epitaxial strain between the cubic BaSnO<sub>3</sub> and orthorhombic LaInO<sub>3</sub>. We will go over that mechanism that creates such “interface polarization”.

In spite of these tremendous progresses, the device performances are currently limited by defects such as threading dislocations, cation vacancies and oxygen vacancies. Once these defects are removed, the perovskite oxide semiconductor BaSnO<sub>3</sub> system, especially when it is combined with other perovskite oxides with high-k and/or ferroelectric properties, is expected to offer much more opportunities for both science and technology.

[1] H. Tomori *et al.*, Appl. Phys. Expr. **4**, 075102 (2011).

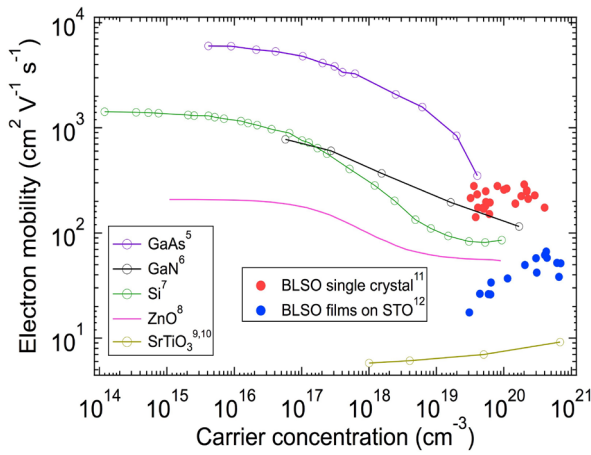


Fig.1: Mobility vs. electron carrier density in various semiconductors in comparison to BaSnO<sub>3</sub>.

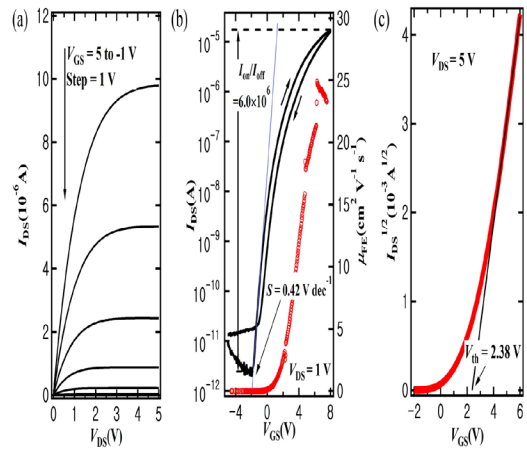


Fig.3: Electrical Properties of an FET made with BaSnO<sub>3</sub> channel layer and HfO<sub>2</sub> gate oxide.

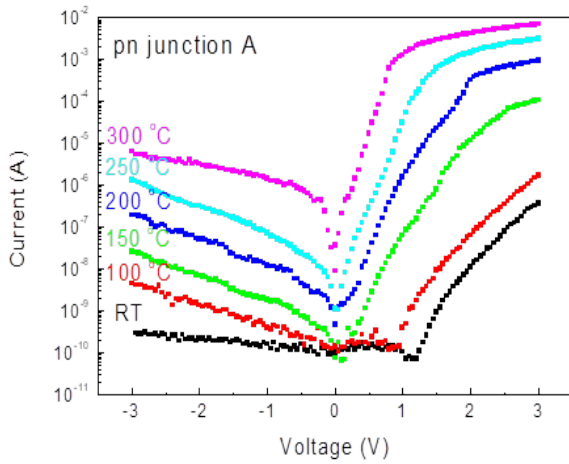


Fig.2: I-V characteristics of pn-junctions of (BaK)SnO<sub>3</sub>/(BaLa)SnO<sub>3</sub> at various temperatures.

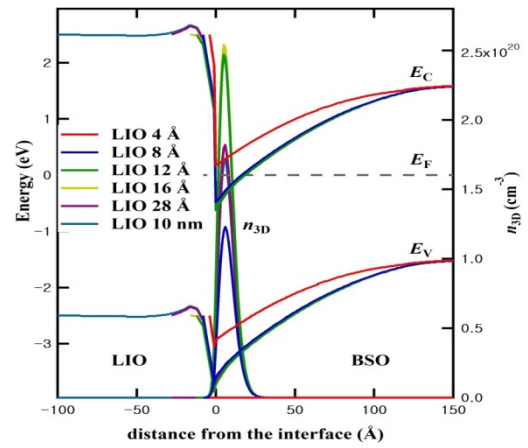


Fig.4: Band diagrams of 2DEG state at the LaInO<sub>3</sub>/BaSnO<sub>3</sub> interface at various LaInO<sub>3</sub> thicknesses.

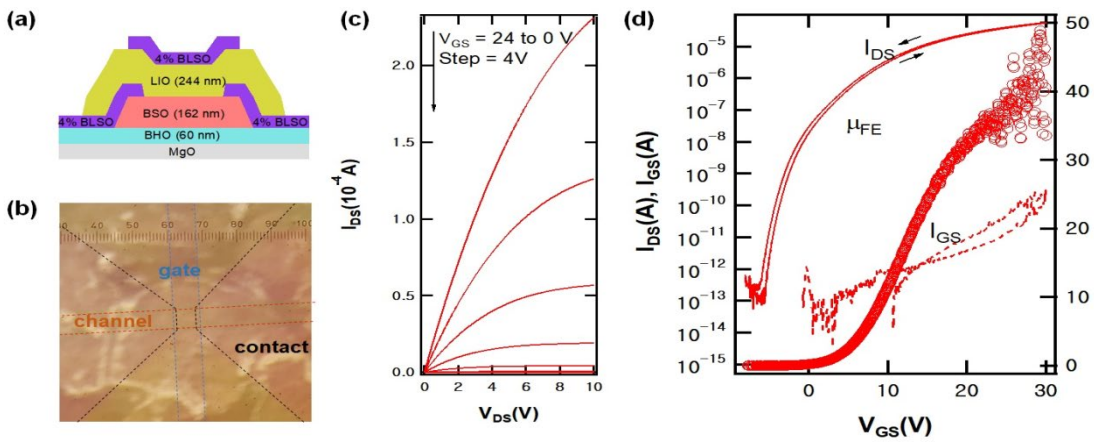


Fig.5: Structure and electrical properties of an FET made with 2DEG at the LaInO<sub>3</sub>/BaSnO<sub>3</sub> interface and the high-k LaInO<sub>3</sub> gate oxide.

## Pockels Effect in Si-Integrated Perovskite Oxides

A.K. Hamze, K.D. Fredrickson, W. Li, and A.A. Demkov

*Department of Physics, The University of Texas, Austin, Texas 78712, USA*

*demkov@physics.utexas.edu*

The Pockels effect (linear electro optic (EO) effect), a change in the index of refraction of a non-centrosymmetric crystal in response to an applied external electric field, has been subject to increasing study in recent years because the effect offers the potential for high speed, low power operations for optical modulation in silicon photonics applications [1-3], which can be used for intra-chip data transmission (an increasingly necessary functionality as copper interconnects reach material limits), neuromorphic logic optical chips [4], and photonic integrated circuits for quantum computing [5-6]. The Pockels effect is most commonly used for optical modulation in the telecommunications industry, where LiNbO<sub>3</sub>, with a Pockels coefficient of ~30 pm/V, is the current gold standard material. Due to the complexity of integrating LiNbO<sub>3</sub> on Si, however, perovskite titanates have recently become the primary subjects of the theoretical and experimental studies into the use of the Pockels effect in silicon photonics. The main focus of these efforts has been BaTiO<sub>3</sub> (BTO), which is particularly attractive due to its integrability with silicon (001) and its large Pockels effect (1,700 pm/V), which remains large even in thin films (and which recently has been shown to approach bulk values [3]). First principles calculations offer a rather useful tool that relates the macroscopic response of the material to its atomic and electronic structure. It has proven to be indispensable when designing Si-integrated EO modulators. I will discuss strain engineering of the Pockels effect in BTO and SrTiO<sub>3</sub> (STO) [7,8], and present the design rules for achieving high Pockels response in materials in terms of soft optical phonon frequencies and Raman susceptibility. The underlying physical phenomena behind the Raman susceptibility, is the dependence of the band gap on phonon modes and is related to large deformation potentials (strong electron-phonon interaction). I will discuss the electro-optic response in thin perovskite films integrated on Si and its relation to temperature and strain.

- [1] S. Abel *et al.*, *Nat. Comm.* **4**, 1671 (2013).
- [2] C. Xiong *et al.*, *Nano Lett.* **14**, 1419 (2014).
- [3] S. Abel *et al.*, *Nat. Materials* **18**, 42 (2019).
- [4] L. Larger *et al.*, *Opt. Express* **20**, 3241 (2012).
- [5] T.D. Ladd *et al.*, *Nature* **464**, 45 (2010).
- [6] J.L. O'Brien *et al.*, *Nat. Photonics* **3**, 687 (2009).
- [7] K.D. Fredrickson *et al.*, *Phys. Rev. B* **98**, 075136 (2018).
- [8] A.K. Hamze and A.A. Demkov, *Phys. Rev. Materials* **2**, 005200 (2018).

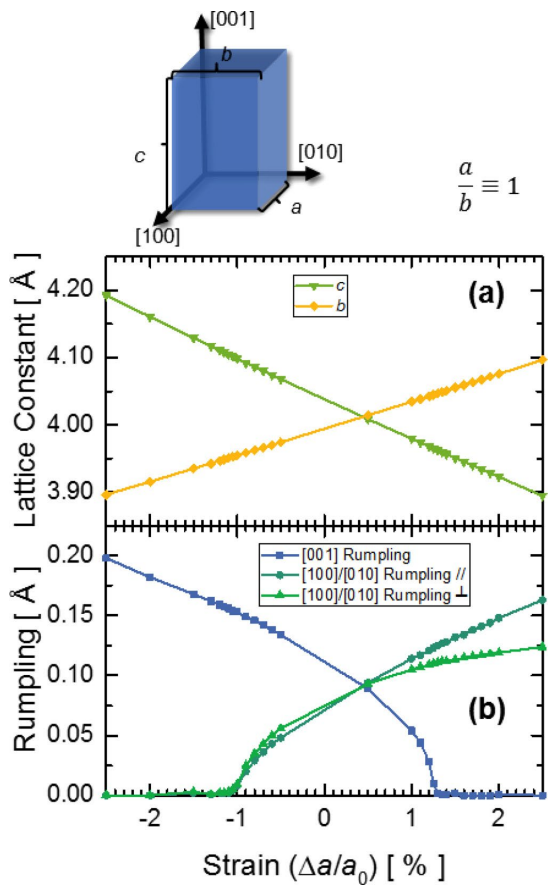


Fig.1: The lattice parameters (a) and rumpling (b) of BTO as a function of strain for the out-of-plane polarized case as shown in schematic above. There are two rumplings for the a and b directions, since the rumpling for the equatorial O is inequivalent from the rumpling for the apical O. No such complication occurs in the c direction.

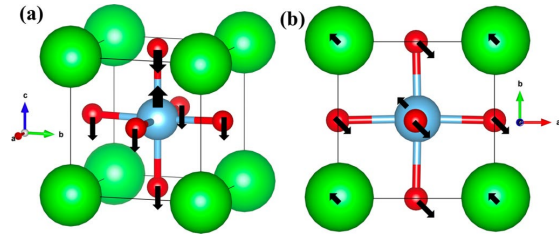


Fig.2: The displacement patterns of the first optical mode of STO which goes soft and drives the structural phase transition. The strontium ions are colored green, the titanium ions are colored blue, and the oxygen ions are colored red.

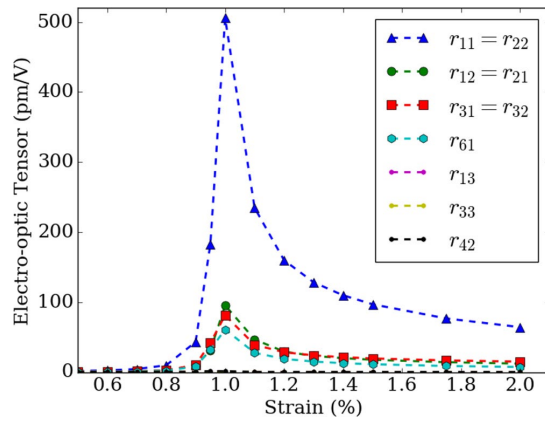


Fig.3: The magnitudes of the largest EO tensor components of STO under tensile strain. The EO response peaks at 1.00% strain.

## Vertical Ga<sub>2</sub>O<sub>3</sub> MOSFETs Fabricated by Ion Implantation Process

M. Higashiwaki<sup>1</sup>, M.H. Wong<sup>1</sup>, K. Goto<sup>2</sup>, H. Murakami<sup>2</sup>, and Y. Kumagai<sup>1</sup>

<sup>1</sup>*National Institute of Information and Communications Technology,  
Koganei, Tokyo 184-8795, Japan*

<sup>2</sup>*Department of Applied Chemistry, Tokyo University of Agriculture and Technology,  
Koganei, Tokyo 184-8588, Japan  
mhigashi@nict.go.jp*

$\beta$ -gallium oxide (Ga<sub>2</sub>O<sub>3</sub>) is an ultra-wide-bandgap semiconductor having an extremely large bandgap of 4.5 eV and a breakdown electric field greater than 6 MV/cm. The availability of high-quality single-crystal wafers is another advantage over existing competitors such as SiC and GaN. These physical and technological properties make Ga<sub>2</sub>O<sub>3</sub> an attractive candidate for power switching electronics. Recently, we succeeded in developing nitrogen (N)-ion implantation doping technology to form *p*-type Ga<sub>2</sub>O<sub>3</sub> [1]. Note that it is almost impossible to obtain *p*-type Ga<sub>2</sub>O<sub>3</sub> with effective hole conductivity as for conventional semiconductors. Therefore, *p*-Ga<sub>2</sub>O<sub>3</sub> is only useful for engineering large energy barriers in the form of *p-n* junctions. We have experimentally confirmed that a N-ion implanted *p*-Ga<sub>2</sub>O<sub>3</sub> region formed in *n*-Ga<sub>2</sub>O<sub>3</sub> can be utilized as a current blocking layer.

In this talk, we will discuss the device process and characteristics of depletion-mode (D-mode) and enhancement-mode (E-mode) vertical Ga<sub>2</sub>O<sub>3</sub> metal-oxide-semiconductor field-effect transistors (MOSFETs) fabricated by using multiple Si- and N-ion implantations [2, 3]. Figures 1(a) and (b) show cross-sectional schematics of the D-mode and E-mode MOSFET structures, respectively. DC drain current–drain voltage ( $I_d$ – $V_d$ ) characteristics of the D-mode and E-mode MOSFETs are shown in Figs. 2(a) and (b), respectively.

This work was partially supported by Council for Science, Technology and Innovation (CSTI), Cross-ministerial Strategic Innovation Promotion Program (SIP), “Next-generation power electronics” (funding agency: New Energy and Industrial Technology Development Organization).

[1] M. H. Wong *et al.*, Appl. Phys. Lett. **113**, 102103 (2018).

[2] M. H. Wong *et al.*, IEEE Electron Device Lett. **40**, 431 (2019).

[3] M. H. Wong *et al.*, Proc. Device Research Conference (2019).

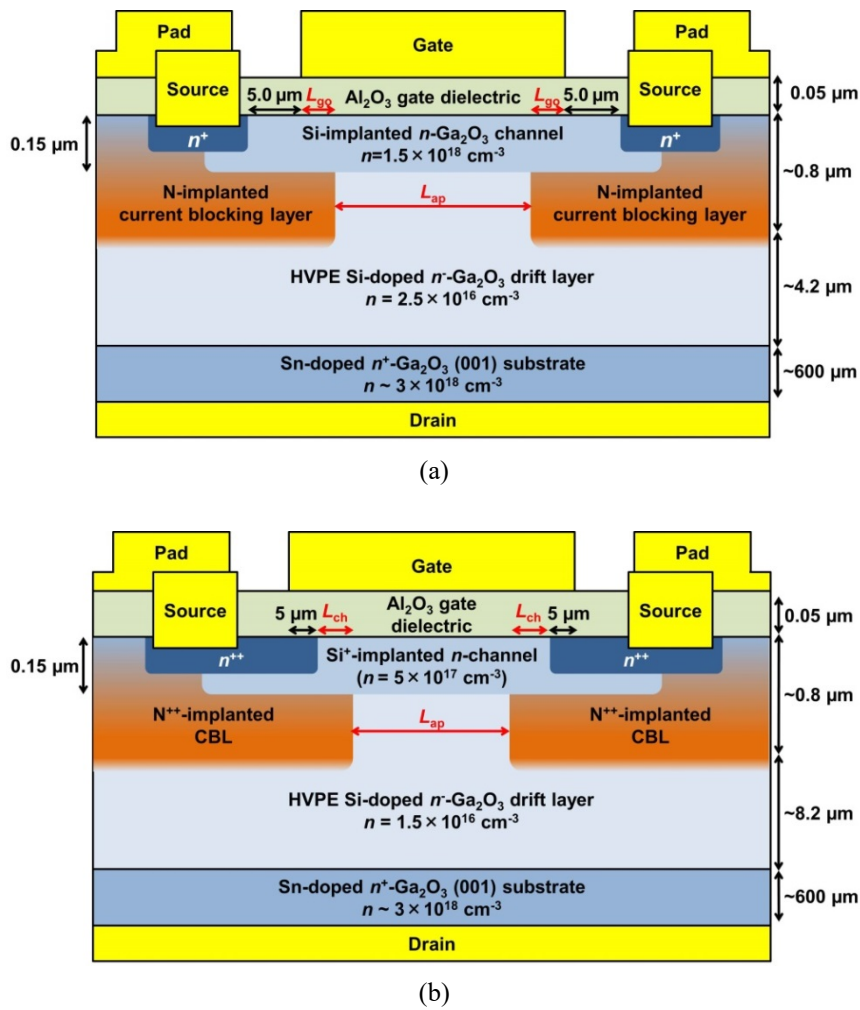


Fig.1: Cross-sectional schematics of (a) D-mode and (b) E-mode vertical  $Ga_2O_3$  MOSFET structures:  $L_{ap}=20 \mu m$  (D-mode and E-mode),  $L_{go}=2.5 \mu m$  (D-mode),  $L_{ch}=5.0 \mu m$  (E-mode).

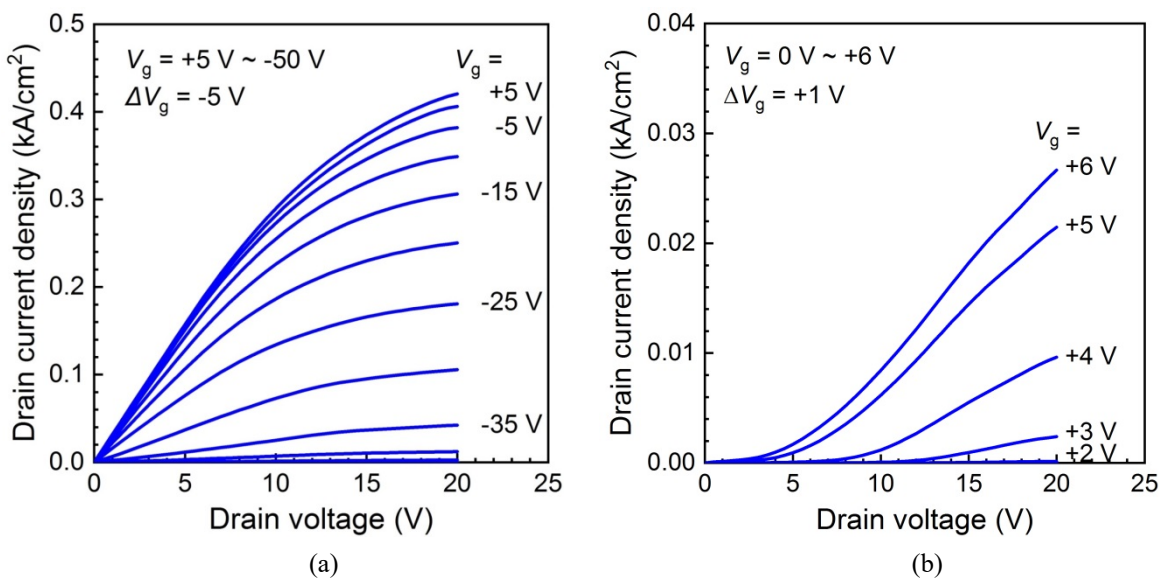


Fig.2: DC  $I_d-V_d$  characteristics of (a) D-mode and (b) E-mode vertical  $Ga_2O_3$  MOSFETs.

## Magnetic Weyl Semimetals!

C. Felser, K. Manna, E. Lui, and Y. Sun

*Max Planck Institute Chemical Physics of Solids, Dresden, Germany*

*felser@cpfs.mpg.de*

Topology a mathematical concept became recently a hot topic in condensed matter physics and materials science. One important criteria for the identification of the topological material is in the language of chemistry the inert pair effect of the s-electrons in heavy elements and the symmetry of the crystal structure [1]. Beside of Weyl and Dirac new fermions can be identified compounds via linear and quadratic 3-, 6- and 8- band crossings stabilized by space group symmetries [2]. In magnetic materials the Berry curvature and the classical AHE helps to identify interesting candidates. Magnetic Heusler compounds were already identified as Weyl semimetals such as Co<sub>2</sub>YZ [3,4], in Mn<sub>3</sub>Sn [5,6,7] and Co<sub>3</sub>Sn<sub>2</sub>S<sub>2</sub> [8-10].

The Anomalous Hall angle helps to identify even materials in which a QAHE should be possible in thin films. Besides this k-space Berry curvature, Heusler compounds with non-collinear magnetic structures also possess real-space topological states in the form of magnetic antiskyrmions, which have not yet been observed in other materials [11].

- [1] B. Bradlyn *et al.*, Nature **547**, 298, (2017).
- [2] B. Bradlyn *et al.*, Science **353**, aaf5037A (2016).
- [3] J. Kübler and C. Felser, Europhys. Lett. **114**, 47005 (2016).
- [4] I. Belopolski *et al.*, Science in print (2019), arXiv:1712.09992
- [5] J. Kübler and C. Felser, Europhys. Lett. **108**, 67001 (2014).
- [6] A.K. Nayak *et al.*, Science Adv. **2**, e1501870 (2016).
- [7] S. Nakatsuji *et al.*, Nature **527**, 212 (2015).
- [8] E. Liu *et al.*, Nature Phys. **14**, 1125 (2018).
- [9] D.F. Liu *et al.*, Science in print (2019).
- [10] N. Morali *et al.*, Science in print (2019) arXiv:1903.00509.
- [11] A.K. Nayak *et al.*, Nature **548**, 561 (2017).

## Formation of Helical States in the Fractional Quantum Hall Regime

T. Wu<sup>1</sup>, Z. Wan<sup>1</sup>, A. Kazakov<sup>1</sup>, Y. Wang<sup>1</sup>, G. Simion<sup>1</sup>, J. Liang<sup>1</sup>, K.W. West<sup>2</sup>, K. Baldwin<sup>2</sup>,  
L.N. Pfeiffer<sup>2</sup>, Y. Lyanda-Geller<sup>1</sup>, and L.P. Rokhinson<sup>1</sup>

<sup>1</sup>*Department of Physics and Astronomy, Purdue University,  
West Lafayette, Indiana 47907, USA*

<sup>2</sup>*Department of Electrical and Computer Engineering, Purdue University,  
West Lafayette, Indiana 47907, USA*

*leonid@purdue.edu*

I will introduce a new platform based on spin transitions in the fractional quantum Hall effect regime where parafermions – higher order non-abelian excitations - can be realized. Local (gate) control of spin transition allows formation of isolated helical domain walls, which consist of counter-propagating edge states of opposite polarization with fractional charge excitations[1]. When superconductivity is induced into such a domain wall from superconducting contacts via proximity effect, parafermions are expected to be formed at the domain wall boundaries. In a multi-gate device a re-configurable network of domain walls can be formed allowing creation, braiding, manipulation and fusion of parafermions. In respect to the quantum computing application parafermions are more computationally intense than Majoranas and are a building block for Fibonacci fermions, even high order non-Abelian particles that can perform universal gate operations within the topologically protected subspace.

[1] T. Wu *et al.*, Phys. Rev. B **97**, 245304 (2018).

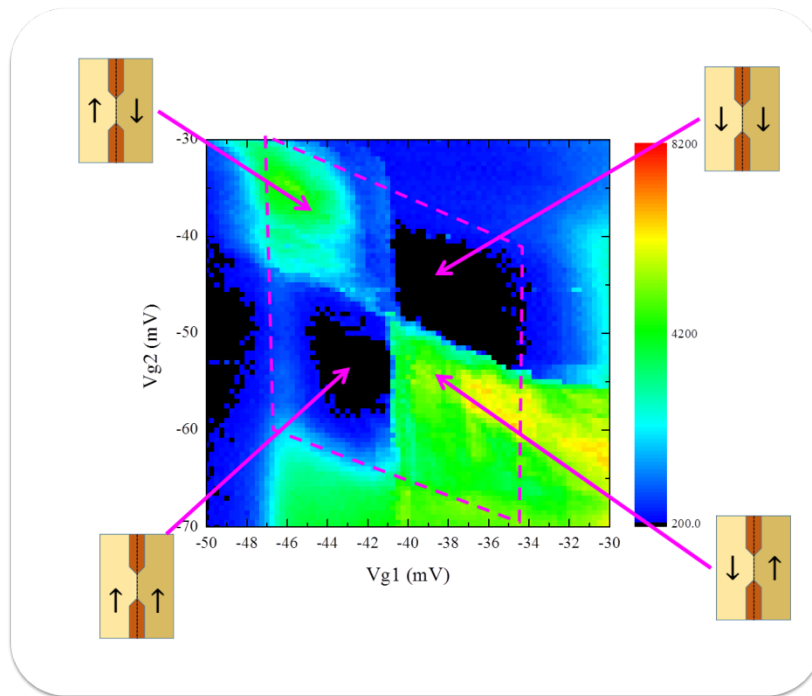


*Fig.1: Formation of helical channels in a multi-gate device at  $\nu = 2/3$  FQHE state. Magenta dotted line marks a region where  $\nu = 2/3$  under overlapping gates  $V_{g1}$  and  $V_{g2}$ . An insulating FQHE state is observed when polarization of  $\nu = 2/3$  states is the same under both gates (black regions), a conducting channel is formed when polarization is different under the two gates. Conductance of this channel does not depend on the direction of magnetic field.*

## Quantum Adiabatic Pumping with Modulating Electron Phase

Y. Tokura

*Faculty of Pure and Applied Sciences, University of Tsukuba,*

*Tsukuba, Ibaraki 305-8571, Japan*

*Tsukuba Research Center for Energy Material Science (TREMS), University of Tsukuba,*

*Tsukuba, Ibaraki 305-8571, Japan*

*tokura.yasuhiro.ft@u.tsukuba.ac.jp*

Quantum adiabatic pumping (QAP) generates an average current even in the absence of an average bias under a slow and periodic modulation of multiple control parameters of the system. This stems from geometrical (Berry-phase like) properties of slow coherent dynamics, and is an active field of research and had been argued in various mesoscopic-transports including, charge [1], spin [2], and entropy generation [3]. In the non-interacting limit, QAP is related to the scattering matrix of the coherent transport [4]. We had investigated the QAP effect by adiabatically modulating the Aharonov-Bohm (AB) phase of the interferometer as well as the local potential in the interferometer [5]. However, it seems no studies have been made of the adiabatic spin-pumping with purely geometric means such as Aharonov-Casher (AC) phase or AB phase. The fundamental question here is whether QAP is possible by only modulating the electron geometric phase.

We studied spin-QAP in Rashba-Dresselhaus-Aharonov-Bohm interferometer and derived an explicit formula of the Berry curvature,  $\Pi_\sigma$ , for each spin component. We confirmed that QAP is absent if we choose AB-phase and AC-phase as control parameters. In contrast, we demonstrated that spin QAP is possible by assuming Rashba and Dresselhaus spin-orbit interaction strengths as control parameters. Explicitly, in the diamond-shape interferometer made of four quantum dots (QDs)[6] (Fig.1), the Berry curvature,  $\Pi_\sigma$ , is obtained (Fig.2). We found the condition of “adiabaticity” being subtle at a certain condition of control parameters.

[1] L.P. Louwenhoven *et al.*, Phys. Rev. Lett. **67**, 1626 (1991).

[2] S. Nakajima *et al.*, Phys. Rev. B **92**, 195420 (2015).

[3] S. Nakajima and Y. Tokura, J. Stat. Phys. **169**, 902 (2017).

[4] P.W. Brouwer, Phys. Rev. B **58**, R10135 (1998).

[5] M. Taguchi *et al.*, J. Phys. Soc. Jpn. **85**, 084704 (2016).

[6] A. Aharony *et al.*, Phys. Rev. B **84**, 035323 (2011).

[7] Y. Tokura, Entropy **21**, 828 (2019).

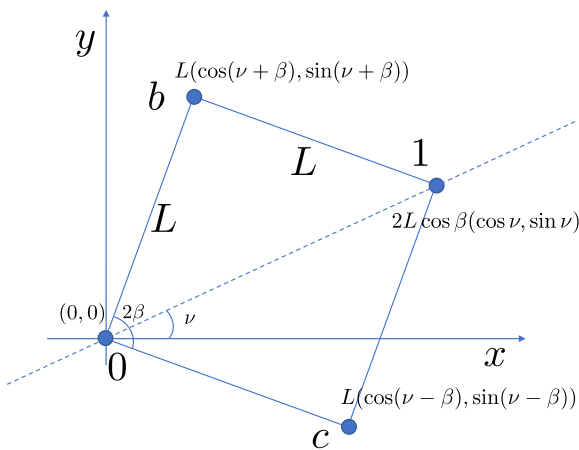


Fig.1: Schematics of the diamond shaped Rashba-Dresselhaus-Aharonov-Bohm interferometer[6] made of four QDs (bullets at  $0, b, c, 1$ ). On the bonds between the QDs, the spin-orbit interaction induces AC phase to the electron. A flux is threading through the interferometer, which introduces AB phase to the electron. At QD 0 and 1, one-dimensional leads (reservoirs) are attached.

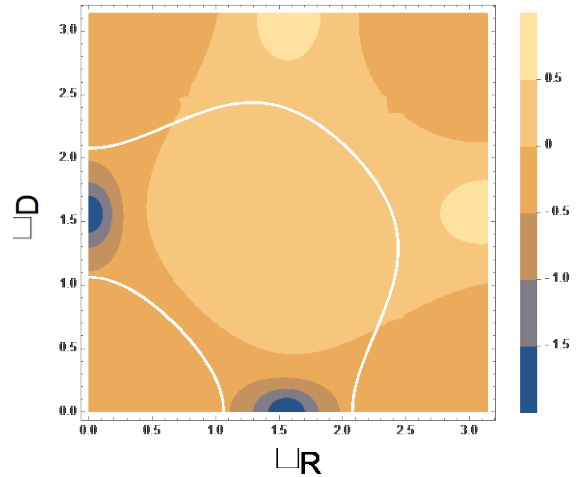


Fig.2: Berry curvature  $\Pi_\sigma$  for a particular spin direction as a function of Rashba ( $\alpha_R$ ) and Dresselhaus ( $\alpha_D$ ) interaction strengths with a fixed AB-phase. Berry curvature for the other spin direction is much smaller. The induced spin current is obtained by integrating this Berry curvature over the area enclosing the trajectory made of two control parameters,  $\alpha_R$  and  $\alpha_D$ . [7]

## Quantum Transport in APAM Wires

D. Mamaluy, J.P. Mendez, and X. Gao

*Sandia National Laboratories, 1515 Eubank SE, Albuquerque, NM 87123, USA*

*mamaluy@sandia.gov*

Atomic Precision Advanced Manufacturing (APAM) [1] is a process of area-selective chemical incorporation of dopants at an atomic scale using the scanning tunneling microscope (STM) technique. Sandia National Laboratories initiated a systematic study (“Grand Challenge”) of the new possibilities that APAM technology opens for nanoelectronics at the atomic scale. There has been a series of attempts to calculate the band structure of Si:P  $\delta$ -layered APAM systems [3-6], however, there is still a significant disagreement between the calculation themselves and the uncertainty in verifying them in the experiment [7]. A very recent experimental ARPES study [7] suggested the existence of a so-far-unexplained, shallow ( $\sim 50$  meV below the Fermi level) conducting band (in the following denoted  $3\Gamma$ ) that is likely responsible for the majority of the current carrying in the studied Si:P-delta layer system. In this work we attempt to explain the origin of this  $3\Gamma$  band and calculate its structure at 4K.

We employ a fully charge self-consistent 2D and 3D quantum ballistic transport formalism (see e.g. [2]) to study the electrical properties of APAM wires and APAM wires with a 10-20nm intrinsic gap shown in Fig. 1 a and b. We first find that an extremely high (up to  $2 \times 10^{14}$  cm<sup>-2</sup>) level of delta-layer donor doping in Si:P  $\delta$ -layer creates an intriguing structure of the highest C.B. band – that may correspond to experimentally observed in work [7]  $3\Gamma$  band. Figure 2a shows the local density of states LDOS(E,z) for this shallow band. It suggests that there exists two distinct free electron “layers” with different kinetic energies. The lower one (-65 meV) corresponds to the electrons that are strongly confined around the delta-layer ( $z=10$  nm in the shown example), while the higher one (-17meV) corresponds to two ( $z=8.5$  and  $z=11.5$ ) layers of electrons with the average position displaced by 1.5 nm from the delta-layer. We then analyze the dependence of LDOS structure on the APAM wire thickness (along z-axis, see Fig. 1a) and predict two new effects: 1) the existence of  $\delta$ -layer induced “protected” (=independent of the wire thickness) strongly localized states below the Fermi level and 2) “geometry induced” (strongly dependent of the wire thickness) higher energy weakly localized states above the Fermi level. Finally, we present our analysis of the experimentally studied APAM wires with 10-20nm intrinsic gaps (Fig. 1b). We predict that contrary to the popular belief, in these nano-scaled  $n^{++}$ -ni- $n^{++}$  structures, the barrier due to the intrinsic region is only of the order of 50 meV, and demonstrate how this (lower than expected) potential barrier height and the consequent much stronger sensitivity to single charged impurities in the gap can explain the observed I-V characteristics in these systems (see Figure 3).

- [1] K. Goh *et al.*, Phys. Rev. B **73**, 035401 (2006).
- [2] D. Mamaluy and X. Gao, APL **106**, 193503 (2015).
- [3] D. J. Carter *et al.*, Phys. Rev. B **80**, 049901 (2009).
- [4] D. W. Drumm *et al.*, NanoscaleRL **8**, 111 (2013).
- [5] J. A. Miwa *et al.*, Phys. Rev. Lett. **110**, 136801 (2013).
- [6] D. J. Carter *et al.*, Phys. Rev. B **87**, 045204 (2013).
- [7] <https://arxiv.org/pdf/1904.10929.pdf>

Sandia National Laboratories is a multimission laboratory managed and operated by National Technology and Engineering Solutions of Sandia, LLC., a wholly owned subsidiary of Honeywell International, Inc., for the U.S. Department of Energy’s National Nuclear Security Administration under contract DE-NA-0003525.

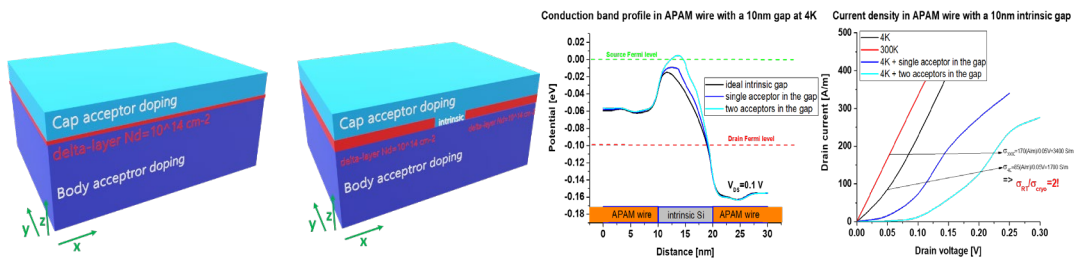


Fig.1: Simulated idealized APAM structures: a) APAM wire, and b) APAM wire with an intrinsic gap (10-20nm).

Fig.3: APAM wire with a 10nm intrinsic gap: the effective 1D c.b. potential (left panel); the corresponding current densities (right panel). Even a single impurity in the gap significantly alters the current.

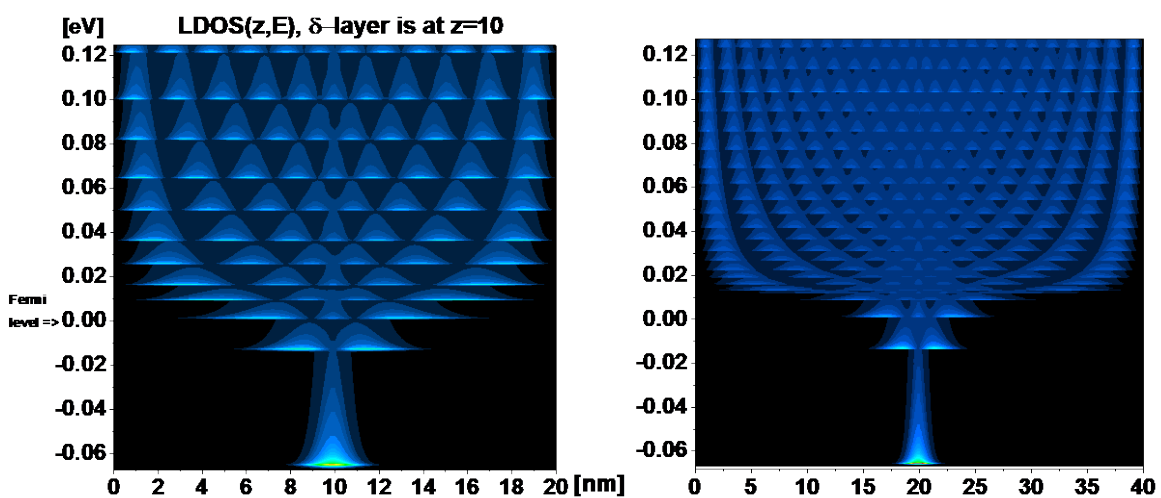


Fig.2: Local density of states  $LDOS(z,E)$  of a simplified Si:P  $\delta$ -layer system: the body and cap thicknesses are assumed to be the same and the acceptor donor level is taken to be  $10^{16} \text{ cm}^{-3}$ . LDOS for two different sample widths are shown: 20nm (left panel) and 40nm (right panel).

## **Giant Zero Bias Anomaly Due to Coherent Scattering from Frozen Phonon Disorder in Quantum Point Contacts**

Y.-H. Lee<sup>1</sup>, S. Xiao<sup>1</sup>, K.W. Kim<sup>2</sup>, J.L. Reno<sup>3</sup>, J.P. Bird<sup>1</sup>, and J.E. Han<sup>4</sup>

<sup>1</sup>*Department of Electrical Engineering, University at Buffalo, Buffalo, New York 14260, USA*

<sup>2</sup>*Center for Theoretical Physics of Complex Systems, Institute for Basic Science (IBS),  
Daejeon 34126, Republic of Korea*

<sup>3</sup>*CINT, Sandia National Laboratories, Department 1881,  
MS 1303, Albuquerque, New Mexico 87185, USA*

<sup>4</sup>*Department of Physics, University at Buffalo, Buffalo, New York 14260, USA*  
*jbird@buffalo.edu*

The coherent scattering of propagating waves has long been studied in the literature, in the context of both classical and quantum transport. Examples include strong and weak localization and universal conductance fluctuations. In this work, we demonstrate [1] an unusual manifestation of coherent electron scattering, in the low-temperature electron transport through quantum point contacts (QPCs). These devices are characterized by a low level of structural (impurity- or defect-related) disorder, which allows us to access a regime in which phonon excitation functions as a controlled source of disorder. We show here how the phonon-induced lattice distortion that is the source of this disorder may be manipulated via the ambient temperature and by the size of the bias ( $V_d$ ) applied to generate transport through the device. The temperature determines the amplitude of the disorder at thermal equilibrium, while the bias allows drifting electrons to stochastically impart energy and momentum to the crystal lattice, thereby leading to the emergence of different disorder behaviors. These concepts are applied to account for a remarkable feature in the QPCs, namely, a giant zero bias anomaly in their differential conductance. The anomaly is characterized by a precipitous drop of conductance, as either the temperature or bias is increased, behavior that we reproduce with nonequilibrium transport calculations. We attribute the anomaly to a coherent scattering process involving multiple quantum channels (or subbands), in a manner that may be controlled directly via the bias and/or temperature. Such a mechanism could open up a pathway to the on-demand control of coherent scattering in the solid state.

**Acknowledgment.** Work supported by the U.S. Department of Energy, Office of Basic Energy Sciences, Division of Materials Sciences and Engineering (Grant No. DE-FG02-04ER46180).

[1] Y.-H. Lee *et al.*, Phys. Rev. Lett. **123**, 056802 (2019).

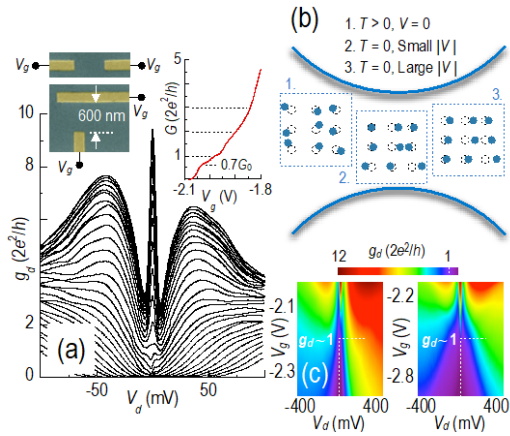


Fig. 1: (a) Differential conductance of a QPC at 4.2 K. Insets are electron micrographs of different QPC geometries. (b) Distinct disorder realizations, corresponding to different regimes of temperature and biasing. These “snapshots” denote the instantaneous displacement of atoms from equilibrium. (c) Contour plots showing differential conductance for the two QPC geometries of Fig. 1(a) [1].

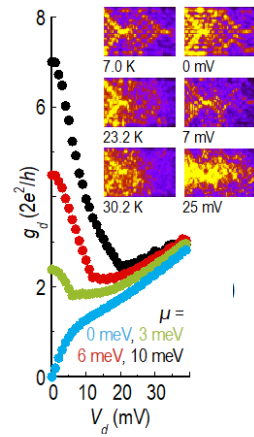


Fig. 2: Calculated differential conductance as a function of source-drain bias and for different chemical potentials in the QPC. Insets show probability density in the QPC for various temperatures (left column) and drain bias ( $V_d$ , right column) [1].

## Electrical, Thermal, and (Some) Unusual Applications of 2D Materials and Heterostructures

C. McClellan, S. Vaziri, I. Datye, C. Bailey, A. Gabourie, M. Chen,  
V. Chen, K. Schauble, R. Grady, and E. Pop

*Electrical Engineering, Stanford University, Stanford CA 94305, USA*

*epop@stanford.edu*

This talk will present recent highlights from our research on two-dimensional (2D) materials including graphene, boron nitride (h-BN), and transition metal dichalcogenides (TMDs). Results span from fundamental measurements and simulations, to applications taking advantage of unusual 2D material properties. We measured record velocity saturation in graphene [1], and the thermal properties of graphene nanoribbons [2]. We have also grown monolayer 2D semiconductors over large areas, including MoS<sub>2</sub> [3], WSe<sub>2</sub>, MoSe<sub>2</sub> [4], and multilayer MoTe<sub>2</sub> and WTe<sub>2</sub> [5]. ZrSe<sub>2</sub> and HfSe<sub>2</sub> have native high- $\kappa$  dielectrics ZrO<sub>2</sub> and HfO<sub>2</sub>, which are of key technological relevance [6]. Improved electrical contacts [7] led to the realization of 10 nm monolayer MoS<sub>2</sub> transistors with the highest current reported to date, near ballistic limits [8]. Current density in such 2D devices is ultimately limited by self-heating and phonon scattering [9], in part due to the weak van der Waals bonds between 2D materials and their environment, which lead to a large thermal resistance of this interface [10]. On the other hand, we exploited this weak interface to achieve extremely good thermal insulators, with effective thermal conductivity lower than air [11], to improve energy efficiency in phase-change memory [12], and as the basis of thermal transistors [13]. The last example could enable control of heat in “thermal circuits” analogous with electrical circuits. These studies reveal fundamental limits and some unusual applications of 2D materials, taking advantage of their unique properties.

- [1] M. Yamoah *et al.*, ACS Nano **11**, 9914 (2017).
- [2] M.-H. Bae *et al.*, Nature Comm. **4**, 1734 (2013).
- [3] K. Smithe *et al.*, ACS Nano **11**, 8456 (2017).
- [4] K. Smithe *et al.*, ACS AMI **1**, 572 (2018).
- [5] M. Mleczko *et al.*, ACS Nano **10**, 7507 (2016).
- [6] M. Mleczko *et al.*, Science Adv. **3**, e1700481 (2017).
- [7] C. English *et al.*, Nano Lett. **16**, 3824 (2016).
- [8] C. English *et al.*, Proc. IEEE IEDM (2016).
- [9] K. Smithe *et al.*, Nano Lett. **18**, 4516 (2018).
- [10] E. Yalon *et al.*, Nano Lett. **17**, 3429 (2017).
- [11] S. Vaziri *et al.*, Science Adv. **5**, eaax1325 (2019).
- [12] C. Neumann *et al.*, Appl. Phys. Lett. **114**, 082103 (2019).
- [13] A. Sood *et al.* Nature Comm. **9**, 4510 (2018).

## 2D Materials for Nanoelectronics: Prospects and Materials Integration Challenges

R.M. Wallace

*Dept. of Materials Science and Engineering, Univ. of Texas at Dallas, USA*

*rmwallace@utdallas.edu*

The size reduction and economics of integrated circuits, captured since the 1960's in the form of Moore's Law, is under serious challenge. Current industry roadmaps reveal that physical limitations include reaching aspects associated with truly atomic dimensions, and the cost of manufacturing is increasing such that only 2 or 3 companies can afford leading edge capabilities. To address some of the "conventions," material's physical limitations, "2D materials" such as graphene, phosphorene, h-BN, and transition metal dichalcogenides have captured the imagination of the research community for advanced applications in nanoelectronics, optoelectronics, and other applications. [1,2] Among 2D materials "beyond graphene," some exhibit semiconducting behavior, such as transition-metal dichalcogenides (TMDs), and present useful bandgap properties for applications even at the single atomic layer level. Examples include "MX<sub>2</sub>", where M = Mo, W, Sn, Hf, Zr and X = S, Se and Te.

In addition to the potentially useful bandgaps at the monolayer thickness scale, the atomically thin layers should enable thorough electric field penetration through the channel, thus enabling superior electrostatic control. Further, with such thin layers, the integration with suitable gate dielectrics can result in a mobility enhancement. Applications "beyond CMOS" are also under exploration. From an interface perspective, the ideal TMD material may be expected to have a dearth of dangling bonds on the surface/interface, resulting in low interface state densities which are essential for efficient carrier transport. The ideal TMD materials have much appeal, but the reality of significant densities of defects and impurities will surely compromise the intrinsic performance of such device technologies. This presentation will examine the state-of-the-art of these materials in view of our research on semiconductor device applications, and the challenges and opportunities they present for electronic and optoelectronic applications. [3,4]

We will focus on our recent results examining the interfacial chemistry associated with contacts and Mo-based TMDs, and the influence of the deposition ambient in view of device applications. Results from our studies of metal depositions on MoS<sub>2</sub>, MoSe<sub>2</sub> and MoTe<sub>2</sub> will be discussed, where the interfacial reactions between various contact metals and the TMD surfaces depend critically on the deposition tool vacuum conditions and can lead to Fermi level pinning. [5-7].

**Acknowledgment.** This research was supported in part by the Semiconductor Research Corporation (SRC) NEWLIMITS Center and NIST through award number 70NANB17H041 and the Erik Jonsson Distinguished Chair at the University of Texas at Dallas.

[1] Z. Lin *et al.*, APL Mat. **6**, 080701 (2018).

[2] N. Briggs *et al.*, 2D Mat., **6**, 022001 (2019).

[3] S.J. McDonnell and R.M. Wallace, JOM **71**, 224-237 (2019).

[4] S.J. McDonnell and R.M. Wallace, Thin Solid Films, **616**, 482 (2016); and references therein.

[5] C.M. Smyth *et al.*, J. Phys. Chem. C, **120**, 14719 (2016).

[6] S.J. McDonnell *et al.*, ACS Appl. Mat. Interf. **8**, 8289 (2016).

[7] C.M. Smyth *et al.*, J. Phys. Chem. C, in press (2019).

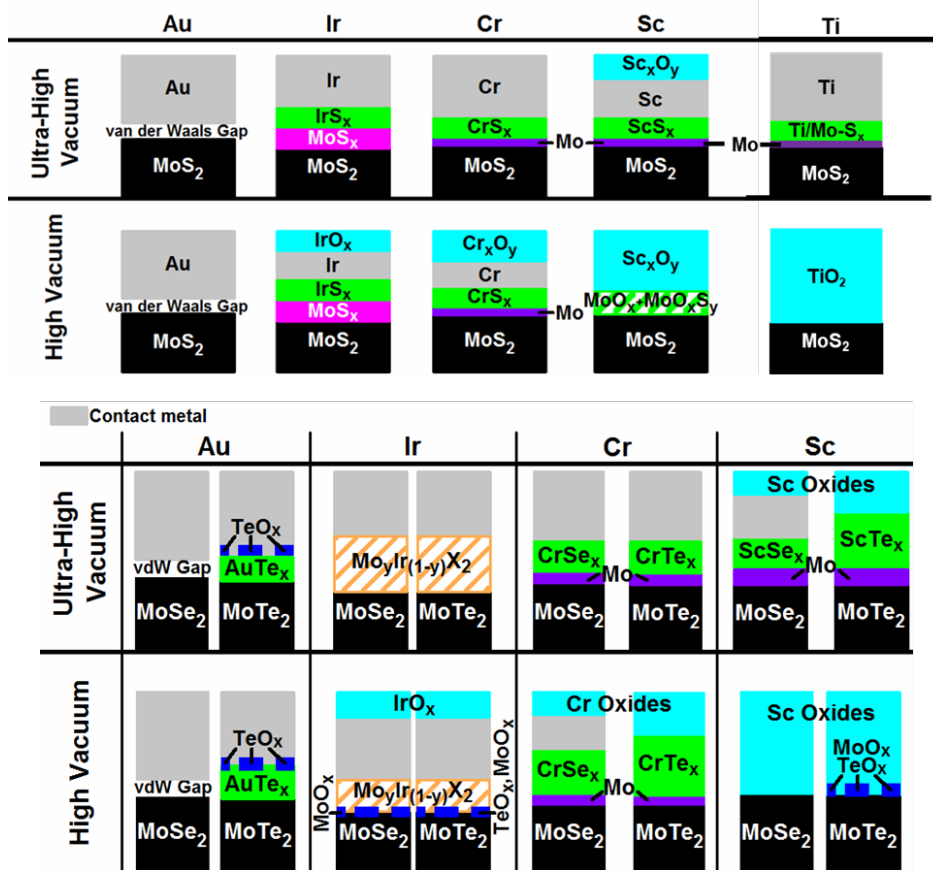


Fig. 1: Schematic of interfacial chemistry observed resulting from the metal contact deposition ambient on Mo-based TMDs. [After 5-7.]

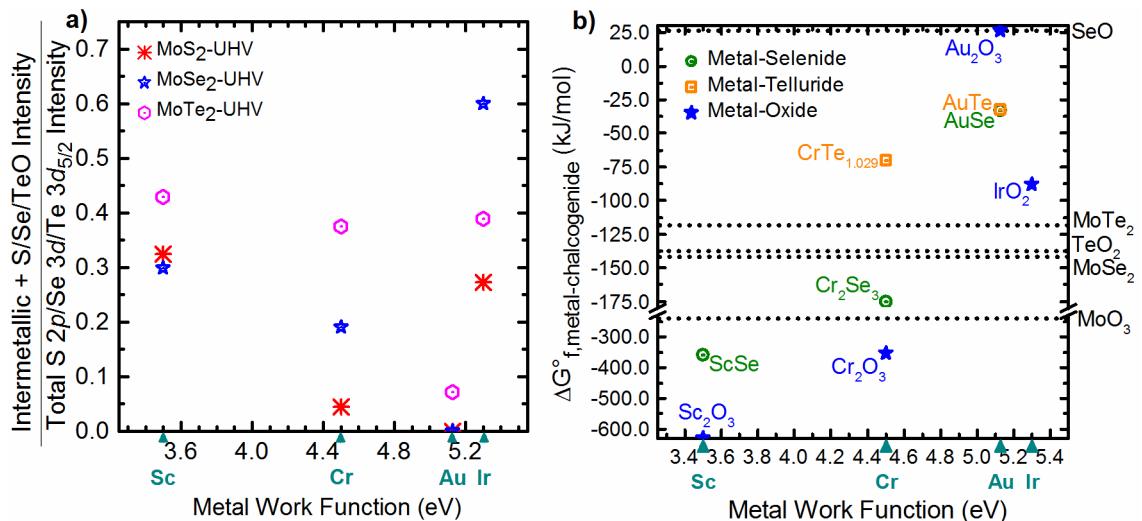


Fig. 2: Reactivity of the metal-TMD systems. The reactivity is gauged according to the XPS core peak intensity ratio of the contact metal-chalcogenide. These are plotted versus the Ir, Au, Cr, and Sc work functions for metal depositions in UHV (in-situ). b) A scatter plot showing the known Gibbs free energy for each metal chalcogenide alloy and relevant metal oxides as a function of metal vacuum work function. The specific compounds are listed on the plot. The dotted lines represent the  $\Delta G^{\circ}_f$  for MoSe<sub>2</sub>,  $\Delta G^{\circ}_f$  for MoTe<sub>2</sub>,  $\Delta G^{\circ}_f$  for MoO<sub>3</sub>,  $\Delta G^{\circ}_f$  for TeO<sub>2</sub>, and  $\Delta G^{\circ}_f$  for SeO. [From 7.]

## Gate-Dependent Valley Lifetimes in Monolayer WSe<sub>2</sub>

M. Ersfeld, L. Rathmann, F. Volmer, M. Heithoff, C. Stampfer, and B. Beschoten

*2nd Institute of Physics and JARA-FIT, RWTH Aachen University, 52074 Aachen, Germany*

*bernd.beschoten@physik.rwth-aachen.de*

Two-dimensional materials offer the possibility to address and to utilize the electron's valley degree of freedom. In this respect, a key question in the field of valleytronics is the actual valley-lifetime in transition metal dichalcogenides (TMDs): There is a huge discrepancy between experimentally measured lifetimes, which range from low nanosecond up to microsecond timescales, and ab-initio studies that predict electron-phonon limited valley lifetimes in the ps range [1]. Here, we report on gate-dependent valley lifetimes in monolayer WSe<sub>2</sub>, which are identified by the combination of time-resolved Kerr rotation (TRKR) and electrical transport measurements. Depending on the position of the Fermi level, we identify two distinct scattering mechanism of bright trions, which are created valley-selectively by a circularly polarized pump pulse. When tuning the Fermi level into either the conduction or the valence band, bright trions can scatter into dark states by inter-valley scattering and polarize the valleys after recombination. The amplitude of the resulting Kerr signal increases linearly with the gate-induced charge carrier density, whereas the valley lifetimes decrease as expected from both electron-phonon and spin-orbit scattering. On the other hand, the longest lifetimes in TRKR are seen when the Fermi level remains in the band gap indicating that the bright trions scatter into long-lived bound states. Our results demonstrate that TMDs are ideal hosts for long-lived localized spin states, on the one hand, and allow for nanosecond valley lifetimes of itinerant charge carries on the other hand.

[1] M. Ersfeld *et al.*, Nano Lett. **19**, 4083 (2019).

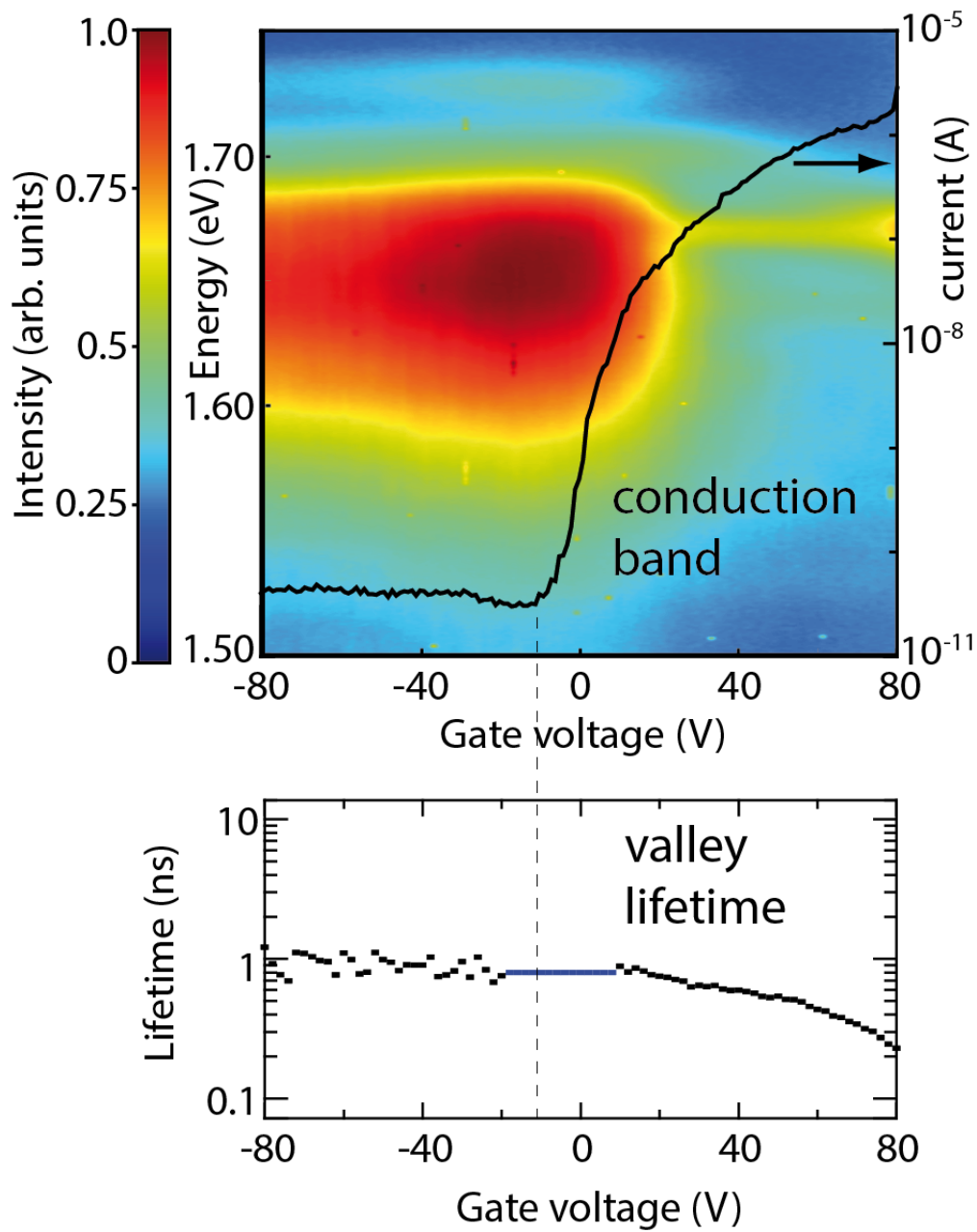


Fig.1: (top) Gate dependent photoluminescence characteristics of electrically contacted monolayer  $WSe_2$ . The device can be tuned into the conduction band as seen by the large increase of the source drain current above zero gate voltage. (bottom) The valley lifetimes as measured from time-resolved Kerr rotation are largest near the onset on the conduction band while they strongly decrease when tuning the Fermi level deeper into the conduction band.

## **Infrared Interband Photodetectors Based on Graphene/Black-AsP Heterostructures**

V. Ryzhii<sup>1</sup>, T. Otsuji<sup>1</sup>, M. Ryzhii<sup>2</sup>, V. Mitin<sup>3</sup>, and M. S. Shur<sup>4</sup>

<sup>1</sup>*Research Institute of Electrical Communication,  
Tohoku University, Sendai, Miyagi 980-8577, Japan*

<sup>2</sup>*Department of Computer Science and Engineering,  
University of Aizu, Aizu-Wakamatsu, Fukushima 965-8580, Japan*

<sup>3</sup>*Department of Electrical Engineering,  
University at Buffalo, SUNY, Buffalo, New York 1460-192, USA*

<sup>4</sup>*Department of Electrical, Computer, and Systems Engineering,  
Rensselaer Polytechnic Institute, Troy, New York 12180, USA*

*v-ryzhii@riec.tohoku.ac.jp*

We propose the infrared interband photodetectors with the graphene-layer (GL) sensitive element and the black-Phosphorus (b-P) or black Arsenic (b-As) barrier layers (BLs). These GL/BL-based infrared photodetectors (GBIPs) exploit the interband transitions from the GL sandwiched between the BLs. The GL serving as the GBIP base is n-doped (GL-base), whereas the GLs playing the roles of the emitter or collector are p-doped. The emitter and collector can also constitute p-doped bulk regions.

Since in b-P and b-As the energy barrier at the GL/BL interface for electrons  $E_C$  is smaller than that for holes  $E_V$  (approximately  $E_V = E_C/2$ ), the absorption of the infrared photons with the energy  $E$  in the range  $2E_V < E < 2E_C$  leads to the photoexcitation of only holes.

The GBIP operation is associated with the photocurrent created by the photoexcited holes propagating in the continuum states of the BLs valence band and the hole injection from the emitter stimulated by the GL-base charge variations enabling the photoconducting gain.

The GBIP can detect the photons with the energies in the range  $2E_G/3 < E < E_G$ , where  $E_G = E_V + E_C$  is the BL energy gap. Taking into account that  $E_G = 150$  meV in the b-As BLs and  $E_G = 300$  meV in the b-P BLs, the pertinent spectral range corresponds to  $100$  meV  $< E < 150$  meV and to  $200$  meV  $< E < 300$  meV for the GBIPs with the b-As and b-P BLs, respectively, i.e., to the far-infrared wavelength range (4 – 12) micrometers. A remarkable feature of the GBIPs is a substantial lowering of the dark current due to a partial suppression of the dark-current gain accompanied by a fairly high photoconductive gain. This results in the elevated values of the GBIP responsivity and detectivity. The GBIP can markedly surpass the quantum well and quantum dot infrared photodetectors, particularly at elevated temperatures, and can also compete with other far-infrared photodetectors.

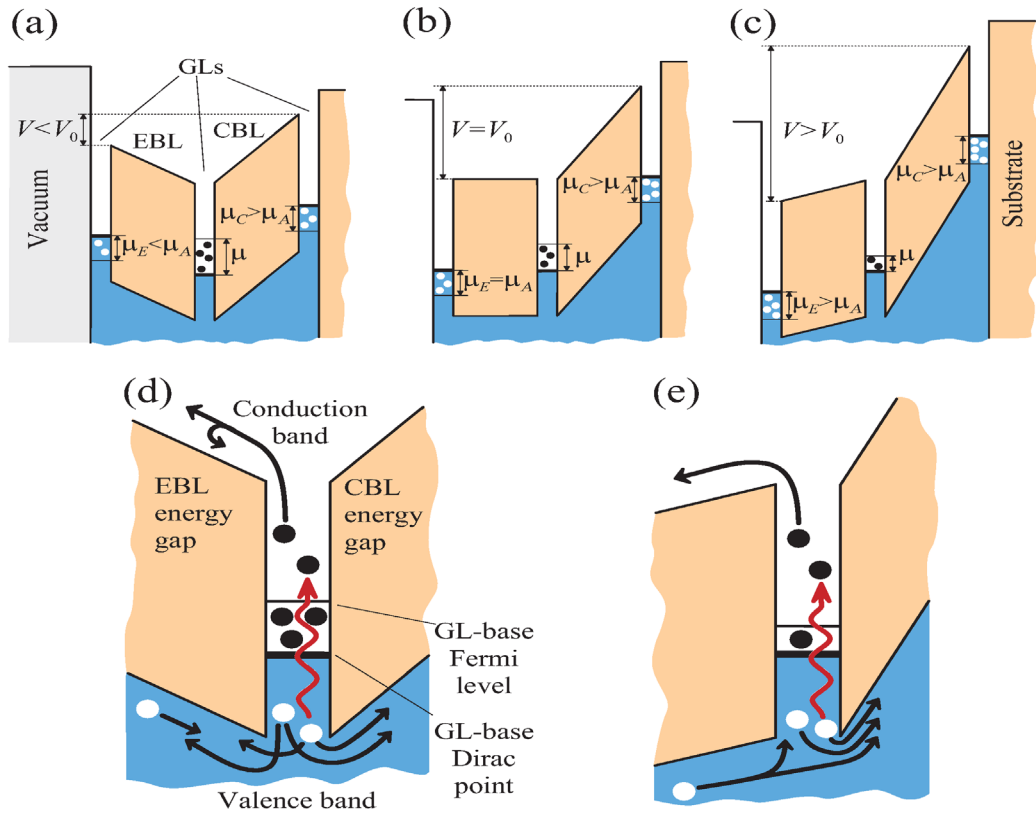


Fig.1: Schematic view of the band diagrams of QBIPs with the GL-base and the GL-emitter and collector at (a) bias voltage  $V$  smaller than the threshold voltage  $V_0$ , i.e.,  $V < V_0$ , (b)  $V = V_0$ , and (c)  $V > V_0$ . Panels (d) and (e) show enlarged fragments of (a) and (c). Arrows indicate the motion of holes (open circles) and electrons (opaque circles). Vertical wavy arrows indicated the radiative transitions with the excitation of holes into the continuum states of the BL valence band.

## Moire Superpotentials and Quantum Calligraphy of Single Photon Emitters in van der Waals Heterostructures

M.R. Rosenberger<sup>1a</sup>, H.-J. Chuang<sup>1b</sup>, C.K. Dass<sup>2</sup>, M. Phillips<sup>1a</sup>, S.V. Sivaram<sup>1a</sup>,  
K.M. McCreary<sup>1</sup>, C.S. Hellberg<sup>1</sup>, J.R. Hendrickson<sup>2</sup>, and B.T. Jonker<sup>1</sup>

<sup>1</sup>Naval Research Laboratory, Washington DC 20375, USA

<sup>2</sup>Air Force Research Laboratory, Wright-Patterson AFB, OH 45433, USA

<sup>a</sup>Postdoctoral associate at NRL through the National Research Council

<sup>b</sup>Postdoctoral associate at NRL through the American Society for Engineering Education  
*berry.jonker@nrl.navy.mil*

Single photon emitters (SPEs), or quantum emitters, are key components in a wide range of nascent quantum-based technologies. A solid state host offers many advantages for realization of a functional system, but creation and placement of SPEs are difficult to control. We describe here a novel paradigm for encoding strain into 2D materials to create and deterministically place SPEs in arbitrary locations with nanometer-scale precision [1]. We demonstrate the direct writing of SPEs in 2D semiconductors based on a materials platform consisting of a WSe<sub>2</sub> monolayer on a deformable substrate using an atomic force microscope nano-indentation process (Figures 1 and 2). This *quantum calligraphy* allows deterministic placement and real time design of arbitrary patterns of SPEs for facile coupling with photonic waveguides, cavities and plasmonic structures.

The weak interlayer bonding in van der Waals heterostructures (vdWh) enables one to rotate the layers at arbitrary azimuthal angles. For transition metal dichalcogenide vdWh, twist angle has been treated solely through the use of rigid-lattice moiré patterns. No atomic reconstruction has been observed to date, although reconstruction can be expected to have a significant impact on all measured properties, and its existence will fundamentally change our understanding of such systems. Here we demonstrate via conductive AFM and TEM that vdWh of MoSe<sub>2</sub>/WSe<sub>2</sub> and MoS<sub>2</sub>/WS<sub>2</sub> undergo significant atomic level reconstruction at twist angles  $\leq 1^\circ$  leading to discrete commensurate domains divided by narrow domain walls [2] (Figure 3), rather than a smoothly varying rigid-lattice moiré pattern as has been assumed in prior work. We show that this occurs because the energy gained from adopting low energy vertical stacking configurations is larger than the accompanying strain energy [3]. Such reconstruction impacts both the local conductivity and the optical properties.

[1] M.R. Rosenberger *et al.*, *ACS Nano* **13**, 904 (2019). DOI: 10.1021/acsnano.8b08730

[2] M.R. Rosenberger *et al.*, *under review* (2019).

[3] M. Phillips and C.S. Hellberg, *ArXiv190902495 Cond-Mat* (2019).

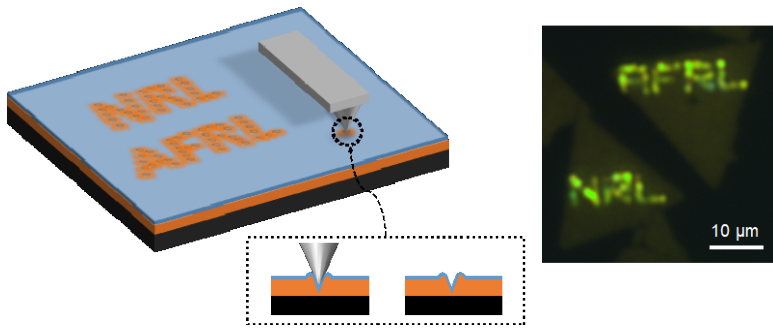


Fig.1: Schematic of an AFM tip indenting the TMD/polymer structure to introduce local strain, creating single photon emitters in any desired pattern. SPEs written to spell out “NRL” and “AFRL”.

Fig.2: Single photon emission occurs only from nano-indented spots in monolayer WSe<sub>2</sub> (left), and the second order auto-correlation function  $g^{(2)}(0) < 0.5$  confirms the SPE character of emission from selected nano-indentations (right).

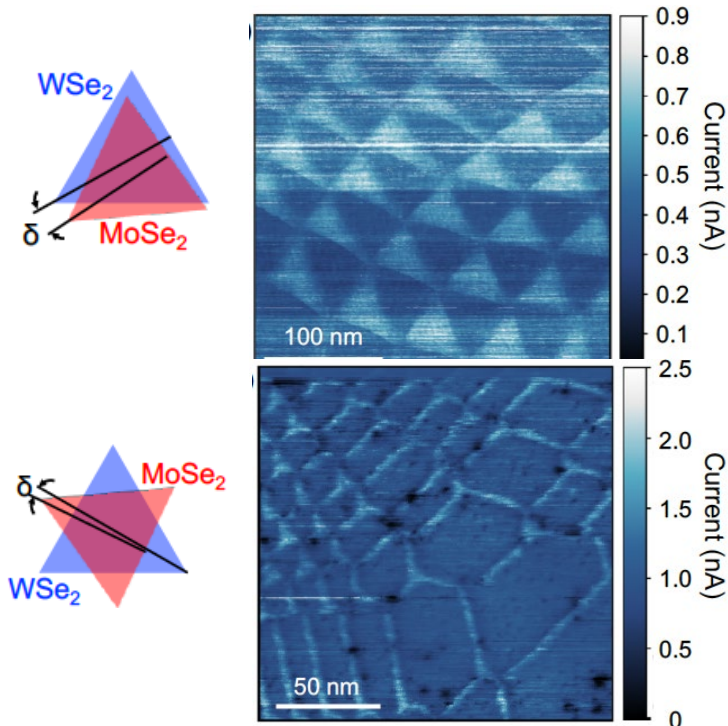
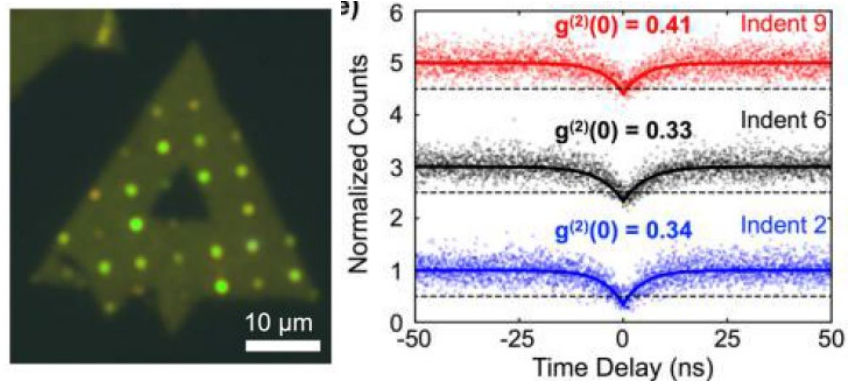


Fig.3: Conductive AFM images of a MoSe<sub>2</sub> / WSe<sub>2</sub> vdW heterostructure for samples with a 1 degree azimuthal offset from 0 degree alignment (top panel) and 60 degree alignment (bottom panel) showing pronounced triangular and hexagonal domains of atomic reconstruction, respectively.

## **Cyclotron Resonance Absorption of Mid-Infrared Light in van der Waals Heterostructures of Graphene and 2D Materials**

T. Machida<sup>1,2</sup>, R. Moriya<sup>1</sup>, M. Onodera<sup>1</sup>, K. Kinoshita<sup>1</sup>, Y. Wakafuji<sup>1</sup>,  
S. Park<sup>1</sup>, S. Masubuchi<sup>1</sup>, K. Watanabe<sup>3</sup>, and T. Taniguchi<sup>3</sup>

<sup>1</sup>*Institute of Industrial Science, University of Tokyo, Tokyo 153-8505, Japan*

<sup>2</sup>*CREST, Japan Science and Technology Agency, Tokyo 102-0076, Japan*

<sup>3</sup>*National Institute for Materials Science, Ibaraki 305-0044, Japan*

*tmachida@iis.u-tokyo.ac.jp*

Charge carriers in graphene, massless Dirac fermions, form a unique sequence of the Landau levels in high magnetic fields. Thus, the cyclotron resonance (CR) in graphene is distinctly different from that in conventional two-dimensional electron systems based on semiconductors. In this work, we study the photovoltaic effect induced by CR absorption of mid-infrared light in van der Waals heterostructures of graphene and 2D materials, fabricated using the robotic transfer technique [1,2] and the PPC dry-transfer technique [3]: (i) Photovoltaic effect induced by photo-Seebeck effect in graphene [4], (ii) Photovoltaic effect induced by photo-Nernst effect in graphene [5], (iii) Electrical control of CR magnetic field in dual-gated TLG [6], (iv) Photo-induced thermionic emission at the graphene/MoS<sub>2</sub> van der Waals Schottky junction [7].

[1] S. Masubuchi *et al.*, *Nature Commun.* **9**, 1413 (2018).

[2] S. Masubuchi and T. Machida, *npj 2D Mat. Appl.* **3**, 4 (2019).

[3] K. Kinoshita *et al.*, *npj 2D Mat. Appl.* **3**, 22 (2019).

[4] K. Kinoshita *et al.*, *Appl. Phys. Lett.* **113**, 103102 (2018).

[5] K. Kinoshita *et al.*, *Appl. Phys. Lett.* **115** (in press).

[6] M. Onodera *et al.* (submitted).

[7] Y. Wakafuji *et al.*, *Appl. Phys. Lett.* **115** (in press).

## **Spatially Selective Enhancement of Photoluminescence in MoS<sub>2</sub> by Exciton-Mediated Adsorption and Defect Passivation**

S. Sivaram<sup>1,#</sup>, A. Hanbicki<sup>1,2</sup>, M. Rosenberger<sup>1,#</sup>, G. Jernigan<sup>1</sup>,  
H.-J. Chuang<sup>1,%</sup>, K.M. McCreary<sup>1</sup>, and B.T. Jonker<sup>1</sup>

<sup>1</sup>*U.S. Naval Research Laboratory, Washington, DC, USA*

<sup>2</sup>*Laboratory for Physical Sciences, College Park, MD, USA*

<sup>#</sup>*National Research Council Postdoctoral Fellow*

<sup>%</sup>*American Society of Engineering Education Postdoctoral Fellow*

*kathleen.mccreary@nrl.navy.mil*

Monolayers of transition metal dichalcogenides (TMDs) are promising components for flexible optoelectronic devices due to their direct band gap and atomically thin nature. The photoluminescence (PL) from these materials is often strongly suppressed by non-radiative recombination. Here, we demonstrate up to a 200-fold increase in PL intensity from monolayer MoS<sub>2</sub> synthesized by chemical vapor deposition (CVD) following a controlled exposure to laser light in ambient. This spatially resolved passivation treatment is air and vacuum stable. A wavelength dependent study confirms that the brightening mechanism requires exciton generation in the MoS<sub>2</sub>, as laser light below the optical band gap fails to produce any enhancement in the PL. We highlight the photo-sensitive nature of the process by successfully brightening with a low power broadband white light source (< 10 nW). We decouple changes in absorption from defect passivation by examining the degree of circularly polarized PL. This measurement confirms that laser brightening reduces the rate of non-radiative recombination in the MoS<sub>2</sub>. A series of gas exposure studies demonstrate a clear correlation between PL brightening and the presence of water. We propose that H<sub>2</sub>O molecules passivate sulfur vacancies in the CVD-grown MoS<sub>2</sub>, but require photo-generated excitons to overcome a large adsorption barrier. This work represents an important step in understanding the passivation of CVD- synthesized TMDs and demonstrates the interplay between adsorption and exciton generation [1].

[1] S.V. Sivaram *et al.*, ACS Appl. Mater. Interfaces **11**, 16147 (2019).

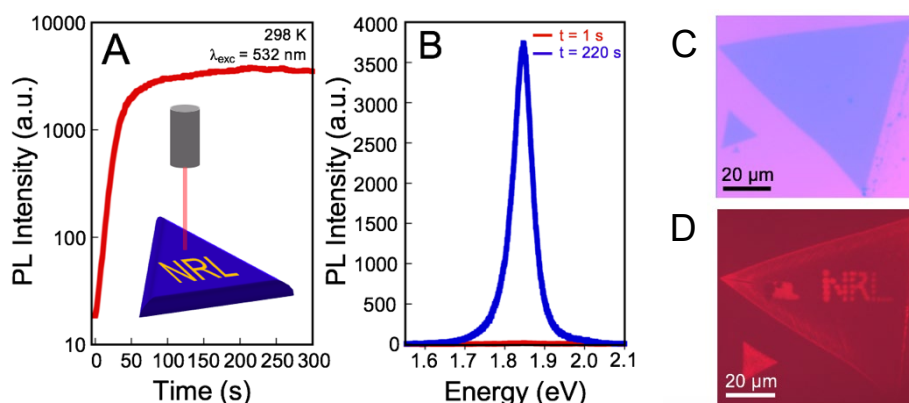


Fig.1: Laser brightening of 1L MoS<sub>2</sub> in air. (A) Photoluminescence intensity as a function of laser exposure time. Semi-log plot shows orders of magnitude increase in PL over a five-minute exposure. Acquisition time is 1 second and spectra are recorded every 2 seconds. Inset: Cartoon illustrates spatially-controlled brightening of an MoS<sub>2</sub> triangle. (B) Plot of spectra acquired at 1 and 220 seconds demonstrates 200x increase in PL intensity. (C) Optical image of MoS<sub>2</sub> after laser brightening in air. Scale bar, 20 μm. (D) Fluorescence image shows brightened regions displaying the letters “NRL.” Scale bar, 20 μm.

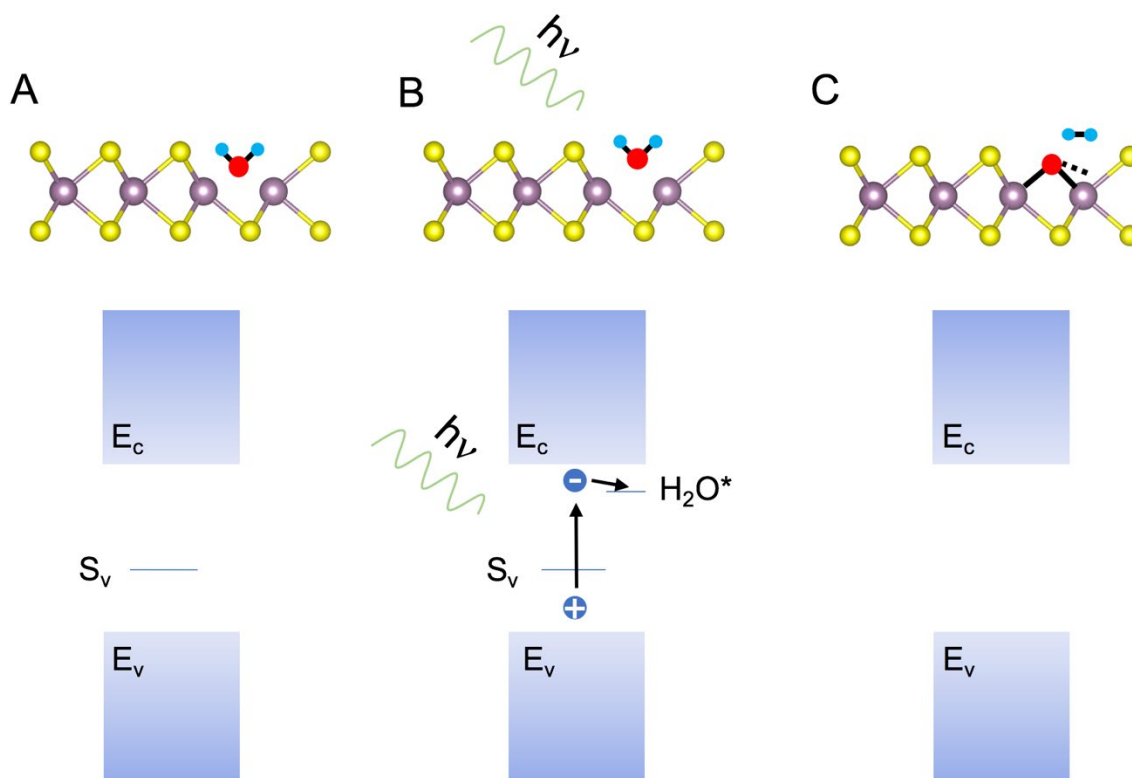


Fig.2: Proposed mechanism for MoS<sub>2</sub> defect passivation. (A-top) Schematic side view of MoS<sub>2</sub> with an H<sub>2</sub>O molecule physisorbed at a sulfur vacancy. (A-bottom) Simple energy diagram showing the conduction band edge ( $E_c$ ), valence band edge ( $E_v$ ), and sulfur vacancy ( $S_v$ ). In the physisorbed state, the H<sub>2</sub>O molecule does not passivate the  $S_v$  defect which acts as a site for non-radiative carrier recombination. (B) Illustration of photon mediated passivation. Incoming light above the optical band gap creates a highly bound exciton which interacts with the physisorbed H<sub>2</sub>O molecule by means of an empty antibonding orbital (H<sub>2</sub>O\*). (C) The exciton-mediated dissociation of H<sub>2</sub>O results in O atom (red) with a valency of -2 bonded to the sulfur vacancy in a trigonal pyramid configuration. The H<sub>2</sub> molecule (blue) desorbs from the surface. This bonding passivates the MoS<sub>2</sub> and removes the mid-gap sulfur vacancy.

## On the Reliability of Back-Gated MoS<sub>2</sub> Field-Effect Transistors

C. Marquez<sup>1,2</sup>, N. Salazar<sup>1</sup>, F. Gity<sup>2</sup>, C. Navarro<sup>1</sup>, G. Mirabelli<sup>2</sup>, R. Duffy<sup>2</sup>, J.C. Galdon<sup>1</sup>,  
P. Hurley<sup>2</sup>, and F. Gamiz<sup>1</sup>

<sup>1</sup>*Nanoelectronics Research Group (CITIC-UGR), Department of Electronics,  
University of Granada, 18071, Granada, Spain*

<sup>2</sup>*Nanoelectronic Materials and Devices Group, Tyndall National Institute,  
University College Cork, T12 R5CP, Cork, Ireland*  
*carlosmg@ugr.es*

Due to the reduced thickness, two-dimensional (2-D) materials have been proposed for an optimal electrostatic control of the channel providing better immunity to short channel effects than the planar silicon counterparts [1]. Among the 2D materials family, the transition metal dichalcogenides (TMDs) and specially molybdenum disulfide (MoS<sub>2</sub>) present surprising electrical properties such as high mobilities, very high ON/OFF ratios, large transconductance and current carrying capabilities [2]. In fact, according to the International Roadmap for Devices and Systems (IRDS) guideline [3], TMDs devices present advantages in terms of higher ON/OFF ratios, enabling reduced power consumption, current leakage and good switching delay with respect to silicon devices. However, the experimental results rarely accomplish the promising theoretical properties for these 2D materials and, despite the advances on reliability characterization [4]–[6], defects and impurities (grain boundaries, corrugation, sulfur vacancies, oxygen incorporation, moisture molecules and oxide ions) still play an important role on the actual drop in performance of the fabricated devices (Schottky barriers and current hysteresis). In this work, we study several reliability implications on back-gated MoS<sub>2</sub> transistors fabricated following a chemical vapor deposition synthesis and a standard CMOS optical lithography and etching processing. Figure 1 depicts the Raman characterization exhibiting the two Raman characteristic bands at 387 (E<sub>2g</sub><sup>1</sup>) and 410 cm<sup>-1</sup> (A<sub>1g</sub>) consistent with the presence of thin MoS<sub>2</sub> layers. Inset shows the scanning electron microscope (SEM) characterization after the lithography and etching processing of the back-gated transistors. Devices with different lengths and widths were fabricated. The drain current-voltage (I<sub>D</sub>-V<sub>D</sub>) characteristic is depicted as a function of the back gate bias (V<sub>BG</sub>) in Figure 2. The nonlinear nature of the curves can be explained by the formation of back-to-back Schottky diodes in the metal-semiconductor interfaces (metal Fermi level pinning due to the presence of defects). Figure 3 shows the transfer characteristic (I<sub>D</sub>-V<sub>BG</sub>) of one of the fabricated devices with current ratios around 10<sup>8</sup>. The observed hysteresis cycle suggests the presence of defects at the MoS<sub>2</sub>-SiO<sub>2</sub> interface which trap and detrapp carriers. To further analyze these trap mechanisms, low-frequency characterization of these devices is presented in Figure 4.

Characteristic flicker noise with  $1/f$  dependence is observed attributing the noise to number of carrier fluctuations. These results are also supported by capacitance-voltage (CV) analyses, low temperature measurements and  $I_D$ -time characteristics.

- [1] M. Chhowalla *et al.*, Nat. Rev. Mater. **1**, 16052 (2016).
- [2] K. Alam *et al.*, IEEE Trans. Electron Dev. **59**, 3250 (2012).
- [3] ITRS, “International Technology Roadmap for Semiconductors” (2017).
- [4] A. Di Bartolomeo *et al.*, Adv. Funct. Mater. **28**, 1800657 (2018).
- [5] Y.Y. Illarionov *et al.*, 2D Mater. **3**, 035004 (2016).
- [6] P. Zhao *et al.*, ACS Appl. Mater. Interf. **9**, 24348 (2017).

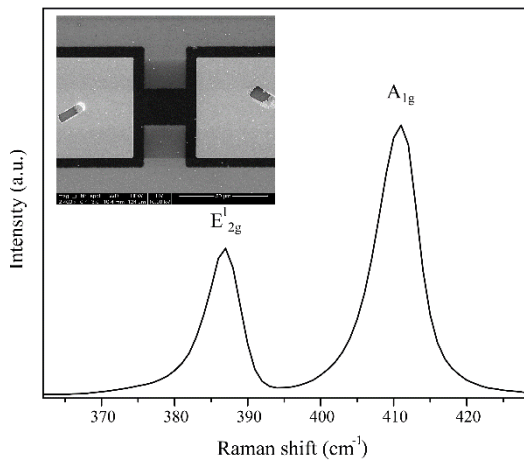


Fig.1: Raman characteristic of  $\text{MoS}_2$  on  $\text{SiO}_2$  substrate. Inset: SEM image of a  $L=25\mu\text{m}$  and  $W=20\mu\text{m}$  back-gated transistor.

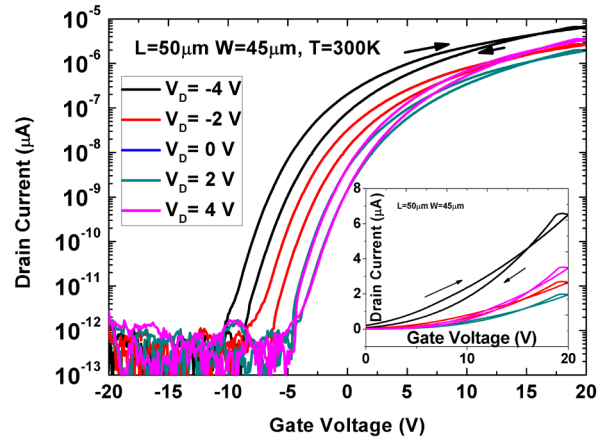


Fig.3:  $I_D$ - $V_G$  of a back-gated device as a function of  $V_D$ . Hysteresis cycle is observed due to defects presence at the interface. Inset: zoom-in showing a unusual crossing point in the current during the hysteresis cycle.

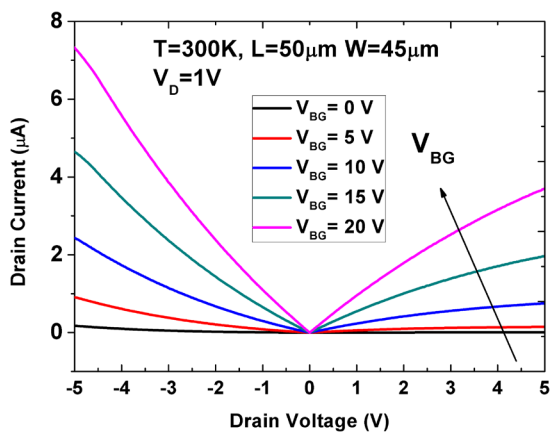


Fig.2: Output characteristic of a  $L=50\mu\text{m}$  and  $W=45\mu\text{m}$  back-gated device as a function of  $V_{GB}$ . Asymmetrical behavior attributed to back-to-back Schottky barriers is observed.

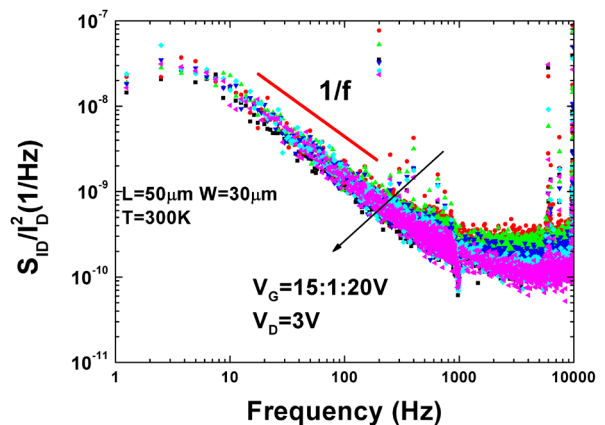


Fig.4: Normalized spectral noise density of the current as a function of the frequency for a  $L=50\mu\text{m}$  and  $W=45\mu\text{m}$  back-gated device. Flicker noise following a  $1/f$  trend is observed.

## **sSNOM Multimodal Imaging of 2D Polar Metals**

S.V. Rotkin<sup>1</sup>, X. Li<sup>1</sup>, N. Briggs<sup>2</sup>, B. Bersch<sup>2</sup>, A. de la Fuente Duran<sup>2</sup>, and J. Robinson<sup>2</sup>

<sup>1</sup>*Materials Research Institute, Department of Engineering Science & Mechanics,  
The Pennsylvania State University, University Park, PA 16802, USA*

<sup>2</sup>*Materials Research Institute, Department of Materials Science and Engineering,  
The Pennsylvania State University, University Park, PA 16802, USA*

*rotkin@psu.edu*

Plasmonic properties will be discussed for newly discovered class of 2-dimensional materials: one-to-few monolayer thick 2D polar metals (2D-PMet) synthesized using confinement heteroepitaxy (CHet)<sup>1-3</sup>. When metal is confined between the SiC substrate and epi-graphene formed on the top of it by thermal sublimation, it is epitaxial to both substrate and graphene layer(s). Because of natural non-uniformities of SiC/graphene confinement structure, the optical properties of 2DPMet are modulated at the ultimate scale of (a few) nanometers, and a characterization technique capable of taking the optical response at a similar spatial resolution is required. Scattering-type scanning near-field optical microscope (sSNOM) allowed us to reveal the mid-infrared (MIR) surface impedance features of the 2D-Ga and In-layers covered with a bilayer/few layer epi-graphene. Both 2D-Ga and In have extremely large optical contrast due to high density of states of PMets, resulting in ultimate light-matter interactions within an atomic-thin layer. Figs.1-2 show typical images taken in 4 channels: AFM z-profile, AFM phase, sSNOM second harmonic,  $S_2$ , amplitude and phase. Correlation of multiple channels, acquired simultaneously, allows to establish structure-property relations for PMets. sSNOM data has been analyzed with two novel algorithms: impedance clustering (revealing metal encapsulation) and photonic decay curves (via 3D sSNOM mapping).

[1] Z.Y. Al Balushi *et al.*, *Nat Mater* **15**, 1166 (2016).

[2] N. Briggs *et al.*, *arXiv preprint* arXiv:1905.09962 (2019).

[3] B. Bersch *et al.*, *arXiv preprint* arXiv:1905.09938 (2019).

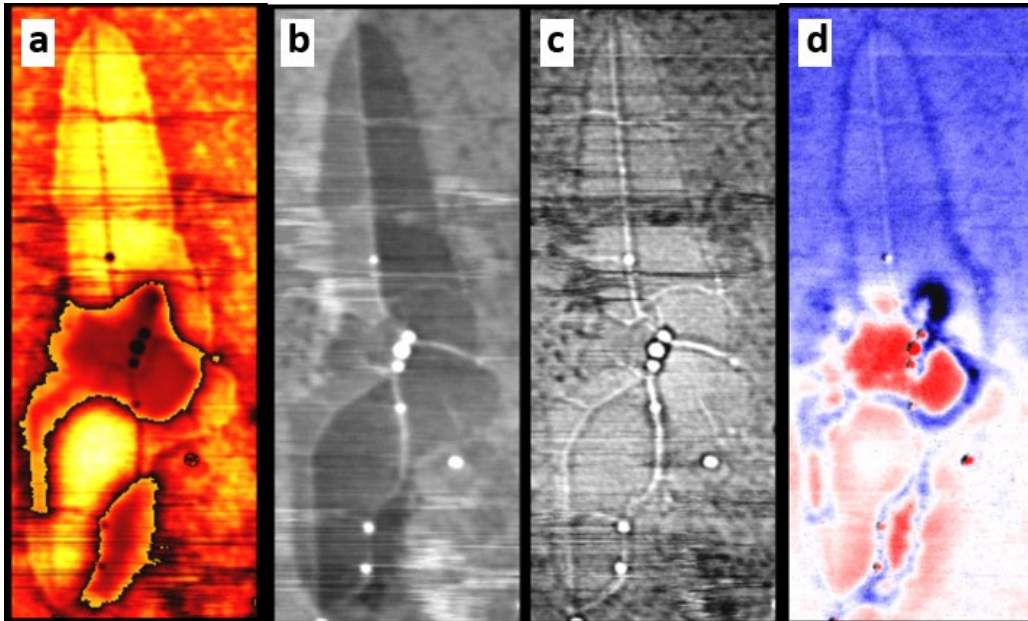


Fig.1: sSNOM image of graphene encapsulated 2D-In layers. (a)  $S_2$ -amplitude, (b) topography, (c) AFM-phase, (d)  $S_2$ -phase. Image size:  $0.8 \mu\text{m} \times 2 \mu\text{m}$ . Excitation wavelength:  $6.33 \mu\text{m}$ . Resolution (pixel size):  $2 \text{nm}$ .

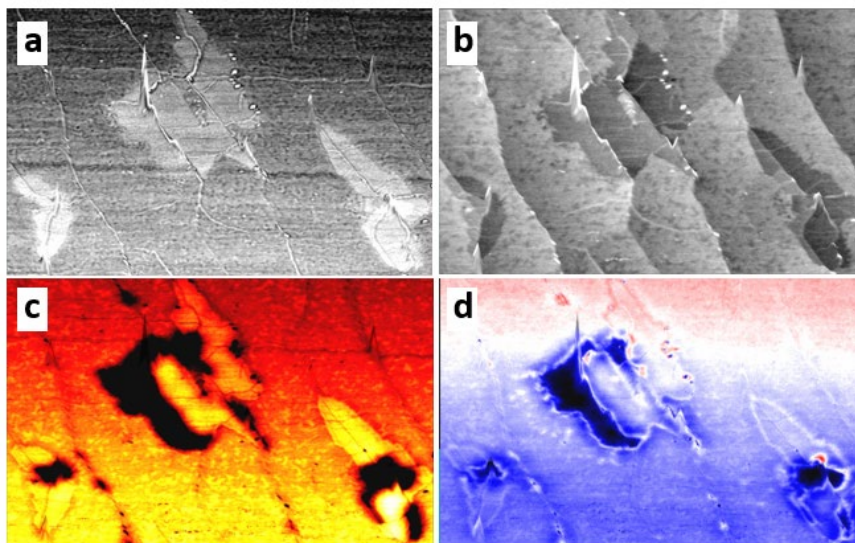


Fig.2: sSNOM image of graphene encapsulated 2D-In layers. (a) Topography, (b) AFM-phase, (c)  $S_2$ -amplitude, (d)  $S_2$ -phase. Image size:  $2.8 \mu\text{m} \times 4 \mu\text{m}$ . Excitation wavelength:  $6.33 \mu\text{m}$ . Resolution (pixel size):  $2 \text{nm}$ .

## Molecular Dynamics Analysis of Effect of Dissolved Hydrogen on Deformation Behavior in Ni-based Superalloys

H. Yanagisawa<sup>1</sup>, C. Liu<sup>1</sup>, Q. Chen<sup>1</sup>, Y. Wang<sup>2</sup>, N. Miyazaki<sup>1</sup>, Y. Ootani<sup>1</sup>,  
N. Ozawa<sup>1</sup>, and M. Kubo<sup>1</sup>

<sup>1</sup>*Institute for Materials Research, Tohoku University, Sendai, Miyagi 980-8577, Japan*

<sup>2</sup>*Division of Mechanical Engineering, Tohoku University, Sendai, Miyagi 980-8579, Japan*  
*honami.yanagisawa@imr.tohoku.ac.jp*

Ni-based superalloys are excellent in high-temperature strength and corrosion resistance, and used for high-temperature and high-pressure part in steam turbines. However, there is a problem that Ni-based superalloys degrade due to stress corrosion cracking in the high-temperature and high-pressure water environment. Therefore, in this study, we focused on stress corrosion cracking caused by intruded hydrogen, and investigated the effect of dissolved hydrogen on the deformation behavior of Ni-based superalloys by the reactive molecular dynamics simulation. In order to reproduce the microstructure of Ni-based superalloys, the Ni<sub>3</sub>Al supercell (35 × 35 × 35 unit cells of Ni<sub>3</sub>Al) was placed in a Ni supercell (40 × 40 × 40 unit cells of Ni). Then, hydrogen atoms were located in the Ni-based superalloy model based on the method of Ref. [1]. The constructed large-scale model was 2,090,957 atoms. In addition, the pre-crack was generated and water molecules were put on the surface of the large-scale model (Fig. 1). To investigate the deformation behavior, the tensile stress was applied to this model along the z direction at a temperature of 1000 K. For comparison, the tensile simulation in the vacuum environment (without water and dissolved hydrogen) was performed at the same conditions. Fig. 2 shows snapshots at strains of 0% and 10%. In the vacuum environment, the pre-crack expanded about 10 Å along the z direction, but almost no change along the x direction was observed. In the water environment, on the other hand, the pre-crack expanded about 7 Å and 10 Å along the x and z directions, respectively. This indicates that the pre-crack progressed along the depth direction by the tensile stress in the water environment. In addition, the crystal structure was analyzed to examine the details of the deformation behavior (Fig. 3). In the crystal, a part of the Ni-based superalloy model changed from the FCC structure to the HCP structure along the direction of 45 degrees to the surface. By the local structural type analysis, stacking faults of the HCP structure were generated after partial dislocation movement along with <1 1 1> plane in the FCC crystal. Also, the volume fraction of the HCP structure was 4.1% in the vacuum environment and 6.9% in the water environment. Therefore, it is suggested that the deformation behavior of Ni-based superalloys is changed by the motion of partial dislocations, which is caused by water and dissolved hydrogen.

[1] J. Song and W.A. Curtin, *Acta Mater.* **59**, 1557 (2011).

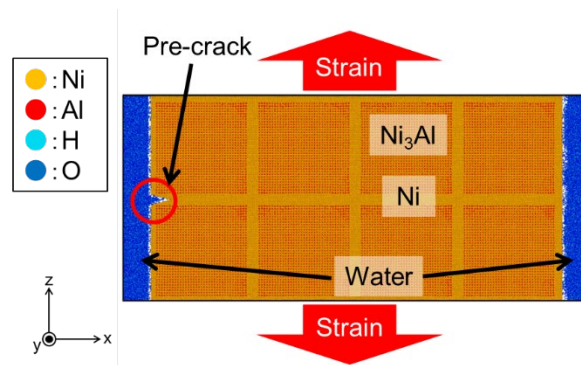


Fig.1: The large-scale model with the pre-crack and water molecules

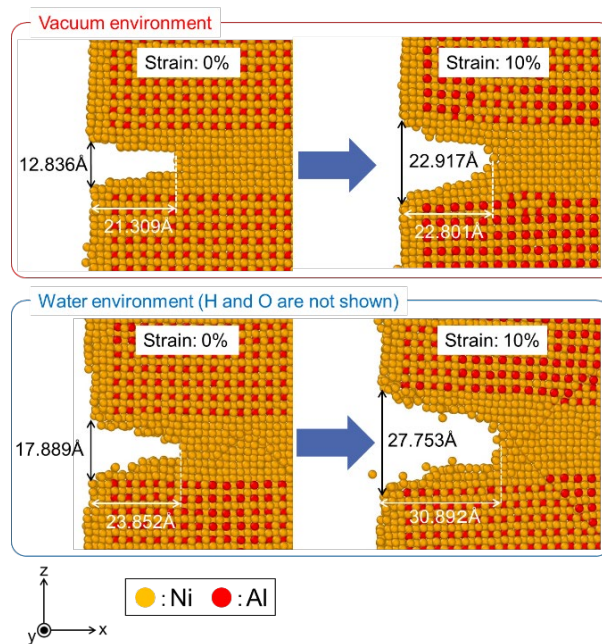


Fig.2: Crack propagation behaviors around the pre-crack

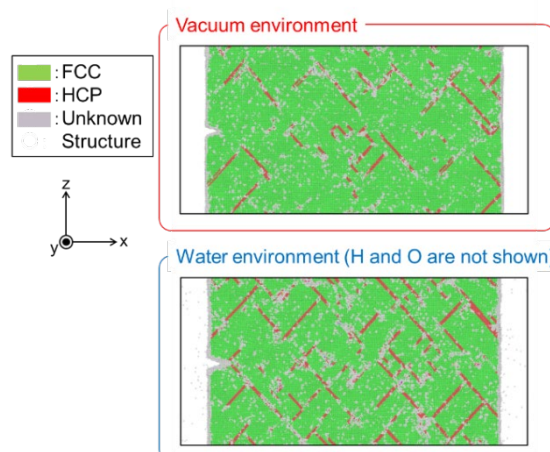


Fig.3: Snapshots colored by atomic structure type after failure at strain of 10%

## **Large-scale Molecular Dynamics Simulations on Chemical Mechanical Polishing Process of AlN Substrate with Nanobubbles**

S. Kimura<sup>1</sup>, W. Yang<sup>1,2</sup>, N. Miyazaki<sup>1</sup>, Y. Ootani<sup>1</sup>, N. Ozawa<sup>1</sup>, and M. Kubo<sup>1</sup>

<sup>1</sup>*Institute for Materials Research, Tohoku University, Sendai, Miyagi 980-8577, Japan*

<sup>2</sup>*Department of Mechanical Systems Engineering, Graduate School of Engineering, Tohoku University, Sendai, Miyagi 980-8579, Japan*

*souta.kimura@imr.tohoku.ac.jp*

Chemical mechanical polishing(CMP) is used to planarize the surface of aluminum nitride(AlN). However, there is a problem that the polishing rate of a nitride semiconductor substrate by CMP is remarkably low. It has been reported that the introduction of nanobubbles into CMP improves polishing rate. In our previous study, we clarified the structural changes of the AlN substrate and the oxidation process of the substrate by simulating the collapse of nanobubbles on the AlN substrate. However, since only one nanobubble could be considered in the previous small model, it was insufficient to examine the effect of the conditions such as the size, density, and number of nanobubbles on the CMP process of the AlN substrate. Therefore, in this study, we performed molecular dynamics collapse simulations of multiple nanobubbles using a large-scale model, and examined the effect of multiple nanobubbles on the CMP process of an AlN substrate.

In this simulation, firstly, the AlN(0001) substrate was terminated with OH groups and water molecules were located over the substrate because the CMP is performed in water environment. Next, nanobubbles were created by spherically removing the water molecules within a certain radius in the cell. In order to elucidate the influence of multiple nanobubble collapse phenomenon on a polishing rate of CMP process of the AlN substrate, we compared collapse simulations of one nanobubble and five nanobubbles (Fig. 1). Figs. 2 and 3 show the velocity distributions in the z-axis direction and the substrate structures after nanobubble collapse. The simulation of one nanobubble greatly deformed the center of the substrate, while the simulation of five nanobubbles deformed the substrate uniformly (Figs. 2 (b) and 3 (d)). Fig. 4 shows average velocity of jet flow. One nanobubble has a large velocity in the center, and a five nanobubbles has a small velocity overall. When one large nanobubble is introduced, the substrate is greatly deformed, but the range is small. When five small nanobubbles are introduced, the substrate is deformed over a wide range, but the deformation is small. It was suggested that there is optimal size and density of nanobubbles for the effective deformation and enough flatness of AlN substrate.

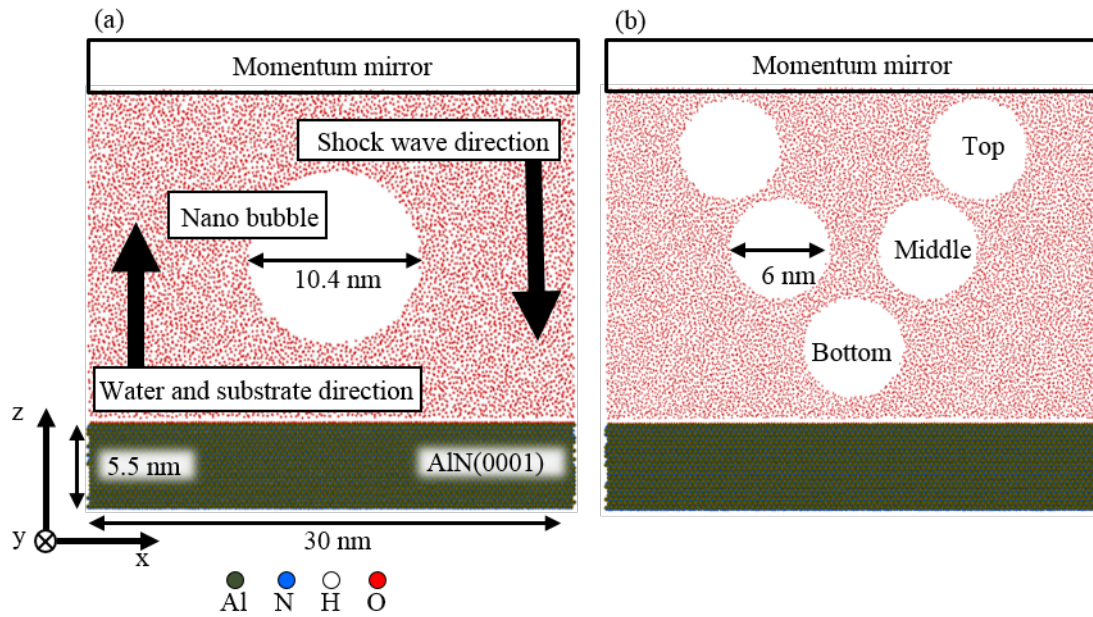


Fig.1: Simulation models of (a) 1 nano bubble and (b) 5 nano bubbles collapse on the AlN(0001) substrate.

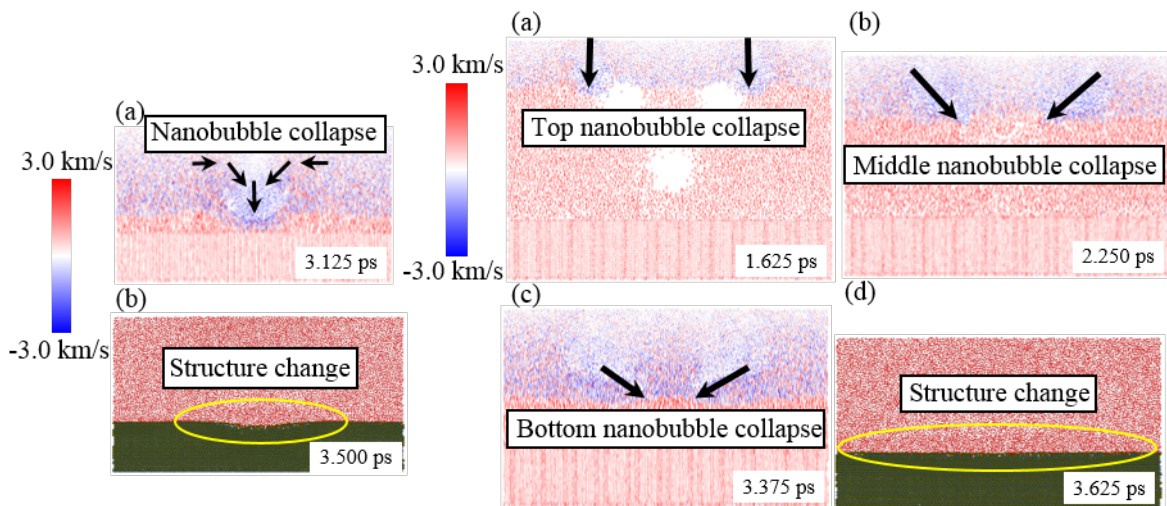


Fig.2: (a) Velocity distribution in the z-axis direction for 1 nano bubble collapse simulation and (b) Substrate structure after nanobubble collapse.

Fig.3: Velocity distribution in the z-axis direction for 5 nano bubbles collapse simulation at (a) 1.625, (b) 2.250, and (c) 3.375 ps. (d) Substrate structure after nanobubble collapse.

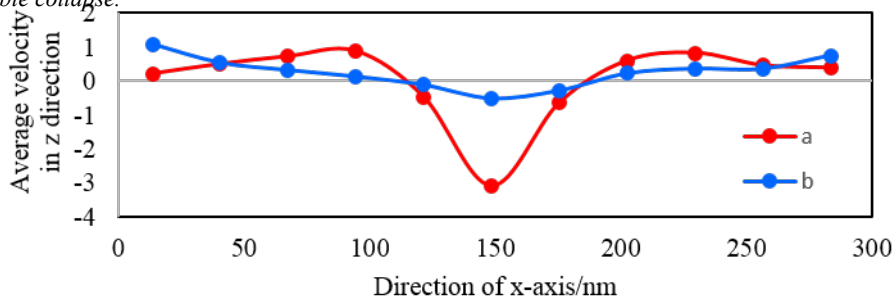


Fig.4: Average velocity of jet flow: (a) 1 nano bubble and (b) 5 nano bubbles collapse on the AlN(0001) substrate.

## **AlGaN-Based UV Light-Emitting Diodes Using Nickel-Doped Aluminum Zinc Oxide Electrodes**

T.H. Park, T.H. Lee, M.S. Chae, and T.G. Kim

*School of Electrical Engineering, Korea University,*

*145 Anam-ro, Seongbuk-gu, Seoul 02841, Republic of Korea*

*tgkim1@korea.ac.kr*

Metal oxide-based thin-film electrodes such as indium tin oxide (ITO) and aluminum zinc oxide (AZO) have been widely studied for their applications to various optoelectronic devices including wide-bandgap light-emitting diodes (LEDs). However, despite this vibrant research, it was difficult to fabricate thin electrode films with low sheet resistance as well as high transparency because these two quantities are mutually contradictory with respect to film thickness.[1,2] A simple way to reduce the resistance is to dope such a film with proper dopants. However, this doping process increases transmittance losses in the film.

In this study, we introduce a new doping method via electrical pumping to achieve low-resistant ( $100 < \Omega/\text{sq}$ ) thin film electrodes with ultra-high transmittance ( $> 90\%$ ). The doping process is conducted by injection of metallic ions from the top electrode into target films (IZO, AZO) through the sacrificial layer (AlN) under an electric field. Then, the Ni-doped thin films are used as p-type TCOs for 365 nm UV LEDs, exhibiting much better optical properties than standard LEDs with 100 nm ITO and AZO electrodes. Figure 1 a-d show a structure of the lateral AlGaN-based 365-nm UV LED with AZO as p-type electrode, typical light output power–current–voltage characteristics, electroluminescence spectra as a function of wavelength (at 100 mA), and microscopic light emission photographs at 20 mA (low current) and 50 mA (high current), respectively, measured for UV LEDs using the reference 150 nm AZO film and the Ni-doped 30 nm and 50 nm AZO films, as an example. More details including the performance of UV LEDs with different thin film (i.e., doped-graphene and ultra-thin ITO) electrodes will be presented at the conference.

[1] Z. Yu *et al.*, *Adv. Mater.* **23**, 3989 (2011).

[2] M. Chae *et al.*, *Nanoscale Horiz.* **4**, 610 (2019).

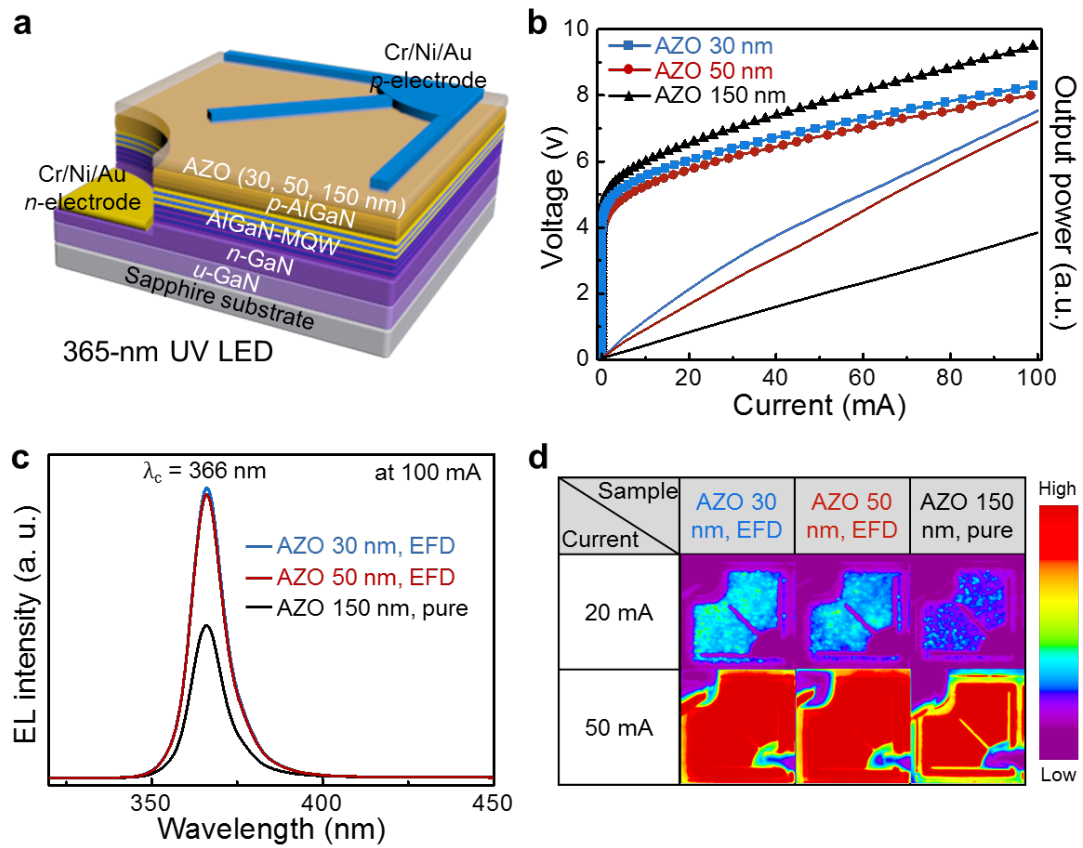


Fig.1: a) Structure of the lateral AlGaIn-based 365-nm UV LED with AZOs as p-type TCEs. b) Typical light output power-current-voltage characteristics of UV LEDs using the reference 150 nm AZO film and the Ni-filament doped 30 nm and 50 nm AZO films. c) Electroluminescence spectra as a function of wavelength measured for each of the LEDs at 100 mA. (d) Microscopic light emission photographs measured at 20 mA (low current) and 50 mA (high current). The linear color scale shows the relative intensity of the emission distribution.

## Electrical Properties of HfO<sub>2</sub> Formed on the p-type Si<sub>1-x</sub>Ge<sub>x</sub> Pretreated with H<sub>2</sub>S Annealing

W. Lee<sup>1</sup>, C. Lee<sup>1</sup>, J. Kim<sup>1</sup>, J. Lee<sup>1</sup>, D. Eom<sup>1</sup>, J. Park<sup>2</sup>, D. Kim<sup>2</sup>, T. Park<sup>2</sup>, and H. Kim<sup>1</sup>

<sup>1</sup>*School of Advanced Materials Science and Engineering, Sungkyunkwan University, Suwon 16419, Republic of Korea*

<sup>2</sup>*Department of Materials Science & Engineering, Hanyang University, Ansan 15588, Republic of Korea*

*hsubkim@skku.edu*

The demand for performance enhancement of the metal-oxide-semiconductor (MOS) field-effect transistors raises the need for new channel materials that are compatible with nano-scaled high-k dielectrics. A Si<sub>1-x</sub>Ge<sub>x</sub> alloyed film is one of the most promising channel materials owing to the tunability of its band gap and carrier mobility using Ge contents [1]. Nevertheless, its poor interface property with the high-k dielectric layers caused by a defective interfacial oxide (Ge-oxide) is a critical drawback that degrades the transistor performance [2]. As a result, various interface passivation studies have been conducted to overcome the poor interface characteristics of high-k on Si<sub>1-x</sub>Ge<sub>x</sub> [3–5]. Recently, thermal pretreatment of a Ge substrate using a H<sub>2</sub>S gas was reported to offer a significant improvement of the interfacial properties with the high-k gate dielectric [6].

In this study, to improve the interface characteristics with a HfO<sub>2</sub> gate dielectric (~5.3 nm), sulfur passivation was conducted on the HF-cleaned p-type Si<sub>1-x</sub>Ge<sub>x</sub> substrate via H<sub>2</sub>S (5%) annealing at 400 °C for 30 s. After fabrication of the MOS capacitors on the p-type Si<sub>1-x</sub>Ge<sub>x</sub> substrates with different Ge concentrations (x = 0, 0.15, and 0.28), various electrical parameters, such as capacitance-equivalent oxide thickness, interface state density, and flat band voltage, were extracted and compared. Based on these electrical properties, the effect of the H<sub>2</sub>S pretreatment and its dependence on the Ge content in Si<sub>1-x</sub>Ge<sub>x</sub> will be discussed.

[1] F. Schaffler *et al.*, *Semicon. Sci. Technol.* **12**, 1515 (1997).

[2] Y. Kamata, *Materials Today* **11**, 30 (2008).

[3] J. Han *et al.*, *Appl. Phys. Express* **6**, 051302 (2013).

[4] K. Sardashti *et al.*, *Appl. Surf. Sci.* **455-463**, 366 (2016).

[5] J. Han *et al.*, *J. Appl. Phys.* **120**, 125707 (2016).

[6] T. Seok *et al.*, *J. Mater. Chem. C* **4**, 850 (2016).

## **Molecular Dynamics Simulation on Interfacial Reaction between LiC<sub>6</sub> / Li<sub>3</sub>PS<sub>4</sub> in All-Solid-State Li Ion Battery Anode**

K. Nagai<sup>1</sup>, Y. Wang<sup>1,2</sup>, N. Miyazaki<sup>1</sup>, Y. Ootani<sup>1</sup>, N. Ozawa<sup>1</sup>, and M. Kubo<sup>1</sup>

<sup>1</sup>*Institute for Materials Research, Tohoku University, Sendai, Miyagi 980-8577, Japan*

<sup>2</sup>*Department of Mechanical Systems Engineering, Graduate School of Engineering,*

*Tohoku University, Sendai, Miyagi 980-8579, Japan*

*kengo.nagai@imr.tohoku.ac.jp*

An all-solid-state lithium ion battery has a potential for greater safety and higher energy densities compared to a conventional Li ion battery with liquid electrolyte. Anode materials consist of graphite as active materials and Li<sub>2</sub>S/P<sub>2</sub>S<sub>5</sub> as electrolytes. The all-solid-state lithium battery charges by intercalating of Li into the graphite layers. For improving charging capacity, the behavior of Li at the interface between the graphite and electrolyte in the anode should be clarified. However, it is difficult to directly observe the behavior of Li by experimental methods. Therefore, in this study, the behavior of Li in the composite of the graphite layers and Li<sub>3</sub>PS<sub>4</sub> particles are investigated by molecular dynamics simulation using reactive force field.

Firstly, we performed a relaxation calculation of a porous model of Li<sub>3</sub>PS<sub>4</sub> particles and graphite layers with intercalated Li atom (LiC<sub>6</sub>). Here, the Li<sub>3</sub>PS<sub>4</sub> particle contained Li defects at a ratio of 10%. After the relaxation, we applied a pressure of 500 MPa to join the Li<sub>3</sub>PS<sub>4</sub> particles and graphite layers (Fig. 1). Secondary, we performed Li diffusion simulation between graphite layers and a porous structure of Li<sub>3</sub>PS<sub>4</sub> particles. Fig. 2 shows the trajectory of the Li atoms at LiC<sub>6</sub> / Li<sub>3</sub>PS<sub>4</sub> interface for 45 ps. We found that the longest diffusion path of Li atoms is on the grain boundaries between the Li<sub>3</sub>PS<sub>4</sub> particles. To discuss the diffusion process of the Li atoms, the snapshots of the Li diffusion simulation around the interface between graphite layers and Li<sub>3</sub>PS<sub>4</sub> particles are shown in Fig. 3. At the beginning, the intercalated Li atoms moved to an edge of the graphite layers (Figs. 3a, 3b). When the Li atom approached to a PS<sub>4</sub> unit on the grain boundary (Fig. 3c), the Li atom moved from the graphite layers to the Li<sub>3</sub>PS<sub>4</sub> particles with rotation of the PS<sub>4</sub> unit (Fig. 3d). After that, another PS<sub>4</sub> unit approached to the Li atom and then the PS<sub>4</sub> unit rotated to catch the Li atom. This lead to the diffusion of the Li atom to another Li<sub>3</sub>PS<sub>4</sub> particle (Fig. 3e). By repeating this rotation behavior of the PS<sub>4</sub> units, the Li atom diffused from the graphite layers toward the electrolytes of the Li<sub>3</sub>PS<sub>4</sub> particles. In conclusion, we found that Li atoms in graphite layers diffused to a Li<sub>3</sub>PS<sub>4</sub> electrolyte by passing through the grain boundaries with rotation of PS<sub>4</sub> units.

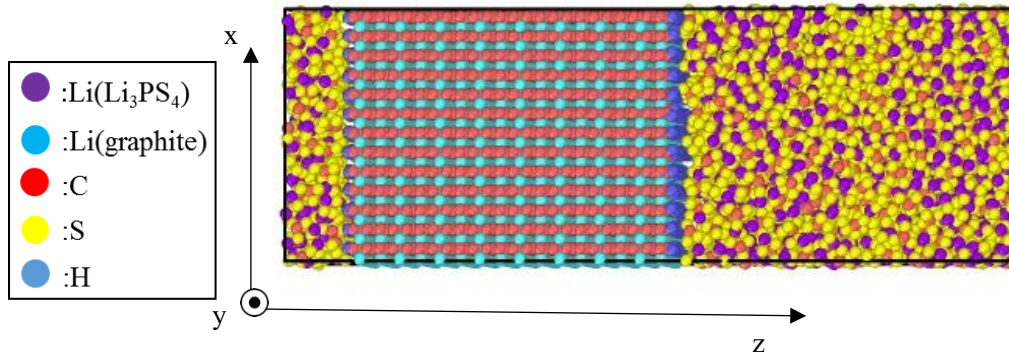


Fig. 1: Calculation model of graphite layers /  $\text{Li}_3\text{PS}_4$  particles.

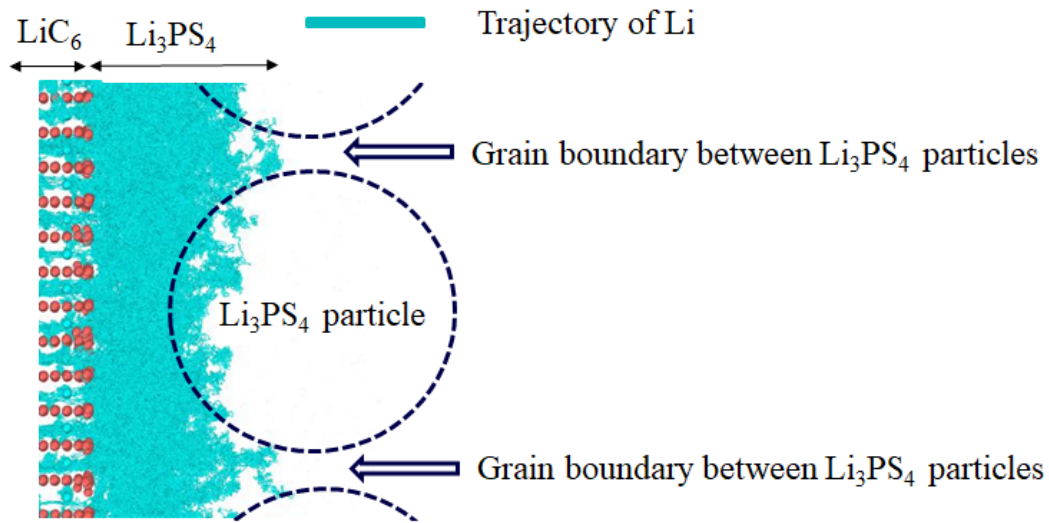


Fig. 2: Trajectory of Li at  $\text{LiC}_6$  /  $\text{Li}_3\text{PS}_4$  interface (P, S and H atoms are not shown).

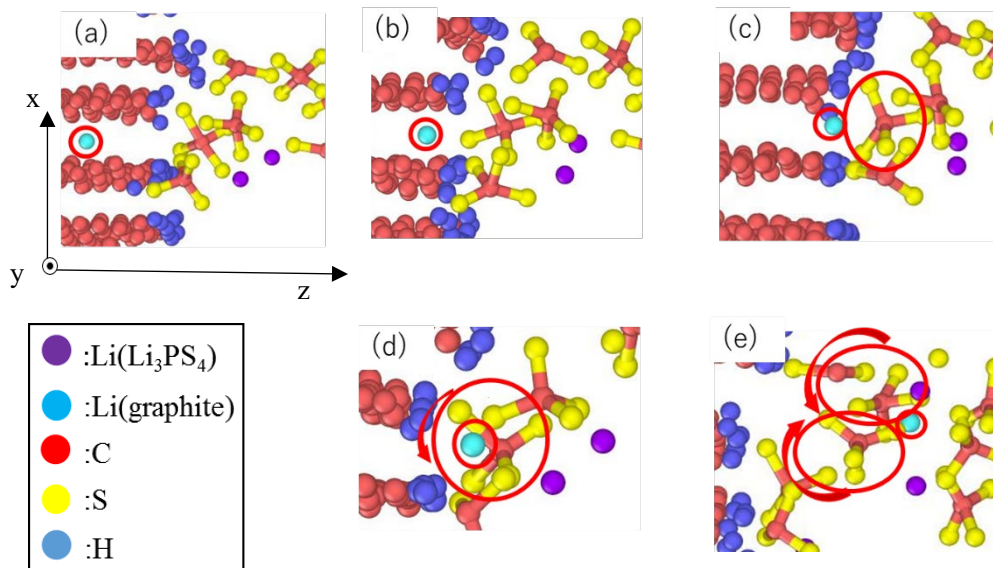


Fig. 3: Snapshots of interfacial reaction between graphite layers /  $\text{Li}_3\text{PS}_4$  particles at (a) 14.00 ps (b) 14.87 ps (c) 15.45 ps (d) 15.80 ps, and (e) 34.10 ps

## Effect of Water in Grain Boundaries on Shear Failure Strength of Silica: Reactive Molecular Dynamics Simulation

S. Yamashita<sup>1</sup>, Y. Wang<sup>1,2</sup>, N. Miyazaki<sup>1</sup>, Y. Ootani<sup>1</sup>, N. Ozawa<sup>1</sup>, and M. Kubo<sup>1</sup>

<sup>1</sup>*Institute for Materials Research, Tohoku University, Sendai 980-8577, Japan*

<sup>2</sup>*Department of Mechanical Systems Engineering, Tohoku University,*

*Sendai 980-8579, Japan*

*shuro.yamashita@imr.tohoku.ac.jp*

Silica (SiO<sub>2</sub>) is one of the most ubiquitous material and widely used as glass. Thus, the mechanical properties of SiO<sub>2</sub> have been studied. However, the effects of the chemical reaction on the mechanical properties are still in debate. It is well known that the failure strength of SiO<sub>2</sub> decreases in the presence of water due to chemical reaction. Thus, it is important to investigate the chemical reaction dynamics in failure process.

In our previous study, we have conducted a shear failure simulation of amorphous silica (a-SiO<sub>2</sub>) which is a model of glass. We found that a shear plane is formed and the strength of a-SiO<sub>2</sub> decreases due to the dissociation of Si-O bonds by hydrolysis reaction. On the other hand, failure mechanism of polycrystalline silica (poly-SiO<sub>2</sub>) is still unclear. Recently nanopolycrystalline stishovite has attracted much attention as super-hard and ultra-tough material [1]. However, the effect of the chemical reaction on the failure mechanism of polycrystalline structure is still unclear. Therefore, in this work, we conducted a shear failure simulation of poly-SiO<sub>2</sub> using reactive molecular dynamics method.

In this study, we applied shear force to poly-SiO<sub>2</sub> model (Fig. 1a). Water molecules were placed in the cavities created at the triplet points of poly-SiO<sub>2</sub> (Fig. 1b). In the shearing process, strain concentrated on the grain boundaries (Fig. 2), and the poly-SiO<sub>2</sub> is broken from the boundaries. In the triplet points, we observed that water in the cavity flowed into the neighboring cavity through the grain boundary (Fig. 3a). Meanwhile, strain at the grain boundaries, where water passes, increased (Fig. 3b). Therefore, the poly-SiO<sub>2</sub> was broken from the boundaries. We also found that the number of water molecules and Si-O-Si decreased, whereas the number of Si-OH increased (Fig. 4), indicating that the hydrolysis reaction, Si-O-Si + H<sub>2</sub>O - Si-OH + Si-OH, occurred. Since the hydrolysis reaction dissociates Si-O bonds, water flowing through the grain boundaries breaks the surrounding Si-O bonds. As a result, failure strength of poly-SiO<sub>2</sub> decreases in water environment due to the hydrolysis reaction.

[1] N. Nishiyama *et al.*, *Scr. Mater.* **67**, 955 (2012).

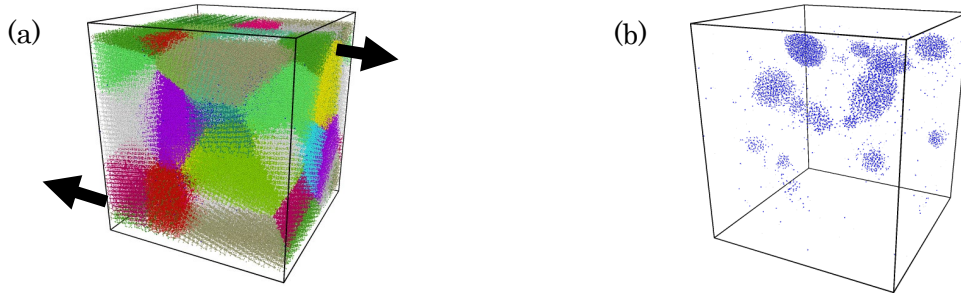


Fig. 1: (a) Simulation model of the poly-SiO<sub>2</sub> model containing water. The color indicates SiO<sub>2</sub> grains. (b) Water molecules in polycrystalline SiO<sub>2</sub> model. The blue and white balls indicate O in water and H atoms, respectively. The arrows indicate the shear direction.

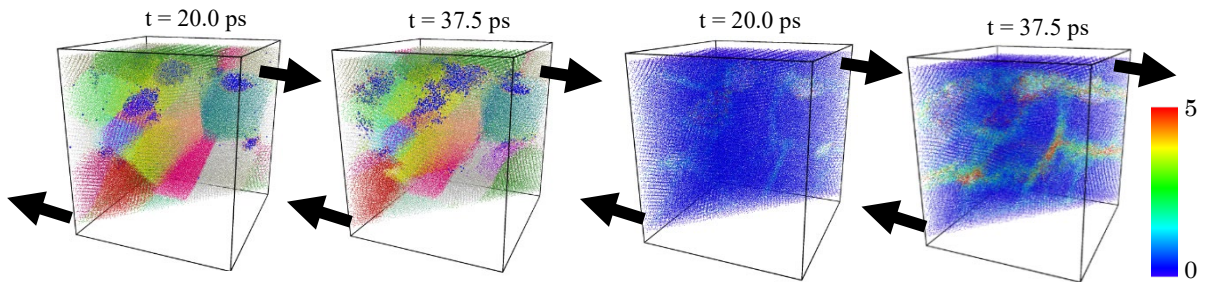


Fig. 2: (a) Shear simulation snapshots of sliced poly-SiO<sub>2</sub> model. The blue, white, and orange balls indicate O in water, H and O in SiOH group, respectively, and the other color indicates SiO<sub>2</sub> grains. (b) Snapshots colored by local shear strain. Water molecules are not shown. The arrows indicate the shear direction.

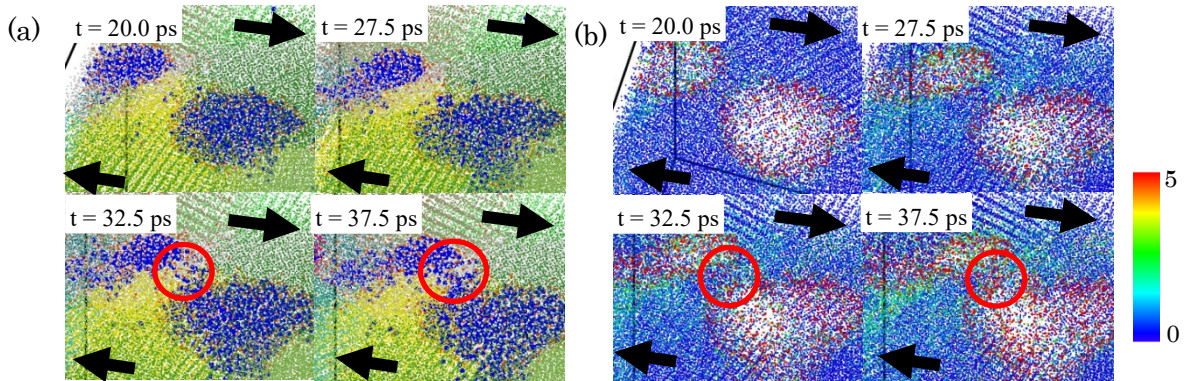


Fig. 3: (a) Snapshots of poly-SiO<sub>2</sub> model. The blue, white, and orange balls indicate O in water, H and O in SiOH group, respectively, and the other color indicates grains. (b) Snapshots colored by local shear strain. Water molecules are not shown. The red circles show flow of water to the neighboring cavity. The arrows indicate the shear direction.

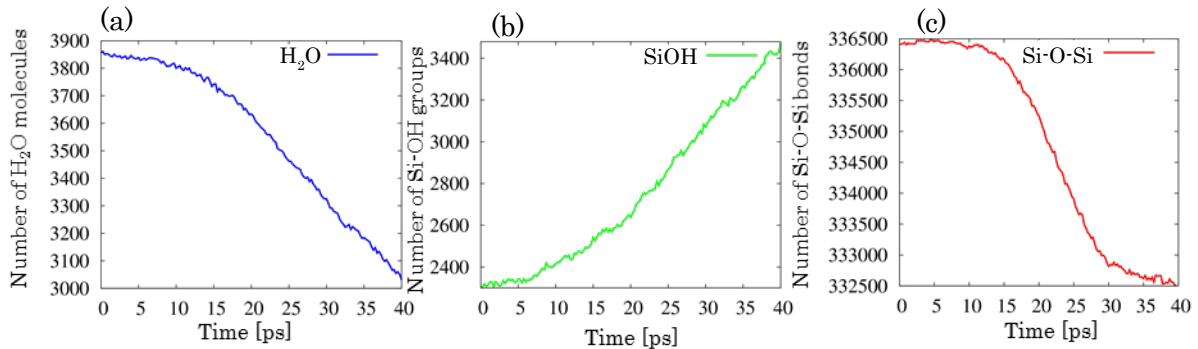


Fig. 4: The number of (a) H<sub>2</sub>O molecules, (b) Si-OH groups, and (c) Si-O-Si bonds.

## **New Modification Method of Sialoglycan on Graphene FET for Selective Detection of Virus**

*K. Yamamoto<sup>1</sup>, T. Ono<sup>1</sup>, N. Miyakawa<sup>2</sup>, Y. Kanai<sup>1</sup>, T. Koyama<sup>1</sup>, M. Tanioku<sup>1</sup>, S. Ushiba<sup>2</sup>,  
A. Shinagawa<sup>2</sup>, K. Inoue<sup>1</sup>, Y. Watanabe<sup>3</sup>, S. Nakakita<sup>4</sup>, T. Kawahara<sup>5</sup>, Y. Suzuki<sup>5</sup>, M. Kimura<sup>2</sup>,  
D. Chiba<sup>1</sup>, and K. Matsumoto<sup>1</sup>*

*<sup>1</sup>Osaka University, Japan*

*<sup>2</sup>Murata Manufacturing Co. Ltd., Japan*

*<sup>3</sup>Kyoto Prefecture University of Medicine, Japan*

*<sup>4</sup>Kagawa University, Japan*

*<sup>5</sup>Chubu University, Japan*

*k-yamamoto@sanken.osaka-u.ac.jp*

We are developing the biosensor using graphene FET to detect the influenza virus. Graphene is the best material for the sensor because of its high mobility and the two dimensional electric gas is on its surface. Using these features of graphene, we have succeeded in the selective detection of the influenza virus as shown in Fig.1. As the human infectious influenza virus bind to only human-type sugar chain, we use this mechanism to detect human infectious influenza virus. Fig.2 shows the SEM image of sugar chain on the surface of the cell, which looks like a black brush. We modified the surface of graphene by the sugar chain and reproduce this structure artificially to detect the virus.

So far, for the modification of sugar chain, we introduced the PBASE first which bound to graphene by van der Waals force, then the sugar chain was connected to PBASE by amide binding as shown in Fig.3(a). This method, however, had low yield and had low reproducibility. In order to solve this problem, we established new method using abiding-biotin bound sugar chain reaction as shown in Fig.3 (b). The abiding-biotin binding have the strong bind because they bind by hydro binding witch is most strong binding in non-covalent bond. First, graphene and PBASE are bound by van der Waals force. Then, streptavidin is bound to PBASE by amide binding. Finally, biotinylated human-type sugar chain is bound to streptavidin by hydro binding. Theses processes are confirmed by BLITS as shown in Fig.4. (1)The carboxylic acid on surface of BLITZ sensor is changed by succinimidyl ester.(2)The streptavidin was bound to the sensor by amide binding. (3)The biotinylated sugar chain was bound to the streptavidin by hydro bond.(4) The human infectious influenza virus was bound to the sugar chain. These signal sequence clearly shows the successful binding of each reaction. So we succeeded in catching the virus through streptavidin- biotinylated sugar chain systems. We tried to detect the human infectious influenza virus using the graphene FET which modified by the human-type sugar chain by the present new method mentioned above.

The graphene FET channel was divided into two regions, one with sugar chain and the other without sugar chain. Fig.5 shows the dependence of the Dirac point shift on the various concentration of virus which bound to the sugar chain. Since blocking is not performed, the obtained results from the region with sugar chain was subtracted from the physical adsorption value of the region without sugar chain. As the virus has negative charge,  $V_{dirac}$  should shift to the positive direction against gate voltage. The concentration of 2.56 HAU virus makes 30mV shift, 25.6HAU virus makes 42mV shift, but 256HAU virus makes almost the same shift as that of 25.6HAU. This means that at the 256HAU, the virus is almost saturated at the binding sugar chain and shows the similar shift with 25.6HAU virus. As we got the large 30mV shift at 2.56HAU, we could expect to detect more low concentration virus than 2.56HAU. The surface of the graphene channel was observed after the detection of virus using AFM as shown in Fig.6. The white points are considered to be the viruses. The density of the virus is 0.0946 per  $1\mu m^2$ . We dyed the virus membrane for fluorescence observation. Emitted light matched well with the white point observed by AFM. Therefore, we could confirm the virus can be caught by the sugar chain modified by the present new method.

Conclusion. Graphene FET, sensitive to environment charge is applied to the biosensor. We have modulated the surface of graphene by the sugar chain and succeeded in the detection of the virus. We developed the new and reproducible method to bind the sugar chain to the graphene using abidingbiotin reaction.

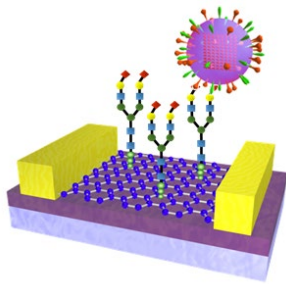


Fig.1: Graphene FET modified by sugar chain for selective detection of virus.

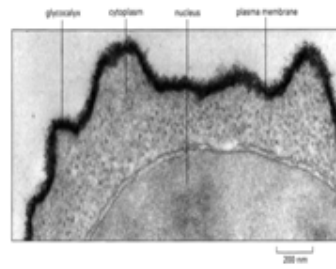


Fig.2: SEM image of sugar chain on the surface of the cell.

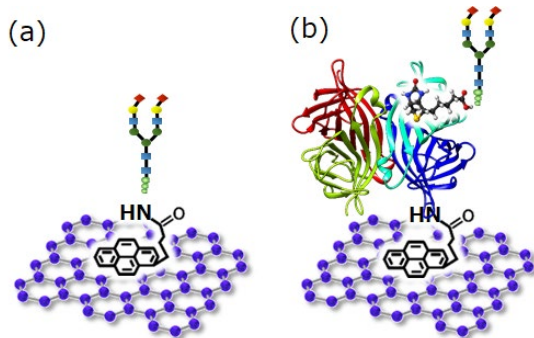


Fig.3: (a) Previous method to modify sugar chain on graphene surface using PBASE linker and sugar chain. (b) Present new method to modify sugar chain on graphene surface using streptavidin-biotin bound sugar reaction.

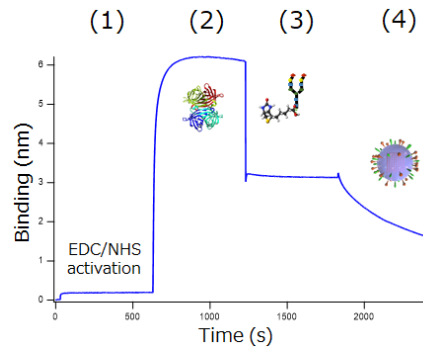


Fig.4: Sequence reaction of streptavidin-biotin bound sugar-virus confirmed by BLITZ method.

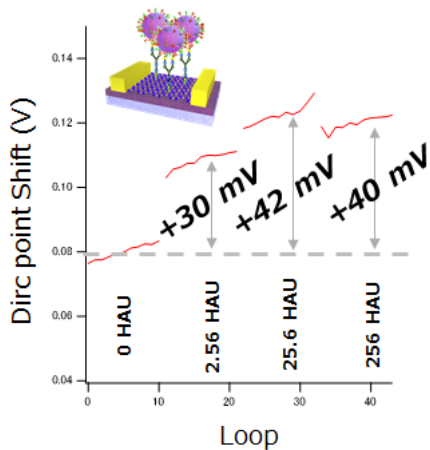


Fig.5: Dependence of  $V_{dirac}$  shift of graphene FET on various virus concentration, which reacts to sugar chain bound to graphene by present new method.

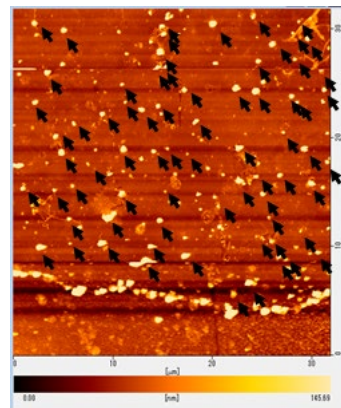


Fig.6: AFM image of Virus on graphene channel through sugar chain modified by present new method.

## **Direct and Precise Length Measurement of Single, Stretched DNA Fragments by Dynamic Molecular Combing and STED Nanoscopy**

N. Kim<sup>1,\*</sup>, H.J. Kim<sup>1,†</sup>, Y. Kim<sup>1,2</sup>, K.S. Min<sup>3</sup>, and S.K. Kim<sup>1,3</sup>

<sup>1</sup>*Department of Chemistry, Seoul National University,  
Gwanak-gu, Seoul 08826, Republic of Korea*

<sup>2</sup>*LumiMac, Inc., 4, Dongnam-ro 2-gil, B1, Songpa-gu, Seoul 05805, Republic of Korea*

<sup>3</sup>*Department of Biophysics and Chemical Biology, Seoul National University,  
Gwanak-gu, Seoul 08826, Republic of Korea*

*\*Current address: Department of Chemistry, Kongju National University,  
Gongju 32588, Republic of Korea*

*†Current address: Department of Chemistry, Columbia University, New York 10027, USA  
seongkim@snu.ac.kr*

A combination of DNA stretching method and super-resolution nanoscopy allows an accurate and precise measurement of the length of DNA fragments ranging widely in size from 117 to 23,130 bp. BstEII- and HindIII-treated  $\lambda$ DNA fragments were stained with an intercalating dye and then linearly stretched on a coverslip by dynamic molecular combing. The image of individual DNA fragments was obtained by stimulated emission depletion nanoscopy. For DNA fragments longer than  $\sim 1000$  bp, the measured lengths of DNA fragments were consistently within  $\sim 0.5$  to  $1.0\%$  of the reference values, raising the possibility of this method in a wide range of applications including facile detection for copy number variations and trinucleotide repeat disorder.

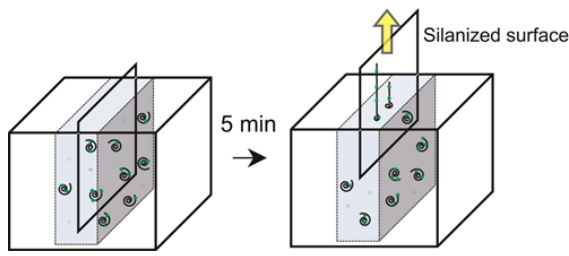


Fig.1: Schematic representation of dynamic molecular combing. A solution containing DNA labelled with YOYO-1 was transferred to a Teflon chamber. A silanized coverslip was immersed in the solution and left there for 5 min. The coverslip was then pulled up at a speed of 200  $\mu\text{m}/\text{sec}$  to yield linearly stretched DNA on the coverslip.

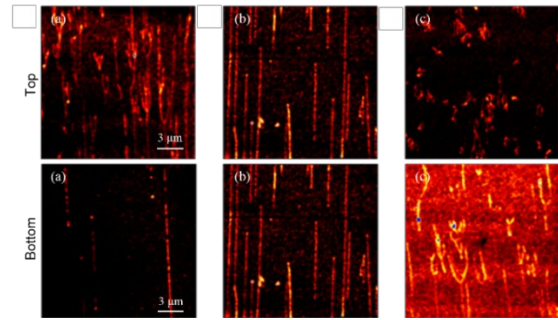


Fig.2: (Top) Comparison of the linearity of combed  $\lambda\text{DNA}$  using different pull-up speeds: (a) 20  $\mu\text{m}/\text{sec}$ , (b) 200  $\mu\text{m}/\text{sec}$ , and (c) 1,000  $\mu\text{m}/\text{sec}$ . (Bottom) Comparison of the image brightness of combed  $\lambda\text{DNAs}$  using different ratio of dye per base pair in the MES buffer: (a) 1:30, (b) 1:5, and (c) 1:1.

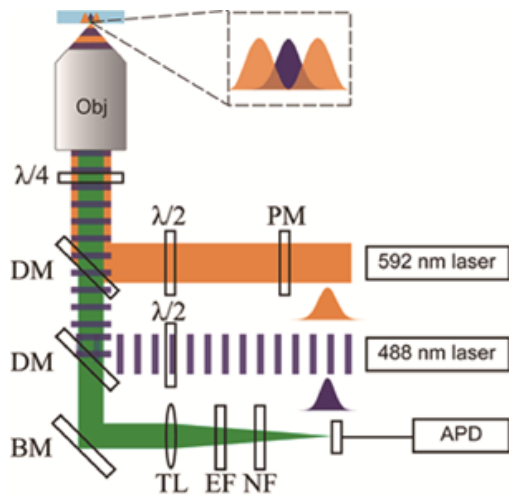


Fig.3: Schematic of our pulsed-CW STED nanoscopy system. PM: phase mask,  $\lambda/2$ : half-wave plate,  $\lambda/4$ : quarter-wave plate, DM: dichroic mirror, BM: broadband mirror, Obj: objective lens, TL: tube lens, EF: emission filter, NF: notch filter, APD: avalanche photodiode.

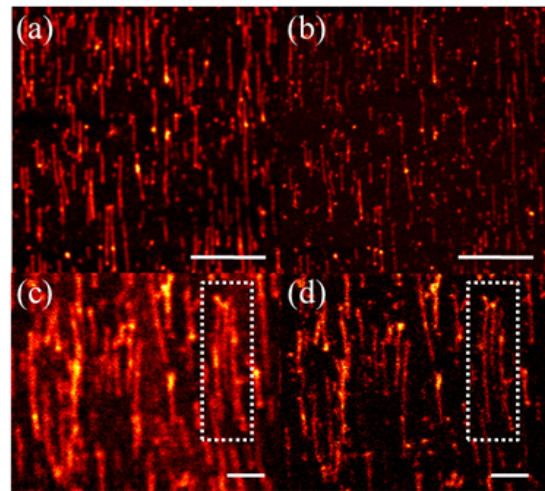


Fig.4: Top: Whole-area images by (a) confocal and (b) STED microscopy for combed  $\lambda\text{DNA}$  fragments digested with *BstEII* restriction enzyme.  $\lambda\text{DNA}$  fragments were stained with YOYO-1, an intercalating dye, and stretched on a coverslip by dynamic molecular combing. Image size: 18  $\mu\text{m} \times 18 \mu\text{m}$ . Scale bar: 5  $\mu\text{m}$ . Bottom: Local images by (c) confocal and (d) STED microscopy for a more densely populated region of DNA fragments. The 3 strands in the white box are shown to be clearly resolved in the STED image. Scale bar: 1  $\mu\text{m}$ .

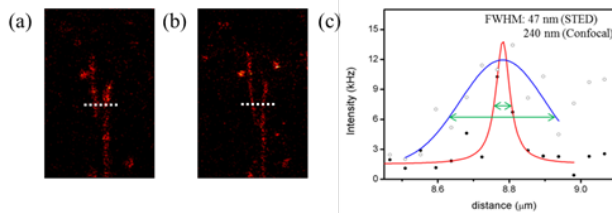


Fig.5: FWHM lateral width of (a) confocal vs. (b) STED images, with (c) their line profiles along the white dashed lines fitted by Gaussian (confocal) and Lorentzian (STED) curve. Because of the low spatial resolution of the confocal image, the signal intensity to the right side of the peak (at distance  $> \sim 8.8 \mu\text{m}$ ) is due to a nearby fragment.

## Comprehensive Modeling of Switching in Perpendicular STT-MRAM

S. Fiorentini<sup>1</sup>, R. Lacerda de Orio<sup>1,2</sup>, S. Selberherr<sup>2</sup>, J. Ender<sup>1</sup>, W. Goes<sup>3</sup>, and V. Sverdlov<sup>1</sup>

<sup>1</sup>*Christian Doppler Laboratory for Nonvolatile Magnetoresistive Memory and Logic at the*

<sup>2</sup>*Institute for Microelectronics, TU Wien, Gußhausstraße 27-29/E360, 1040 Vienna, Austria*

<sup>3</sup>*Silvaco Europe Ltd., Cambridge, United Kingdom*

*viktor.sverdlov@tuwien.ac.at*

Introduction of non-volatility in modern integrated circuits dramatically reduces the stand-by power and leakages. Spin-transfer torque (STT) magnetoresistive random access memory (MRAM) combines high speed, excellent endurance, and low costs and is promising for applications ranging from IoT and automotive applications to embedded DRAM and L3 caches [1]. In MRAM the binary information is stored as the parallel/anti-parallel configuration of the magnetic layers in a magnetic tunnel junction (MTJ). The switching between the two configurations is achieved by passing current through the MTJ. In simulating STT switching, for simplicity it is usually assumed that the current density  $J(\mathbf{r},t)$  is position- and time-independent [2]. Practically, however, it is the voltage which remains constant at switching rather than the current density. As the relative magnetization alignment is locally modified at the switching, so is the local tunneling resistance. Thus, different current densities are flowing through different parts of the MTJ with different magnetization alignments (Fig.1). Therefore, the assumption of a constant current density is questionable, especially in MTJs with a tunneling magnetoresistance ratio (TMR) larger than 200% [3].

In order to validate the assumption of the constant current density for evaluating the switching time, we first consider the model in which the total current is fixed, but the current density is determined by the local magnetization alignment and the corresponding local TMR. The switching times depend on the realization of the stochastic magnetic field mimicking the magnetization fluctuations at room temperature. It turns out that the average switching times within the models with the fixed current and the fixed current density are very similar for both parallel (P) to anti-parallel (AP) and AP to P switching of a perpendicular MTJ (Fig.2). However, the switching for the fixed, constant voltage, with a value chosen so that the initial current and the torque are the same, looks quite different (Fig.2) [4]. The difference is due to the fact that in the model with fixed voltage the current depends on the varying resistance of the MTJ. In order to compensate the effect of the varying resistance, the current  $J$  value in the models with the fixed current must be increased by ~10% for AP to P and decreased by ~5% for P to AP switching, for TMR=200%. Fig.3 demonstrates that after these corrections the switching times as a function of the stray field within the fixed voltage and fixed current models are very similar.

The dependence of the current correction in relation to the value providing the same initial torque is shown in Fig.4 as a function of the TMR. The results imply that the use of the constant current density model is justified also in the realistic case of switching at a constant voltage, provided that the current is appropriately corrected for the P to AP and the AP to P scenario.

**Acknowledgment.** This work was supported by the Austrian Federal Ministry for Digital and Economic Affairs and the National Foundation for Research, Technology and Development.

- [1] S. Sakhare *et al.*, Proc. IEDM, 420 (2018).
- [2] A. Makarov *et al.*, Semic. Sci. Tech. **31**, 113006 (2016).
- [3] D. Aurelio *et al.*, J. Magn. Magn. Mat. **321**, 3913 (2009).
- [4] S. Fiorentini *et al.*, Proc. SISPAD, 57 (2019).

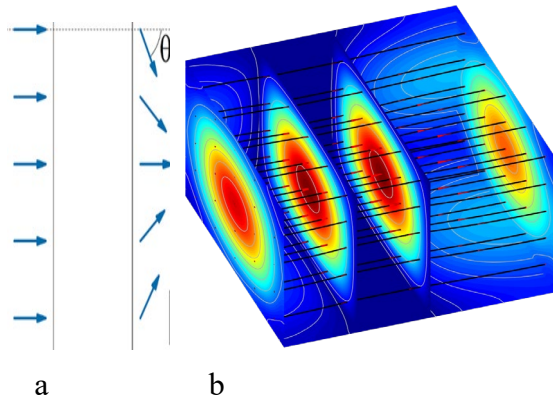


Fig.1: (a) Position dependent magnetization alignment in an MTJ and (b) the current density distribution under a fixed voltage  $V$ .

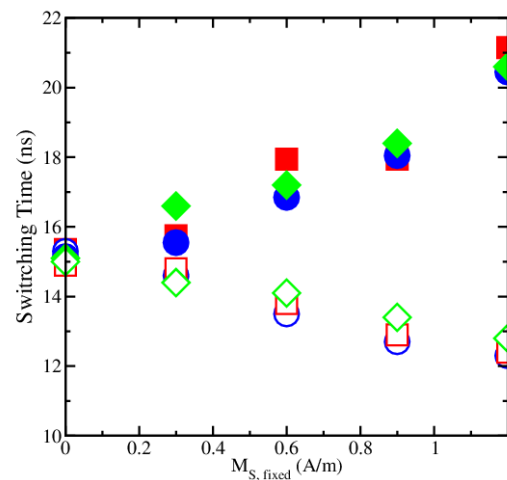


Fig.3: All three models give consistent results, if the current  $I$  is corrected from its initial value  $I=V/R$  as described in the text.

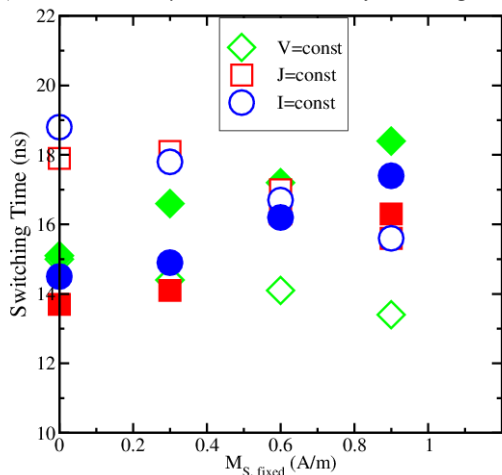


Fig.2: Switching times for three models with a fixed voltage  $V$ , fixed current  $I=V/R$  ( $R$  is the resistance before switching), and fixed current density  $J$ . The size of the open (P->AP) and filled (AP->P) symbols corresponds to the width of the switching time distribution.

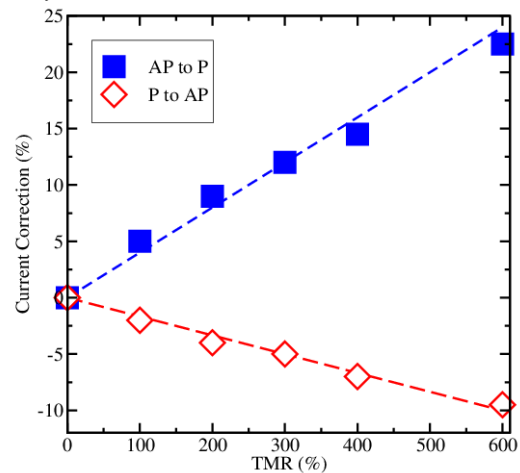


Fig.4: The correction to the current  $I$  as a function of TMR, which must be given in order for all three models to give consistent results, for both parallel to anti-parallel and anti-parallel to parallel switching. The dashed lines represent a linear fit.

## Properties of Gallium Oxide Grown by In-situ Plasma Oxidation and Its Effect on High-*k* MOS Capacitor on GaAs

D. Shin<sup>1</sup>, H. Cho<sup>1</sup>, S. Park<sup>1</sup>, D.-H. Ko<sup>1</sup>, and H.-J. Oh<sup>2</sup>

<sup>1</sup>*Department of Materials Science and Engineering, Yonsei University, Seoul, 03722, Korea*

<sup>2</sup>*BIT Micro Fabrication Research Center, Yonsei University, Seoul, 03722, Korea*

*hi5hj@yonsei.ac.kr*

For over 3 decades, high-mobility metal-oxide-semiconductor field-effect transistor (MOSFET) researchers have looked for a suitable gate insulator of the gate stack on GaAs channel. The MOS gate stack on GaAs has been notorious for its poor electrical properties such as high leakage current density caused mainly from high degree of interface trap density at the gate oxide/GaAs interface. Motivated by analogy with the SiO<sub>2</sub> dielectric on Si channel, the gate stack with a Ga<sub>2</sub>O<sub>3</sub>/GaAs interface was demonstrated low density of interface states and enhancement-mode MOSFETs [1, 2]. However, these successful MOS fabrications require ultra-high vacuum molecular beam epitaxy (UHV MBE) techniques to achieve the Ga<sub>2</sub>O<sub>3</sub>/GaAs interface [3]. We applied an in-situ plasma oxidation technique prior to HfO<sub>2</sub> deposition using metal-organic chemical vapor deposition (MOCVD) to fabricate high-*k* MOS gate stack with a GaO<sub>x</sub>/GaAs interface. The MOCVD is one of the standard CMOS fabrication processes in the semiconductor fabrication industry. The leakage current density of the HfO<sub>2</sub> gate stack on GaAs was reduced to  $7.7 \times 10^{-8}$  A/cm<sup>2</sup> with the in-situ plasma oxidation from  $1.8 \times 10^{-2}$  A/cm<sup>2</sup> at V<sub>FB</sub>-1 V. We have found that a GaO<sub>x</sub> layer with a decent interfacial quality was produced by the in-situ plasma oxidation and the layer can passivate MOCVD HfO<sub>2</sub> high-*k* gate stack on GaAs from its degradation during the device fabrication processing. In addition, we have explored the GaO<sub>x</sub> formation technique at different process conditions for further applications of the interesting gallium oxide properties in electrical devices [4].

**Acknowledgment.** This work is supported by the National Research Foundation (NRF) of the Ministry of Science and ICT of Korea (2017R1A2B2004986).

[1] A. Callegari *et al.*, Appl. Phys. Lett. **54**, 332 (1989).

[2] M. Passlack, J. Vac. Sci. Technol. B **23**, 1773 (2005).

[3] M. Passlack *et al.*, IEEE Trans. Electron Dev. **44**, 214 (1997).

[4] S.I. Stepanov *et al.*, Rev. Adv. Mater. Sci. **44**, 63 (2016).

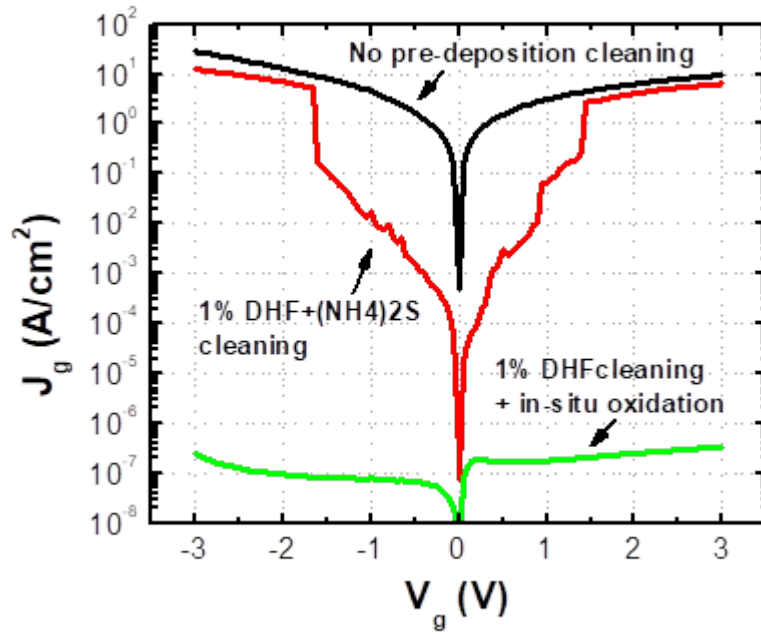


Fig.1: Gate leakage current density curves of TaN/HfO<sub>2</sub>/GaAs MOS capacitors with different processes on GaAs channel including chemical cleaning process prior to high-k MOCVD.

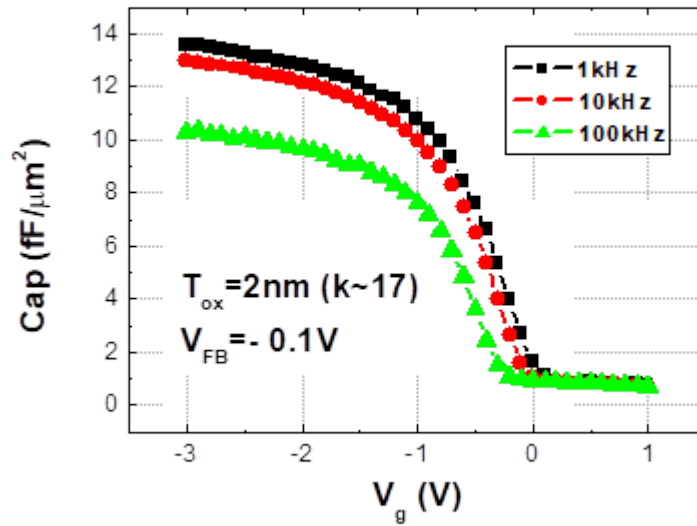


Fig.2: C-V characteristics of GaAs MOS capacitor at various frequencies for HfO<sub>2</sub>/in-situ plasma oxide gate stack on p-GaAs. The values of  $T_{ox}$  and  $V_{FB}$  are extracted from C-V at 1kHz.

## Potentials for Single Electron State Processing

M. Ballicchia<sup>1</sup>, M. Nedjalkov<sup>1</sup>, S. Selberherr<sup>1</sup>, and J. Weinbub<sup>2</sup>

<sup>1</sup>*Institute for Microelectronics, TU Wien, Austria*

<sup>2</sup>*Christian Doppler Laboratory for High Performance TCAD,*

*Institute for Microelectronics, TU Wien, Austria*

*josef.weinbub@tuwien.ac.at*

Entangletronics, as an emerging research area, aims at manipulating and controlling electron coherence for device operations. Most famously, the Young double-slit setup or the Aharonov-Bohm ring are fundamental structures to control the interference pattern of electrons. Both provide theoretical insights [1] and foundations for advanced applications, e.g., information processing [2]. Alternatively, electron control can be established by specifically shaped electric potentials, called lenses, which can split [3] or focus a single electron state, e.g., for improving the device performance [4]. Recently, it has been observed that the operation of such lenses can be emulated by two potential wells, such as the potentials of two attractive dopants [5]. A well-pronounced interference pattern can be observed. The process has been further investigated regarding the effect of different physical settings, such as the distance between the wells, their potential, and the parameters of the initial electron state. Here, we report the indicative case of a double dopant structure acting as a lense. The well potentials, the injected electron kinetic energy, and the initial condition  $k_{0y}$  are the same as in [5], however, reflecting boundary conditions are imposed. Fig. 1 shows the details of the geometry and the initial condition. The classical density (left) spreads evenly across the wire in the bottom part and is concentrated towards the central axis of the wire by the attractive potentials. This illustrates that (i) the effect of the boundaries can be controlled by the potential and the distance between the wells. The quantum evolution (right) demonstrates (ii) a well-pronounced interference effect. Notably, the interference pattern shown on a screen (i.e. a crosscut at a certain  $y$ -position) placed at  $y = 16\text{nm}$  (iii) gradually transforms to a strong central peak for screen positions beyond  $y = 19\text{nm}$ . Fig. 2 (left) shows the effect of reducing the left well potential by 50%. This result suggests that (iv) the lense focus can be gradually adjusted with respect to the cross section of the wire by a corresponding variation of the potential difference between the wells. In Fig. 2 (right), the interference patterns of the symmetric and asymmetric cases are compared in the  $y = 16\text{nm}$  screen (red). The peak of the focused electron density and its shift caused by the asymmetry is well-pronounced in the  $y = 26\text{nm}$  screen (blue). The results (i)-(iv) suggest alternative approaches for a coherent manipulation of the electron state.

- [1] P. Pearle, Quantum Stud.: Math. Found. **5**, 391 (2018).
- [2] C. Bäurle *et al.*, Rep. Prog. Phys. **81**, 056503 (2018).
- [3] P. Ellinghaus *et al.*, Phys. Stat. Sol. RRL **11**, 1700102 (2017).
- [4] P. Ellinghaus *et al.*, Proc. SISPAD, 24 (2015).
- [5] J. Weinbub *et al.*, Phys. Stat. Sol. RRL **12**, 1800111 (2018).

**Acknowledgment.** The financial support by the Austrian Science Fund (FWF): FWF-P29406-N30, the Austrian Federal Ministry for Digital and Economic Affairs, and the National Foundation for Research, Technology and Development is gratefully acknowledged.

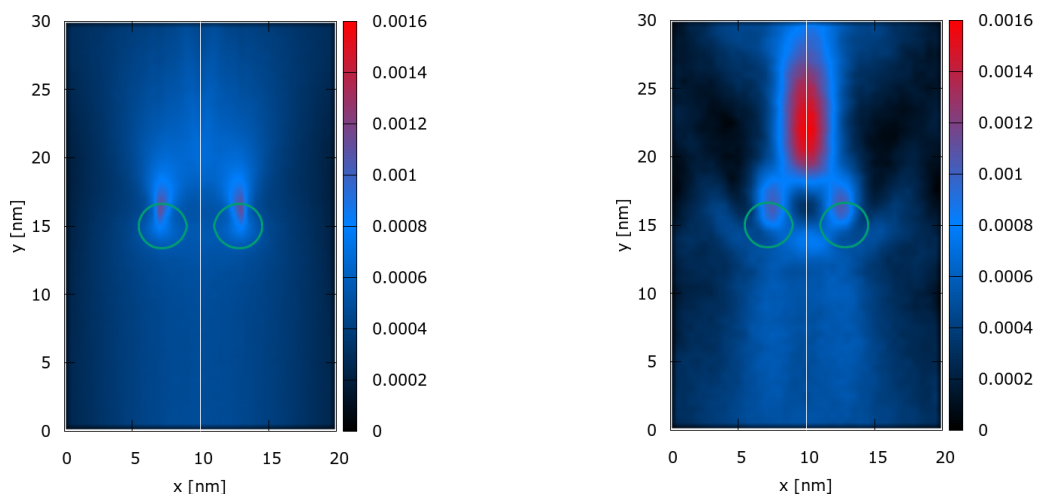


*Fig. 1: Classical (left) and quantum (right) electron densities obtained for the same – periodically injected (every 1fs) and centered at the bottom – initial condition, i.e., a minimum uncertainty Wigner packet with the standard deviation  $\sigma = 8\text{nm}$  and the central wave vector  $(k_{0x}, k_{0y}) = (0, 0.837/\text{nm})$  corresponding to an energy of 0.14eV. The initial condition's classical interpretation is a distribution function comprising two Gaussian functions in space and momentum. Green isolines at 0.175eV indicate the places of the potentials.*

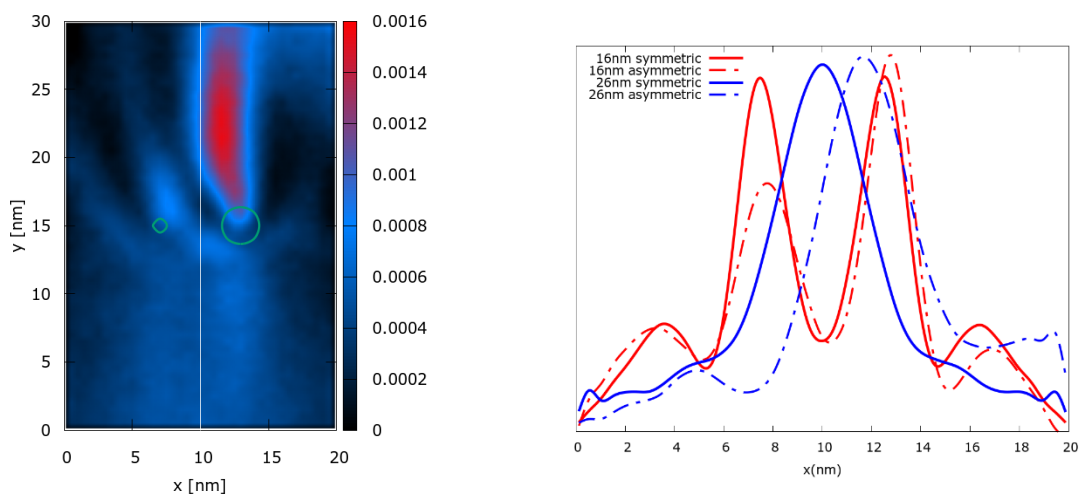


*Fig. 2: The reduced potential (by 50%) causes a shift of the focused density (left). The focusing effect as well as the effect of the potential asymmetry is well visible on screens at different positions (right).*

## **On the Theory of the Energetic Spectrum of Vicinal Superlattices: The Role of Crystal Potential**

V.A. Petrov

*Institute of Radio Engineering and Electronics  
Russian Academy of Sciences, Moscow, Russia  
vpetrov@cplire.ru*

As is known, the existence of superlattice effects in quantum wells (QWs) on vicinal planes initiated with the appearance in these systems of a new crystallographic translation period in the plane of quantum wells  $A \gg a$  ( $a$  - lattice constant). The emergence in these vicinal superlattices (VSLs) of the periodic system of atomic steps allows to explain the appearance of minigaps (MG) in the energetic spectrum of particles in QWs by the scattering of electrons on such steps. At the same time it is evident that the contribution to the MG formation should also be made by all crystallographic planes in the area of localization of the particle wave function. This paper theoretically shows that the consideration of only crystal potential and of the potential locating the particle in VSL on vicinal planes results in the appearance of MG even without taking into account of the step structure of the QW boundaries. A method has been developed that makes it possible to calculate the energetic spectrum of these systems for the arbitrary localizing potential by leaving the effective mass approximation in single-valley semiconductors of the GaAs type.

For the cases of the rectangular QW analytical expressions have been obtained for MG magnitudes which depend on the parameters of the crystal and localizing potentials as well as on angles that define the orientation of the QW planes in the crystal. It has been shown that for VSL of the GaAs type the magnitudes of MGs approximate several meV.

## Substrate-Dependent Morphological Change of MoS<sub>2</sub> During Atomic Layer Deposition

W. Ahn<sup>1</sup>, H. Lee<sup>2</sup>, Y. Cho<sup>2</sup>, H. Kim<sup>1</sup>, M. Leem<sup>1</sup>, H. Lee<sup>1</sup>, K.-E. Byun<sup>2</sup>, H.-J. Shin<sup>2</sup>,  
and H. Kim<sup>1,\*</sup>

<sup>1</sup>*School of Advanced Materials Science and Engineering, Sungkyunkwan University,  
Suwon 16419, Republic of Korea*

<sup>2</sup>*Samsung Advanced Institute of Technology, Suwon 16678, Republic of Korea*  
*hsubkim@skku.edu*

The practical application area of MoS<sub>2</sub> strongly depends on its preferred growth direction during synthesis. For example, the MoS<sub>2</sub> film predominantly grown in a lateral direction has a high electron mobility with an inactive surface, which is advantageous for the transistor application. On the contrary, the vertically aligned MoS<sub>2</sub> crystal has a high chemical reactivity due to the presence of a large edge region with many dangling bonds, which can be used for the catalyst application [1, 2].

In this study, we synthesized the MoS<sub>2</sub> films on various substrates (SiO<sub>2</sub>, Al, and Au) via an atomic layer deposition process using MoCl<sub>5</sub> and H<sub>2</sub>S precursors at 420 °C, and observed intriguing morphological evolution (a change in the preferred growth direction) of MoS<sub>2</sub>, strongly dependent on the underlying substrates. The surface morphology, microstructure, and optical properties of the synthesized MoS<sub>2</sub> films were examined and compared using various characterization tools, such as scanning electron microscopy, transmission electron microscopy, atomic force microscopy, Raman spectroscopy, and photoluminescence spectroscopy. The origin for the observed dependence of the morphological change on the substrate surfaces will be discussed based on the thermodynamic analyses and the precursor adsorption energy calculations.

[1] K.H. Ruiz *et al.*, *J. Alloys Compd.* **74**, 100 (2018).

[2] T.A. Ho *et al.*, *Chem. Mater.* **29**, 7604 (2017).

## Synthesis of MoS<sub>2</sub> via Sulfurization of a MoO<sub>2</sub>-Evapoated Film

H. Kim<sup>1</sup>, T. Park<sup>2</sup>, M. Leem<sup>1</sup>, H. Lee<sup>1,3</sup>, W. Ahn<sup>1</sup>, E. Lee<sup>3</sup>, and H. Kim<sup>1</sup>

<sup>1</sup>*School of Advanced Materials Science and Engineering, Sungkyunkwan University,  
Suwon 16419, Republic of Korea*

<sup>2</sup>*Semiconductor R&D Center, Samsung Electronics, Hwaseong 18488, Republic of Korea*

<sup>3</sup>*Analytical Engineering Group, Samsung Advanced Institute of Technology,  
Samsung Electronics, Suwon 16678, Republic of Korea*

*hsubkim@skku.edu*

For practical application of two-dimensional transition metal dichalcogenide materials including MoS<sub>2</sub> to the electronic devices, various synthesis methods have been actively studied. As one of the strategies to synthesize a large area MoS<sub>2</sub> thin film, thermal sulfurization of pre-deposited films, such as Mo metal [1] and MoO<sub>3</sub> [2, 3], have been proposed.

In this presentation, we propose a MoS<sub>2</sub> synthesis method using thermal sulfurization of an amorphous MoO<sub>3-x</sub> film that is pre-deposited via e-beam evaporation of a MoO<sub>2</sub> powder. To find an optimal process condition, the compositional, microstructural, and optical properties of the synthesized MoS<sub>2</sub> films were characterized while the thickness of the pre-deposited film and the sulfurization temperature were varied. The sulfurization of a ~1 nm-thick MoO<sub>3-x</sub> film at 780 °C formed a monolayer MoS<sub>2</sub> film with a direct bandgap of ~1.9 eV, and successful operation of the SiO<sub>2</sub> bottom-gated field-effect transistors with the synthesized film was demonstrated.

[1] Y.J. Zhan *et al.*, *Small* **8**, 966 (2012).

[2] Y.C. Lin *et al.*, *Nanoscale* **4**, 6637 (2012).

[3] N. Salazar *et al.*, *Phys. Chem. Chem. Phys.* **19**, 14020 (2017).

## **Enhancement of Power Conversion Efficiency of Quantum-Dot and Perovskite Solar Cells by Controlling Electron Transporting Layer**

I.H. Jung

*Department of Chemistry, Kookmin University,*

*77 Jeongneung-ro, Seongbuk-gu, Seoul 02707, Republic of Korea.*

*ihjung@kookmin.ac.kr*

Colloidal quantum dot (CQD) and organic-inorganic metal halide-based perovskite solar cells have received significant attention as promising next generation solar cells due to their high efficiencies and low-cost solution-processibilities. Recently, julolidine-based cathode buffer materials were developed, which was effectively improved the power conversion efficiency and long-term stability of perovskite and quantum-dot solar cells.[1,2]

The high dipole moment of -10.07D was achieved by strong intramolecular charge transfer interaction between julolidine and cyanoacetic acid. The treatment of julolidine-based cathode buffer materials on the ZnO layer formed the self-assembled monolayer on ZnO surface and effectively reduced the work function of ZnO, facilitating the electron transporting properties in the devices. As a result, all the solar cell parameters were improved simultaneously by ZnO modification due to the enhanced  $V_{bi}$ ,  $E_{int}$ , and charge collection efficiency. Our study suggested that formation of self-assembled monolayer with high dipole moment on the ZnO surface can be a universal strategy for improving power conversion efficiency of solar cells.

[1] R. Azmi *et al.*, *Adv. Energy Mater.* **8**, 1701683 (2018).

[2] R. Azmi *et al.*, *Nano Energy* **39**, 355 (2017).

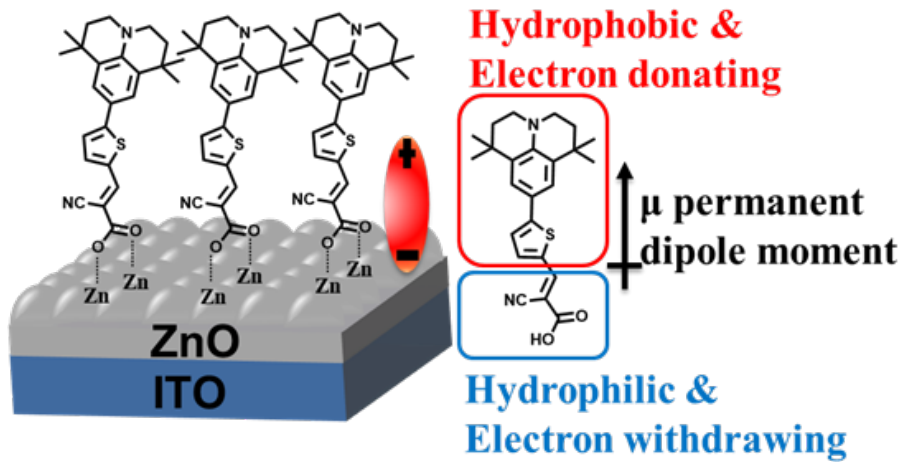


Fig.1: Surface treatment of ZnO layer via Julolidine-based cathode buffer layer.

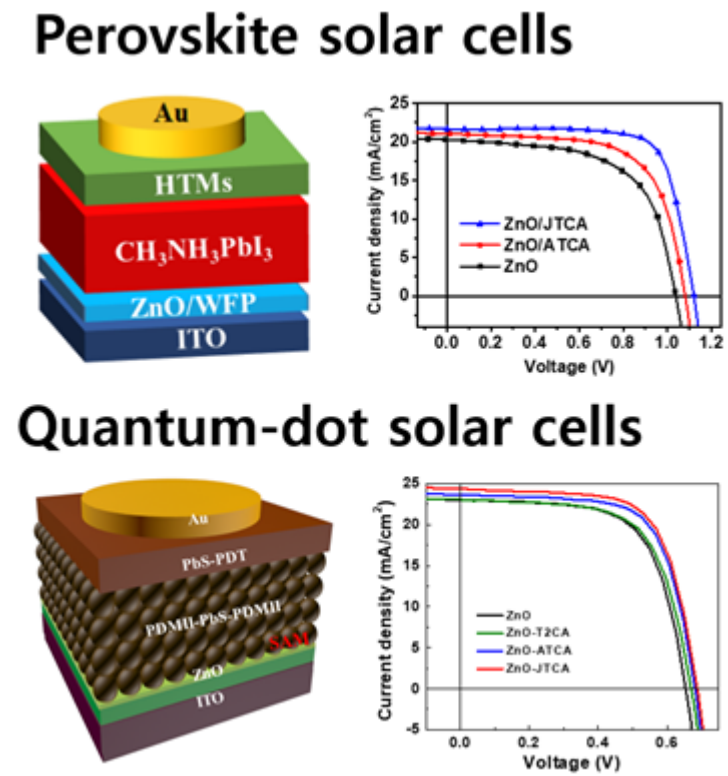


Fig.2: Improved power conversion efficiency of perovskite and quantum-dot solar cells via surface treatment of ZnO layer.

## **Tailored Electronic Properties of Zr-doped SnO<sub>2</sub> Nanoparticles for Efficient Planar Perovskite Solar Cells with Marginal Hysteresis**

Y.W. Noh and J.W. Jung

*Department of Advanced Materials Engineering for Information & Electronics,  
Kyung Hee University, 1732 Deogyong-daero, Giheung-gu, Yongin-si,  
Gyeonggi-do 446-701, Republic of Korea  
wodndwjd@khu.ac.kr*

Elemental doping has been demonstrated as an effective way to improve the electronic properties in the semiconducting metal oxides. [1] In particular, the doped metal oxides exhibit the tailored electronic structure of materials to increase the conductivities, to reduce the trap-state density, as well as to modify the energy levels matching by modulating the carrier density. So far, many semiconducting metal oxides including SnO<sub>2</sub> have been demonstrated the improved electrical properties with the elemental doping, and they have been successfully employed in high-performance optoelectronic devices. [2] In specific, the electron transport properties of SnO<sub>2</sub> have been improved by various doping elements with different valence states, such as Li<sup>+</sup> or Mg<sup>2+</sup>, yet they still suffer from bulk defects, relatively low electron mobility, requirement of high-temperature sintering process, and thus the corresponding devices have shown inferior PCEs than the TiO<sub>2</sub>-based planar perovskite solar cells. [3-5] Thus, more facile elemental doping of SnO<sub>2</sub> is needed not only for achieving higher photovoltaic performance but also via the more compatible method for low-temperature solution processing. We herein synthesized Zr-doped SnO<sub>2</sub> colloidal nanoparticles (NPs) were synthesized by the successive hydrolysis-dehydration reaction in aqueous solution, as depicted in Figure 1. The opaque precursor solution became the transparent yellowish solution, and these solutions were stable up to several months regardless of Zr-doping. Figure 1b shows the XRD patterns of un-doped and Zr-doped SnO<sub>2</sub> NPs thin films with a specific scatterings at 26.6°, 33.8°, 38.0°, 51.8°, 54.4°, 62.0°, and 65.4° correspondingly indexed to (110), (101), (200), (211), (220), (310), and (112) reflections of the tetragonal phase of crystalline SnO<sub>2</sub> (JCPDS card no. 41-1445). [6] The planar heterojunction device exhibited a substantial improvement of power conversion efficiency from 17% to 19%, which suggests an efficacy of Zr-doping of SnO<sub>2</sub> NPs for use in perovskite solar cells as an electron transporting layer. (Figure 2) The details of fundamental electronic properties of Zr-doped SnO<sub>2</sub> NPs and the corresponding device analyses will be discussed.

- [1] S.K. Pathak *et al.*, *Adv. Funct. Mater.* **24**, 6046 (2014).  
 [2] J.H. Lee *et al.*, *Electrochim. Acta* **284**, 253 (2018).  
 [3] J.H. Lee *et al.*, *J. Power Sources.* **412**, 425 (2019).  
 [4] M. Park *et al.*, *Nano Energy* **26**, 208 (2016).  
 [5] L. Xiong *et al.*, *J. Mater. Chem. A* **4**, 8374 (2016).  
 [6] G. Yang *et al.*, *Adv. Mater.* **30**, 1706023 (2018).

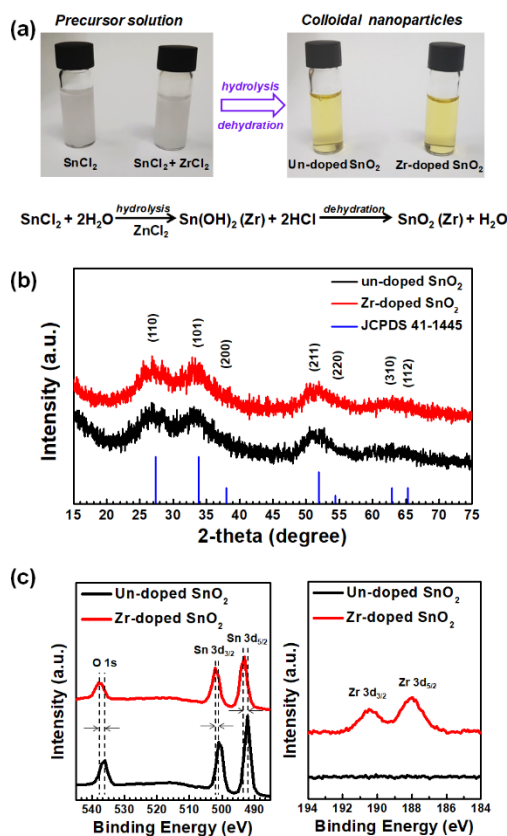


Fig.1: (a) Photograph images for precursor and colloidal NPs solutions with and without Zr-doping. (b) X-ray diffractograms and XPS spectra of un-doped and Zr-doped  $\text{SnO}_2$  NPs thin films.

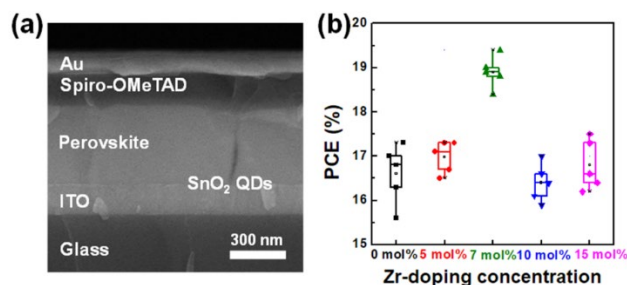


Fig.2: (a) Cross-sectional SEM image of device employing Zr-doped  $\text{SnO}_2$  NPs, (b) statistical analysis of PCEs of the devices with regard to Zr-doping concentration.

## The Modification of the Band Gap, Energy Transfer Between Dopants, and Crystal Structure Refinement of Ce<sup>3+</sup> and Cr<sup>3+</sup> Co-Doped Lu<sub>3</sub>(Al,Ga)<sub>5</sub>O<sub>12</sub> Persistent Luminescence Phosphors

J. Kim<sup>1</sup>, C.K. Lee<sup>1,2</sup>, and Y.J. Kim<sup>1</sup>

<sup>1</sup>*Department of Advanced Materials Engineering, Kyonggi University, Suwon 16227, Korea*

<sup>2</sup>*Malvern Panalytical, a division of Spectris Korea Ltd., Seongnam 13595, Korea*

*yjkim@kgu.ac.kr*

Persistent luminescence phosphors can emit lights in the ultraviolet, visible, or near infrared regions for a long time (minutes ~ days) after the excitation irradiation has been ceased. They have attracted great attentions in the fields of displays, safety signs, bioimaging, photocatalysts, and solar cells [1]. The electron transfers between luminescent and trapping centers via the conduction band of host materials are responsible for the persistent luminescence. Accordingly, it is important to control the band gap of the host materials [1,2].

In this study, Ce<sup>3+</sup> and Cr<sup>3+</sup> ions co-doped Lu<sub>3</sub>Al<sub>5-x</sub>Ga<sub>x</sub>O<sub>12</sub> (LAG<sub>x</sub>O:Ce<sup>3+</sup>,Cr<sup>3+</sup>) nanoparticles were prepared using a sol-gel-combustion process, and a correlation between the crystal structure and persistent luminescence was investigated. Lu<sub>3</sub>Al<sub>5</sub>O<sub>12</sub> has a wide band gap of ~ 7.0 eV, and its unit cell consists of two distinct Al<sup>3+</sup> sites (tetrahedral and octahedral sites). The Rietveld refinement confirmed that the Ga<sup>3+</sup> ions preferred the tetrahedral sites rather than the octahedral sites. The photoluminescence spectra exhibited the broad green emission bands of Ce<sup>3+</sup> and weak red peaks of Cr<sup>3+</sup>. The band gap of LAG<sub>x</sub>O gradually decreases with an increase in the amount of Ga: approximately 7.0, 6.5, 6.3, and 5.8 eV for  $x = 0, 2, 3,$  and  $5,$  respectively [3]. This behavior affected the de-trapping properties and thus led to the persistent luminescence of Ce<sup>3+</sup> for  $x = 2$  and  $3,$  which resulted from the electron transfer between Ce<sup>3+</sup> luminescent and Cr<sup>3+</sup> trapping centers via the conduction band of LAG<sub>x</sub>O. In addition, the evolution of the photoluminescence spectra was explained based on the crystal field strength, particle morphology, and fluorescence decay curves.

[1] Y. Li *et al.*, Chem. Soc. Rev. **45**, 2090 (2016).

[2] J. Ueda *et al.*, J. Mater. Chem. C **3**, 5642 (2015).

[3] A. Katelnikovas *et al.*, J. Lumin. **131**, 2754 (2011).

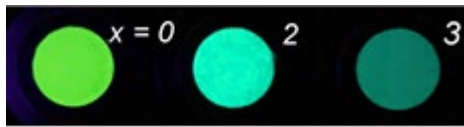
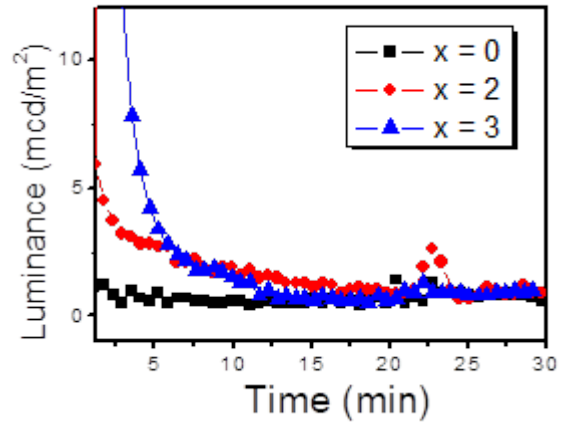
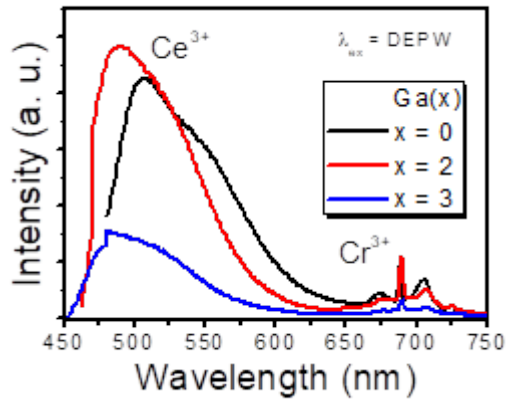


Fig.1: (Top) The photoluminescence spectra and (Bottom) photographs of  $\text{Lu}_3\text{Al}_{5-x}\text{Ga}_x\text{O}_{12}:\text{Ce}^{3+},\text{Cr}^{3+}$  powders under dominant excitation peak wavelengths (450 nm for  $x = 0$ ; 430 nm for  $x = 2$  and 3).

Fig.3: Persistent decay curves of  $\text{Lu}_3\text{Al}_{5-x}\text{Ga}_x\text{O}_{12}:\text{Ce}^{3+},\text{Cr}^{3+}$  powders.

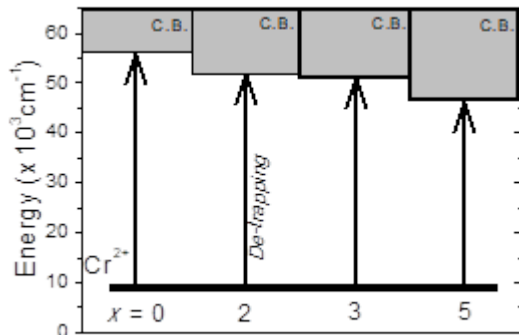


Fig.2: Band structures of  $\text{Lu}_3\text{Al}_{5-x}\text{Ga}_x\text{O}_{12}:\text{Ce}^{3+},\text{Cr}^{3+}$  powders.

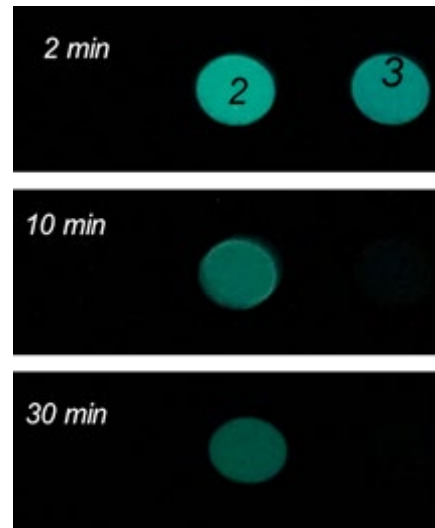


Fig.4: Photographs of  $\text{Lu}_3\text{Al}_{5-x}\text{Ga}_x\text{O}_{12}:\text{Ce}^{3+},\text{Cr}^{3+}$  powders after switching off the irradiation.

## Nanocrystal Quantum Dot Lasing: From Novel Concepts to Novel Devices

V.I. Klimov

*Chemistry Division, Los Alamos National Laboratory, Los Alamos, NM, 87545, USA*

*klimov@lanl.gov*

Colloidal semiconductor quantum dots (QDs) are attractive materials for realizing highly flexible, solution-processable optical gain media with readily tunable operational wavelengths [1, 2]. However, QDs are difficult to use in lasing due to extremely short optical gain lifetimes limited by nonradiative Auger recombination [3]. This, in particular, is a serious obstacle for realizing cw optically and electrically pumped lasing devices. Recently, we have explored several approaches for mitigating the problem of Auger decay by taking advantage of a new generation of core/multi-shell QDs with a radially graded composition that allow for considerable (nearly complete) suppression of Auger recombination [4, 5]. Using these specially engineered QDs, we have been able to realize optical gain with direct-current electrical pumping [4], which has been a long-standing goal in the field of colloidal nanostructures. Further, we have applied these dots to practically demonstrated the viability of a ‘*zero-threshold optical gain*’ concept using not neutral but negatively charged particles wherein the pre-existing electrons block either partially or completely ground-state absorption (Fig. 1a) [5, 6]. Such charged QDs are optical-gain-ready without excitation, which allows us to reduce the lasing threshold to record-low values that are well below a fundamental single-exciton-per-dot limit (Fig. 1b-d) [6]. Most recently, we have developed QD devices that operate as both an electroluminescent (EL) structure and a distributed feedback optically pumped laser [7]. By carefully engineering a refractive-index profile across the device stack, we have been able to demonstrate low-threshold lasing even with a very thin EL-active region, which comprises only three monolayers of the QDs. All of these recent developments demonstrate a considerable promise of colloidal QDs for implementing solution-processable optically and electrically pumped lasers operating across a wide range of wavelengths.

- [1] V.I. Klimov *et al.*, *Science* **290**, 314 (2000).
- [2] V.I. Klimov *et al.*, *Nature* **447**, 441 (2007).
- [3] V.I. Klimov *et al.*, *Science* **287**, 1011 (2000).
- [4] J. Lim *et al.*, *Nat. Mater.* **17**, 42 (2018).
- [5] K. Wu *et al.*, *Nat. Nanotech.* **12**, 1140 (2017).
- [6] O.V. Kozlov *et al.*, *Science* **365**, 672 (2019).
- [7] J. Roh *et al.*, *Nat. Comm.*, *in press* (2019).

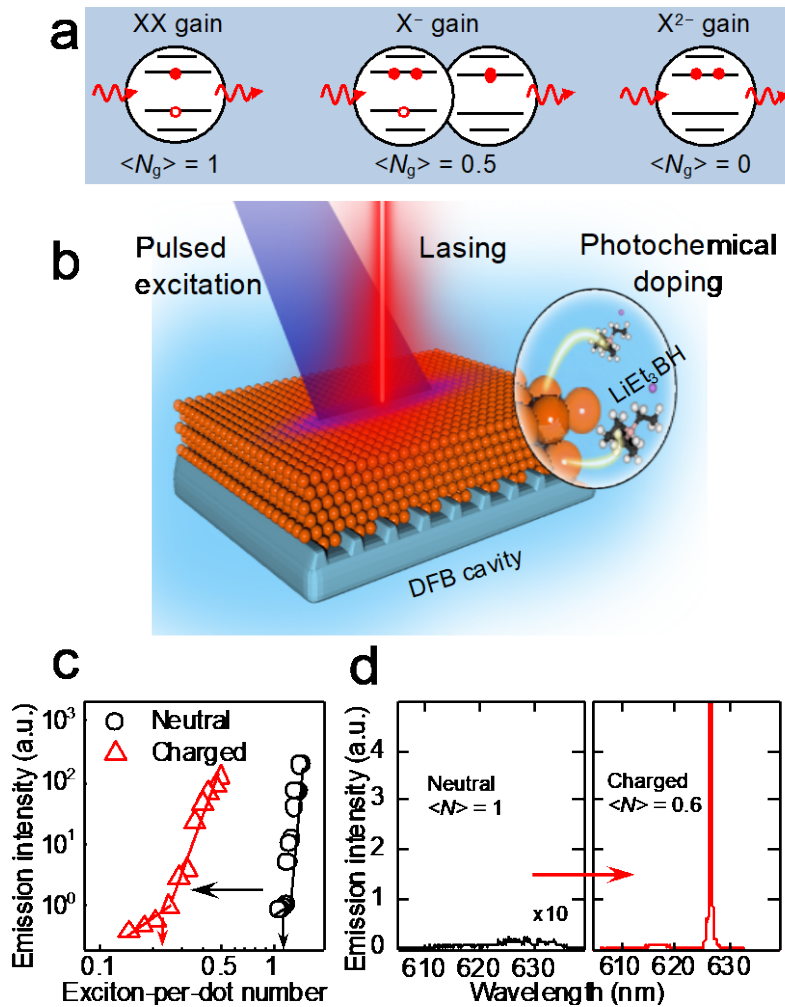


Fig.1: Sub-single-exciton lasing using charged quantum dots (QDs) [5, 6]. a, The condition of optical gain threshold for neutral (left), singly-charged (middle), and doubly-charged (right) QDs is met when the average per-dot number of excitons ( $\langle N \rangle$ ) introduced by a pump source is, respectively, 1, 0.5, and 0. The latter corresponds to the peculiar situation of 'zero-threshold optical gain' [5]. b, Schematics of a charged-QD distributed-feedback (DFB) laser. This device is immersed into a solution of  $\text{LiEt}_3\text{BH}$ , which acts as a sacrificial photo-reductant. Optical pumping of the device leads to in situ QD photodoping with up to  $\sim 3$  extra electrons per-dot on average ( $\langle n_e \rangle$ ). c, The dramatic, more than 4-fold reduction of the lasing threshold upon QD charging. In the case of  $\langle n_e \rangle$  of  $\sim 3$ , the lasing threshold is reduced to the sub-single exciton value of  $\langle N \rangle = 0.31$ . d, Prior to charging, the excitation level  $\langle N \rangle = 1$  does not lead to lasing (left panel). However, upon charging with  $\langle n_e \rangle = 3.1$ , the same sample lases even at a lower pump level  $\langle N \rangle = 0.6$  (right panel).

## Quantum Mechanical Shift Current in Polar Semiconductors

M. Kawasaki<sup>1,2</sup>, M. Nakamura<sup>1</sup>, H. Hatada<sup>2</sup>, S. Inagaki<sup>2</sup>, M. Sotome<sup>1</sup>, T. Morimoto<sup>2</sup>,  
T. Kaneko<sup>1</sup>, N. Ogawa<sup>1</sup>, N. Nagaosa<sup>1,2</sup>, and Y. Tokura<sup>1,2</sup>

<sup>1</sup>*RIKEN Center for Emergent Matter Science (CMES), Wako, 351-0198, Japan*

<sup>2</sup>*Department of Applied Physics and Quantum-Phase Electronics Center (QPEC),*

*University of Tokyo, Tokyo, 113-8656, Japan*

*m.kawasaki@riken.jp*

We discuss a novel manifestation of quantum mechanical current flow in solids upon photoexcitation. From old days, bulk photovoltaic effect has been known to exist in non-centrosymmetric crystals such as poled ferroelectrics exemplified by BaTiO<sub>3</sub> [1]. Naive explanation was that the drift current flows due to electric field uncompensated by insufficient formation of electric double layer on the surfaces of polar crystals. Now, it is proposed and confirmed that a quantum mechanical effect, described by the Berry's connection of Floquet bands, drives photocurrent called "shift current" as a second order optical process [2, 3]. We present experimental observations of photovoltaic effect in such polar materials systems as LaFeO<sub>3</sub>/SrTiO<sub>3</sub> interfaces [4], a ferroelectric organic TTF-CA [5], and a polar semiconductor SbSI [6]. Ultrafast THz spectroscopy [7] and device physics [8, 9] studies have elucidated interesting features of the shift current. This phenomenon is one of the most important topics of topological electronics [10].

- [1] W.T.H. Koch *et al.*, *Ferroelectrics* **13**, 305 (1976).
- [2] S. M. Young *et al.*, *Phys. Rev. Lett.* **109**, 116601 (2012).
- [3] T. Morimoto and N. Nagaosa, *Sci. Adv.* **2**, e1501524 (2016).
- [4] M. Nakamura *et al.*, *Phys. Rev. Lett.* **116**, 156801 (2016).
- [5] M. Nakamura *et al.*, *Nature Commun.* **8**, 281 (2017).
- [6] N. Ogawa *et al.*, *Phys. Rev. B (R)* **91**, 241203 (2017).
- [7] M. Sotome *et al.*, *PNAS* **116**, 1929 (2019).
- [8] M. Nakamura *et al.*, *Appl. Phys. Lett.* **113**, 232901 (2018).
- [9] T. Morimoto *et al.*, *Phys. Rev. Lett.* **121**, 267401 (2018)
- [10] Y. Tokura *et al.*, *Nature Phys.* **13**, 1056 (2017).

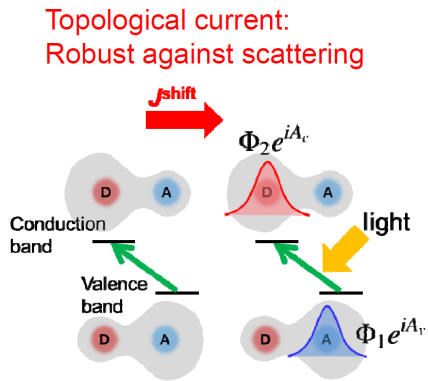


Fig.1: Real space schematic of photo-excitation of electrons and resulting shift current in a non-centrosymmetric semiconductor.

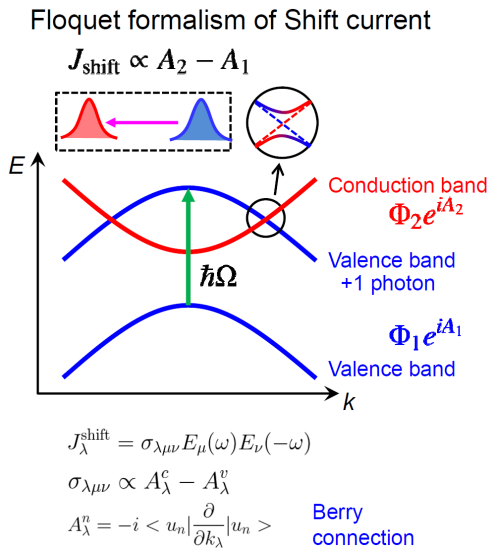


Fig.2: Momentum space schematic of photo-excitation of Floquet band and resulting shift current due to Berry connection.

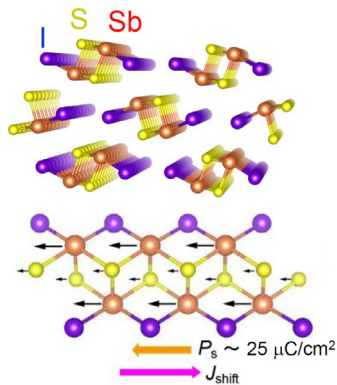


Fig.3: Schematics of the crystal structure and electric polarization in a ferroelectric semiconductor SbSI.

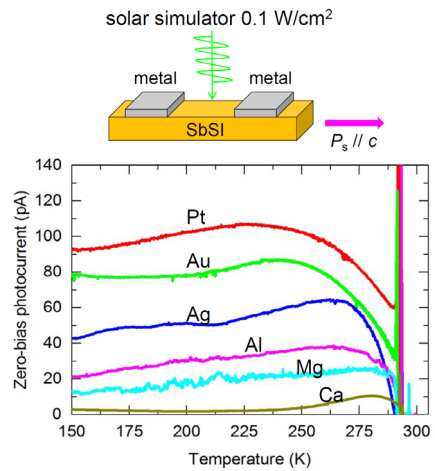


Fig.4: Electrode dependence of the shift current for SbSI.

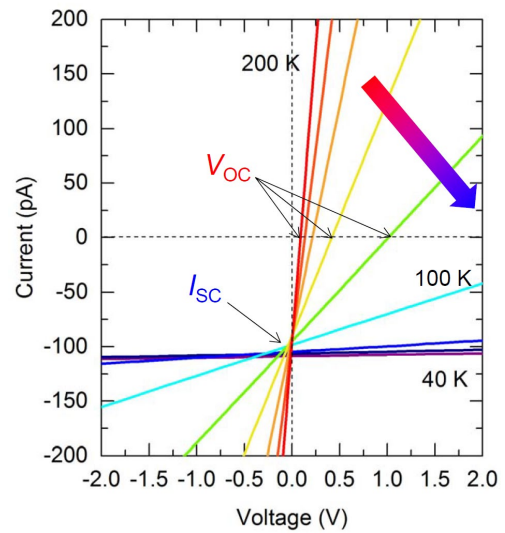


Fig.5: Current-voltage relation as a function of temperature.

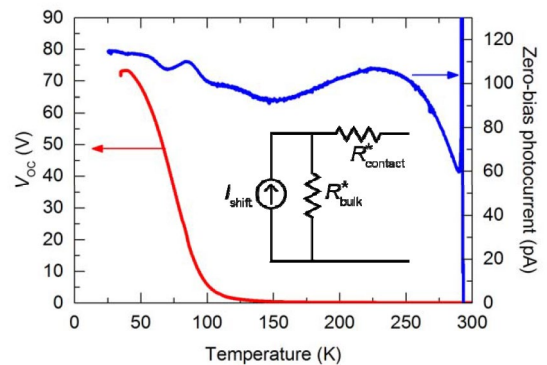


Fig.6: Shift current is nearly temperature independent, while open circuit voltage strongly depends of temperature. Inset is a possible equivalent circuit.

## Magneto-Transports in a Light Irradiated Ge/SiGe Two-Dimensional Hole system

G.G. Maia<sup>1</sup>, K. Sawano<sup>2</sup>, and A. Oiwa<sup>1</sup>

<sup>1</sup>The Institute of Scientific and Industrial Research, Osaka University,  
Ibaraki, Osaka 567-0047, Japan

<sup>2</sup>Advanced Research Laboratories, Tokyo City University,  
Setagaya, Tokyo 158-0082, Japan  
oiwa@sanken.osaka-u.ac.jp

Si-based quantum dots (QDs) are comprehensively studied toward realization of fault-tolerant quantum computing because of relatively long electron spin coherence time due to suppressed influenced nuclear spins. Recently QDs formed in a Ge/SiGe two dimensional hole gas has been reported as an alternative candidate for spin qubits [1]. Here we focus on the magneto-transport properties of a Ge two-dimensional hole system with light irradiations toward quantum interfaces, which can transmit quantum states from photons to hole spins, as a constituent of quantum repeaters.

We fabricated a Hall bar from a 20-nm Ge/Ge<sub>0.6</sub>Si<sub>0.4</sub> quantum well and performed standard transport measurements with LED irradiations to elucidate the presence of persistent photoconductivity. Shubnikov-de Haas oscillation was observed. The carrier density and mobility were obtained  $7 \times 10^{11} \text{ cm}^{-2}$  and  $8500 \text{ cm}^2/\text{Vs}$ , respectively, in dark. Even after 950-nm LED irradiations for several times, the carrier density and mobility did not change significantly, unlike the persistent photoconductivity in GaAs/AlGaAs heterostructures. This indicates the robustness of the gate-defined nanostructures formed in the Ge/SiGe hole systems.

[1] N.W. Hendrickx *et al.*, Nat. Comm. **9**, 2835 (2018).

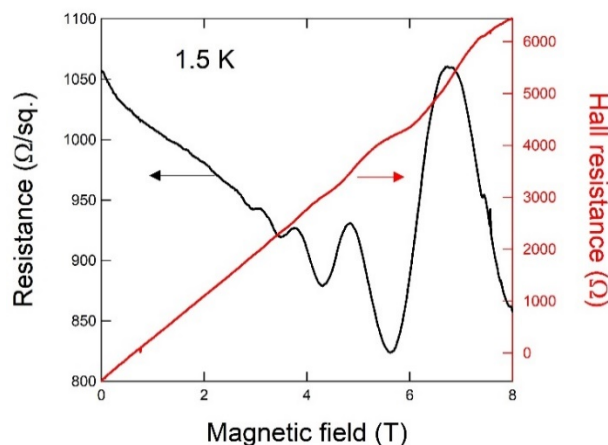


Fig. 1: Magnetoresistance and Hall resistance of a Ge/SiGe quantum well measured at 1.5 K.

## Tunable Strong Coupling in Terahertz Metasurfaces

R. Yahiaou, Z.A. Chase, C. Kyaw, and T.A. Searles

*Department of Physics and Astronomy, Howard University, Washington, D.C. 20059, USA*

*Thomas.searles@howard.edu*

Recently, the study of ultrastrong light-matter coupling has gained increased interest due to its potential application in optoelectronics, plasmonics and circuit quantum electrodynamics. One common way to achieve strong coupling is to place an emitter near or inside an optical cavity. In this case, the emitter-cavity system, the spatial overlap between the emitters and the cavity is often the key factor that limits the light-matter coupling strength. The cavities can be either photonic microcavities, which can have very high quality factors, or surface plasmon resonators, whose mode volume can be in the deep subwavelength regime. In contrast to microcavities, where the light field is confined by two metallic layers or dielectric mirrors, an alternative approach to achieve strong coupling is provided by metamaterials (MMs) in which the confinement is provided by the evanescent field of localized plasmons. This has led to the demonstration of strong-coupling regime with a number of quantum systems including phonons [1], intersubband transitions [2] and cyclotron resonances [3]. In addition, resonant coupling leads to light-matter hybridization into two normal modes with an energy separation known as the vacuum Rabi splitting (VRS).

In this work, we investigate a THz planar metamaterial and observe the excitation of a polaritonic state as well as a VRS with a coupling strength of  $\sim 21\%$ . Strong splitting results in the formation of a forbidden frequency gap that can be evaluated as a transparency window caused by the hybridization of two eigenmode (Figure 1). The physics of the transparency window is analogous to the lattice induced transparency effect [4] in which there are limited demonstrations in the literature of strong coupling due to cavity-cavity interactions. Further, we show that by increasing the capacitive gap width of the MM unit cell, we increase the overall capacitance of the MM and demonstrate an anti-crossing behavior; a key signature to strong-light matter coupling. Lastly, we present graphene micro-ribbons and a nanohole array in a carbon nanotube film as two tunable platforms for actively tuned strong coupling in hybrid metasurface devices.

[1] D.J. Shelton *et al.*, *Nano Lett.* **11**, 2104 (2011).

[2] A. Gabbay *et al.*, *Appl. Phys. Lett.* **98**, 203103 (2011).

[3] G. Scalari *et al.*, *Science* **335**, 1323 (2012).

[4] J.A. Burrow *et al.*, *Opt. Lett.* **44**, 2705 (2019).

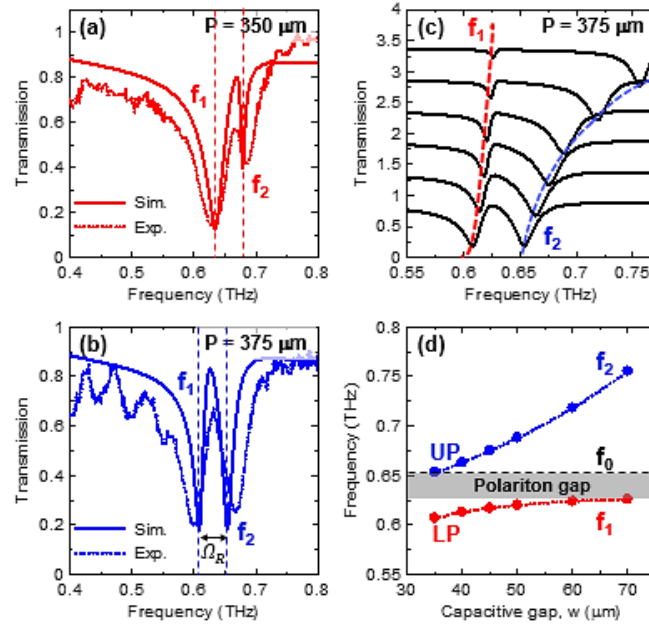


Fig.1: (a)-(b) Simulated (solid line) and measured (dashed line) transmission spectra of the CSRRs array for  $P = 350 \mu\text{m}$  and  $375 \mu\text{m}$ , respectively. (c) The transmission spectra for different values of the capacitive gap width  $w$ , when  $P = 375 \mu\text{m}$ . From bottom to top,  $w = 35, 40, 45, 50, 60$  and  $70 \mu\text{m}$ , respectively. (d) The simulated resonance position of the excited eigenmodes extracted from the spectra.

## Optical Nonlinear Waves in a Graphene Waveguide

G.T. Adamashvili

*Department of Physics, Technical University of Georgia, Kostava str. 77, 0179, Georgia  
guram\_adamashvili@ymail.com*

A theory of resonant breathers under the condition of nonlinear coherent interaction of waveguide TM-modes with a two-dimensional layer and a graphene monolayer (or graphene-like two-dimensional material) is developed. Resonance nonlinear pulses can propagate in the system when the waveguide TM-modes are in resonance with the optically active impurity atoms or semiconductor quantum dots of the transition layer. The optically resonant breathers of waveguide TM-modes can be excited within the McCall-Hahn mechanism, where a nonlinear coherent interaction waveguide TM-modes takes place via Rabi-oscillations of the carrier density, if the conditions for self-induced transparency are fulfilled. When the area of the pulse of waveguide TM-modes is rather small, a breather ( $0\pi$  pulse) is formed. Explicit analytical and numerical expressions for a surface breather ( $0\pi$  pulse) of self-induced transparency are obtained [1]. It is shown that the optical conductivity of graphene exponentially reduces the amplitude of the breather in the process of propagation.

[1] G.T. Adamashvili and D.J. Kaup, Phys. Rev. A **99**, 013832 (2019).

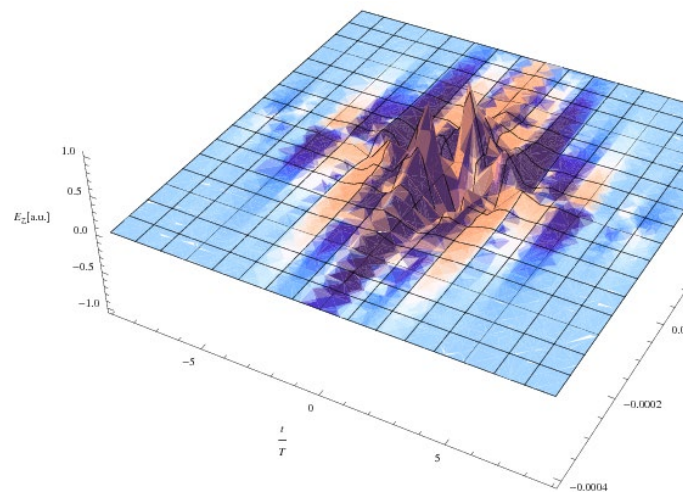


Fig.1: The function  $E_z(x, 0, t)$  the nonlinear wave for the waveguide TM-mode is presented.

## **Bethe Salpeter Calculations of Trions in MoS<sub>2</sub>**

D.R. Gulevich<sup>1</sup>, Y.V. Zhumagulov<sup>1</sup>, A.V. Vagov<sup>2</sup>, and V. Perebeinos<sup>3</sup>

<sup>1</sup>*ITMO University, St. Petersburg 197101, Russia,*

<sup>2</sup>*Theoretische Physik III, University at Bayreuth, 95440 Bayreuth, Germany,*

<sup>3</sup>*Department of Electrical Engineering, University at Buffalo,*

*The State University of New York, Buffalo, NY 14260, USA*

*vasilipe@buffalo.edu*

Transition metal dichalcogenide monolayers are semiconductors with a direct transition at the K-point of the Brillouin zone. The band structure of these materials has unique features that makes them ideal candidates for valleytronics. Tightly bound negative trions, a quasiparticle composed of two electrons and a hole, can be optically optically created with valley and spin polarized holes. They possess a large binding energy and large oscillator strength, such that they dominate optical spectra even at room temperature. Here, we solve Bethe-Salpeter equation for three particle wavefunction at finite momentum. Our results enable us to explain existing data on temperature and doping dependence and predict new spectroscopic features in doped MoS<sub>2</sub>.

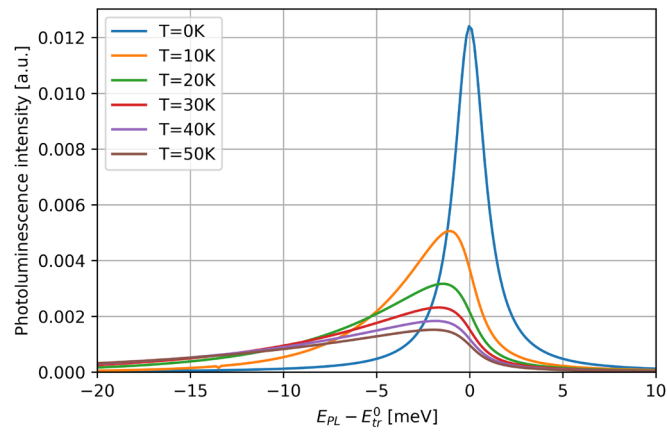


Fig.1: Temperature dependence of the calculated photoluminescence of a doped MoS2. As the temperature increases, we find an asymmetric broadening and red shift of the emission peak.

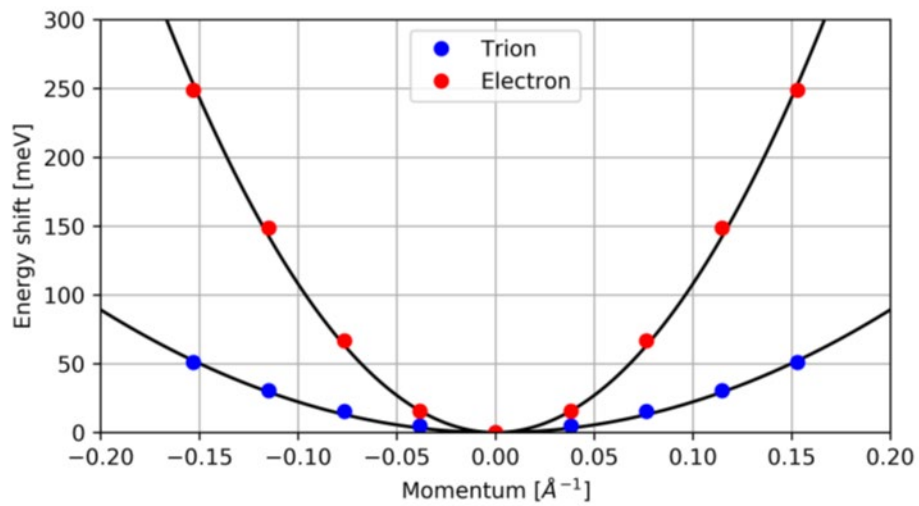


Fig.2: Band structure calculations of a trion, showing approximately two-fold enhancement of the effective mass due to the Coulomb interactions.

## Plasmon Reflection in Graphene Junctions: Transfer Matrix Approach

V. Semenenko and V. Perebeinos

*Department of Electrical Engineering, University at Buffalo,*

*SUNY, Buffalo, New York 14260-1900, USA*

viachesl@buffalo.edu

In this work, we apply transfer matrix (TM) approach for direct calculation of complex reflection and transmission coefficients in graphene junctions of three different types (see Fig. 1a-c). To do this, in contrast to original problem of plasmon scattering, where regions of incident/reflected and transmitted plasmons are infinite (see Fig. 1a-c) and Refs. 1–3), we transform the original junctions geometries to periodic ones (see Fig. 1d-f). Our analysis shows that TM-approach does work in certain periodic structures, which are mainly determined by lengths  $W, L$  of the areas in a unit cell and by a complex phase shift between the corresponding oscillations in adjacent unit cells, according to the Bloch theorem. Calculated reflectance coefficients (see Figs. 2-4) are verified by 1) matching them with analytical expressions known previously [1, 2] and 2) by checking energy flux conservation in the scattered plasmons.

For the case of discontinuous-wafer-junction (see Fig. 4) we have found the following model function fitting well the calculated data:

$$r = \frac{|\lambda_1^\alpha - \lambda_2^\alpha|^\beta}{(\lambda_1^\alpha + \lambda_2^\alpha)^\beta}, \quad \lambda_k = (1 + \varepsilon_k)^{-1} \quad (1)$$

with the parameters shown in the table.

$\varepsilon_2$	$\alpha$	$\beta$
1	0.899	1.838
3.9	0.851	1.931
7	0.835	1.921
10	0.849	1.969

Obtained results can be useful in designing cavities and waveguides based on graphene and other conducting 2D materials.

[1] B. Rejaei, A. Khavasi, *J. Opt.* **17**, 075002 (2015).

[2] B.-Y. Jiang *et al.*, *Opt. Ex.* **26**, 17209 (2018).

[3] A.J. Chaves *et al.*, *Phys. Rev. B* **97**, 035434 (2018).

[4] V. Ryzhii *et al.*, *J. Appl. Phys.* **96**, 7625 (2004).

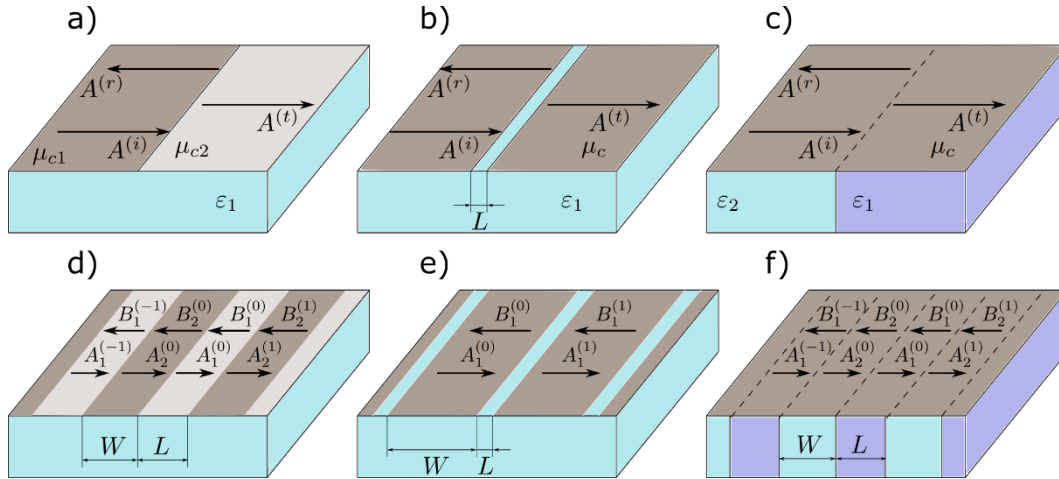


Fig. 1: Sketches illustrating original scattering problems (top row) and corresponding periodic structures for analysis using transfer matrix approach (bottom row) in the cases of three types of junctions: (a, d) discontinuous graphene doping, (b, e) gap in graphene and (c, f) discontinuous dielectric constant of supporting wafer.

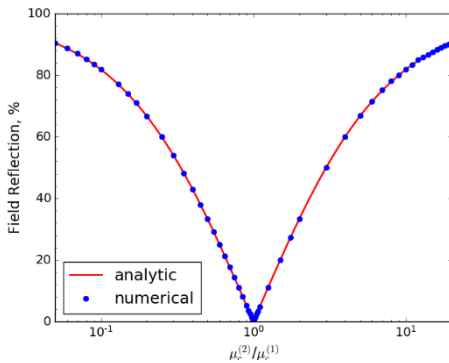


Fig. 2: Numerically (circles) and theoretically (solid line) calculated field reflection coefficient's absolute value in the case of discontinuous-doping-level-junction versus ratio of the Fermi energies on the right to left sides of the junction. Numerical calculations were conducted for suspended graphene i.e. for  $\epsilon_1=1.0$  and fixed Fermi energy of graphene in the area of incident plasmon on the left size of the junction  $\mu_c^{(l)}=300$  meV.

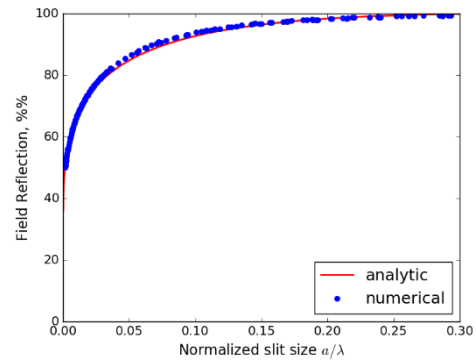


Fig. 3: Numerically (circles) and theoretically (solid line) calculated field reflection coefficient's absolute value in the case of gap-in-graphene-junction versus ratio of the gap's width to plasmon wavelength in graphene. Numerical calculations were conducted for suspended graphene i.e. for  $\epsilon_1=1.0$  and Fermi energy 300 meV.

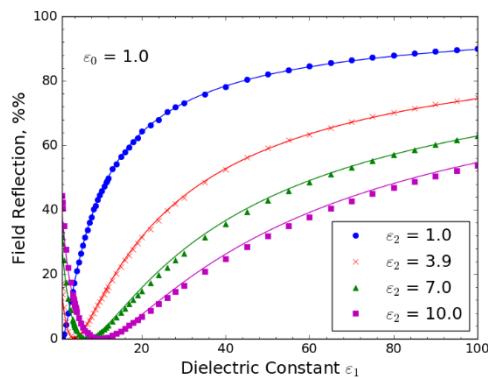


Fig. 4: Numerically calculated field reflection coefficient's absolute value in the case of discontinuous-wafer-junction versus dielectric constant  $\epsilon_1$  of the wafer under the transmitted plasmon area. The dependencies are calculated for Fermi energy of graphene equals to 300 meV and for different dielectric constants  $\epsilon_2$  of wafer under the incident plasmon area. Solid line of certain color is the fit of the same color dependency with the model function (1).

**PVRD-FASP:  
A Tool for Modeling Reliability and Durability of CdTe Solar Cells\***

A.R. Shaik and D. Vasileska

*School of Electrical, Computer and Energy Engineering, Arizona State University,*

*Tempe, AZ, 85287-5706, USA*

*vasileska@asu.edu*

The study of defect dynamics is crucial to understand and develop innovative ways to improve reliability of electronic and photovoltaic devices. Point defects are well studied in modeling the diffusion/thermal activation of dopants [1]. Sentaurus (Synopsys TCAD tool) has ChargedReact model for diffusion [2] while Victory (Silvaco TCAD tool) has five-stream model for diffusion [3]. Both of these models treat dopant diffusion in materials comprehensively by solving the continuity equations for five species, namely dopant, two point defects (interstitial and vacancies) and two dopant-defect pairs. These are the most advanced and accurate models available.

Herein, we present PVRD-FASP solver ([www.pvrdfasp.com](http://www.pvrdfasp.com)) which, for the first time, treats defects and carriers on an equal footing and calculates the driving fields by simultaneously solving the 2D Poisson with the 2D drift-diffusion-reaction equations [4]. The simulator uses calculated density functional theory (DFT) results for the diffusion barriers, diffusion prefactors, transition levels, formation energies etc., and provides a path to integrate the defect chemical reaction formalism into TCAD modeling. A graphical user interface (GUI) was created in the initial stages of the project that allows easy incorporation of material/DFT parameters, geometry, chemical reactions of interest and the associated parameters and analysis of results. The tool is robust, it has much improved stability and accuracy of numerical algorithms with respect to the previous version of the PREDICTS Unified Solver [3]. The PVRD solver has been verified by comparison to Silvaco simulations of structures of interest, and used in the analysis of Cu diffusion in CdTe, impact of interface states, explaining experimentally observed hysteresis in transient analysis, etc.

[1] Sentaurus Process User Guide, Synopsys, version P-2019.03 (2019).

[2] Victory Process User's Manual, Silvaco, version 7.22.3.R (2018).

[3] D. Guo *et al.*, *J. Phys D: Appl. Phys.* **51**, 15 (2018).

[4] A.R. Shaik *et al.*, *IEEE J. Photovoltaics* **9**, 1602 (2019).

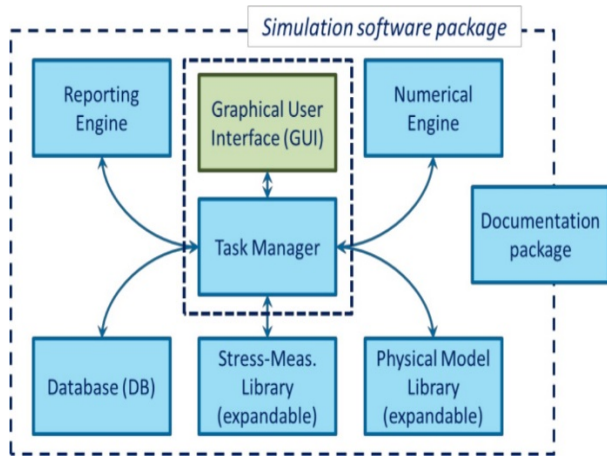


Fig.1: 1 Software modules used in coding the PVRD-FASP solver:

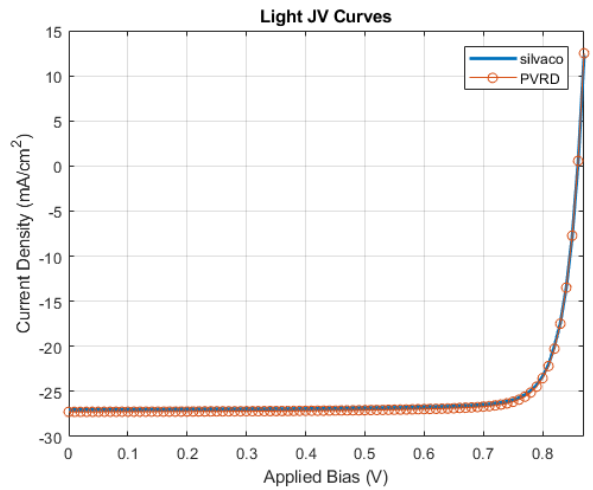


Fig.2: Comparison of JV curves for CdTe solar cell. This comparison validates our formalism to study point defects and charge carriers on equal footing.

Table 1. Reactions considered in the Cu diffusion in single crystal

**Reaction Number    Reactions in ZnTe Layer**

- 1                     $[Cu_iCu_c]^0 \Leftrightarrow Cu_i^+ + Cu_c^-$
- 2                     $Null \Leftrightarrow e^- + h^+$
- 3                     $N_A^0 \Leftrightarrow N_A^- + h^+ ; N_A^- \Leftrightarrow N_A^0 + e^-$
- 4
- 5
- 6
- 7

**CdTe simulation.**

**Reactions in CdTe Layer**

- $[Cu_iCu_c]^0 \Leftrightarrow Cu_i^+ + Cu_c^-$
- $Null \Leftrightarrow e^- + h^+$
- $Cu_i^+ + Cd_c^0 \Leftrightarrow [Cu_iCd_c]^+ \Leftrightarrow Cu_c^- + Cd_i^{2+}$
- $Cu_i^+ \Leftrightarrow Cu_i^0 + h^+ ; Cu_i^0 \Leftrightarrow Cu_i^+ + e^-$
- $Cu_c^- \Leftrightarrow Cu_c^0 + e^- ; Cu_c^0 \Leftrightarrow Cu_c^- + h^+$
- $Cd_i^{2+} \Leftrightarrow Cd_i^+ + h^+ ; Cd_i^+ \Leftrightarrow Cd_i^{2+} + e^-$
- $Cd_i^+ \Leftrightarrow Cd_i^0 + h^+ ; Cd_i^0 \Leftrightarrow Cd_i^+ + e^-$

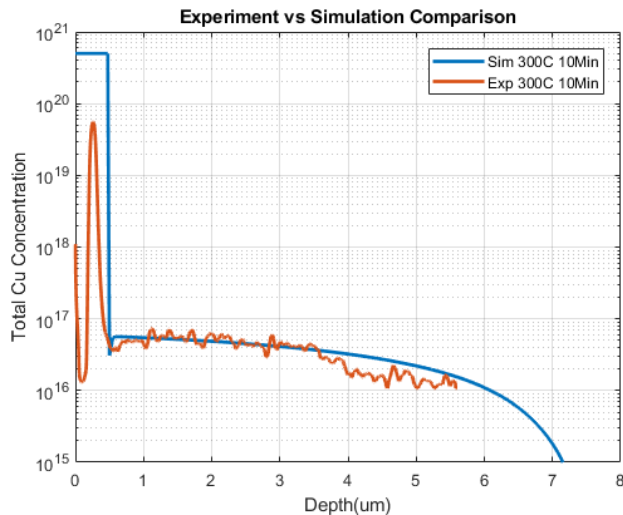


Fig.3a: Copper profile comparison with 10min 300°C anneal recipe

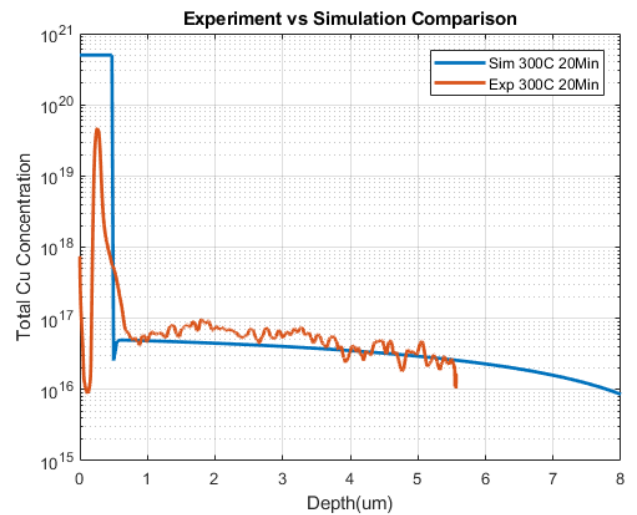


Fig.3b: Copper profile comparison with 20min 300°C anneal recipe

## High-Speed Growth of III-V Materials by HVPE for Low-Cost Smart Stacked Multijunction Solar Cells

T. Sugaya<sup>1</sup>, R. Oshima<sup>1</sup>, Y. Shoji<sup>1</sup>, K. Makita<sup>1</sup>, and A. Ubukata<sup>2</sup>

<sup>1</sup>*National Institute of Advanced Industrial Science and Technology (AIST),  
1-1-1 Umezono, Tsukuba, Ibaraki 305-8568, Japan*

<sup>2</sup>*Taiyo Nippon Sanso Corporation, Tsukuba, Ibaraki 300-2611, Japan  
t.sugaya@aist.go.jp*

Cost reduction and improved conversion efficiency are the most important issues in the wide-scale deployment of solar photovoltaic systems. Multijunction solar cells provide ultra-high efficiencies by the effectively utilizing the solar spectrum through the interconnection of different kinds of solar cells. Even though multijunction solar cells have the highest reported efficiencies and have been commercialized for space and concentrator applications, they are not used widely because of their high cost. Therefore, it is necessary to lower the manufacturing cost for implementing large-scale terrestrial III-V modules. In our previous work, we have proposed a novel low-cost semiconductor bonding method called smart stack technology for mechanically stacked multijunction solar cells. This technology utilizes Pd nanoparticle alignment to interconnect the top and bottom cells with low bonding resistances and minimal optical absorption losses as shown in Fig. 1 [1]. Pd nanoparticle alignment can be formed by a self-assembled phenomenon using low-cost spin coating method, which is very attractive for interconnecting different kinds of solar cells. We have demonstrated an InGaP/AlGaAs/Si 3-junction solar cell with an efficiency of 30.8% under AM1.5 as shown in Fig.2 [2]. An InGaP/AlGaAs top cell was grown by metal organic vapor phase epitaxy. However, the epitaxial cost of III-V materials is extremely high, and it is essential to reduce the material and depreciation costs for III-V top cells. High speed growth would be a possible pathway to lower the cost of III-V devices. We have developed hydride vapor-phase epitaxy (HVPE) to obtain ultrafast growth and low material cost of III-V solar cells. We achieved ultra-high growth rates of over 120  $\mu\text{m/h}$  for GaAs [3] and 140  $\mu\text{m/h}$  for InGaP [4] growth using HVPE as shown in Fig. 3 and Fig. 4, respectively. The solar cell characteristics of these materials will be discussed in the presentation.

[1] H. Mizuno *et al.*, Appl. Phys. Lett. **101**, 191111 (2012).

[2] K. Makita *et al.*, Proc. EUPVSEC, 1AP.1.1 (2019).

[3] R. Oshima *et al.*, J. Photovolt. **9**, 154 (2019), Proc. ICCGE (2019).

[4] Y. Shoji *et al.*, Appl. Phys. Expr. **12**, 052004 (2019).

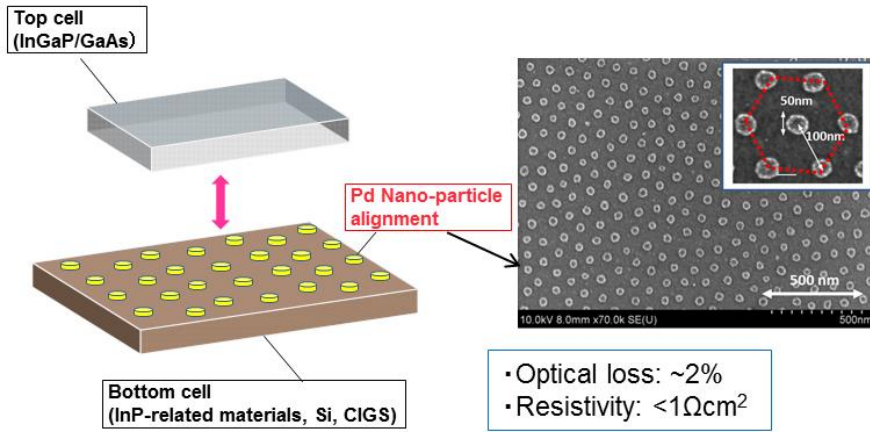


Fig.1: Schematic drawing of a stacking structure and a surface SEM image of Pd nanoparticle alignment.

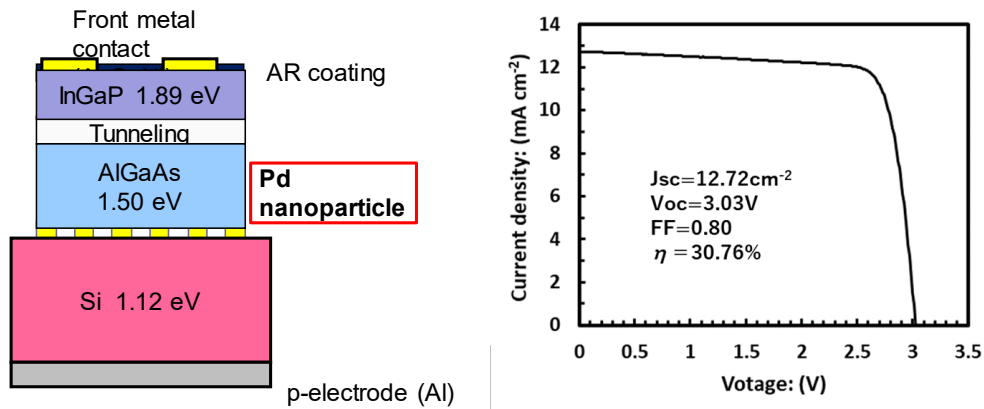


Fig.2: Schematic layer structure of an InGaP/GaAs/Si 3-junction solar cell and its I-V characteristics.

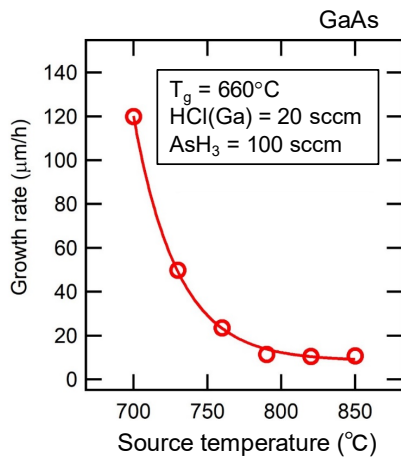


Fig.3: GaAs growth rates as a function of source temperatures.

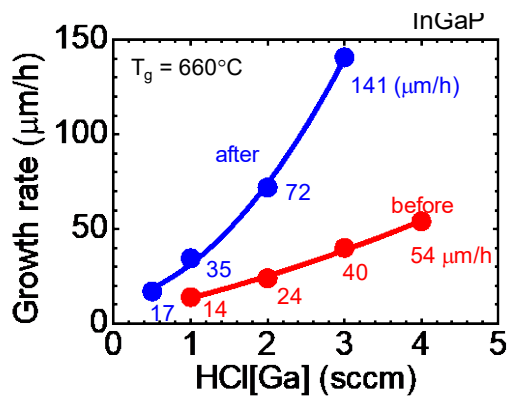


Fig.4: InGaP growth rates as a function of HCL flow rates. The nozzle shape is improved in HVPE reactor. Highest growth rate of  $141\mu\text{m/h}$  is realized by improving nozzle shape.

## Lattice-Matched Dilute-N GaNPAs on Silicon for Tandem Solar Cells

Y. Zou, R. Vatan Meidanshahi, C. Honsberg, and S. Goodnick<sup>1</sup>

*School of Electrical Computer and Energy Engineering, Arizona State University,  
Tempe, Arizona 85287, USA  
stephen.goodnick@asu.edu*

Silicon based photovoltaics has reached efficiencies of over 26% in recent years [1], which is close to the Shockley-Queisser limit for this technology considering Auger recombination. To exceed this limit while maintaining the substantial cost benefits of Si based technology, Si based multijunction (tandem) solar cells are currently of great interest, with an integrated top cell technology on Si having a bandgap of between 1.7-1.8 eV ideally. Based on detailed balance calculations, the conversion efficiency limit for a two junction tandem on Si with this top cell bandgap is close to 45%. One approach, investigated here, involves lattice matched III-V materials based on GaP and alloys thereof.

GaP is the only III-V material that is lattice matched to Si, however its bandgap of 2.26 eV is too large for good tandem performance in a series constrained epitaxial structure. Further, the interface between GaP and Si (100) is heterovalent, resulting in dangling bonds and subsequent interface state formation, in addition to the potential formation of antiphase domain defects in the III-V material, all of which degrade solar cell performance. We have recently investigated this interface through first principles modeling [2], in which various intermixed, terraced and hydrogen passivated structures were simulated. Hydrogen passivation is found to be most effective in bridging dangling bonds at the interface and resulting in nearly ideal heterojunction electronic structure (Figs. 1 and 2).

To reduce the bandgap to an acceptable range for Si tandems, dilute nitrides of GaP and GaPAs are currently being investigated in novel back contacted solar cell architectures. We have theoretically investigated the optical and transport properties of dilute nitrides latticed matched to Si using an  $sp^3d^5s^*s_N$  tight binding model in which  $s$ -like N orbitals are included in the basis set (Fig. 3), which gives excellent agreement with experiment (Fig. 4). Including a third terminal through inclusion of an interdigitated back contact (IBC) structure (Fig. 5), the three terminal maximum efficiency has a broad maximum over a wide range of top cell bandgaps, which loosens the material constraints on the epitaxial growth. Using the calculated absorption coefficients and low field mobility from the above tight binding model, we incorporate this into a TCAD model for the three terminal structure, and find in unoptimized structures, simulated efficiencies over 34% with realistic material parameters (Fig. 6).

[1] K. Yoshikawa *et al.*, Nat. Energy, **4**,17032 (2017).

[2] R.V. Meidanshahi *et al.*, Prog. Photovoltaics Res. Appl. **27**, 724 (2019).

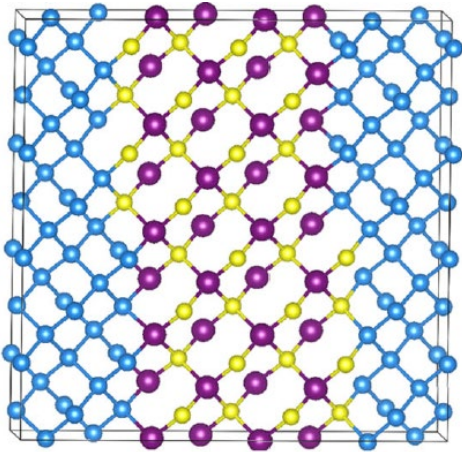


Fig.1: The atomic structure of the GaP/Si(001) supercell with single-layer terraced (1-Terraced) interface. The purple, yellow, and blue atoms correspond to Ga, P, and Si atoms, respectively.

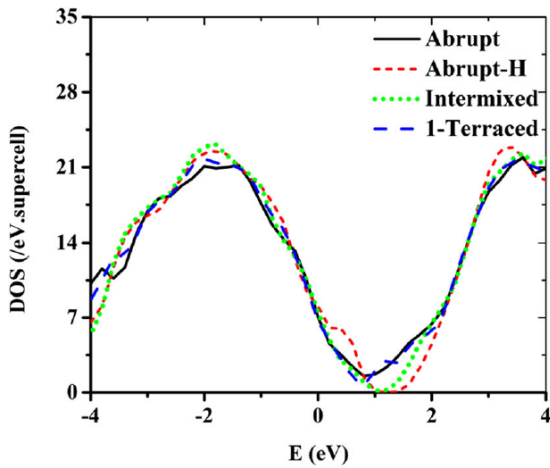


Fig.2: The electronic density of states of GaP/Si(001) with different interface atomic structure..

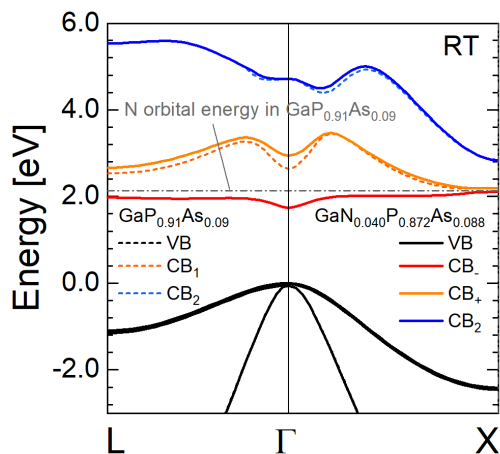


Fig.3: The band structure calculated from the  $sp^3d^5s^*$  model for  $GaN_{0.040}P_{0.872}As_{0.088}$  (solid lines) and from the  $sp^3d^5s^*$  model for  $GaP_{0.91}As_{0.09}$  (dashed lines).

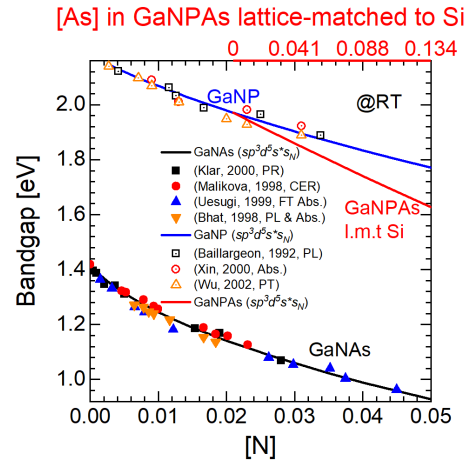


Fig.4: Calculated (solid lines) and reported experimental (symbols) bandgaps of dilute-N GaNP and GaNAs at room temperature (RT). The bandgaps of GaNPAs lattice-matched to Si are plotted from calculation (red solid line)..

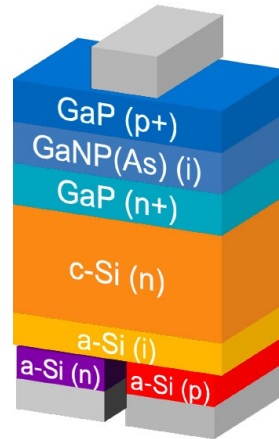


Fig.5: Schematic structure of a three terminal GaNP(As)/Si tandem solar cell structure..

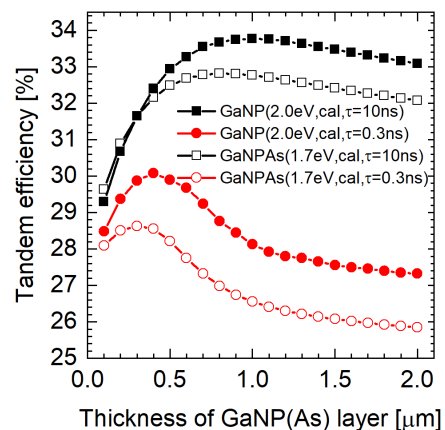


Fig.6: Calculated efficiency versus III-V layer thickness for different assumed trap limited lifetimes in the GaNP(As) layer..

## Hot Carrier Dynamics in Bulk and 2D Perovskites

V.R. Whiteside<sup>1</sup>, H. Esmailpour<sup>1</sup>, S. Sourabh<sup>1</sup>, G.E. Eperon<sup>2</sup>,  
M.C. Beard<sup>2</sup>, and I.R. Sellers<sup>1</sup>

<sup>1</sup>*Department of Physics & Astronomy, University of Oklahoma,  
Norman, OK 73019, USA*

<sup>2</sup>*National Renewable Energy Laboratory, Golden, CO 80401, USA*  
*vrw@ou.edu*

The effect of carrier-carrier and carrier-phonon interactions are presented in  $n = 1$  (2D)  $(\text{BA})_2\text{PbI}_4$  Ruddlesden-Popper thin films and their effect compared to that of conventional  $\text{MAPbI}_3$ . While temperature dependent photoluminescence (PL) shows the well-studied structural phase transitions and evidence of LO phonon scattering in  $\text{MAPbI}_3$ , the 2D  $(\text{BA})_2\text{PbI}_4$  films produce subtler properties. At low temperatures evidence of two competing intrinsic exciton transitions are observed, in addition to several extrinsic transitions attributed to impurities in the  $(\text{BA})_2\text{PbI}_4$  films. At higher temperature, the  $(\text{BA})_2\text{PbI}_4$  is dominated by two intrinsic excitons that are attributed to localization caused by deformations of the  $\text{PbI}_4$  framework mediated by the organic interlayers. Although both complexes are well separated from the continuum (490 meV or greater), their interaction with phonons is quite different. In the case of the more strongly bound (*deeper*) complex, the strong excitonic nature and short range interaction of this exciton is mediated by the emission of LO phonon replicas. In the case of the less localized (*shallower*) exciton with the lower binding energy and more extended wavefunction, the phonon interaction manifests itself in stronger carrier-phonon scattering and evidence of large, stable polarons.

These results suggest that hot carrier thermalization in perovskites is dominated by the strength and nature of the exciton-phonon interaction, which rather counter-intuitively can stabilize hot carriers even at elevated temperatures if large, stable polarons are formed. To support this hypothesis, comparisons of hot carrier dynamics and electron-phonon interactions in transient absorption and CW PL are made on a number of stable and well-studied perovskite thin films ( $\text{FAPbI}_3$ ,  $\text{FAPbBr}_3$ , and  $(\text{FA,MA})\text{PbI}_3$ ). Specifically, correlations are made between the LO phonon energy and broadening, electron-phonon interaction (Fröhlich coupling), exciton binding energy, and the presence and stability of hot carriers.

**Acknowledgment.** This work is funded through the Department of Energy EPSCoR Program and the Office of Basic Energy Sciences, Materials Science and Energy Division under Award No.# DE-SC0019384.

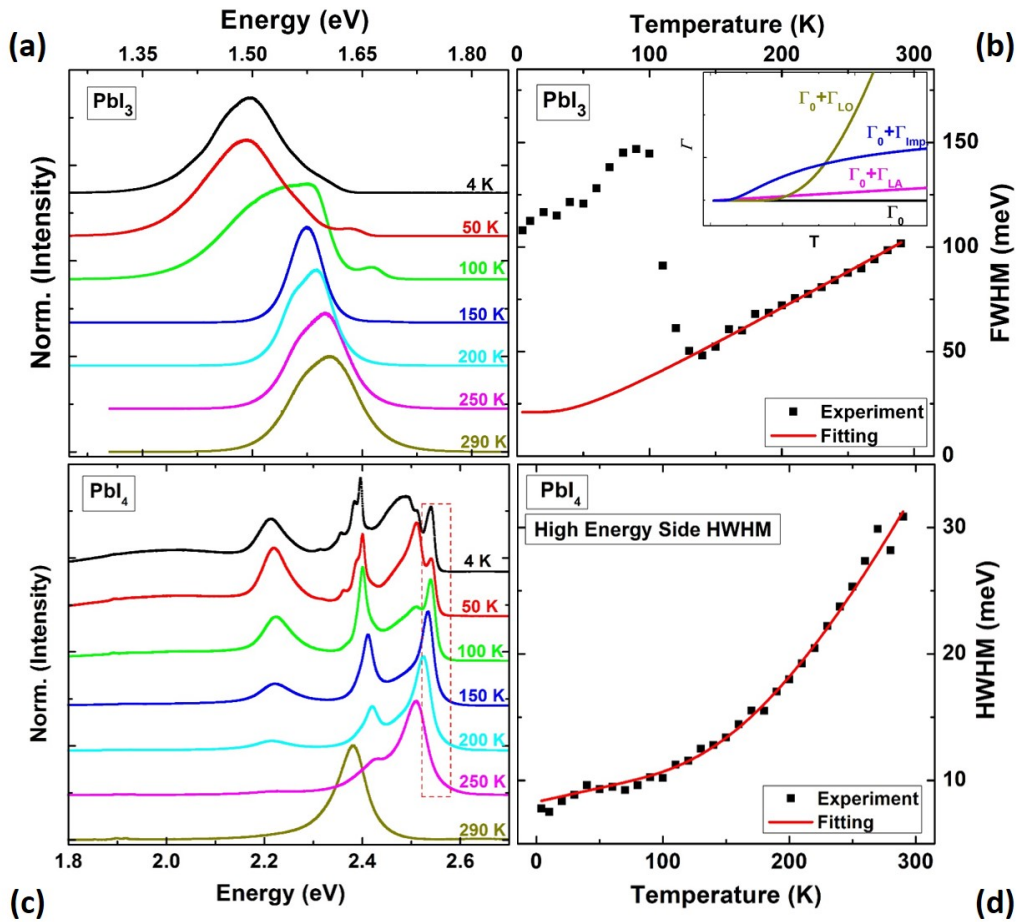


Fig.1: Temperature dependent PL from 4.2 K to 300 K, in 50 K increments for (a) MAPbI<sub>3</sub> and (c) (BA)<sub>2</sub>PbI<sub>4</sub>, respectively. The FWHM as a function of temperature is shown for MAPbI<sub>3</sub> in (b). The dependent HWHM for (BA)<sub>2</sub>PbI<sub>4</sub> is shown in (d). The inset to (b) shows the idealized temperature dependence of the various coupling parameters involved in the broadening of the PL. The red solid line is the fit to the data in (b) and (d).

## Valley Photovoltaics: Evidence for a True Hot Carrier Solar Cell

D.K. Ferry<sup>1</sup>, H. Esmailpour<sup>2</sup>, K.R. Dorman<sup>2</sup>, T.B. Mishima<sup>2</sup>, M.B. Santos<sup>2</sup>,  
V.R. Whiteside<sup>2</sup>, and I.R. Sellers<sup>2</sup>

<sup>1</sup>*School of Electrical, Computer, and Energy Engineering, Arizona State University,  
Tempe, AZ 85287, USA*

<sup>2</sup>*Homer L. Dodge Department of Physics and Astronomy, University of Oklahoma,  
Norman, OK 73019, USA  
ferry@asu.edu*

There has been an increasing attention to the possibility of hot carrier solar cells in recent years, as an approach to circumvent the Shockley-Queisser limit for single band gap cells [1-3]. Usually this has followed a plan of reducing LO phonon emission by invoking quantum wells and phonon bottlenecks as well as energy selective filtering of the extracted carriers. Recently, it was proposed that a true hot carrier solar cell could be created by the use of valley photovoltaics, where photo-excited carriers were created in, and extracted from, higher lying L valleys of the absorber conduction band [4]. Recent experiments using an InP/InAlAs/InGaAs/InAlAs structure with lightly doped In<sub>0.53</sub>Ga<sub>0.47</sub>As absorber layer has shown that carriers can be trapped, and extracted, via the L valleys effectively (Fig. 1), and that an open-circuit voltage of 1.38 V can be achieved [5]. The latter clearly violates the accepted bandgap limit for the open-circuit voltage. Several key properties have been presented that indicate this lofty goal can be achieved in the relatively near term: specifically, power independent (and 1-sun 300 K) hot carrier generation with operating voltages well in excess of the absorber band gap; evidence of scattering and harnessing of stable hot carriers across the solar spectrum; and the ability to harness low energy carriers via a combination of the long minority carrier diffusion lengths and subsequent interface (electric field) driven scattering of such carriers to the upper satellite valleys. However, barriers still remain to effective extraction of the carriers, and these must be overcome to achieve the desired results (Fig. 2).

[1] L.C. Hirst *et al.*, IEEE J. Photovoltaics **4**, 1526 (2014).

[2] J.A.R. Dimmock *et al.*, Prog. Photovoltaics Res. Appl. **22**, 151 (2014).

[3] V.R. Whiteside *et al.*, Semicond. Sci. Technol. **34**, 094001 (2019).

[4] D.K. Ferry, Semicond. Sci. Technol. **34**, 044001 (2019).

[5] H. Esmailpour *et al.*, *submitted for publication*

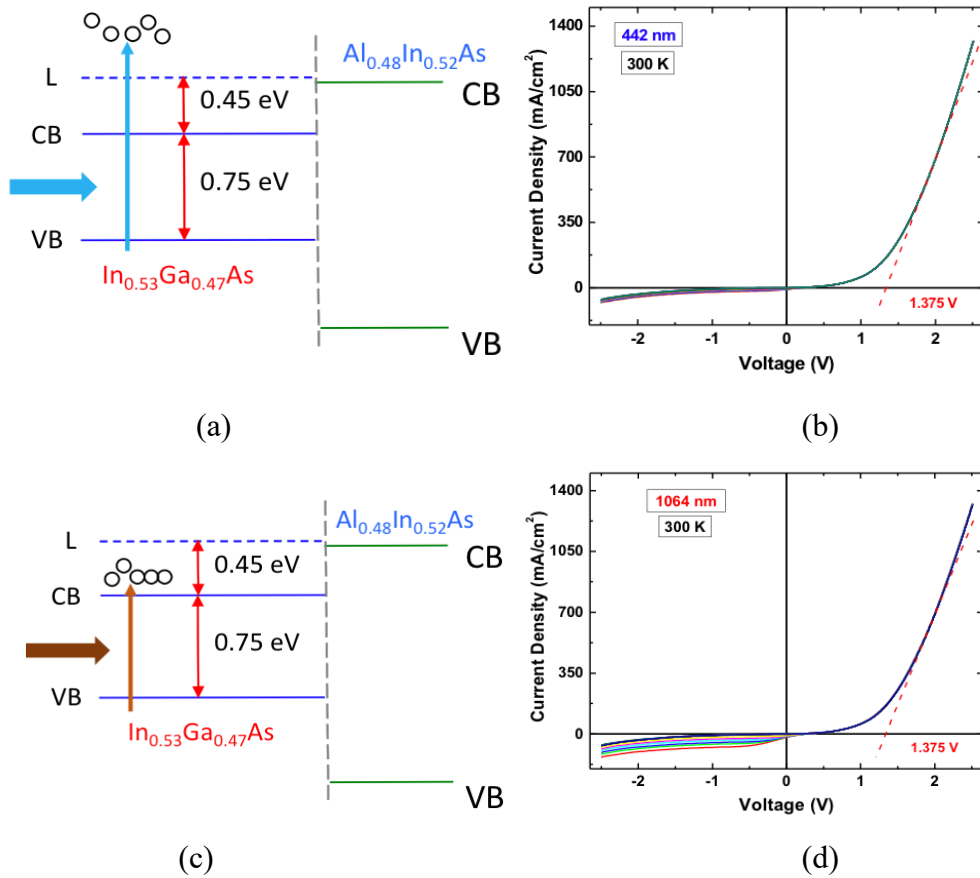


Fig.1: (a) Illustration of excitation by 442 nm laser of carriers above the L valley in the InGaAs, which results in (b) an open-circuit voltage greater than the band gap. (c) Excitation by 1064 nm laser of carriers below the L valley. (d) The resulting of the same open-circuit voltage shows that the very high electric field in the InGaAs excites carriers into the L valley, where they lead to the observed results.

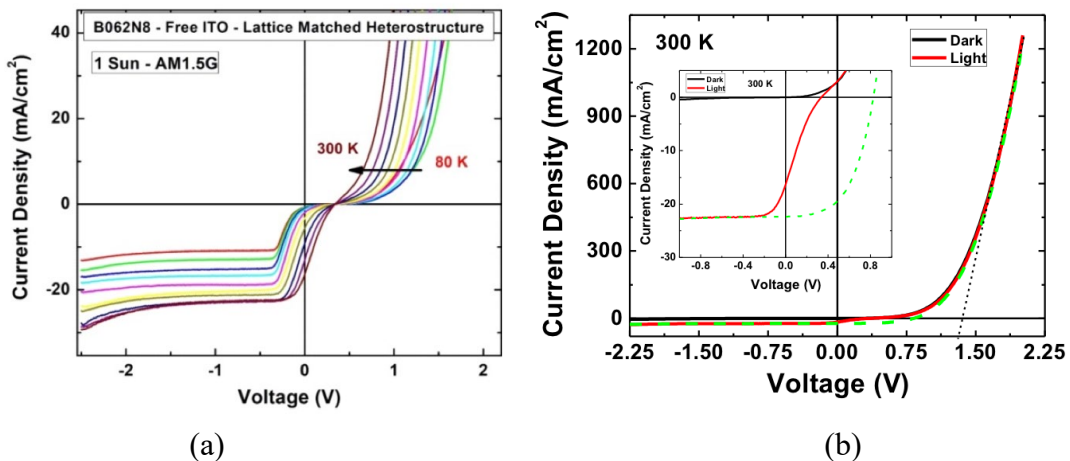


Fig.2: (a) Temperature effect on the cell under 1 sun illumination. (b) Comparison of light and dark current at room temperature and 1 sun illumination. The inset is a blowup of the region around the origin. The collapse of the current and reduction in the open-circuit voltage in the fourth quadrant is characteristic of a barrier to carrier extraction likely caused by the L valley in InGaAs trying to feed carriers into the  $\Gamma$  valley of the InAlAs (this requires a phonon with low probability). The green curve is an adjustment of the dark current to the peak reverse current and reflects the reduced open-circuit voltage of 0.82 V. This green curve has a fill factor of ~66%.

ISBN 978-0-578-61722-0



9 780578 617220